Thèse de doctorat
de
L'Universite Paris-Saclay
preparee a
Ecole Polytechnique

Ecole Doctorale n°573
Interfaces : approches interdisciplinaires, fondements, applications et innovation.

Spécialité de doctorat: Mécanique

Par

M. Cyprien Guermonprez

Plateforme microfluidique pour des mesures de la croissance
bactérienne en gouttes.

Thèse présentée et soutenue à Palaiseau, le 13 Décembre 2016 :

Composition du Jury :

M. Didier Mazel	Professeur, Institut Pasteur	Président
M. Jean-Christophe Barret	Professeur, Université de Bordeaux	Rapporteur
M. Axel Buguin	Professeur, Université Pierre et Marie Curie	Rapporteur
Mme. Cécile Cottin-Bizonne	Professeur, Université de Lyon	Examinateur
M. Charles Baroud	Professeur Ecole Polytechnique	Directeur de thèse
M. Sébastien Michelin	Professeur Ecole Polytechnique	Co-directeur de thèse

Titre : Plateforme microfluidique pour la mesure de la croissance bactérienne en gouttes.

Mots clés : Microfluidique, Goutte, Microbiologie, Croissance bactériene.

Résumé : Dans ce manuscrit, nous présentons une nouvelle puce microfluidique pour l'étude de la croissance de bactéries. Nous étudions tout d'abord la production de gradient de soluté dans des canaux microfluidiques pour créer, dans n'importe quelle puce microfluidique, différents environnements chimiques. Ensuite, nous développons une deuxième plateforme permettant l'encapsulation de bactéries avec leur milieu de culture dans des micro-gouttes. Ces gouttes sont directement produites dans un tableau où elles sont stockées. La spécificité de cette technologie réside dans la production des gouttes de façon passives grâce à un système de pièges capillaires intégrés dans la géométrie de la puce. La répartition initiale des bactéries dans les gouttes suit une distribution de Poisson donnant lieu à des mesures précises de la concentration en bactéries dans l'échantillon de départ. Cette distribution est en outre utilisée pour identifier des symbioses entre plusieurs espèces bactériennes. Le stockage des gouttes à des emplacements fixes permet le suivi individuel de chaque contenu de goutte au cours du temps. Contrairement au mesure classique de croissance bactérienne, nous sommes en mesure de suivre 1 500 courbes de croissance ce qui donne accès aux distributions statistiques de chacun des paramètres de croissance. Des gouttes gélifiées sont utilisées pour récupérer chaque goutte individuellement en dehors de la puce afin de réaliser des analyses plus approfondies lorsqu'un phénotype particulier est détecté. Enfin, les deux plateformes sont combinées en une troisième puce pour étudier la réponse des bactéries aux traitements antibiotiques. Nous présentons comment peuvent être réaliser des antibiogrammes avec 13 concentrationS sur cette ultième puce avant de l'utiliser pour faire des tests de susceptibilité aux antibiotiques avec des mesures digitales ou dynamiques.

Title : Droplet-based Microfluidic Platform for Quantitative Microbiology

Keywords : Microfluidic, Droplet, Microbiology, Bacteria growth.

Abstract : In this work, we present a new microfluidic platform dedicated to the study of bacteria growth in constant or varying environment. The production of different environments is first investigated through a concentration gradient producer adaptable to any microfluidic device. Then, a second device is presented, in which bacteria cells are encapsulated in nanoliter droplets with nutrient and stored in a large array. The novelty of the developed technology relies on the passive production of thousands of droplets thanks to capillary traps hard-coded in the chip geometry. The initial distribution of the bacteria cells follows a Poisson distribution which allows precise cell concentration quantification and novel perspectives for bacteria symbiosis investigation. The fixed location of the droplets in the array allows for the visual inspection of any of them in time. Contrary to classical bacteria growth measurements, we follow $1,500$ growth curves in parallel which leads to the statistical distribution of each individual growth parameters. In addition, the use of gelified droplet enables the recovery of any individual droplet out of the chip. Extracted bacteria cells are viable and thus, suitable for further analysis when specific phenotypes are identified. Finally, the concentration gradient producer is combined with the bacteria culture platform to study the bacteria response to antibiotic stresses. This final chip is first used to perform antibiograms by testing 13 antibiotic concentrations on a single chip. Then, it is extended to drug susceptibility testing to antibiotics with end-point or dynamical measurements.

Droplet-based Microfluidic Platform for Quantitative Microbiology

Cyprien Guermonprez

Remerciements

inconditionnel dans toutes mes lubies.

Résumé de la thèse en français

Dans ce manuscrit, nous présentons une nouvelle technologie microfluidique dédiée à l'étude de la croissance de bactéries. Cette technologie se décline sous deux versions, l'une permettant de créer plus d'un millier de cultures bactériennes identiques sur quelques centimètres carré, l'autre permet de cultiver des colonies de bactéries dans différents environnements chimiques. Cette thèse a pour but de détailler le fonctionnement de la technologie ainsi que d'en présenter les applications potentielles. Le travail est organisé en quatre chapitres.

Nous étudions tout d'abord la production de gradient de soluté dans des canaux microfluidiques pour créer, dans n'importe quelle puce microfluidique, différents environements chimiques. Ce chapitre donne une explication des principes physiques à l'origine de la création du gradient chimique dans un réseau d'échelle. La création du gradient s'avère dépendre de deux paramètres sans dimension, d'une part le ratio entre les résistances hydrodynamiques du canal de distribution et des branches où s'établit les différentes concentrations en soluté et d'autre part le nombre de Péclet, ratio entre les temps caractéristiques d'advection et de diffusion. Le premier est entièrement déterminé par les paramètres géométriques du réseaux d'échelle et n'est pas impacté par les propiriétes physiques des fluides utilisés (viscosité, tension de surface, ...). Pour une géométrie fixée et un soluté donné, le nombre de Péclet est ajustable seulement en modifiant le débit en entrée de puce, cela permet d'atteindre trois profiles de gradient sans changer le design de la puce allant du profile constant au profile sigmoïdal en passant par le profile linéaire. La compréhension des éléments fondamentaux de la création du gradient nous permet d'étendre le principe au cas de large chambre microfluidique pour la production d'un gradient continu et l'adapter à notre plateforme de culture bactérienne présentée dans le deuxième chapitre.

Cette plateforme permet l'encapsulation de bactéries avec leur milieu de culture dans des gouttes de 2 nL. Ces gouttes sont directement produites dans un tableau où elles sont stockées. La spécificité de cette technologie réside dans la production des gouttes de façon passives grâce à un système de pièges capillaires intégrés dans la géométrie de la puce. Cette technique assure un contrôle précis de la taille des gouttes et permet la réplication de 1 495 micro-environnements identiques sur quelques centimètres carré. Un suivi de la croissance des bactéries a montré que leur croissance est limitée par la quantité de nutriments disponibles initialement dans chaque goutte. Même si la quantité de nutriment est identique pour chaque goutte, la répartition initiale des bactéries dans les gouttes suit une distribution de Poisson dont le paramètre caractéristique dépend de la concentration initiale en bactérie et le volume des gouttes. Ainsi, une mesure précise de la concentration en bactéries dans l'échantillon de départ peut être déduite du nombre de gouttes vides après incubation. La deuxième partie du chapitre explore le potentiel de cette distribution notamment pour identifier des compétions ou symbioses entre plusieurs espèces bactériennes. Dans le cas d'interactions, une analyse plus fine des gouttes d'intérêt est rendue possible

grâce à un système de récupération individuelle avec un système de dé-gélification à l'aide d'un laser infra-rouge.

Le stockage des gouttes à des emplacements fixes permet le suivi individuel et en parallèle de chaque contenu de goutte au cours du temps. Plus d'un millier de courbes de croissance peuvent ainsi être établies sur une seule puce. Une mesure des paramètres de croissance communément mesurés sur les courbes de croissance de population résulte en distributions statistiques des paramètres individuels. Contrairement aux mesures classiques de croissance bactérienne qui donne accès au comportement au niveau de la population, les distributions de paramètres de croissance permet d'observer les comportements individuels, notamment les dynamiques de croissance des bactéries qui se divisent lentement car elles sont souvent supplanté par une croissance excessive des cellules qui se divisent plus rapidement et consomme donc une plus grande quantité de nutriments. Un premier déblayage des différentes méthodes de modélisation de la croissance bactérienne est aussi fourni. Le développement de modèle de croissance permettrait de remonter à des information au niveau de la division cellulaire.

Enfin, le producteur de gradient et la plateforme de culture bactérienne sont combinées en une troisième puce pour étudier la réponse des bactéries aux traitements antibiotiques. L'application d'un gradient de concentration spatialement stable sur la plateforme de culture répète 115 fois 13 concentrations différentes. La puce est utilisée pour faire des antibiogrammes avant d'étendre le spectre des possibilités aux tests de susceptibilité aux antibiotiques avec des mesures digitales ou dynamiques.

Ce travail donne une preuve de concept technologique de la plateforme microfluidique. Son couplage avec un instrument d'automatisation les procédés de chargement et d'incubation permettrait sa pénétration dans des milieux non spécialistes comme des laboratoires de microbiologie. Un certains nombre d'applications ont dors et déjà été débutées comme la découverte de nouvelle conditions de culture *in vitro* pour des bactéries non cultivable en dehors de leur milieu naturel ou encore l'étude de l'émergence de la résistance aux antibiotiques. Avec le nombre de plus en plus important de corrélation établies entre notre environnement microbien et notre santé, l'utilisation d'une telle technologie aura d'importantes retombées économiques et sociétales.

Contents

Chapter 1

Introduction

In the early days of microfluidics, physical studies of single or two-phase flow in microchannels were devoted to the development of new methods enabling elementary operations on a fluid sample. The similarities between the electronic governing equations and the linear relationship between the pressure and the flow rate for laminar flows inspired the development of electronic equivalent systems such as the multiplexed micro-valve techniques that allow for complex fluid handling, compartmentalization and peristaltic pumping.[1] Single phase flow also investigated problematics of fluid mixing through the production of concentration gradient using tree-like architectures,[2] transversal diffusion systems,[3,4] Taylor-Aris dispersion[5] or serial dilution.[6] The use of multiple-phase flow led to the development of droplet microfluidics. In this area, different methods of droplet production were invented in the early 2000s, from T-junction breakup[7] to capillary flow-focusing[8] and planar flow-focusing.[9] Beyond droplet production, various techniques of droplet sorting were also proposed, either by dielectrophoresis,[10] by optical means,[11] or through the use of surface acoustic waves,[12] in addition to methods for merging or breaking drops, or mixing their contents.[13,14]

Once the protocols for individual operations were established, they were combined together to create platforms that integrated multiple operations. For example, a platform coupling droplet production and sorting was used to perform directed evolution of enzymes. This enabled screening of libraries of $\sim 10^7$ enzymes and selection of rare mutants with enhanced catalytic rates.[15] These advanced results are only possible through the use of microfluidics techniques which display specific abilities for fast analysis, high-throughput screening, process automation, parallelization and integration of numerous operations on a single chip. Thus, further development of microfluidics is expected to enable the emergence of other applications especially in microbiology. The whole process of combining basic operations into multifunctional platforms and then the development of new specific applications allowed microfluidic technologies to mature and to emerge on the 'slope of enlightenment' in the Gartner Hype Cycle (Fig. 1.1 and[16]) with the first entrepreneurial success stories like
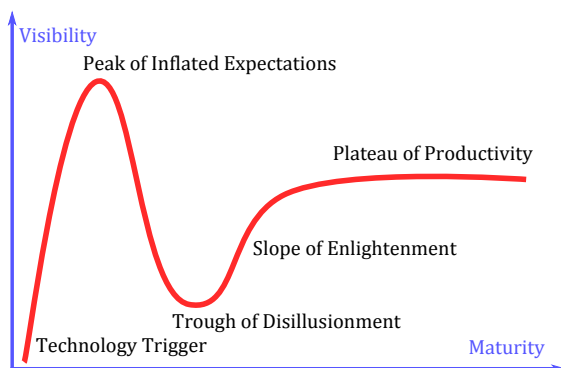
Figure 1.1: Gartner Hype Cycle describing the maturation stages encountered by a new technology.

RainDance, Fluidigm and Stilla Technologies – a spin-off start-up from LadHyX.

1.1   Current challenges for new microfluidics devices

In spite of the large number of droplet-based microfluidic tools that have appeared lately, their penetration into non-specialist labs remains limited. The multiwell plates are still preferred for quantitative measurements in biology labs rather than microfluidic devices. In addition to its versatility and ease of use, the multiwell format features several key functionalities: (i) samples are isolated in their respective wells; (ii) well contents can be monitored in real time; (iii) the contents can be stimulated several times by pipetting additional compounds into the wells; and (iv) each well population can be retrieved separately at any time for further processing. To date, the two microfluidic systems that come closest to integrating this whole range of functionalities are single-phase and valve-based devices,[17] and electrowetting-on-dielectric (EWOD) chips.[18,19] Both systems are programmable, they can address a broad range of problems from DNA extraction[20] to chromatography[6] . However, this comes at the cost of complex microfabrication processes, and an increasing complexity of the device manipulation when the number of reaction steps becomes large.

There has recently been a rise in awareness to the importance of developing simpler microfluidic protocols, while maintaining a high standard on the device robustness.[21,22] In line with these preoccupations, droplet microfluidics has attracted broad attention.[23–30] Compared with valve-based and EWOD devices, droplet microfluidic systems rely on easier microfabrication and are better suited to handle large numbers of reactions. Several droplet-based renditions of a multiwell plate have been proposed, in the form of static arrays of droplets.[23] Many of these variations consist in designing quasi-2D geometries, where linear channels are connected to in-line or side pockets for droplet storage.[31–36] In other cases, droplets are stored in truly 2D chambers. These ensure a high degree of robustness since they are very tolerant to flaws or impurities. Indeed, in a linear channel the

presence of a single defect or dust can block all downstream flow, while in a wide chamber the liquid simply flows around the impurity. In such 2D geometries, storage is performed either using traps[37,38] or simply by packing the droplets in large chambers.[39–41] In all cases, sample encapsulation and droplet monitoring are readily achieved. Yet, only a couple of platforms allows for the addition of a new stimulus to the encapsulated cells,[23,35] and none offer solutions for single-droplet retrieval.

1.2   Existing technologies for bacteria cells studies

The idea of encapsulating bacteria cells in nanoliter droplets is not novel. A recent work of Kaminski *et al.*[22] nicely reviews the existing techniques in droplet-based microfluidics for microbiology. Interestingly, they compare droplet-based microfluidics to the other existing techniques for bacterial culture along two axes : the level of control over the culture process and the scale of the miniaturisation and parallelisation. The advent of microfluidics enabled not only to scale down the size of compartmentalization of the bacteria culture sampling, but also the automation of complex protocols often encountered in biological experiments. This automation enables for higher throughput of operations and analysis. The miniaturization of culture compartments has also brought out three different levels of observation for bacteria proliferation namely population, colony and single cell levels, with each level giving access to different types of information.
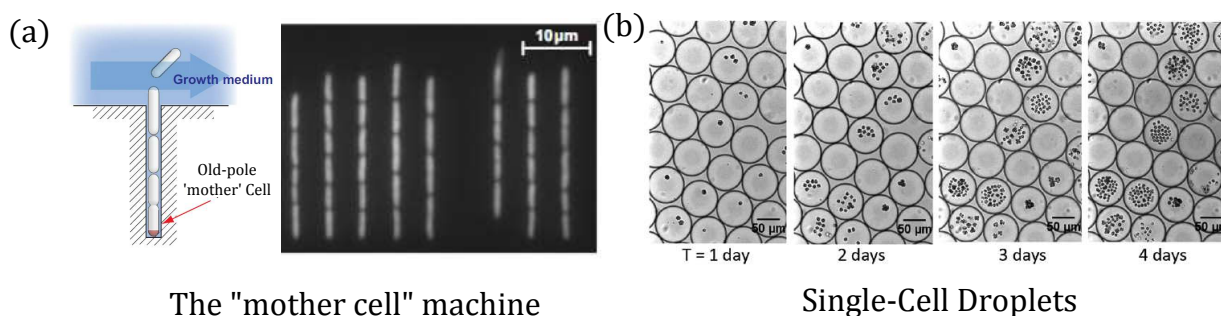
Figure 1.2: Figure extracted from.[42] a) Mother Cell Machine snapshot which allows for single cell analysis.[43] b) Single-cell culture in droplets.[39]

1.2.1   Correspondence between bacteria growth technique and level of observation

Classical techniques such as the Petri dishes and micro-well plates provide information at the population level by describing the global population behaviour. These techniques have fashioned the way microbiological experiments are made today. Yet, they give no insight

on the composition of the population : are all bacteria cells identical? Are they ageing or dividing all the same way with the same dynamical properties? This limitation was exposed by novel microfluidic techniques such as the mother cell machine (Fig. 1.2a).[43] This machine traps individual cells in microchannels and cultivates them in a continuous tangential flow of culture medium. With such technology, quantitative measurements were performed at the cell level with a very high precision, which led to the study of cell ageing[43] or the elucidation of major cell division mechanisms.[44] Such experiments highlighted an inherent stochasticity within bacterial populations in terms of division events timing or division size. Even though the mother cell machine permits very high content information on the stochastic behaviour of individual cell division, it fails to integrate the social interactions that often play a key role in the bacteria cell development. This is rendered observable at the colony level. A colony is defined by all the descendants of a single cell confined at the same location as in a droplet for example (Fig. 1.2b). This level of study gives access to the variability of the physiological parameters between monoclonal populations of a same species.

Each level of observation can also be characterised by its culture principle.[22,42] The observation of population or colony levels is generally performed in batch systems. Batch cultures confine cells in a finite space (e.g. microfluidic chambers, droplets or microwells) giving access to a finite amount of nutrient. Such structures are associated to a poor control of the cultivation environment. The secreted metabolites[1] are indeed accumulating in the batch during the cell proliferation. More robust environmental control is ensured by the mother cell machine which maintains a constant culture medium flow that rapidly diffuses towards the old-pole mother cell (Fig. 1.2a). As some regulatory systems of the cell metabolism are extremely sensitive, minor changes in the microenvironment may rapidly result in the regulation of the cell cycle.[42] This is why a precise control of the environment is generally required for finding quantitative relations between physiological parameters and the extracellular environment. Finally, as each scale of observation corresponds to different cultivation environments, different levels of controllability and different range of information, this will result in different types of model to describe or predict bacteria growth within those systems. In the same way that quantum mechanics deals with stochastic equation and the classical mechanics with deterministic laws, the single cell level is better described by random processes while growth curves of bacteria population are ruled by deterministic equations systems.

1.2.2   Existing droplet-based technologies

Some droplet-based microfluidic technologies for microbiology already exist. They are mainly dedicated to bacteria susceptibility to antibiotics testing,[36,45,46] bacterial social in-

---

[1]Metabolites describe all the chemical secreted by cells during their growth.

teraction[47,48] or lineage evolution.[49] Leung *et al.*[50] proposed a programmable valve-based device made of an array of 95 chambers that is used to trap droplets containing bacteria cells (Fig. 1.3a). The device can expose any individual chamber to any combination of 8 reagents allowing them to identify taxonomic genes or perform whole genome amplification on the bacteria strain *S.typhimurium*. The advantage of using valves relies on the addressability of the system such that each chamber content can be individually and dynamically monitored. However, the microfabrication and the programming of such device is complex which limits its adaptability to a broader range of applications as well as its use in non-specialised fields. Even though a large spectrum of reagent combinations is programmable, the number of repetitions is limited by the number of the chambers, which does not enable quantification of the variability between the bacterial colonies.

Baraban *et al.*[46] developed a Millifluidic Droplet Analyser (MDA, Fig. 1.3b) to investigate bacteria growth raising the number of droplet up to a thousand. Droplets are stored in tubings system rolled around two cylinders. By controlling the flow rate of the continuous oil phase, droplets can be easily monitored and observed. Droplets content is determined as they pass by an optical detector. The temperature of the whole device can be also maintained at 37 °C, which enables to follow the dynamical properties bacterial colony growth. For long term cell culture, their robotic system can add fresh medium as well as oxygen. The monitoring of the inlets flow rates allows for the production of concentration gradients between the droplets for drug testing or to apply a selective pressure on bacterial populations.[51] The technology is however limited by the complexity of the surrounding robotic system and the cumbersome cylinders for the droplets storage. In addition, the droplets are monitored in a one-dimensional tubing which fixes a minimum time to observe the whole set of droplets and enables the retrieval of droplets out of the chip at a single point of the tube. This impedes the parallelization of the extraction process.
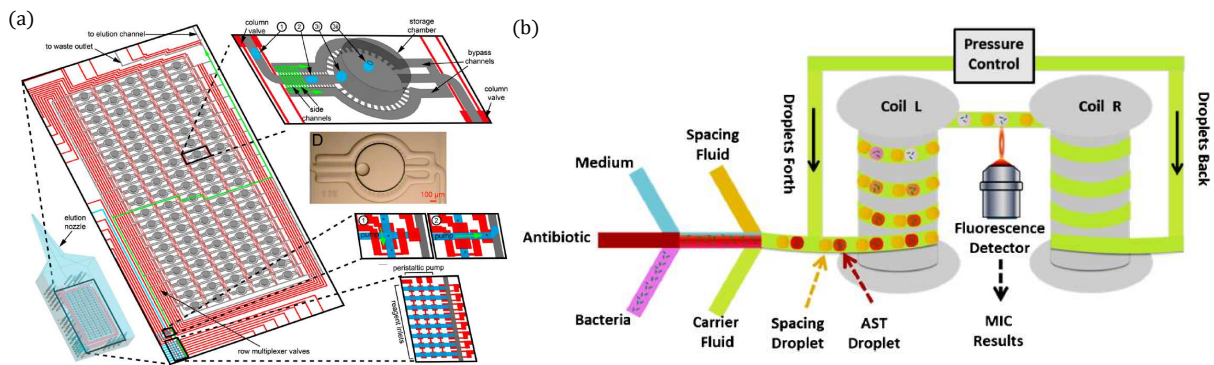
Figure 1.3: a) Valve-based device developed by Leung *et al.*[50] b) The MDA instrument developed by Baradan *et al.*[46]

The two presented technologies show how basic microfluidic operations can be combined. However, the integration of multiple features renders the microfluidic devices highly com-

plex. An interesting way to simplify the microfluidic operations is to hard-wire the fluid handling in the chip geometry. Derszi *et al.*[36] developed a microfluidic platform (Fig. 1.4a) that requires only 5 pipetting steps to perform an antibiogram with 11 concentrations of ampicillin on *E.coli* (Fig. 1.4b). The novelty dwells in the absence of external pumping system to control the formation of sub-microliter droplets. Therefore, such technologies require no instruments specific to microfluidics labs and are easily integrable in existing microbiological protocols. The use of the passive pumping based on capillary forces recalls the paper-based microfluidics technologies or other open microfluidics platforms.[26] Their designs require deep insights on the physical properties of the fluids and also a precise synchronisation of the operation handlings. This can limit its parallelization to a higher number of repetitions and device operations.
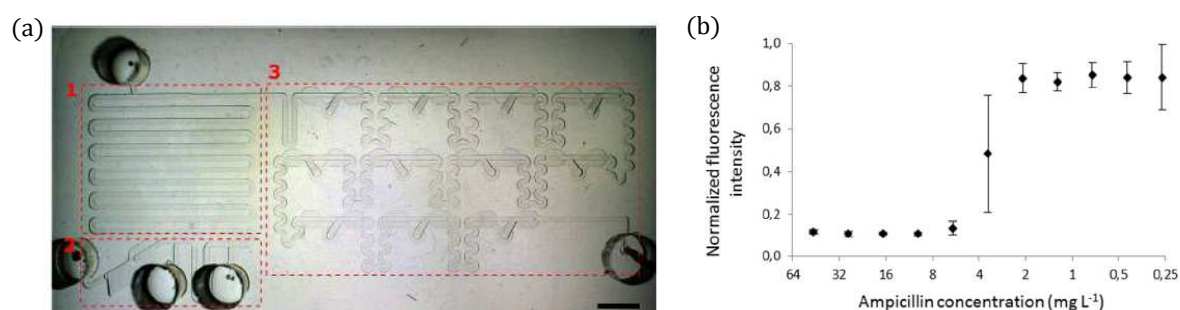
Figure 1.4: a) Chip design by Garstecki's group for easy fluid handling operations. b) Resulting antibiogram of *E.coli* for ampicillin. Extracted from.[36]

1.3   Objectives and structure of the thesis

In this PhD thesis, a droplet-based microfluidic platform is developed for the quantification of bacteria growth in varying environment. This work establishes the technological framework for future fundamental applications in biology. The development of such technology does not rely only on the hardware design but also on the demonstration of the platform capabilities in term of cell observation, microbiological operations, control of cell environment and data analysis. The multiplicity of the chip operations results from the integration of a large panel of complementary scientific backgrounds, which renders this manuscript highly multidisciplinary. Briefly, the hardware design integrates fundamental studies on surface tension, advection-diffusion and laminar flow distribution in micro-channels (physics and mechanics). Parallel observation of thousands droplets with the corresponding data extraction require the programming of a software (informatics). The theoretical tools developed for the analysis and the modelling of the experimental data rely on applied mathematics results. Finally, the design of bacterial strains that emit fluorescent protein and the understanding of their main physiological parameters with or without antimicrobial stress

request fundamental knowledges in microbiology.

The particularity of the presented technology relies on the hard-coding of the chip features in its geometry. This renders the technology versatile, robust and easy to use which meets the current challenges identified for new microfluidic technologies. The platform integrates more than 10 years of microfluidic research in Charles Baroud's group. It consists in the production of $1,495$ static aqueous droplets in fluorinated oil in a two-dimensional array. The droplets production is based on the capillary trap principle[28,52] and is combined with a concentration gradient producer which enables the application of external antibiotic stresses on the encapsulated bacteria cells at various intensities. The array structure enables also the direct visualisation of each droplet for time-resolved measurements and the individual retrieval of any of them at any time.
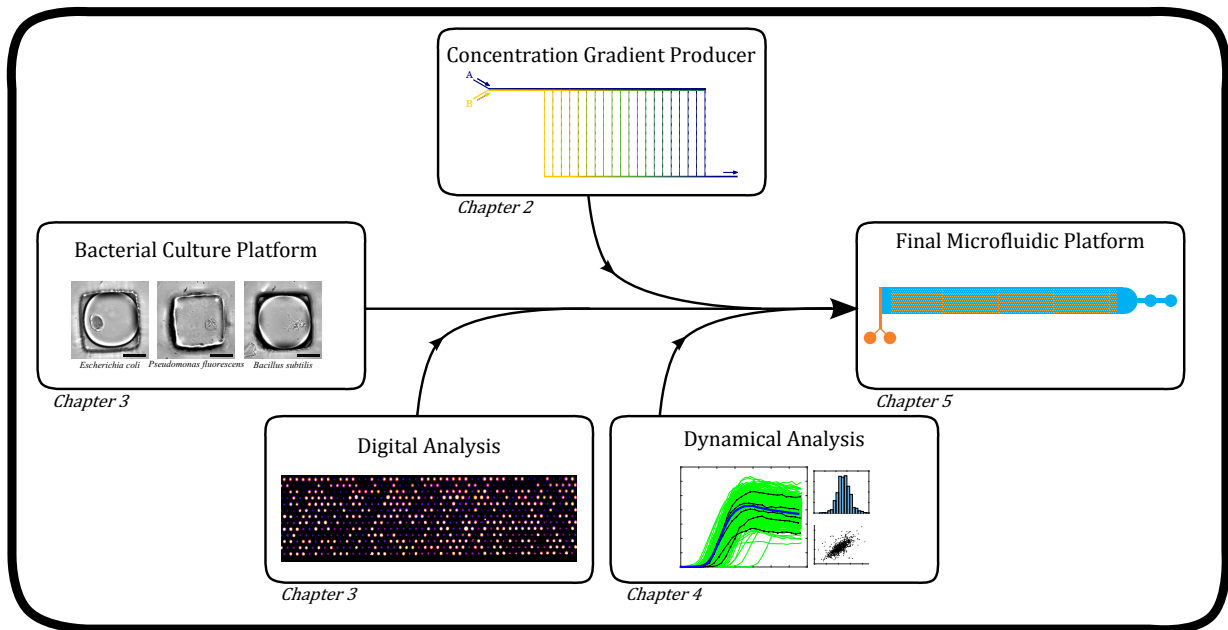
Figure 1.5: Organisation of the manuscript. Each block is assembled in a single microfluidic platform.

As the developed microfluidic chip integrates several functionalities, the thesis is organized such that each level of the device complexity is either developed independently (chapter 2) or added step by step (chapters 3 and 4) until the last chapter where the developed features are all combined together in a final platform with a demonstration of its abilities for the drug susceptibility testing on bacteria cells. Figure 1.5 illustrates the structure of the thesis by presenting each block of the final microfluidic chip. At each newly added block, we present the experimental protocols, develop the theoretical background and explore the potential microbiological applications conferred by the supplementary features.

This work has led to the publication of two papers. The first paper[53] presents the first block on the concentration gradient producer. The second paper[54] gathers most of the technological features developed in chapters 3,4 and 5.

1.4   Manuscript Contents

In the chapter 2, the theoretical study of a microfluidic ladder network allowing for the production and control of a concentration gradient is presented. By performing the study of the fluid dynamics we are able to predict the distribution of a given solute inside the device. This first block provides physical insights on the gradient production and control lead us to define design rules for its adaptation to a larger range of microfluidic devices and especially our bacteria culture platform.

Chapter 3 introduces the 'generic chip', the second block of our technological development. It corresponds to a simple design for the production of static droplets anchored in an array of capillary traps for bacteria cell culture. First, the experimental protocol to grow any bacterial strain is described in addition to the on-chip culture conditions characterisation. Then, the extraction of any particular droplet of interest out of the chip is investigated. For the retrieval, an external infra-red laser is used to avoid additional microfluidic operations for droplet handling inside the chip. Bacteria cells can be genetically modified to express fluorescent proteins while they are growing. The distinction between empty and non-empty droplets is therefore easily determined on inseminated chips after their incubation. This end-point measurement constitutes the third block of the study and it is called the 'digital analysis'. It provides a binary result of the growth or no-growth in a given droplet. Using the Poisson theory, the initial cell concentration can be quantified and the mean initial number of cells per droplets estimated. The extension of the digital analysis to several species yields potential detection of competition or symbiosis between bacterial species with solely a single time point analysis.

In chapter 4, time-resolved measurements are added to the digital analysis. These provide further information on the dynamical properties of bacteria growth. This fourth block increases the information content that we can extract from the chip for even more quantitative analysis. We first define the dynamical parameters used to characterise bacteria growth and review the classical model underlying those parameters. Then, the software developed during the PhD is presented. It allows for the establishment of growth curves from the timelapse experiments. This is followed by the analysis of the growth curves that highlights the natural variability observed within bacterial populations. The confrontation of our experimental measurements of parallel bacterial colonies with the existing models and culture techniques helps us to define guide lines for the development of a stochastic

model which would simulate on-chip bacteria growth.

The four blocks developed above are combined in chapter 5. After a review of the current challenges for drug susceptibility testing, the microfluidic concentration gradient producer is adapted to the generic chip in a single microfluidic chip. This provides a way to apply and monitor antibiotic stresses to bacterial culture in a dynamical fashion. Both digital and dynamical analysis are also integrated to study the impact of antibiotics on bacteria growth, from the susceptibility curves establishment to the dynamical response of *E.coli* to aminoglycosides.

Chapter 2

Concentration Gradients in a Microfluidic Network

In this chapter, the first block of the final device is built by studying the distribution of flow rate and solute concentration within a network of parallel microfluidic channels with a single input and single output. Using a combination of theoretical modeling and microfluidic experiments, we aim to obtain general design rules to adapt the presented gradient producer to any type of microfluidic design.

The low value of the Reynolds number (Re) typical in microfluidics inhibits efficient mixing of different species. This in turn places significant obstacles to the generation of controlled concentration contrasts, for example for cell migration,[55] protein crystallisation tests,[56] or enzyme kinetics measurements.[57,58] In response to this constraint, several methods have been suggested for generating controllable concentration gradients in microchannels, taking advantage of the reproducible laminar flows. For example, successive fusions of highly concentrated initial droplets with droplets of pure solvent has been shown to produce a train of droplets with varying conditions .[23,59,60] Taylor-Aris dispersion was also used to establish a streamwise concentration gradient, which was then encapsulated into individual droplets.[61]

In single-phase flows, several devices combining solute diffusion with a flow in a network of channels have been developed in order to tailor a concentration profile of one or several solutes.[3,62,63] In those system, the distribution of the diffusing species is determined by the relative importance of advection by the solvent's flow and diffusion of the solute,[62] which can be used to tune the concentration profile in a given device. Indeed, although the flow distribution does not depend on the total flow rate for low Re flows, the time available for diffusion to operate will decrease with higher flow rates. This has been shown to play a major role in determining the final concentration gradient.[62]
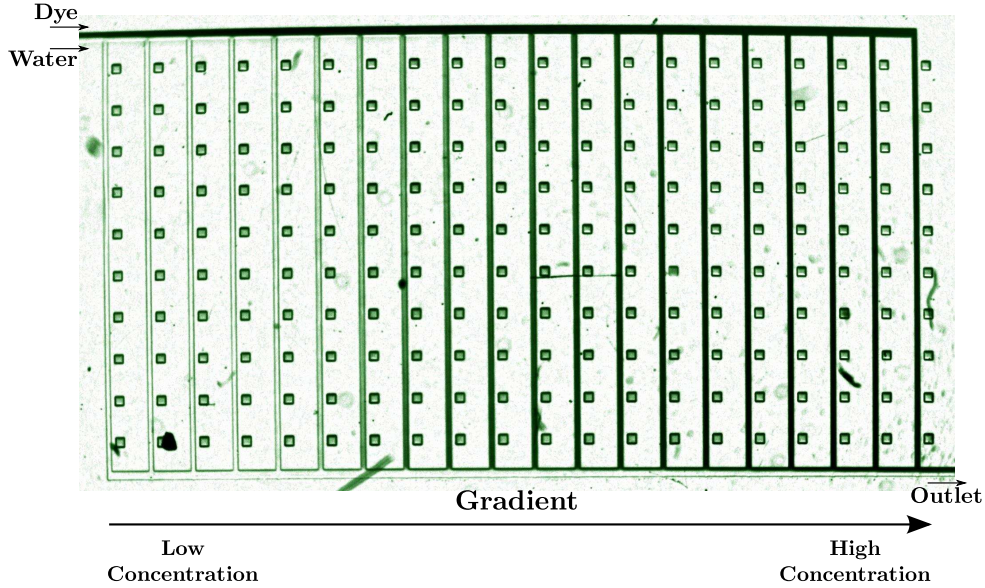
Figure 2.1: Experimental image of the ladder network with a dye concentration. Two streams (dye and pure water) are injected from the top-left region and flow into the network, before exiting from the outlet at the bottom-right. A concentration gradient is formed in the parallel vertical channels.

Few studies have however modeled the concentration distribution within such devices analytically[3] or numerically.[64,65] Here, we present a new modeling approach that provides theoretical foundation for the physical understanding of the gradient generation control while focusing on a particular gradient-generating device initially introduced by Selimović et al.,[65] as shown in figure 2.1. Compared with the well known tree-like geometry,[62] this device allows for the production of a gradient on a smaller footprint and in a more robust manner. We extend the observations of Selimović et al.[65] by providing a simplified physical model based on two dimensionless parameters. We show that the solute gradient can be tailored by controlling these two parameters, and we provide design tools for adapting the device to more complex microfluidic networks.

After describing the experimental parameters in Section 2.1, we model the flow distribution in the parallel ladder network in Section 2.2. This distribution displays a non-trivial U-shaped velocity whose depth is determined by a single geometric parameter that describes the ratio of fluidic resistances in different parts of the network. Once the flow-rate distribution is known, the solute transport is modeled by solving an advection-diffusion model in Section 2.3. This introduces a second non-dimensional parameter, the Péclet number (Pe), and it is the combination of these two dimensionless parameters that determines the global solute profile in the network. All the theoretical predictions are confirmed using experimental measurements. Finally, two possible applications of this work are presented: the first one combines the present design with self-digitization principle to encapsulate the

controlled concentration in nanoliter chambers, while the second one extends the present design to create a continuous concentration gradient within an open flow chamber for its adaptation to a wider range of microfluidic devices.

2.1   Experimental Methods

The detailed microchannel geometry is shown in Fig. 2.2. Two independent solutions are injected at entrances A and B and flow side-by-side in the inlet channel before they are distributed through the distribution channel between the branches. The flows are controlled with a syringe pump (Cetoni Nemesys), or through a pressure controller (Fluigent MFCS), and the behavior within the microchannels is observed through an inverted microscope (Nikon TE-2000) as described below.
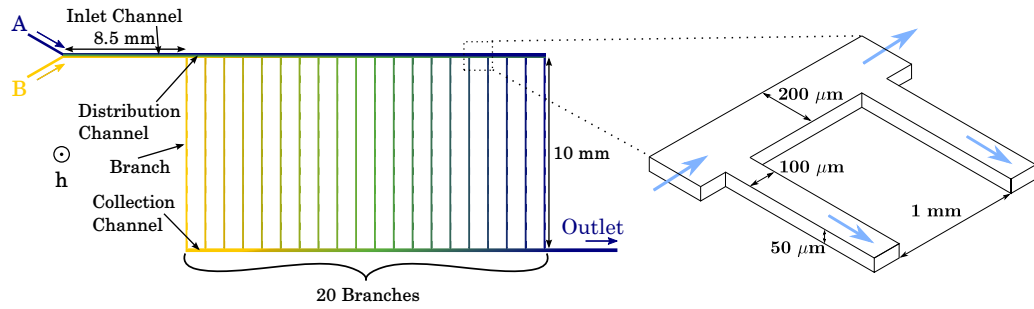
Figure 2.2: Microfluidic network structure with dimensions. For flow rate measurements, a 10 branches device is used, while for concentration profiles measurement, a 20 branches ladder network is used.

2.1.1   Chip microfabrication

All experiments are conducted in polydimethylsiloxane microchannels (PDMS, Dow Corning Sylgard 184) plasma-sealed onto glass slides. The mold fabrication process is based on dry film photoresist soft lithography techniques, as descibed in detail by Fradet et al.[66] A unique photoresist layer (Eternal Laminar) is laminated onto a clean glass coverslip, using anoffice laminator (PEAK PS320) set at 100°C, and exposed to UV (Hamamatsu Lightningcure LC8) through a photomask designed on Inkscape corresponding to the channel design (Fig. 2.2). Then, the mold is developed in a solution of carbonate potassium (1% w/w, Sigma-Aldrich). Once cured and plasma sealed, the channel surfaces remain untreated in the case of experiments with solely an aqueous phase. However, hydrophobic surfaces are obtained for the experiments described in section 2.4 using aqueous phase in fluorinated oil FC40 (3M FLuorinert) with $0,5\%$ (w/w) pegylated surfactant (008-FluoroSurfactant, RAN Biotechnology). Hydrophobia is obtained by filling the device with an electronic coating

EG-1720 (Acota Ltd, Knights Way, Shrewsbury, UK), then baking at 110°C. The surface treatment is repeated three times to ensure perfect coating. Two chip designs are used: 15 μm height for flow rates measurements and 50 μm height for experiments involving concentration gradients.

2.1.2   Flow rate measurements

The flow rate in the distribution channel and branches is measured using non diffusing tracer particles (LifeTechnologies, 1.0 μm FluoSpheres) diluted in aqueous solutions. The solution is injected at 1 μL/min in both entrances and filmed using Photron Fast Camera at 30× magnification. In steady flow, microparticles follow the streamlines, which can then be visualized using image superposition as presented on Fig. 2.3.

At each branching node, a clear separating streamline is visible between the fluid that is diverted into the side branch and the fluid that continues through the distribution channel (dashed line on Fig. 2.3). The upstream distance between the bottom wall and the separation line is denoted e_i for node i. Away from the branching site, the depth-averaged Hele-Shaw flow is uniform along the channel width. Hence, conservation of mass at node i provides a relation between e_i and the flow rate within the distribution channel upstream (Q_i) and downstream (Q_{i+1}):

$$1 - \frac{e_i}{w} = \frac{Q_{i+1}}{Q_i} \quad 1 \leq i \leq N-1, \tag{2.1}$$

where w is the width of the distribution channel. Therefore, the flow rate $(Q_i)_{i=1...N}$ along the distribution channel is obtained by measuring $(e_i)_{i=1...N}$ and by noting that $Q_1 = Q_A + Q_B$. Finally, the flow rate distribution $(q_i)_{i=1...N}$ in the parallel branches is computed using mass conservation as $q_i = Q_i - Q_{i+1}$, noting that $q_N = Q_N$.

2.1.3   Concentration gradients measurements

To quantify the concentration gradients generated in the chip, a 10 mmol 2,6-dichlorophenolindophenol (DCPIP) solution is injected at entrance A while pure water is pumped in at inlet B. Q_A and Q_B are always identical and range from 0.5 μL/min to 20 μL/min. DCPIP has a diffusion coefficient[58] $D = 0.77 \times 10^{-9}$ m^{2}s^{-1}.

The concentration levels are obtained from measurements of the light absorbance through the blue DCPIP solution. The local absorbance $\mathcal{A}$ is related through Beer's law to the local concentration of absorbing species (here DCPIP), noted C (in mol/m^3) :
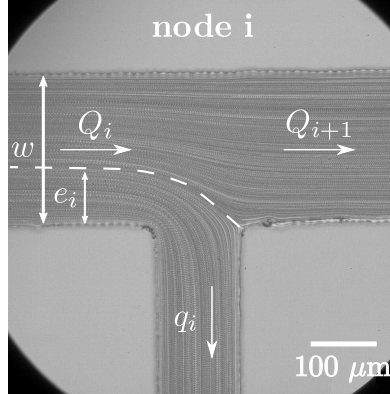
Figure 2.3: Stack projection of 122 images of micro particles flowing through node i. e_i is the distance from the lower wall to the separation line (white dashed) between the fluid that gets into a side branch and the remaining flow that continues through the distribution channel.

$$\mathcal{A} = \epsilon h C \quad \text{with} \quad \mathcal{A} = -\log \frac{I}{I_0}, \tag{2.2}$$

with ϵ the molar extinction coefficient (in $\text{mol}^{-1}\text{m}^{-1}$) of DCPIP, h (in m) the optical path length of light which corresponds to the channel height. I and I_0 are the measured intensity and the background intensity, respectively. Experimentally, I_0 corresponds to the intensity through pure water flow ($C = 0$ mM). In practice the local concentration C is obtained by measuring the local intensity I and comparing it with I_0 and a reference value I_{ref} that corresponds to the undiluted DCPIP concentration C_{ref}. This yields:

$$\frac{C}{C_{\text{ref}}} = \frac{\log \frac{I}{I_0}}{\log \frac{I_{\text{ref}}}{I_0}}. \tag{2.3}$$

2.2 Model and flow distribution in a ladder network

In this section, we study the flow distribution in the ladder network (Fig. 2.2). We develop a simple model based on a resistance network that can predict the flow rates along the distribution channel and in every branch. After confirming the model by experimental measurements, we extend the theoretical prediction to the case of a continuous device and give a design tool for adapting the branch length to obtain any kind of flow rate distribution.

2.2.1 Hydrodynamic Resistance Network

When the depth and width of each microchannel are small in comparison with its length, a 1D-hydrodynamic resistance model can be used, namely by relating through the hydrodynamic Ohm's law, $\Delta P = R_{hyd}Q$, the pressure loss ΔP between the channel segment's inlet and oulet to the flow rate Q through that segment. The hydrodynamic resistance of a channel with rectangular cross-section is given by $R_{hyd} = a(w/h)R_{hyd}^*$, with $R_{hyd}^* = \mu L/w^2 h^2$, μ the dynamic fluid viscosity, $a(w/h)$ a geometric factor:[67]

$$a(\gamma) = \frac{\pi^3 \gamma^2}{8} \left(\sum_{n=1,3,5,\dots}^{\infty} \frac{n\gamma}{\pi n^5} - \frac{2}{\pi^2 n^5} \tanh(n\pi\gamma/2) \right)^{-1} \tag{2.4}$$

with $\gamma = w/h$ and L, w and h are the channel length, width, and height, respectively ($h < w$).

Thus, the microfluidic network can be represented as a hydrodynamic resistance network (Fig. 2.4), where p_i (resp. p_i^f) is the pressure at node i in the distribution (resp. collection) channels. Similarly, Q_i and Q_i^f are the flow rates upstream of node i in the distribution and collection channels. The distribution and collection channels have the same geometric characteristics, and the side branches are all identical. We note R the hydrodynamic resistance between two nodes of the distribution or collection channel segment, and R_b the hydrodynamic resistance of each branch. Kirchhoff's law applied between nodes $i-1$ and i (see Fig. 2.4) yields:

$$R_b \left(q_i - q_{i-1} \right) = R \left(Q_i^f - Q_i \right) \quad \text{for } 2 \leq i \leq N, \tag{2.5}$$

and from mass conservation,

$$Q_1 = \sum_{k=i}^{N} q_k + \sum_{k=1}^{i-1} q_k \tag{2.6}$$

for all $1 \leq i \leq N$. Equations (2.5)–(2.6) can be recast in terms of the normalized flow rate $\tilde{q}_i = q_i/Q_1$ in the branches :

$$\tilde{q}_i - \tilde{q}_{i-1} = \frac{R}{R_b} \left(\sum_{k=1}^{i-1} \tilde{q}_k - \sum_{k=i}^{N} \tilde{q}_k \right) \quad \text{for } 2 \leq i \leq N, \tag{2.7}$$

$$\sum_{k=1}^{N} \tilde{q}_k = 1. \tag{2.8}$$

The previous system is controlled by a single parameter, R/R_b, which solely depends on the network's geometry:

$$\frac{R}{R_b} = \frac{a\left(\frac{w}{h}\right)}{a\left(\frac{w_b}{h}\right)}\left(\frac{L}{L_b}\right)\left(\frac{w_b}{w}\right)^2,$$ (2.9)

with L_b, w_b and h_b the length, width and height of the branches. For a given geometry (or a given R/R_b), the normalized branch and distribution channel flow rates, $\tilde{q}_i$ and $\tilde{Q}_i$ with $1 \leq i \leq N$, are computed from Eqs. (2.7)–(2.8), and

$$\tilde{Q}_i = \sum_{k=i}^{N} \tilde{q}_k.$$ (2.10)
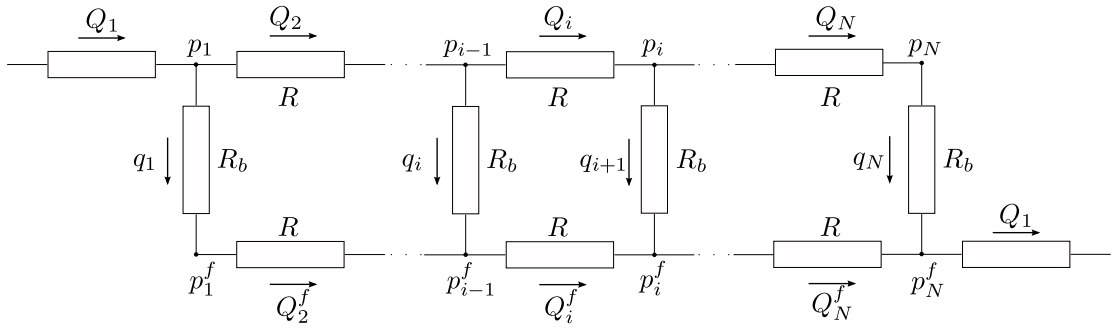
Figure 2.4: Equivalent resistance network: R and R_b are the hydrodynamic resistances of a segment between two nodes and of a branch, respesctively. p_i and p_i^f are the pressure at the entrance and the exit of branch i, respectively. The flow rates in the branches are written q_i. Q_i and Q_i^f correspond respectively to distribution channel and collection channel inter nodes flow rates, while Q_1 is the global inlet flow rate.

2.2.2 Flow rate distribution

For a given network geometry (i.e. given R/R_b), the distribution profile of flow rates in the parallel branches is obtained from Eqs. (2.7)–(2.8). The flow rate displays a U-shaped distribution, with the highest flow rates in the first and last branches and lower values in the middle of the ladder, as plotted on Fig. 2.5a for three values of R/R_b. A larger contrast between the maximum flow rates and the flow rate in the middle branches is observed when R/R_b is increased. For R/R_b= 0.43, 85% of the global inlet flux Q_1 flows through the first two and last two branches. This quantity decreases to 46% for R/R_b= 0.043. At R/R_b= 0.0043 the fluid is more equally distributed between the branches with a low contrast $|q_{\max} - q_{\min}|/Q_1 \leq 2\%$. Hence, high branch resistances give more homogeneous flow rate distributions than low branch resistances.

The U-shaped profile can be explained by calculating p_i and p_i^f, the values of the inlet and outlet pressures for each branch (Fig. 2.5c). Applying the conservation of flow rate at node i in the distribution or collection channels, as well as Ohm's law gives:
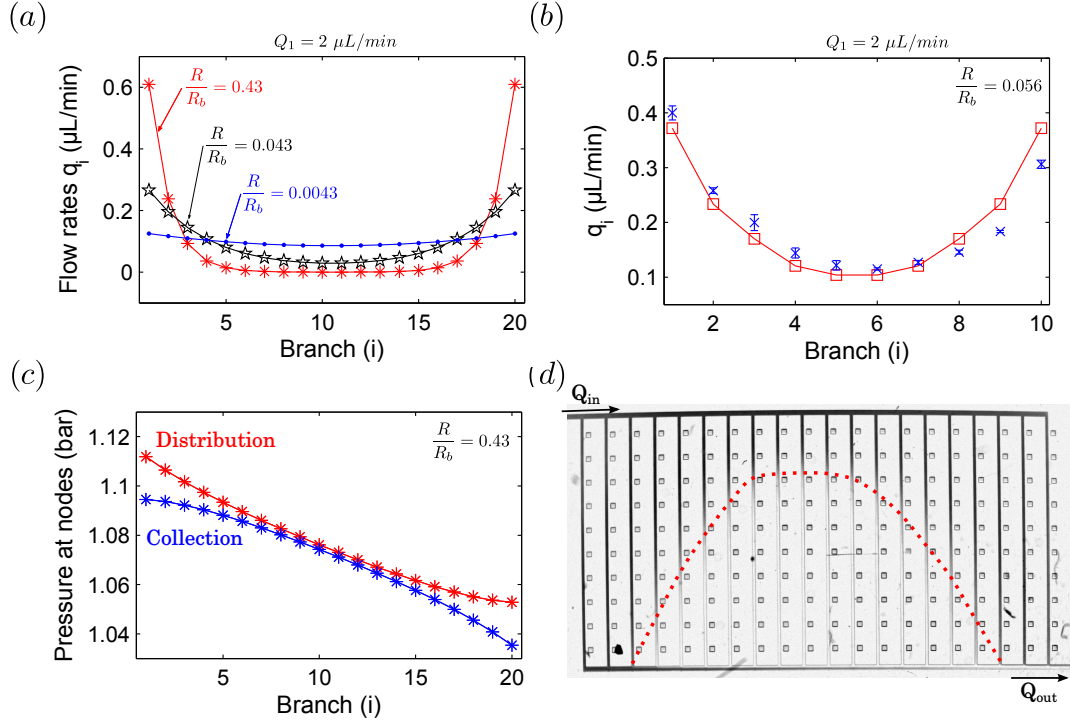
Figure 2.5:   (a) Simulated flow rate distributions for three different geometries. In each case, the branch resistance is changed such that the ratio $\frac{R}{R_b}$ is varying. (b) Pressures at nodes $(P_i)_{i=1...N}$ and $(P_i^f)_{i=1...N}$ for $\frac{R}{R_b} = 0.43$. (c) Comparison between numerical ($\square$) and experimental ($\times$) branch flow rate distribution for a ten branches device with $Q_A = Q_B = 1\mu\text{L/min}$ and $\frac{R}{R_b} = 0.043$. (d) Image of a device filling process with only one species: DCPIP at 6mM .

$$p_{i+1} - 2p_i + p_{i-1} = Rq_i, \tag{2.11}$$

$$p_{i+1}^f - 2p_i^f + p_{i-1}^f = -Rq_i. \tag{2.12}$$

Equations (2.11)–(2.12) show that the inlet and outlet pressure distributions have opposite convexity: since q_i is defined as positive in the notations of Fig. 2.4, the inlet (resp. outlet) pressure distribution is convex (resp. concave), a result confirmed in Fig. 2.5(c). The branch flow rate is simply proportional to the difference between the two pressures at each i; thus, the flow will always be higher at the edges of the ladder and smaller in the center. This result contrasts with the linear pressure drop along a simple channel with no side exits.

This theoretical prediction is confirmed experimentally for $R/R_b = 0.53$ (Fig. 2.5b). The experimental flow rates, which are obtained from the method described in Section 2.1, are in very good agreement with the model predictions in the first channels. In the last

channels, we observe the accumulation of measurement errors due to the resolution of the pictures used (figure 2.3) and the particles size. This leads to a discrepancy with the model, although the agreement remains good.

The signature of this velocity profile is best visualised by injecting a colored solution into a ladder filled with pure water. The filling process occurs sooner near the beginning and end of the ladder network than in the central region, as shown on the snapshot of Fig. 2.5d. This distribution of flow rate has an important practical consequence: changing the contents in the device is therefore limited by the time required to fill the central region and would require a volume greater than the total volume in the device.

2.2.3 Extensions of the resistance network model

Finally, we present an extension of the hydrodynamic resistance model of Section 2.2.1 to the limit case where the distance between two consecutive nodes tends to 0. This limit transforms the discrete recurrence equations (2.7)–(2.8) into a single continuous equation. This yields an exact analytical solution of the flow distribution in such ladder network.

When the distance between two nodes $L \to 0$, an infinity of infinitely thin branches can be placed aside the distribution channel (Fig. 2.6a). In this case, the system of discretized equations (2.7)–(2.8) can be described with continuous variables. The hydrodynamic resistances of the ladder network of figure 2.4 can be considered as constant linear resistances densities (ρ) for the distribution channel and as linear conductance density (g) for the branches (Fig. 2.6b). A linear flow rate density q is defined, such that the flow rate dq flowing through the branches between x and $x + \mathrm{d}x$ is $\mathrm{d}q = q(x)\mathrm{d}x$. The continuous parameters are related to the discretized problem through the following relationships :

$$R = \int_{x_i}^{x_{i+1}} \rho \mathrm{d}x \tag{2.13}$$

$$R_b = \frac{1}{\int_{x_i}^{x_{i+1}} g \mathrm{d}x} \tag{2.14}$$

$$\forall i \in [\![1; N-1]\!] \quad q_i = \int_{x_i}^{x_{i+1}} q(x)\mathrm{d}x, \tag{2.15}$$

with x_i the absciss of the nodes i.

With this new model, Kirschoff's law (2.5) applied on the elementary mesh of figure 2.6b becomes :

$$\frac{1}{g}\frac{\mathrm{d}q}{\mathrm{d}x} = \rho(Q^f(x) - Q(x)), \tag{2.16}$$

with ρ and g constants. The mass conservation (2.6) yields the following relationships:

$$\frac{\mathrm{d}Q^f}{\mathrm{d}x} = -\frac{\mathrm{d}Q}{\mathrm{d}x} = q(x). \tag{2.17}$$
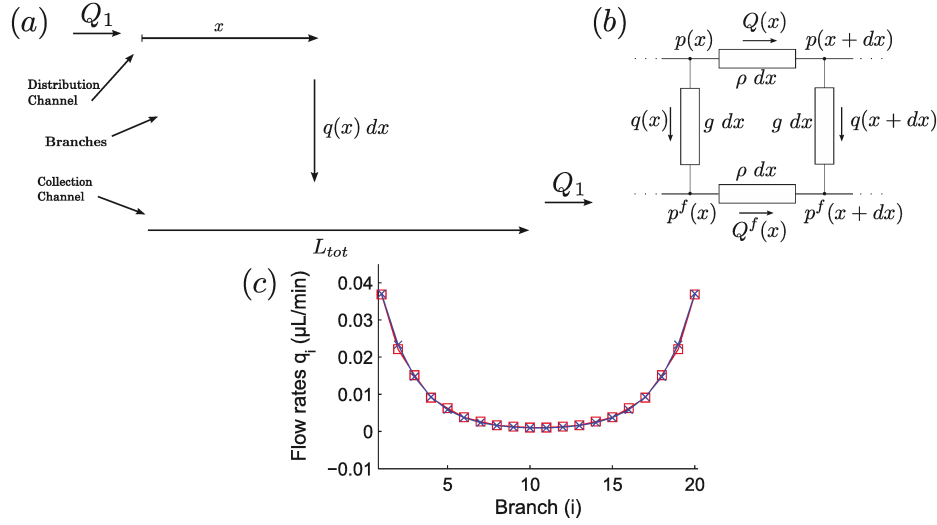
Figure 2.6: (a) Schematic of the hypothetical continuous case, where the branch flow rates are considered as linear flow rate density. (b) Equivalent continuous resistance network: ρ is the linear hydrodynamic resistances of the distribution channel. g corresponds to the linear hydrodynamic conductance of the side 'branches'. p and p^f are the pressure in the distribution and collection channels, respectively. The linear flow rate density in the branches is written q. Q and Q^f correspond respectively to flow rates in the distribution and collection channels, while Q_1 is the global inlet flow rate. x is the the distance between the first branch and the point where quantities are evaluated, $x \in [0, L_{tot}]$.(c) Comparison between the analytical solution q and the discretized solution q_i .

By combining the first derivative of equation (2.16) with (2.17), a second order differential equation for q is deduced:

$$\frac{\mathrm{d}^2 q}{\mathrm{d}x^2} = 2\rho g q(x). \tag{2.18}$$

By using the boundary conditions $Q(0) = Q^f(L_{tot}) = Q_1$ and $Q^f(0) = Q(L_{tot}) = 0$, the analytical expression for the flow rate density can be derived:

$$q(x) = \frac{kQ_0}{2} \left(\frac{\cosh(kx)}{\tanh\left(\frac{kL}{2}\right)} - \sinh(kx) \right). \tag{2.19}$$

This equation can be verified by comparing the analytical solution (2.19) with the discretized solution thanks to equation (2.15). Figure 2.6c shows that the two solutions collapse. This resolution technique corresponds only to a theoretical scheme and cannot be assimilated to the experiment where the branches would be replaced by a single large chamber as described in section 2.4. A simple argument is that for $x = 0$ and $x = L_{tot}$ the wall condition imposes a zero velocity $q(x = 0) = q(x = L_{tot}) = 0$, and here the solution gives the highest flow rate close to those abscisses.

2.3 Solute concentration distribution through an advection-diffusion model

In this section we use the results of the previous section on the flow rate distribution to solve an advection-diffusion problem that can predict the concentration distribution of a dye between the branches. Contrary to the flow distribution study where only one solution flows into the microfluidic device, here a co-flow of a dyed solution and pure water is injected as shown on figure 2.2b. The numerical model is followed by experimental measurements.

2.3.1 Solute Advection-Diffusion
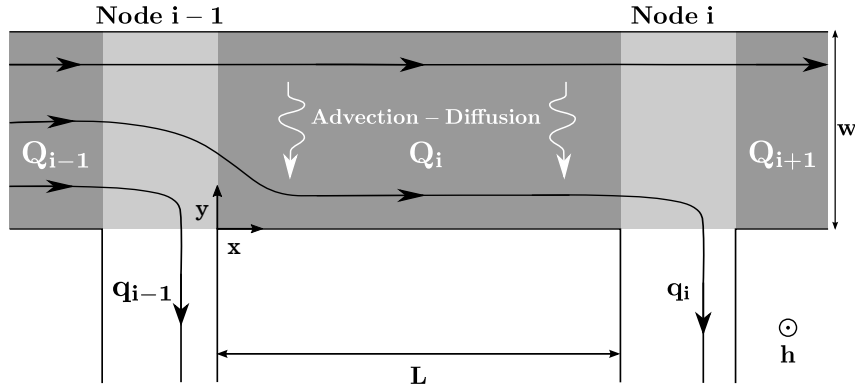
Figure 2.7: Schematic of an distribution section between nodes i and $i+1$. Advective transport dominates near each node (light grey zones), while the solute distribution between two nodes results from a balance between advection and cross-flow diffusion (dark grey zones).

Because of the discrete nature of the network, the solute dynamics can be modeled by distinguishing what happens within a channel segment and in the vicinity of a branching node. The channel and branch heights being small, diffusion is expected to act quickly in that direction and a two-dimensional model is assumed for the depth-averaged concentration and velocity. Away from the branching nodes, the depth-averaged flow velocity within the segment is uniform. Because the length of the segment is large compared to its width, we neglect stream-wise diffusion. As a result, the relative solute concentration, $\tilde{C} = C/C_{\text{ref}}$, is modeled by the following two-dimensional advection-diffusion equation within the segment:

$$\text{Pe}\,\tilde{Q}_i \frac{\partial \tilde{C}}{\partial \tilde{x}} = \frac{\partial^2 \tilde{C}}{\partial \tilde{y}^2}, \tag{2.20}$$

with $\tilde{x} = x/L$ and $\tilde{y} = y/w$, the non-dimensional coordinates and $\tilde{Q}_i = Q_i/Q_1$, the reduced flow rate. The Péclet number,

$$\text{Pe} = \frac{Q_1 w}{DLh}, \tag{2.21}$$

is the ratio of the typical diffusion time across the distribution channel, w^2/D, to the advection time scale along the entire channel $Q_1/(wLh)$, with D the solute diffusion coefficient. Equation (2.20) is solved using finite differences and a Crank-Nicholson scheme for each segment.The details of the numerical resolution is given in appendix A.

Near a branching node, the solute dynamics is dominated by the flow reorganization in that region (Figure 2.3), and because of the small extent of that region, diffusion can be neglected while the flow reorganizes. The solute concentration profile downstream from node i is therefore directly obtained by stretching the upstream profile in the cross-stream direction to account for the spreading of the streamlines in the distribution channel. The spreading results from the flow rate reduction after crossing node i. In the side branch, diffusion quickly homogenizes the solute concentration downstream of the branching node ($Pe_{\text{branch}} \sim$) so that the measured concentration can be defined as its average value.

For $Q_A = Q_B$, the solute concentration distribution at the entrance of the inlet channel is a centered Heaviside function. The evolution of the concentration profile along the inlet channel is determined from Eq. (2.20). Then, the solute concentration profile downstream of node i and its value in the i-th branch are computed using the method described above (light grey section on Fig. 2.7), while the evolution of the concentration profile in the distribution channel is computed between two nodes using Eq. (2.20) (dark grey section on Fig. 2.7).

2.3.2 Concentration gradient profiles

The flow rate distribution in the branches depends on a single geometric parameter. In addition to this flow rate distribution within the ladder, the solute concentration profile also depends on the relative importance of advection and diffusion, measured by the Péclet number, which now acts as the second dimensionless number controlling the gradient formation process. Experimentally, Pe can be adjusted by changing the inlet flow rate Q_1 for a fixed channel geometry and diffusing species. To simplify the analysis, we first analyze the concentration gradient dependence on the Péclet number for a fixed geometry, then we integrate both parameters to obtain a full map of the accessible concentration gradient profiles.

Figure 2.8 shows the resulting concentration distribution for R/R_b=0.043 as a function of Pe. Three main types of profiles can be distinguished, referred to in the following as "flat", "gradient" and "step" concentration profiles. The flat profiles are obtained for low Pe, when diffusion is sufficiently fast to homogenize the concentration in the distribution channel after a few nodes. The step profile is obtained for large Pe, when diffusion is almost negligible: the first branches are filled with pure solvent injected at entrance A, while the last ones are filled with pure solute solution. Finally, gradient profiles correspond to the intermediate regime, when both advection and diffusion are significant.
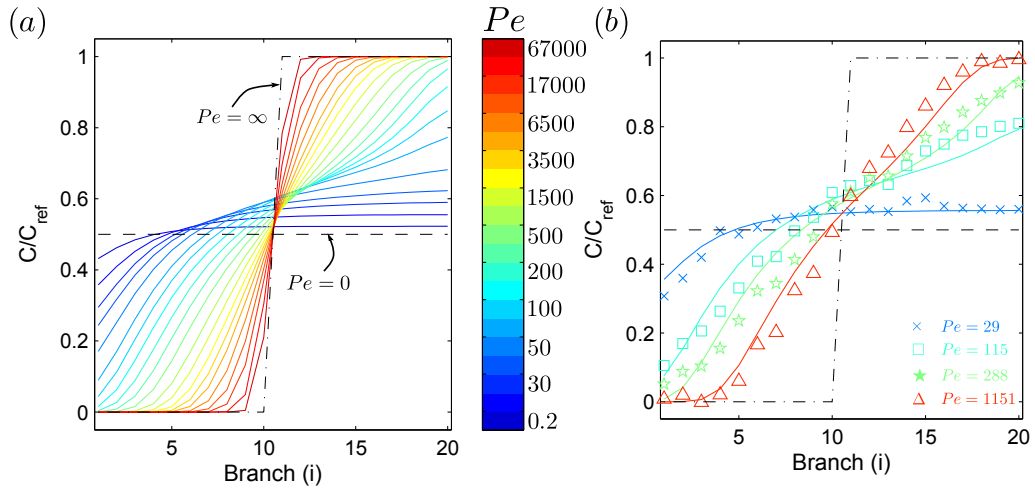
Figure 2.8: (a) Concentration profiles for Péclet numbers from 0.2 to 6.7×10^4 for a fixed geometry R/R_b=0.043, obtained from the numerical simulation (Section 2.3.1). The extreme "flat" and "step" gradients are also plotted (dashed and dotted-dashed curves). (b) Comparison between the experimental data and the numerical model for four different flow rates: $Q_1 = 1, 4, 10,$ and 20 μL/min.

Again, the numerical predictions shown in Fig. 2.8a are confirmed experimentally in Fig. 2.8b, for four different values of Pe. In our case, the Péclet number is only flow rate dependent, a modification of the flow rate leads to a change in concentration profile. For the lowest value of Pe the concentration profile reaches a plateau after a few nodes, while higher values of Pe yield a more contrasted concentration profile across most of the ladder. Note that the concentration field for the highest flow rate displays a flat shape at the initial and final branches, thus beginning to approach the limiting case for very high Pe.

2.3.3 Geometrical Parameters Mapping

We can now use our numerical simulations to characterize the global evolution of the gradient profile with both control parameters, R/R_b and Pe. More specifically, we quantify the non-uniformity of the gradient bewteen the branches by a contrast ratio (Figure 2.9),

which is taken as an ansatz for the "quality" of the gradient for a given device and flow rate. This contrast ratio is defined as the root-mean-squared (rms) of the difference between the actual normalized concentration, $\tilde{C}(\tilde{x})$, and the linear gradient case, $\tilde{C}^*(\tilde{x}) = \tilde{x}$. The evolution of the contrast ratio is shown in Fig. 2.9a for various R/R_b and Pe.
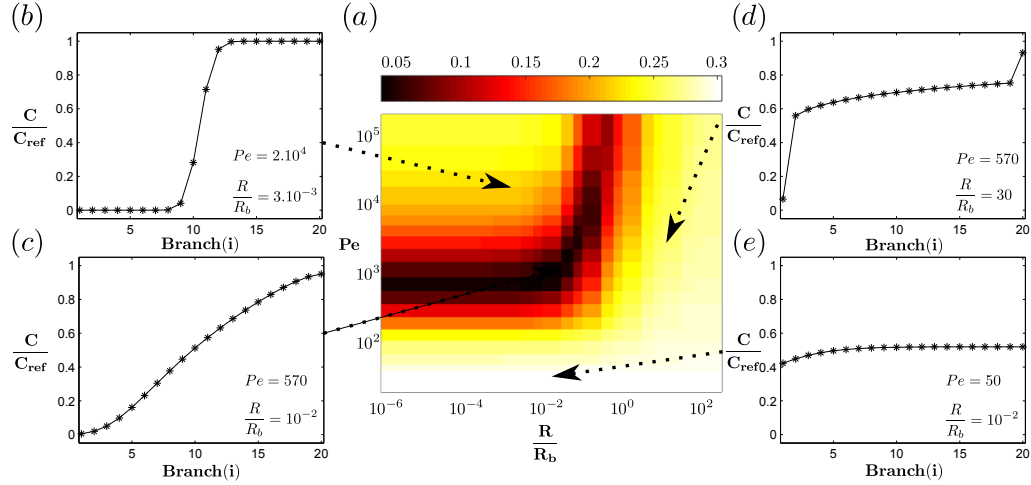
Figure 2.9: (a) Map of a comparison between the concentration gradient and a constant gradient, giving the root mean square of their difference (color bar) for various geometrical parameters $\frac{R}{R_b}$ and Péclet numbers Pe. (b),(c),(d),(e) draw the concentration gradient profiles for four points of the map (a). (b) and (c) belong respectively to the 'step' and 'gradient' regimes, while (d) and (e) are examples of 'flat' regime.

The dark red canyon indicates profiles with behaviors close to a uniform gradient (Fig. 2.9c) and corresponds to gradient profiles that present high contrasts between all successive branches. The bright regions correspond to profiles that present a poor contrast between some branches, and are the result of three different regimes. High Péclet numbers ($Pe > 10^4$) and low resistance ratio ($R/R_b < 10^{-2}$) correspond to a uniform flow rate distribution amongst the branches and slow diffusive effects (Fig. 2.9b). Therefore, the fluid has the behavior close to a non diffusing species regularly distributed in each side branch, with the expected distribution of a step concentration profile.

Conversely, when R/R_b is greater than 1, more than 90% of the fluid flows through the first branch and the last branch, which means that only 10% of the inlet flow goes through the rest of the branches, which cannot have a high branch concentration contrast even with rapid diffusing effects. Consequently, for high values of R/R_b flat profiles are obtained, as shown of Fig. 2.9d. Finally for Péclet numbers below 10^2, the network geometry does not affect the concentration gradient profiles because the diffusive effects are swift enough to produce flat concentration profiles for any flow rate distribution (Fig. 2.9e).

2.4   Extensions

Several extensions of the device described above can be developed, in order to apply the gradients in a range of applications and overcome some of the limitations.

For instance, having a continuous flow can be poorly adapted to long term observation on time scales relevant to biological experiments, which may require instead a controlled initial concentration in a closed volume. For such situations, the gradient produced by the ladder network can be frozen within small chambers adjacent to the parallel channels, as shown in Fig. 2.10a. Here, ten 2 nL-chambers are connected to each branch through highly resistive bypasses (Fig. 2.10a enlargement). Given sufficient time, the concentration within each chamber equilibrates with the channel to which it is connected.

The filling process of these chambers proceeds in three steps: The device is first filled with water in order to remove all the air bubbles, taking advantage of PDMS porosity. Second, a concentration gradient is applied and the chambers are progressively filled with the same concentration as in the branch they are connected to. Finally, when the gradient is completely established in every chamber, fluorinated oil (FC40 with surfactant) is flushed in the device at 345 mbar for half a second. The small dimensions of the by-passes compared to the branch dimensions prevents the oil from entering into the chambers and allows then to be isolated. In this way 200 independent chambers are filled with a well-controlled concentration, and can be used to perform 10 repetitions at 20 different conditions in a single experiment. The chamber concentrations agree with the model prediction (Fig. 2.10b)

A different approach is to remove the need for the ladder structure by working in a wide and thin flow chamber, as shown in Fig. 2.10c-d. This format will be adapted in the last chapter where anchored droplets in the wide chamber must be submitted to variable concentrations of solute. Here the regularity of low Reynolds flows ensures that the fluid follows well-separated and stationary streamlines, with no mixing taking place except by diffusion. In contrast the lack of parallel channels changes the underlying fluidic equilibria since the flow in this micro-Hele-Shaw cells rapidly equilibrates on a global scale to adapt to the boundary conditions. This makes the device operation more robust, therefore simpler, and improves the dynamic performance during changes of regime.

To mimic the highly resistive branches of the discrete device, the side chamber must have a high hydrodynamic resistance compared to the resistance of the distribution channel. To ensure this resistance contrast, we design the chip with a large height for the distribution channel and a thin height for the wide chamber. The device consists of three parts: (i) a distribution channel, 200 μm wide and 150 μm deep; (ii) a wide thin chamber placed alongside the distribution channel, having width 10 mm and height of 15 μm; and (iii) a collection channel, whose dimensions are equal to those of the distribution channel. In the example shown in Fig. 2.10d, local indentations (50 μm deep) are made in the roof of the
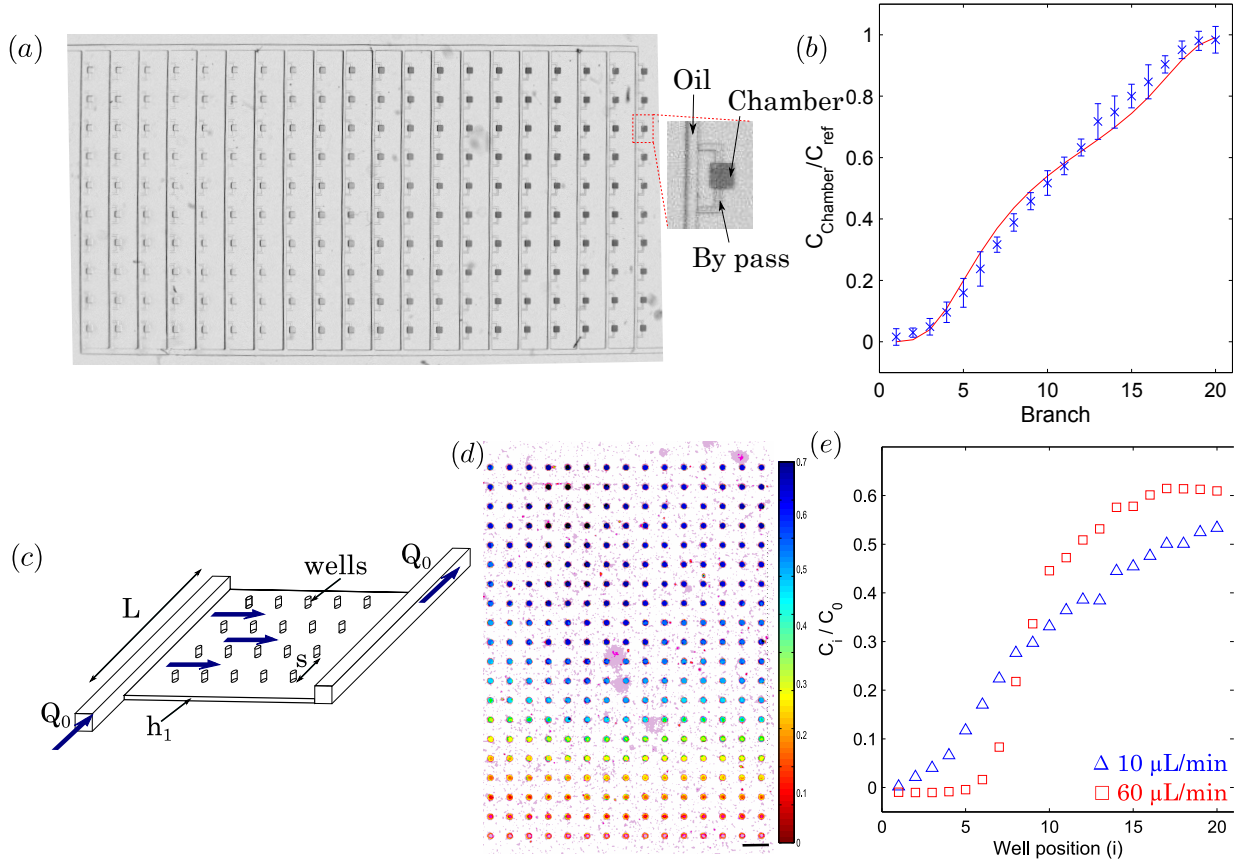
Figure 2.10: Beyond the ladder network: (a) Ladder containing an array of 2 nL chambers filled with controlled and contrasted concentration. (b) Experimental concentration profile for a global flow rate of 10 μL/min before oil flushing at 345 mbar (squares and triangles) and the corresponding model prediction (solid line). Error bars are calculated with the 10 concentrations measured on each branch. (c) Continuous two-dimensional implementation of the device: the ladder network is replaced by a wide and thin flow chamber. (d) False color image of the concentration profile within the chamber. Each colored dot corresponds to a well within the chamber. (e) Experimental concentration profile for two flow rates.

chamber in order to improve the imaging sensitivity.

When a 10 mM DCPIP solution co-flows with water in the distribution channel, a concentration gradients is observed orthogonally to the flow direction (Fig. 2.10d). Its evolution depends on the flow rate in a similar fashion as the discrete case (Fig. 2.10c, e): At high flow rates (60 μL/min), a step concentration gradient profile is obtained, while at lower flow rate (10 μL/min), the chip produces an almost constant gradient. However, the models for flow rate and solute concentration distributions in this device become much more complex and the numerical resolution goes beyond the scope of this manuscript.

2.5   Summary and conclusions of chapter 2

This chapter addresses a simple question but in the process uncovers new physical insight about the distribution of flows and molecules in a complex geometry. The first result shows that the flow is distributed in a non-trivial manner, with preferential paths going through the initial and final branches of the ladder (Fig. 2.8). This contradicts a naive implementation of the principles of Stokes flows, which would suggest that the flow must distribute equally in each branch of the ladder, since the path from the inlet to the outlet through any of the branches would follow a succession of micro-channels of equal hydrodynamic resistance. Instead, we find that the extraction of fluid from the distribution channel at each node leads to a reduction of the flow rate beyond that node and thus to a nonlinear dependence of the pressure on position. The symmetric situation takes place in the collection channel, with the net effect of having a higher driving pressure across the extreme nodes and a lower driving pressure near the middle of the ladder. While the non-monotonic flow distribution is always present, a single control parameter R/R_b determines its amplitude.

Next, we considered the interplay of advection and diffusion within this geometry in setting up non homogeneous concentration profiles within the network. A second control parameter was introduced, namely the Péclet number (Pe), a measure of the relative importance of advection and diffusion in the process. Depending on those two control parameters, three broad categories of distribution profiles were identified: a flat concentration profile for low Pe or large R/R_b, a step regime for large Pe and low to moderate R/R_b, and finally a regime that displays a well-distributed gradient in a central region of this parameter space. In practice however, any one of the three regimes may be interesting for different applications; the near step-like regime of Fig. 2.9(b) allows for the exploration of a logarithmic variation in concentrations, especially in the initial regions of the device where the concentrations are low. In contrast, the flat regime of Fig. 2.9d would allow a small range to be explored in detail. The models developed here enable the user to predict the distribution profile created in the device, and to select the design parameters to achieve a particular profile. The present work focused on a model situation in which all of the branches were regularly spaced and geometrically equivalent, which significantly reduced the number of independent design parameters. The hydrodynamic resistance of the branches can however be modified, most easily by changing their lengths, in order to tune the flow rate distribution and thus the concentration profile of the solute more finely. A full design optimization is then possible to tailor the details of the conditions in the different parts of the microfluidic network.

Finally, we have extended our work to two furthers designs. The concentration profile can be frozen in time within small side-chambers, which allow the concentration profile to remain after the flows have been interrupted. But, it requires a long setup period, determined by the time necessary to fill the most downstream chamber in the middle section

of the device. The total volume required to reach this steady state was measured to be about 60 times the total volume of the ladder network. The second extension completely removes the ladder network and is able to obtain well-controlled gradients within a wide and thin cell, which renders the setup time much faster but the gradient requires a constant flux of the fluids. This will be adapted in the last chapter to apply a concentration gradient on our second microfluidic platform dedicated to bacteria growth and presented in the following chapter.

Chapter 3

Droplet-based microfluidic platform for parallel culture of bacterial colonies

As stated in the introduction, the complexity of a microfluidic device in terms of design, micro-fabrication and usage, generally increases with the number of integrated operations. Handling of bacterial systems often requires a large number of operations such as bringing or removing a solute, inducing the emission of a fluorescent protein or sorting cells such that the integration of the full range of required operations on a single microfluidic chip could highly increase the complexity of the device. Therefore, keeping the device simplicity to its minimum is a very challenging goal for the development of a microfluidic platform dedicated to microbiology. This is however a requirement for its adoption in non-specialist areas that are microbiology labs for several reasons. First, the simplicity of a new technology ensures its versatility and its possible derivation for a broad range of applications. Second, biological studies must be repeated to demonstrate the reproducibility and statistical relevance of the experiments. This can be performed by the ability of microfluidic device to automatise and parallelize on-chip operation which strongly depends on its sensitivity to the control parameters (pressure controller, temperature, surfactant concentration or operations synchronisation) and therefore on its robustness.

The multiplicity of the operations for microbiological studies is partly due to the involvement of living organisms. A bacteria cell is indeed a sensitive system made of a complex cascade of biochemical reactions. Carbon sources (derivatives of glucose) and oxygen contained in the natural environment are used to produce metabolites, heat and cell mass as shown on figure 3.1. The efficiency of the inner cascade of reactions, called metabolism, relies on the presence of ions, mineral or vitamins in the surrounding microenvironment. For *in-vitro* cultures, a bacteria cell allocates its energy to one or multiple outputs depending on the quality of the culture medium. A good quality culture medium will result

in a rapid and efficient growth while a poor medium will restrict the bacteria to its basal metabolism. Therefore, suitable environment for bacteria growth contains the fundamental needs of cells in terms of nutrient and oxygen[1] to replicate their natural microenvironment for accurate biological studies.
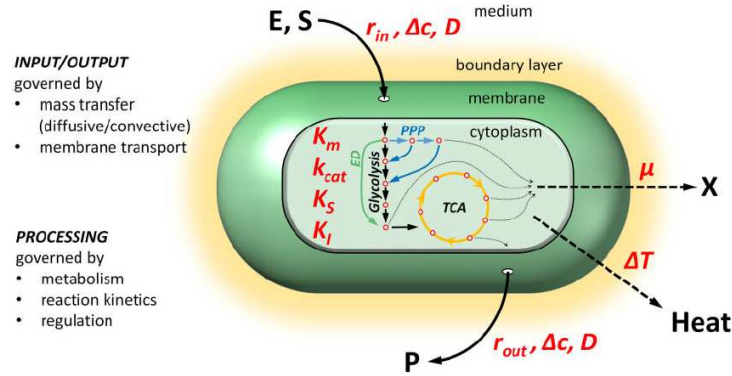
Figure 3.1: Scheme of the global functioning of a bacteria cell. Extracted from Dusny *et al.*[42]

In this chapter, the *generic chip* is presented. This microfluidic device allows for the production of $1,495$ droplets stored in an array. In spite of its very simple design, it produces a suitable environment for bacteria growth and enables large ranges of operations and applications for microbiology.

The first part presents the microfluidic design and the main chip functionalities. After describing the process to produce thousands of static droplets in a large array, the experimental method to grow any type of bacterial species is described. We demonstrate the abilities to perform common features of classical Petri dish as well as its capabilities to enumerate cells and target rare mutant. Finally, a technique using an infra-red laser is presented to extract any selected droplet out of the chip.

The second part, is focused on the quantification of cell concentration through statistical analysis, called the *digital approach*. Using the Poisson distribution of the bacteria in the generic chip, the initial cell concentration can be calculated. This method is then applied to the case of two bacterial species for the detection of species interactions. Finally, the method is extended to any number of species to demonstrate how the combination of the bacterial culture and droplet recovery can be used to determine new bacterial culture conditions on a single chip.

---

[1]Two types of bacteria exist: aerobic and anaerobic bacteria cells. The aerobic type need oxygen to process the carbon sources, while anaerobic cells are sensitive to oxygen which produces their death. Here, we work mainly with aerobic bacteria.

This chapter is built on the preliminary work of Gabriel Amselem,[28] who studied the physical mechanism of droplets breaking in a single trap.[28] He also initiated the first experiments that use this mechanism to encapsulate and culture bacterial colonies. One of the specific features of this device is the capability of extracting any droplets out of the chip. This uses the infra-red laser set-up developed by Charles Baroud and María Luisa Cordero[68] several years before the start of my PhD. The experimental work was done with Benoit Drogue, a post-doc researcher in our lab. The calculation on *in vitro* culture conditions discovery was made with the essential help of Loïc Henriet, PhD student at CPHT lab of École Polytechnique and Antoine Barizien, PhD student at LadHyX.

In addition, I contributed to reduce the chip design to its simplest geometry and confirmed the preliminary experiments on bacteria culture made by Gabriel. I coded the numerical analysis to extract quantitative data from experimental measurements. I improved the experimental set-up for the droplet recovery through the design of small extraction chambers. Finally, I adapted classical results on cell distribution in droplets to identify species interaction and expand the boundaries of the digital approach towards new microbiological challenges.

3.1 Generic Chip for Bacteria Cell Culture and Retrieval

3.1.1 Microfluidic device and protocol

The device developed here consists of a wide chamber with a 2D geometry, connected to two inlets and one outlet. The device is routinely microfabricated using the same methods as described in 2.1 with three layers of photoresist : the main chamber with a height of $35~\mu m$ and two layers of $50~\mu m$ for the anchors. It results in an array of $1,495$ square indentations (anchors) etched on the chamber ceiling, at a density of ~ 900 anchors/cm^2, see Fig. 3.2a,b. This geometry was chosen to provide regions of low confinement, within the anchors, surrounded by regions of high confinement. These "confinement gradients" allow the production of large forces, by providing local minima of the surface energy of the aqueous-oil interfaces.[69]

Droplets formation. Before the beginning of an experiment, the whole device is rendered hydrophobic and filled with a fluorinated oil. The experiment begins when the aqueous cell suspension is injected into the device, forming a puddle of aqueous phase that fills the entire chamber. Then, fluorinated oil (FC40+0.5% surfactant) is flowed into the chip, pushing the cell suspension out of the chamber (Fig. 3.3a). As the water-oil interface advances, some of the aqueous phase is trapped in each of the anchors. This deforms the
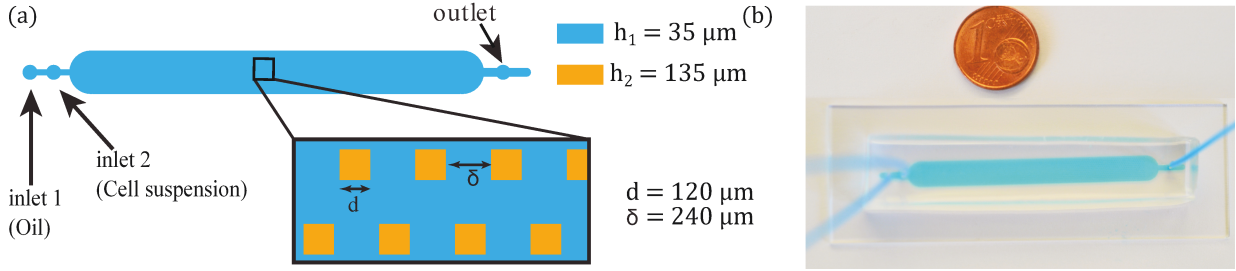
Figure 3.2: (a) Typical design of a microdroplet multiwell device. The central chamber has dimensions 0.5×4.8 cm and contains a 2D array of 113×15 surface-tension anchors. Square anchors have side dimension $d = 120 \; \mu m$, spaced by $\delta = 240 \; \mu m$. The chamber height is $h_1 = 35 \; \mu m$ and the anchor height $h_2 = 135 \; \mu m$. (b) The device, which fits on a microscope slide, is connected to two inlets and one outlet.

puddle locally, until the geometry of the interface reaches a critical shape beyond which a droplet breaks off and remains in the low confinement region (Fig. 3.3b). Using an oil flow rate of 10 μL/min, droplets are created at 10 Hz, such that the whole chip is loaded within 3 minutes. The presence of corners allows oil to drain out of the square anchors rapidly.
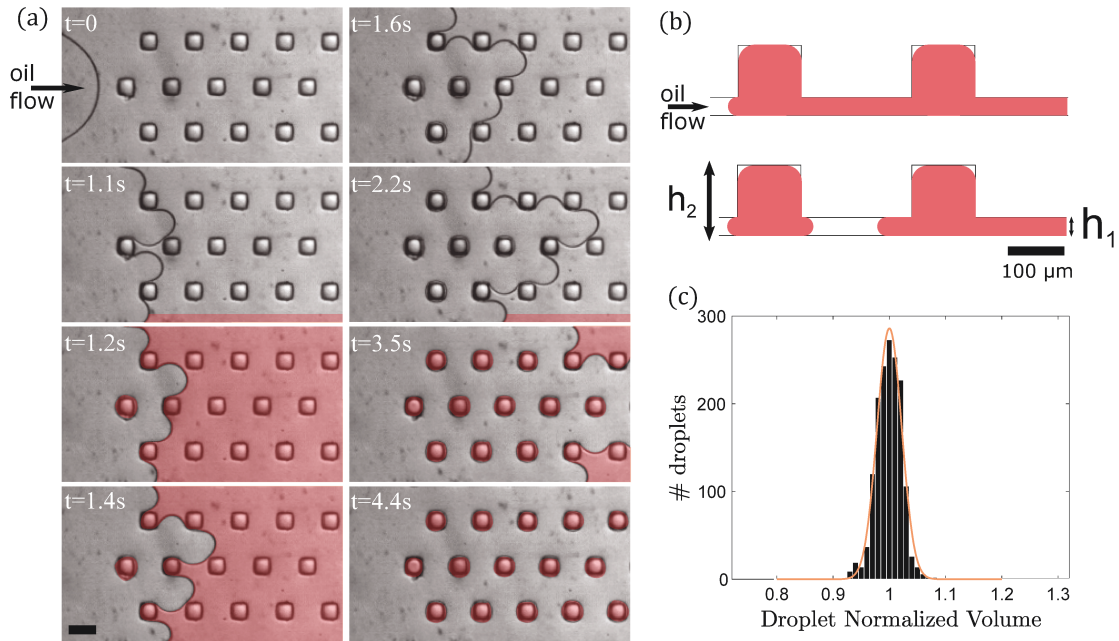
Figure 3.3: (a) Time-lapse of the drop formation process. The cell sample is coloured in red for better visualisation. Scale bar: 200 μm. (b) Cross-sectional schematic of the breaking process on anchors. The aqueous sample initially fills large regions and then get divided into isolated droplets that fill each of the anchors. (c) Experimental histogram of the normalized droplet volumes on one chip. The orange line is the best gaussian fit to the data, leading a standard deviation $\sigma = 0.02$.

Droplets formed by breaking up a large puddle on surface-energy anchors have a precisely controlled size. In our setup, droplets have a mean volume of 2 nL, with standard deviations ranging between 2% and 5% (see Fig. 3.3c for the droplet size distribution on one chip, and Appendix B.1 for more data). The dispersion in droplet size varies slightly from chip to chip, and depends on the precision in microfabrication and on the effectiveness of the hydrophobic surface treatment. The good monodispersity is due to the mechanism of break-up, detailed for a single droplet in.[28] Briefly, the aqueous puddle adapts its shape to minimize the surface energy in the channel. For small interface deformations, the puddle can find static equilibrium shapes specific to the stress applied by the surrounding continuous oil phase. But as the oil pushes the interface further from the equilibrium position, the local shape forms thin necks that remain connected to the anchor, , see figure 3.4b. When these necks extend beyond a critical deformation, they cannot reach an equilibrium shape anymore, which causes them to break up and to leave a droplet in the anchor. This scenario takes place even for quasi-static motion of the interface and is mainly dependent on the device geometry. It is nearly independent of physical parameters – such as fluids viscosities, visco-elasticity, or surface tension – and of the velocity at which the oil phase is driven.[28]
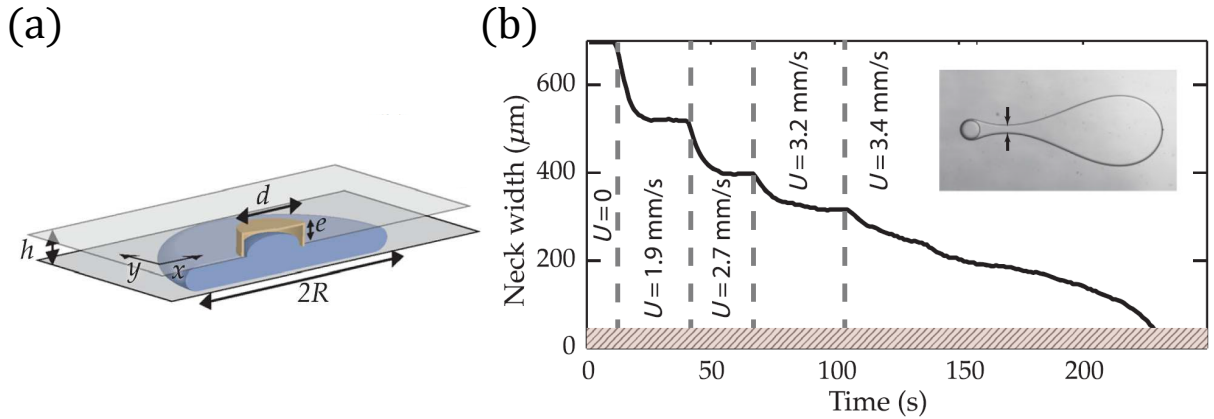
Figure 3.4: a) Scheme of a large droplet trapped by an anchor. b) Neck width evolution for an increasing flow rate until the breaking event – extracted from Amselem *et al.*[28]

The breaking mechanism has not been studied further for the large chamber case. Few snapshots, shown in figure 3.5, highlight the breaking process. The necks can be observed right before each droplets breaking. They are formed by two oil threads pushing on both side of each anchor the aqueous puddle towards the exit. The streamlines in the aqueous phase are observed thanks to the use of 4 μm diameter micro-particles. Two types of flows are observed right before the breaking event. When the two surrounding threads are symmetrical (anchor 2 in Fig 3.5), the particles inside the anchor do not move in a particular direction. Yet, when they are asymmetrical (anchor 1 in Fig. 3.5), the water-oil interface moves towards the longer threads (left side in anchor 1). This results in a rotating flow inside the anchor.
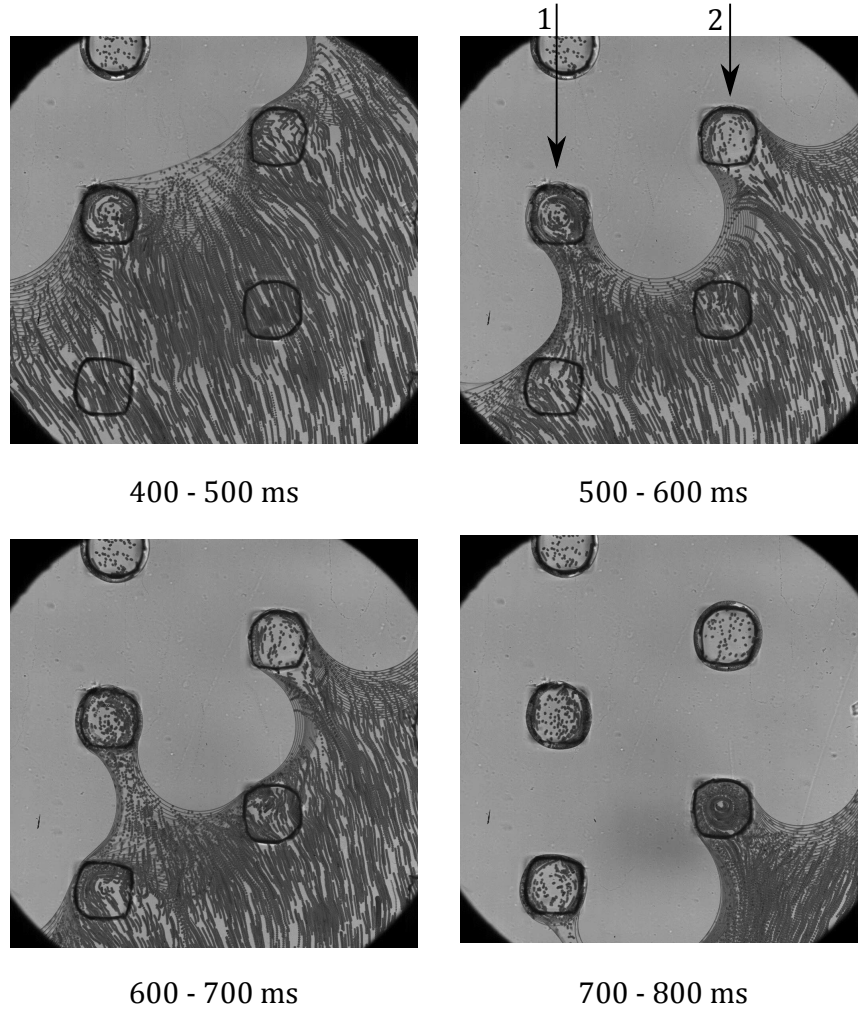
Figure 3.5: Streamlines in the aqueous phase during breaking events in the case of several anchors. The streamlines are highlighted with $4~\mu m$ micro-particles as described in chapter 2. This corresponds to minimum intensity projection of frames from a movie of droplets formation within the generic chip.

In a large chamber, droplet size heterogeneity is partly due to the flow-induced deformation of the PDMS. To overcome the PDMS deformation, one could think about placing a glass slide above the chamber while curing the PDMS, adding micro-pillars in the chambers, or microfabricating the chip out of stiffer material such as cyclic olefin copolymer (COC). In our experiment, we kept PDMS chips as COC prevents oxygen from entering the microfluidic device which is essential for bacteria growth, see 3.1.2. Moreover, we will take advantage of its deformation to recover droplets out of the chip (see section 3.1.5). We found that using flow rates of 10 muL/min and lower led to satisfactory monodispersity. As the droplet production and storage are both determined by the anchor geometry, the device operation can be performed by pushing the oil syringe by hand, leading nevertheless

to an excellent partitioning of the sample.

3.1.2   Cell culture

Now that we have a technique to create large array of static droplets, we need to verify if this can be used to culture bacteria cells. As bacteria cells have doubling time ranging from $\sim$ 20 min to several hours, the observation of thousands colonies in parallel requires to observe them on a long period of time and we need to image and re-visit every droplet at any time point. Therefore, a static array of anchored droplets makes the perfect candidate for such long term experiments. The dynamical analysis will be developed further in chapter 4. The details of the strains used in the experiments are given in Appendix B.2.

Cells of a fluorescent strain of *Escherichia Coli* (*E.Coli* pGlo, expressing a plasmid encoded GFP with ampicillin resistance) are encapsulated in liquid droplets of LB broth to validate the microfluidic setup as a viable microbial culture platform. As in standard liquid cultures, cells grow in their planktonic state and are freely moving within the droplet. A time-lapse sequence of such a condition is shown in Fig. 3.6a. Each droplet plays the role of an independent, miniature liquid batch culture. In this operating mode, the device fills the functions of a high-density microwell plate, by allowing for the parallelization of thousands of cultures, while guaranteeing continuous visual access to all of them.

The microfluidic device can also be used in a different manner, by working with droplets that mix low-gelling agarose with cells resuspended in growth medium. This mode mimics the way Petri dishes are used with an agar layer, for colony inspection, mutant isolation or cell enumeration. The protocol for breaking agarose droplets on the anchors is exactly the same as for liquid droplets, as the break-up process is not influenced by the physical properties of the fluids at play. Droplets are formed at room temperature, when agarose is in its liquid state. The immobilized agarose droplets are then gelified by placing the device at 4 °C for 30 minutes. After gelification, the microfluidic chip is placed in an incubator at 37 °C, a temperature that allows the bacteria to proliferate while the agarose droplets remain in their gel state. In gelified droplets, single *E.Coli* bacteria grow to form compact 3D microcolonies, as shown in Fig. 3.6b, and can readily be observed in bright field and fluorescence imaging.

Cell culture is not specific to *E.Coli*, other species can be grown on chip and present different 3D-microcolonies morphologies. As examples, we show in Fig. 3.7a bacterial colonies from single *E.Coli*, *Bacillus Subtilis* and *Pseudomonas Fluorescens* cells, after 16 hours of culture. While *E.Coli* and *P. fluorescens* form compact round shaped micro-colonies, *B.Subtilis* colonies develop in dendritic patterns. Colonies of *P.Fluorescens* have a more

(a)

Cells

1 h   3 h   6 h   9 h   12 h   15 h

(b)

1 h   3 h   6 h   9 h   12 h   15 h
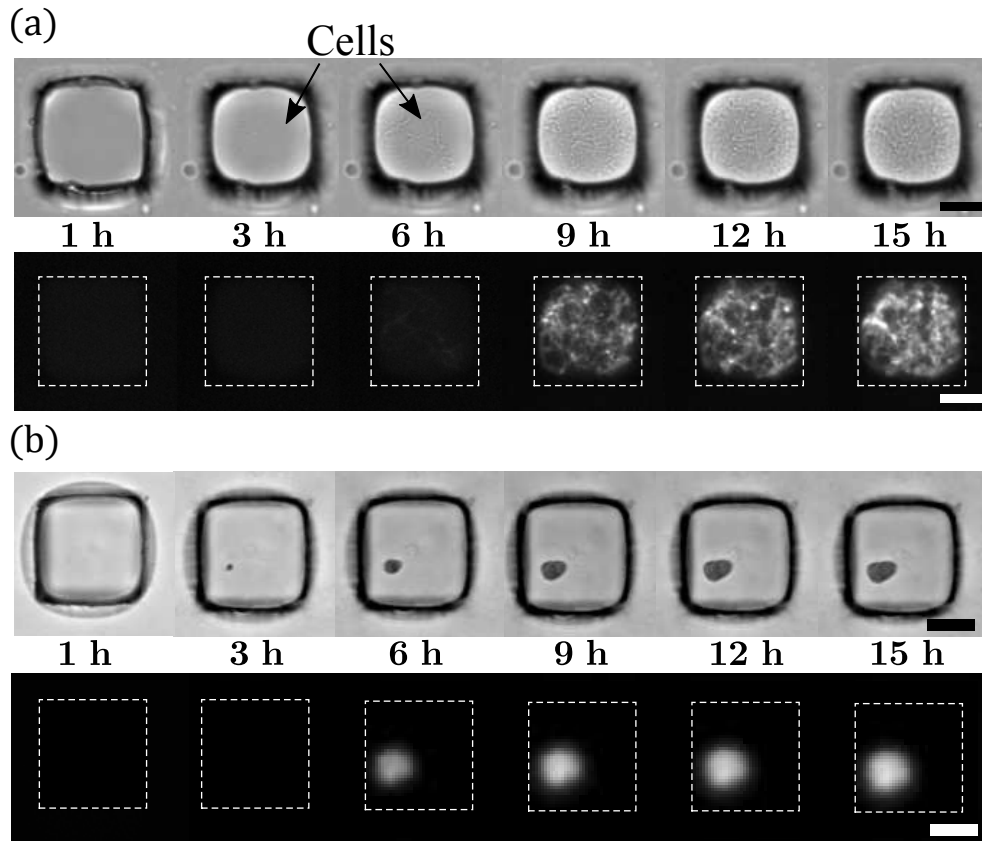
Figure 3.6: (a) Growth of fluorescent *E. coli* pGlo mutants in a liquid droplet containing Luria-Bertani (LB) broth. Top: bright field image. (b) Same bacteria growth in a gelified agarose droplet. For a,b – Top: bright field image. Bottom: fluorescence image. Scale bar: 50 μm .

rough aspect and a lower optical density than colonies of *E.Coli*. This visual inspection recalls the signature of different colonies on agar-coated petri dishes, where colonies of different species may present different shapes, patterns and colors.[70]

In addition to cells and culture medium, the droplets can also contain any molecule of interest. As an example, *E.Coli* pGlo (fluorescent) and WT (non-fluorescent) cells were co-encapsulated in gel droplets containing three concentrations of ampicillin (0, 5 or 50 μg/ml, Fig. 3.7b). In absence of ampicillin, both WT and pGlo mutants grow as round shaped colonies (Fig. 3.7b-panel 2). At an ampicillin concentration of 5 μg/ml, cell division of *E. coli* WT is impaired but not completely abolished, as shown by the small and filamentous shape of non-fluorescent WT colonies, typical of stressed bacteria. Under the same conditions, pGlo mutants still form round shaped micro-colonies, as their growth is not modified (Fig. 3.7b-panel 3). When the ampicillin concentration inside the droplet is set to 50 μg/ml, only mutants are able to grow (Fig. 3.7b-panel 4). These examples demonstrate how standard microbiology protocols can be directly applied in the microfluidic device and

(a)

Escherichia coli   *Escherichia coli*   *Pseudomonas fluorescens*   *Bacillus subtilis*

(b)

No bacteria   No ampicillin   Ampicillin   Ampicillin
                                       5 µg/ml   50 µg/ml
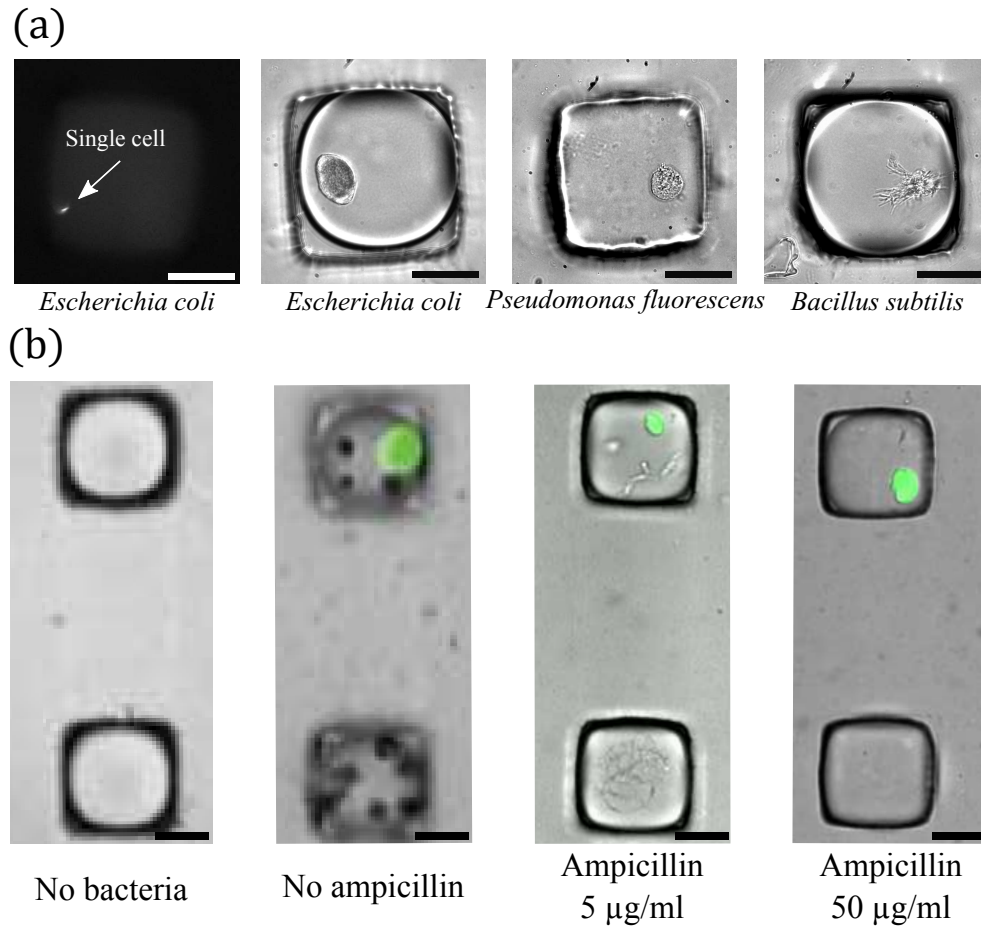
Figure 3.7: (a) Left picture: Single *E. coli* pGlo bacterium, seeded in a gel droplet. Other pictures: three species colonies after 16 hours of growth. (b) Panel 1: empty chip test for external contamination. Panel 2,3,4 : 3D colonies of WT (non-fluorescent) and pGlo mutants (fluorescent) co-encapsulated in gelified droplets (ratio 100:1) with 0, 5 and 50 µg/mL of ampicillin respectively. Images taken after 16 hours of growth. Scale bar: 50 µm .

interpreted in the same ways by observing the colony morphologies.

3.1.3   Growth Limitation.

Bacteria growth is ensured by two main factors, which are nutrient and oxygen in the case of aerobic strains. Nutrients are essential material to synthesise proteins and to increase the cell mass, such that no nutrient yields no growth.[71] Moreover, aerobic bacteria are extremely fond of oxygen. Oxygen shortage yields drastic changes in their metabolism[72,73] and therefore affects their growth.

Nutrient.   To prove that the droplet nutrient content is a limitation to growth and that the use of agarose gel does not imply further limitation, we perform the culture of *E.Coli* MG1655 with a continuous flow of culture medium surrounding the droplets. Timelapse pictures of two example wells are shown in figure 3.8. One can observe that contrary to figure 3.6b, the colonies become bigger and bigger as LB medium is continuously renewed, bringing new nutrient for the colonies growth.
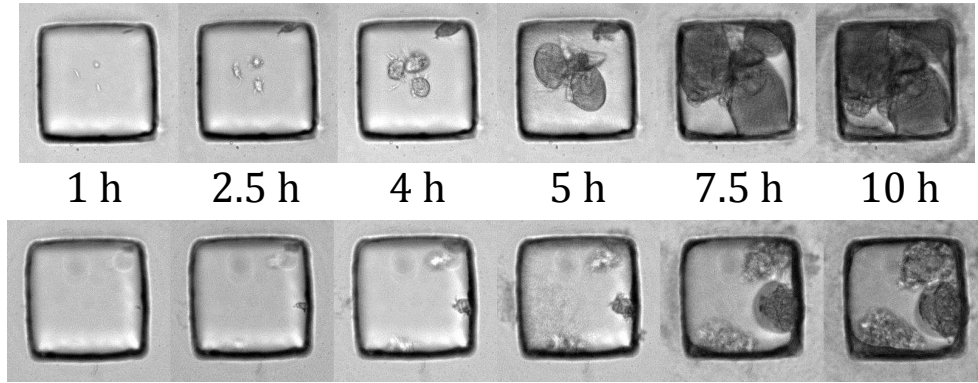
Figure 3.8: Two examples of timelapse images of *E.Coli* MG1655 culture in agarose droplets surrounded by a continuous flow of LB medium at 6 μL/min.

This observation has been quantitatively confirmed by filling six chips with six different initial concentrations $[LB]_0$ of culture medium ranging from 0.05 to 6 times the reference concentration used in our experiments, written $1X$ namely one time the reference, see appendix B.2 for more details. Figure 3.9 displays the result of the mean final colony size x_{max} function of the initial culture medium concentration. The following power law is measured on the experimental curve:

$$x_{max} \propto [LB]_0^{2/3} . \tag{3.1}$$

The quantity x_{max} is the number of bacteria cells inside the droplets at the end-point time. It is assumed to be proportional to the fluorescent level of the colony.

Oxygen.   Mahler *et al.*[74] recently found that the culture of bacteria cells in sub-nanoliter droplets rapidly suffer from oxygen shortage (hypoxia). They measured that an *E.Coli* culture in 170 pL droplet starting with a single cell in fluorinated oil bath enters in hypoxic condition after 110 min. In their supplementary material, an expression for the time T required for exponentially growing bacteria to consume all the oxygen initially contained
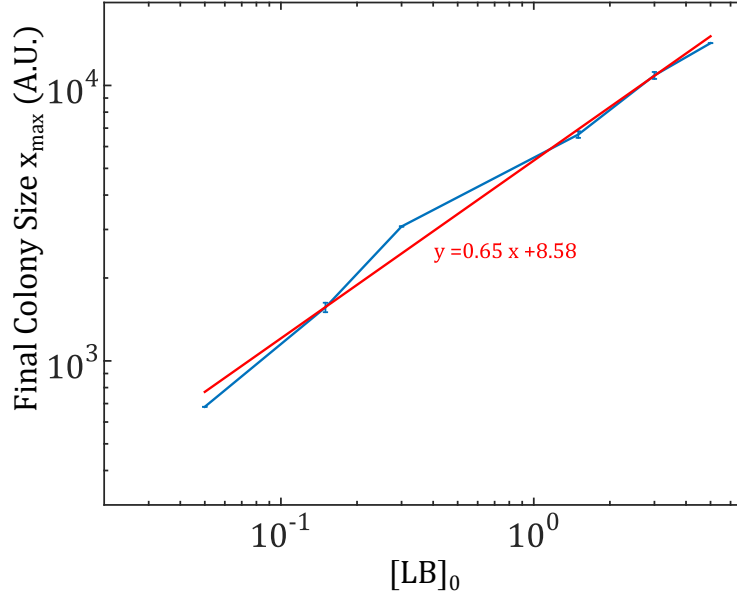
Figure 3.9: Final colony size as a function of the initial medium concentration withing the droplet. The colony sizes are calculated as the mean level intensity of all the droplets containing colonies and the error bars correspond to the equivalent standard deviation.

in a droplet of volume V_d is derived. Assuming that there is no supplementary source of oxygen, they found that:

$$T = \frac{t_d}{\ln(2)} \ln \left(1 + \frac{\ln(2)[O_2]_0}{\alpha_c t_d N_0} V_d \right), \tag{3.2}$$

with $t_d = 0.5$ h, the doubling time, $[O_2]_0 = 0.2$ mmol/L, oxygen solubility in complex medium, $\alpha_c = 2.78 \times 10^{-15}$ mol/cell/h, the oxygen uptake rate per cell and N_0, the initial number of cells inside the droplet. With our experimental conditions, $N_0 \sim 1$ and $V_d \sim 2$ nL, we find that an exponentially growing colony will consume the entire droplet oxygen in $T = 3.8$ h. This is exactly the typical time during which growth is observed (3.6 h for *B.subtilis* and 3.1 h for *E.coli*). Therefore, it is possible that oxygen is limiting the bacteria.

However, PDMS is a material very permeable to oxygen and oxygen is highly soluble in fluorinated oil. This can provide a sufficient amount of oxygen to support the bacteria growth until the nutrient shortage. No specific measurement has been performed on the oxygen level inside the microfluidic chamber for neither its dynamical evolution or its homogeneity amongst the droplets. Yet, several techniques exist to measure oxygen in microfluidic droplet such as ruthenium tris(-dipyridyl) dichloride hexahydrate (RTDP) (Sigma-Aldrich) as in[75] or the OXANO sensor used in[74] and should be definitively performed for further

microbiological development.

To simply detect any possible influence of oxygen limitation, we perform *E.Coli* MG1655 culture in a chip with a continuous flow of fluorinated oil previously oxygenated and no change has been observed in term of colony size. This in addition to the final size dependence on the initial culture medium concentration make us think that the on-chip cultivation of bacteria cells is limited by the nutrients rather than by oxygen shortage. An exact measurement of the oxygen distribution within the chamber would confirm this assumption.

Water Evaporation. As PDMS is permeable to gas, it is also permeable to vapour through the mechanism of pervaporation.[76,77] With a microfluidic chips incubated at 37 °C to allow bacteria proliferation, the pervaporation is favoured as shown in figure 3.10a. The agarose gel beads shrink by drying out completely. After 13 h incubation, the bacteria colonies are not observable any more.

The droplet volume is extracted from the timelapse bright field images by detecting the area of the droplet through image analysis (see 4.2), then converted in radius or volume by assuming the droplet spherical [2]. Figure 3.10b shows that in the established evaporation regime, the droplet volume has a linear decrease with a roughly constant evaporation rate of 0.053 nL/h. This is confirmed in the insert of figure 3.10b which displays the radius rate as a function of the radius and shows a dependency in $1/R^2$:

$$\left| \frac{\mathrm{d}R}{\mathrm{d}t} \right| \propto \frac{1}{R^2} \ \Rightarrow \ \underbrace{4\pi R^2 \frac{\mathrm{d}R}{\mathrm{d}t}}_{\mathrm{V(t)}} = \mathrm{C}, \tag{3.3}$$

with C a constant and V(t) the droplet volume. As the droplet characteristic volume is 1 nL, the characteristic time of droplet evaporation is $\tau_e \sim 1/0.053 = 19$ h, which is in accordance with what we observed on figure 3.10a. In the same experimental condition, the strongest evaporation has been observed for the wells positioned close to the microfluidic chamber walls with higher evaporation rate up to 0.0922 nL/h. This observation may also suggest that the diffusion of gas is more efficient on the side of the chamber rather than in the middle, which can result in irregularities between the droplets in term of the oxygen supply.

By placing the microfluidic chip immersed in water or PBS during incubation, we prevent from pervaporation as we saw earlier in figure 3.6a,b. For all the experiment the chips will be incubated in immersed conditions which ensures to neglect the pervaporation for several days.

---

[2]This assumption is very rough as the droplet is not spherical for the first few hours and fits the cubic well geometry. It results an underestimation of the initial volume.

(a)

1h   4h   7h   10h   13h   16h

(b)
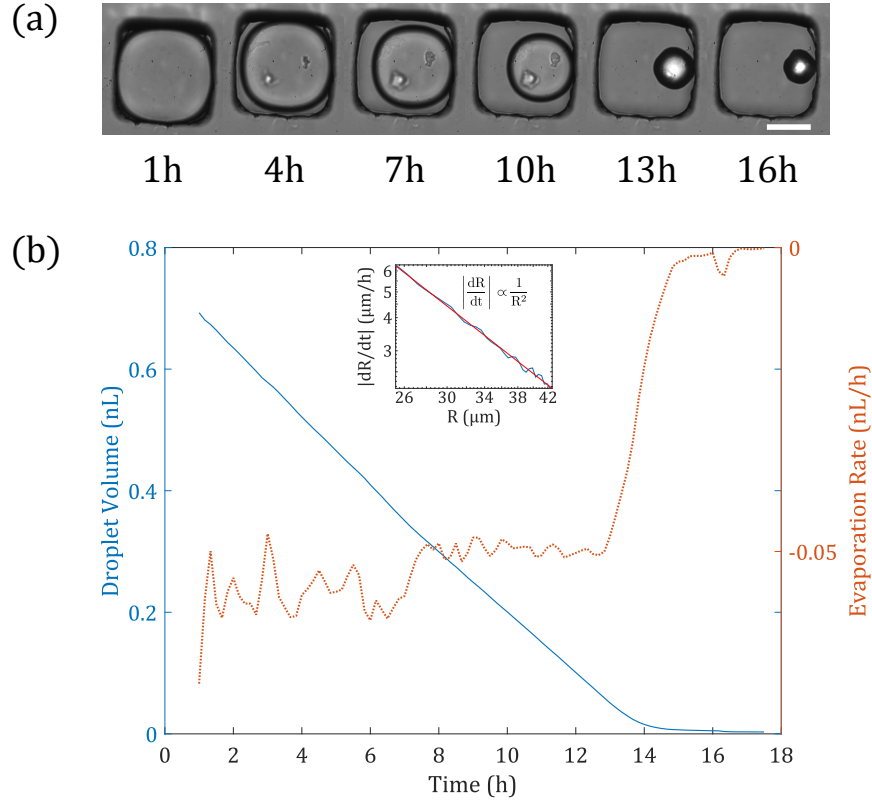
Figure 3.10: a) Timelapse images of a chip incubated in non-immersed conditions at 37 °C. The pictures are taken with a $40X$ magnification. b) Droplet volume plotted as a function of time with its evaporation rate dV/dt. The insert shows the radius variation rate $\|dR/dt\|$ as a function of the radius R in a loglog scale.

3.1.4 Cell Enumeration and Rare Mutant Detection

Apart from allowing species to be visually inspected, the microfluidic device can be used for enumerating the bacteria in a sample or for detecting rare events within a mix. Since the quantification hinges on the control of unwanted contaminations, we begin by testing the device robustness against external contamination. This is confirmed since no micro-organisms are observed in the droplets, after 16 hours of incubation with culture medium, when we do not specifically put bacteria in them (Fig. 3.7b-panel1). As all the conditions are gathered to allow bacteria growth, external contamination would lead to the proliferation of micro-organisms. Such organisms can come from volatile spores, operator hands or sneeze during the sample preparation. To prevent any contamination, all the instruments are sterilized and sample are prepared under laminar flow.

There are three ways of enumerating the bacteria, which require different microscopy resolutions. When devices are inoculated, single bacteria can be observed under the microscope at a 40X magnification, as shown in Fig. 3.7a: detection of the droplet contents can take

place without waiting for the colonies to grow and can be used for the visualisation and analysis of the first divisions. This mode of bacterial detection however requires high optical resolution, with access to length scales $\sim 1\ \mu m$, which generates a large amount of data and the acquisition time become extremely large as the number of studied wells increases.

To detect bacteria with lower (*e.g.* 10X) magnification objectives, enumeration can be carried out on bacterial micro-colonies after 10–20 hours of growth, see Fig. 3.7b-panel 2. Note that more than one bacterium per droplet can be encapsulated and still form distinguishable, independent micro-colonies. By seeding on average 7 cells per droplet, it is possible to detect a single mutant colony within more than $10,000$ WT colonies ($7 \times 1,495$). This is almost two orders of magnitude higher than what is currently achievable in a single Petri dish, where the threshold for mutant detection is of one mutant per 200 wild-type cells.[78]

The above methods require to identify and count each encapsulated colony (or single cell) in order to estimate the initial cell concentration. Yet, the large number of wells available on the generic chip also enables a "digital" approach to be used, and obtain quantitative measurements of the initial sample.[79] In this approach, the contents of each well are treated as a digital signal, *i.e.* either taking a one or zero value, depending on the presence or absence of signal of interest. This approach has been applied to the quantification of nucleic acids (digital PCR) and was shown to provide higher sensitivity and better quantification than analog techniques[80] and will be developed in details later in the second part of the chapter, see section 3.2.

3.1.5 Extraction of individual colonies

The identification of mutants or specific phenotypes can become frustrating if it is not possible to extract the target droplet from the array for further culture or analysis. This operation is particularly difficult in most microfluidic approaches and remains a blocking point for the adoption of microfluidics by biologists. Here we take advantage of our 2D geometry to recover individual droplets out of the chip selectively, since extracting a single droplet from the array does not disturb the rest of the anchored drops.

The extraction protocol relies on melting selectively an individual agarose droplet by heating it with a focused laser. The infrared laser is directed through the microscope objective to a spot size of around $2\ \mu m$ and can be positionned at any location within the field of view of the microscope (see Fig. 3.11a and appendix B.3 for detailed setup). Therefore by focusing the laser spot within a particular droplet for a few seconds, the agarose is melted only within the chosen drop. Then by imposing an oil flow beyond a critical value

(a)

(b)
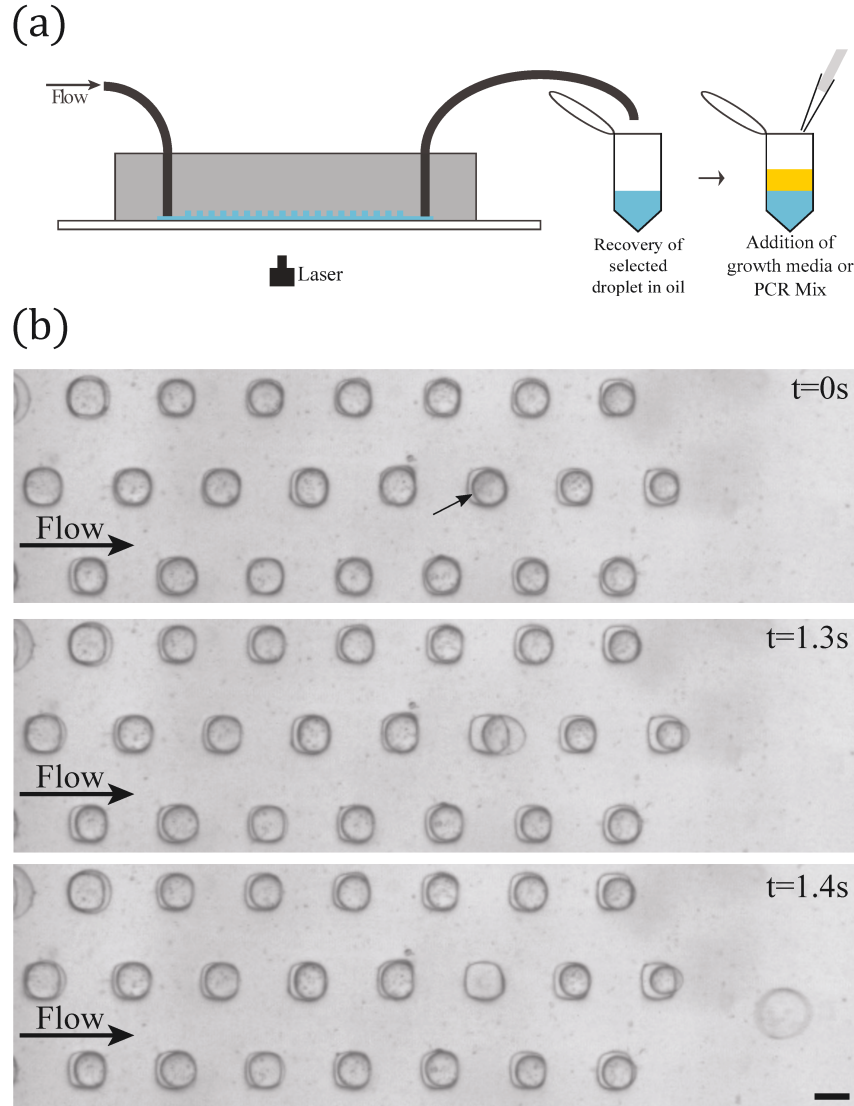
Figure 3.11: (a) Sketch of the extraction setup. (b) Snapshots of the droplet recovery. The droplet indicated by an arrow and colored in red for better visualization has been liquefied using the laser. Scale bar: 200 μm .

of 280 μL/min, the liquid droplet is pushed outside of its trap and recovered in a micro-centrifuge tube outside of the device, as shown in Fig. 3.11. In contrast with the work reported by Fradet et al.,[81] the anchor dimensions and the difference in rigidity between liquid and gel drops here makes the recovery process robust and fast. During this process all the gelified droplets remain immobilized inside the chip, rigidly constrained in their respective traps. The protocol can be repeated to recover as many droplets as needed out of the chip. To ensure that no cross contamination occurs during retrieval, a washing step with oil is generally performed between each droplet recovery.

As a proof of concept, a chip with agarose droplets encapsulating pGlo mutants is incubated overnight, such that bacteria form individual colonies. Then, a droplet containing a colony is recovered in microcentrifuge tube (see Fig. 3.12), along with the oil used to extract it. From this step on, two different paths are explored : either the extracted bacteria are subcultured, or a Polymerase Chain Reaction (PCR) is performed.
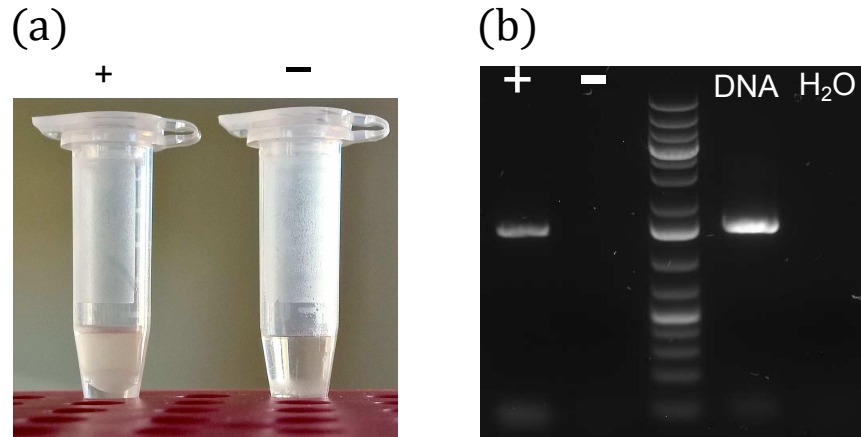
Figure 3.12: (a) Overnight incubation result of positive recovered droplets (+) and empty recovered droplets (-). (b) Droplet contents amplification result. DNA from a single bacteria-filled droplet (+) are detected on the gel and not from empty droplets (-).

For subculturing, LB broth is either added to all tubes containing a single droplet and samples are incubated two days at 37 °C under agitation, or in the extraction chamber. Bacterial growth of the expected strain was observed only for droplets containing a microcolony, see Fig 3.12a. As the growth was performed in presence of ampicillin, the extracted bacteria correspond effectively to the loaded strain. This result indicates that the retrieval process does not alter the viability of the extracted cells.

For PCR amplification on the recovered droplets, the expected amplicon was detected for positive samples (tubes containing a single positive droplet), while no DNA fragment was amplified for negative droplets, see Fig. 3.12b. Even if further optimizations are needed to reduce the risk of cross-contaminations, the generic chip is the first device enabling such a wide range of high-throughput phenotypic measurements that can be directly associated to genotypic analyses out of the chip.

As the droplet size is very small compared to the recovering tube, it is complex to verify systematically the recovery of the droplet. To circumvent this problem, we design small collection chambers that can host one or multiple droplets extracted from the chip (Fig. 3.13a). At each extraction, the outlet of the main chamber is connected to one of the

(a)

Laser

Collection Chamber

(b)

25 x

Collection Platform
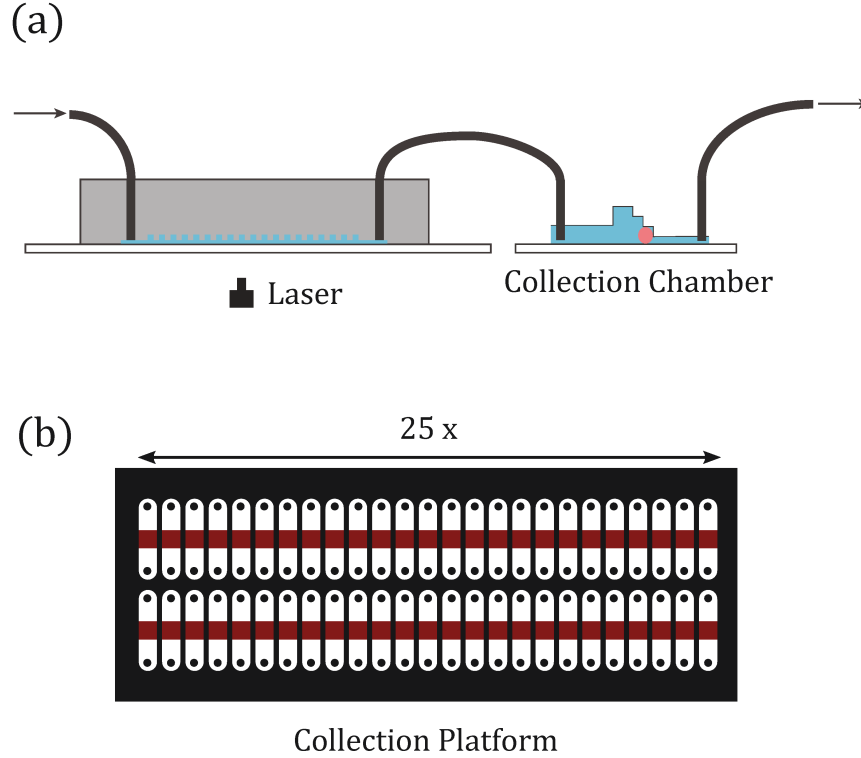
Figure 3.13: (a) Collection chambers are placed at the outlet to recover the extrated droplets. (b) 2×25 collection chambers can be placed on a microscope slide.

50 collection chambers that can be placed on a microscope slide (Fig. 3.13b). The chamber consists of a series of steps that blocks the extracted droplets in the chamber for visual control of the extraction (Fig.3.14). As the extraction processes involves very high flow rates, pillars have been added to prevent the PDMS from bending, which would allow the droplets for escaping from their capillary trap.

In addition to the visual control of the extraction process, the collection chambers can also be used to bring growth medium or PCR mix to perform the post-treatment directly on-chip to avoid another chance to loose it. Finally, the content can be retrieved out off the collection chamber by flowing the continuous phase backwards.

Over 90% of the extracted droplet have been successfully controlled. We think the lost droplets might have been attached to channel imperfection or tubing connection. The rest of the failures is when several droplets where extracted whereas only one was expected as shown on figure 3.14. Although the extraction efficiency was sufficient for our current use, more sensitive experiment would require further developments to bring the success rate up to 100%.
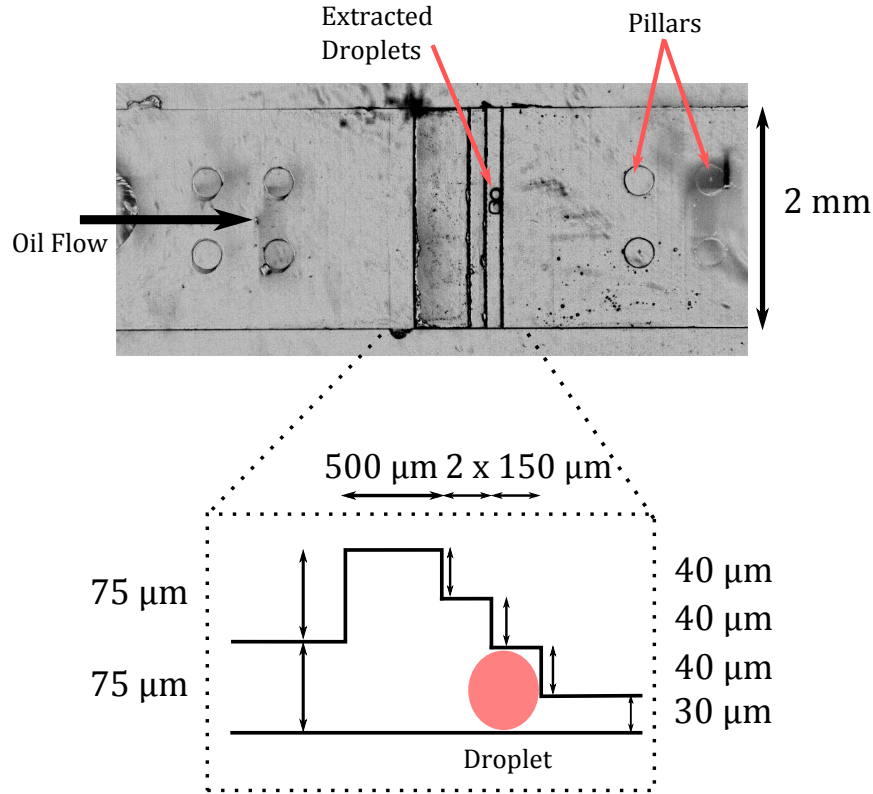
Figure 3.14: Picture of two agarose droplets trapped in an extraction chamber with dimensions (dimensions are not scaled for better visibility).

3.2 Cells distribution in large droplets array

The encapsulation of bacteria cell with an agarose gel yields the formation of distinguishable colonies as presented in 3.1.2 and figure 3.16b. To enumerate the number of cell in every droplet, one could go through the tedious process of manually counting every colony in every droplet. However, this estimation can be performed in a more efficient way by using a 'digital' approach. The term digital relies on the fact that each droplet signal is considered as positive or negative depending on the presence of a colony or not. As all the strains used are fluorescent, the presence of a bacterial colony is easily determined on fluorescent images as shown on figure 3.17. This technique is particularly efficient as it requires low resolution images (≤ 6.5 μm /px) resulting in scan and analyse time of less than one minute.

Contrary to the previous section which presents experimental results of culturing bacteria growth on our generic platform, this section derives theoretical tools based on the digital approach. After describing how to extract the number of positive droplets from low resolution images, we recall the basic principle and main results of the digital approach of cell

enumeration using the Poisson distribution. Although this distribution limits the number of droplets containing a single cell, we take advantage of it by analysing the case of two species distributions to predict the number of co-localization and even species interactions. Finally, this theoretical tool is extended to a large number of species to study symbiosis in large bacterial ecosystems such as mice microbiome.

3.2.1   Image Analysis for digital approach

Once the colony are formed, their fluorescence response is strong enough to be easily detected with a low resolution scanner (SensoSpot-Fluorescence, Sensovation AG, Germany) and images the entire chip at 6.5 μm/pixel (Fig.3.15a).

The well detection is achieved thanks to the open source software ImageJ, specially designed to perform image analysis. Due to the basal fluorescent level of the agarose gel, the function 'Find Maxima' on ImageJ can provide a good detection of all the well positions (Fig. 3.15b). A custom Matlab program uses the well position to measure the fluorescent level for each well. As we just need to discriminate positive droplets from negatives ones, we look for maximising their contrast between empty droplets by setting the fluorescent level as the mean of the 10 highest pixels.

The histogram of the measured fluorescent level is shown on figure 3.15c. Two groups
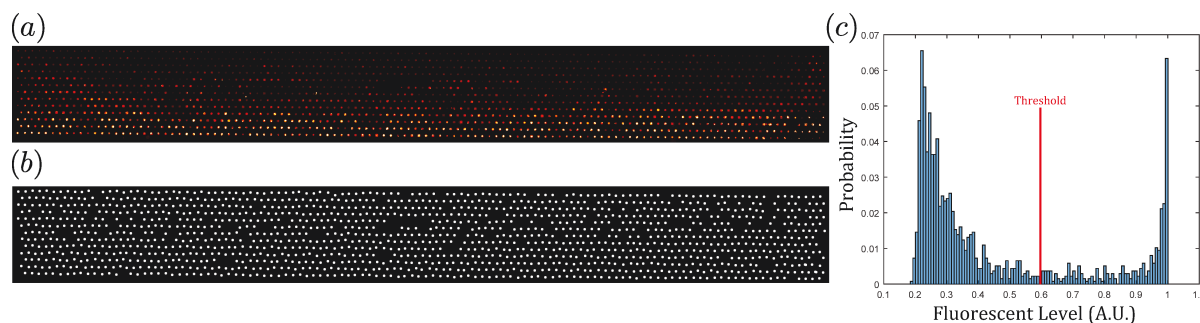
Figure 3.15: a) Scan of the microfluidic platform with a low resolution scanner (6.5 μm/px). The raw image has been modified with the red hot lookup table from ImageJ for better visualisation. For this example, we intendedly chose an experiment with only a few rows of grown colonies. b) Result of the well detection using the 'Find Maxima' function of ImageJ. c) Histogram of the fluorescent level for each detected well. In order to discriminate the most the positive wells from the negative ones, we define this level by the mean of the 10 highest pixels. The threshold set by the Matlab *graythresh* function to separate negative droplets from the positive ones is also shown.

can be eventually identified by setting manually a threshold. The fluorescent values below the threshold corresponds to the negative droplets whereas the values above the threshold

stand for the positive droplets. The result consists in a binary matrix with 1 if the well is positive and 0 if not. If the fluorescent signal of the colonies is not intense enough, the two population signal densities get closer and the efficiency of the threshold method is therefore altered. The method to deduce the initial cell concentration from the experimental measurement will be now presented.

3.2.2 Cells distribution in encapsulation process

The basic principle of a digital approach relies on the Poisson theory for finding a rare event in a random experiment. Assuming that cells are homogeneously distributed in the original suspension, that droplets are monodisperse, and that the number of cells in a given droplet is independent from the contents of other droplets, the distribution of the number of cells per droplet follows a Poisson law.[82]

To understand this result, let us consider an initial batch of volume V containing N bacteria cells. Let us then choose randomly a droplet of volume v_d amongst the initial sample volume V. We can therefore define the random variables $(x_i)_{i \in [[1,N]]}$ which take the value 1 if the bacteria number i is in the chosen volume v_d. Thus, the variables x_i follow a Bernoulli law:

$$\forall i \in [[1, N]] \quad \mathbb{P}(x_i = x) = \begin{cases} \frac{v_d}{V}, & \text{if } x = 1, \\ 1 - \frac{v_d}{V}, & \text{if } x = 0. \end{cases} \tag{3.4}$$

It results that the random variable giving the number of bacteria in the chosen droplet $n_0 = \sum_{i=1}^{N} x_i$ follows a binomial law of parameters $(N, v_d/V)$. As in our experiment $N \sim 1,000$ (large value) and $v_d/V \sim 10^{-3}$ (rare event), the law of n_0 can be approximated to a Poisson law (cf inequality of Le Cam[83]) :

$$\mathbb{P}(n_0 = k) \sim \frac{\lambda^k}{k!} e^{-\lambda} = p_k \quad (k = 0, 1, ...) , \tag{3.5}$$

with $\lambda = \frac{N v_d}{V} = c v_d = \mathbb{E}(n_0)$, the average number of colonies per droplet and c, the initial cell concentration.

By knowing the number of empty droplets, the Poisson law p_k enables us to estimate the initial number n_0 of bacteria cells per droplet. The experimental fraction $\hat{p} = \frac{N_+}{N_+ + N_-}$ of positive drops to the total number of drops is used to build an estimator $\hat{\lambda}$ of λ, for the initial sample cells distribution within the droplets. By noticing that $\hat{p} = 1 - p_0$, one can deduce :

$$\hat{\lambda} \simeq - \ln(1 - \hat{p}) \tag{3.6}$$

The error made by taking $\hat{\lambda}$ instead of λ can be evaluated statistically. The 95% confidence interval of the real ratio of positive drops to the total number is $[p_{\min}, p_{\max}] =$

$[\hat{p} - 1.96\ \sigma_{\hat{p}}, \hat{p} + 1.96\ \sigma_{\hat{p}}]$, with $\sigma_{\hat{p}} = \sqrt{\frac{\hat{p}(1-\hat{p})}{n_d}}$ the standard deviation of $\hat{p}$.[82] Thus, from this interval and equation (3.6) we can calculate our 95% confidence interval on λ.

For the microfluidic device containing $1,495$ independent droplets of volume 2 nL, the range of concentrations that can be estimated with a relative error smaller than 20% spans two orders of magnitude, from $\sim 7 \times 10^4$ to $\sim 3 \times 10^6$ cells/mL.

(a)

(b)

(c)
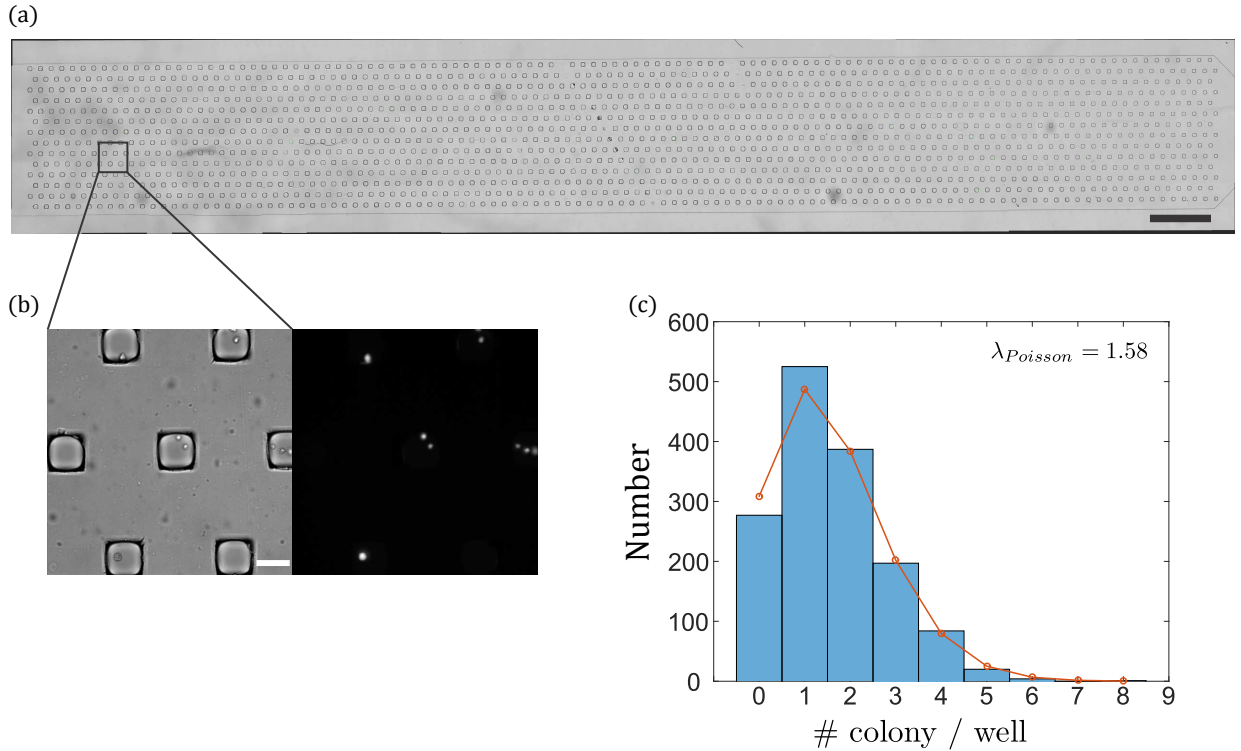
Figure 3.16: (a) Snapshot of the chip with 1,495 individual droplets containing 3D colonies of fluorescent bacteria. Scale bar: 2 mm. (b) Zoomed view on the anchors. Left: bright field image. Right: Fluorescence image. Scale bar: 100 μm . (c) Experimental distribution of the number of colonies per droplet (dots), and best fit to a Poisson distribution (bars).

We experimentally verify that the number of cells per droplet follows indeed a Poisson distribution by counting the number of colonies in each solidified gel drop, as shown in Fig. 3.16c. The resulting distribution is fitted with a Poisson distribution using λ as the sole fitting parameter. For this particular example, we observe a mean density of 1.58 cells per droplet after the breaking processes. The good agreement between the measured and fitted distributions can be attributed to the weak physical interactions between bacteria during the loading process and to the good monodispersity of the compartment sizes in the chip.

As a proof of concept of the digital enumeration method, a sample of *E.Coli* with an initial known concentration of 1 cell/nL is loaded on the device and scanned on a low-resolution slide scanner (SensoSpot®-Fluorescence, Sensovation AG, Germany) after 24 hrs incubation at 37 °C. We count $N_+ = 941$ positive anchors on the fluorescence image (Fig. 3.17), and $N_- = 135$ empty droplets[3]. This leads to an average initial number of bacteria per droplet and its associated 95% confidence interval of $\hat{\lambda} = 2.07 \pm 0.15$ cells/droplet. The droplet volume being 2 nL, we indeed recover the expected concentration of cells in the initial sample, that is $1.0 \cdot 10^6$ cells/mL.
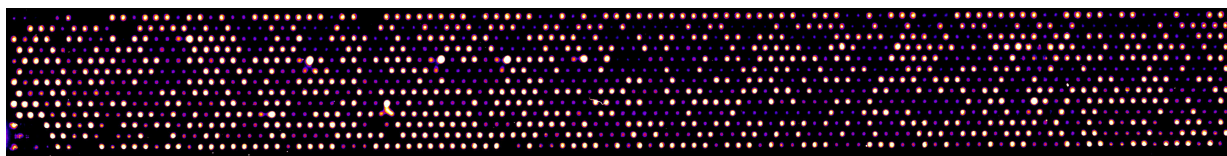
Figure 3.17: Low-resolution image taken on a slide scanner, on which the digital approach is performed.

Compared with direct visualisation of the colonies in each droplet, the digital approach simplifies the work flow by allowing us to work with lower resolution images, which makes them fast to acquire and analyse. Indeed, the slide scanner has a spatial resolution of 6.5 μm, which is sufficient to differentiate positive and negative droplets, although not sufficient to count the colonies with each drop. More importantly, this allows us to obtain a quantification of cells cultured in liquid medium, without requiring gelified droplets in which colonies can be distinguished for manual counting.

Finally, when comparing most of our experimental data, we found that for constant initial optical densities, i.e. constant cell concentrations, the Poisson coefficient measured on-chip differs from a chip to another. We think that this lack of consistency is due to the agarose viscosity. As the agarose is very viscous at 37 °C, the pipetted volume is not constant from an experiment to another which results in variation of the effective mixing ratio and thus of the effective optical density of the sample loaded in the microfluidic chip. The digital quantification is therefore essential to know the real cell concentration loaded into the chip.

3.2.3 Co-culture of two bacterial strains

The Poisson distribution can be extended to the co-culture case of two bacteria species. Let us consider an experiment where in the initial batch *E.coli* and *P.fluorescens* are mixed with initial cell concentrations of $\lambda_1 = 0.48$ and $\lambda_2 = 2.46$, respectively. The

---

[3]The reader may notice that $N_+ + N_- = 1076 < 1,495$, because the experiment has been made before we standardised the number of wells to $1,495$.

two species can be separately followed as they express different fluorescent protein : the Green Fluorescent Protein (GFP) for *E.coli* and the Red Fluorescent Protein (RFP) for *P.fluorescens* . When the initial sample is loaded on the $1,495$ wells chip and incubated overnight, four types of droplet will be revealed by the digital analysis : empty droplet, *E.coli* only droplet (Fig 3.18a), *P.fluorescens* only droplet (Fig. 3.18b), co-localization droplet with both *E.coli* and *P.fluorescens* (Fig. 3.18c).

(a)   (b)   (c)
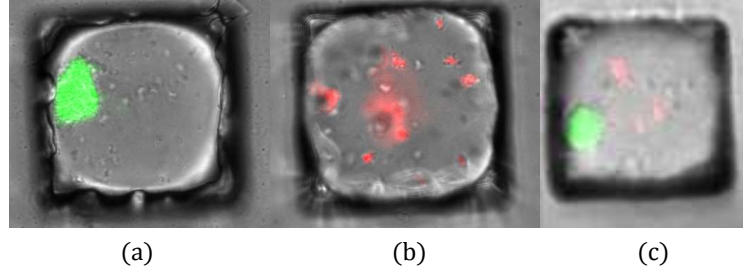
Figure 3.18: Snapshots of non-empty wells from an example of co-culture experiment. a) Droplet with *E.coli* only (40X). b) Droplet with *P.fluorescens* only (40X). a) Co-localization of *E.coli* and *P.fluorescens* in the same droplet (10X).

In such experiment, is it possible to predict the number of co-localization, empty or single species droplets given their initial concentration λ_1, λ_2? If one of the species concentration is too large ($\lambda \gg 1$), this species will grow in all of the droplets and the problem is reduced to the single species problem as in 3.2.2. If now both species are diluted enough, we can uses the Poisson theory to predict the different amount of each droplets. As for a single species, it is convenient to estimate the probability of absence $\mathbb{P}(k = 0)$ and then deduce the probability of presence $\mathbb{P}(k \neq 0) = 1 - \mathbb{P}(k = 0)$.

Calculus derivation.   We start by estimating the number of droplet containing *E.coli* . The probabilities for *E.coli* to be present in the droplet number l is:

$$\forall l \in [1..n_d] \quad \mathrm{P}_l^1 = 1 - e^{-\lambda_1}. \tag{3.7}$$

If M_1 represents the random variable corresponding to the number of droplet containing *E.coli* , we can estimate the probability for this variable to take the value m_1. When $M_1 = m_1$, m_1 droplets are positives and $n_d - m_1$ droplets are negative, such that:

$$\mathbb{P}(M_1 = m_1) = \binom{n_d}{m_1}(1 - e^{-\lambda_1})^{m_1} \left(e^{-\lambda_1}\right)^{n_d - m_1} \tag{3.8}$$

This corresponds to a binomial law of parameters $\left(n_d, 1 - e^{-\lambda_1}\right)$ such that the expected number of droplet containing *E.coli* is

$$\mathbb{E}(M_1) = \sum_{m_1=0}^{n_d} m_1 \mathbb{P}(M_1 = m_1) = n_d(1 - e^{-\lambda_1}). \tag{3.9}$$

The same derivation can be performed for *P.fluorescens* such that the number of droplets containing *P.fluorescens* is $\mathbb{E}(M_2) = n_d(1 - e^{-\lambda_2})$.

The estimation for the number of co-localisation uses also the same type of derivation, but this time with the probability to have both species in the droplet l :

$$\forall l \in [1..n_d] \quad \mathrm{P}_l^{1,2} = \left(1 - e^{-\lambda_1}\right)\left(1 - e^{-\lambda_2}\right). \tag{3.10}$$

By defining M the random variables describing the number of co-localisation droplets we find

$$\mathbb{E}(M) = n_d \left(1 - e^{-\lambda_1}\right)\left(1 - e^{-\lambda_2}\right) = \frac{\mathbb{E}(M_1)\mathbb{E}(M_2)}{n_d} \tag{3.11}$$

and

$$\sigma^2(M) = n_d \left(1 - e^{-\lambda_1}\right)\left(1 - e^{-\lambda_2}\right)\left(1 - \left(1 - e^{-\lambda_1}\right)\left(1 - e^{-\lambda_2}\right)\right)$$
$$= \frac{\mathbb{E}(M_1)\mathbb{E}(M_2)}{n_d}\left(1 - \frac{\mathbb{E}(M_1)\mathbb{E}(M_2)}{n_d^2}\right). \tag{3.12}$$

Species interaction criterion. From this preliminary calculation, it is possible to derive a criterion that determines whether an interaction exists between the two species using solely the end-point scan after the colonies growth.
Let be m_1^0 ,m_2^0, the initial numbers of droplets containing *E.coli* and *P.fluorescens* , respectively; m_1 ,m_2, the number of droplets containing respectively *E.coli* and *P.fluorescens* measured on chip at the end; $m_{1,2}$, the number of co-localized droplets measured on chip; n_d the total number of droplets; and m_2^k the number of droplets that were containing both species at the initial time and contained only *E.coli* at the end such that : $m_{1,2}^0 = m_{1,2} + m_2^k$. By using the equation (3.11) $m_{1,2}^0 = m_1^0 m_2^0 / n_d$ and the fact that $m_2^0 = m_2 + m_2^k$, we obtain an expression for m_2^k :

$$m_2^k = \frac{m_1^0 m_2 - m_{1,2} n_d}{n_d - m_1^0}. \tag{3.13}$$

In the case where *P.fluorescens* has no impact on *E.coli* , the number of positive droplets observed for *E.coli* corresponds to the initial number of droplets containing *E.coli* such that $m_1^0 = m_1$. This allows to calculate the result of equation (**??**). If the equation is not zero, it means that some of the co-localized droplets have turned into single species droplets resulting from the competitive interaction between the two species. If $m_2^k > 0$ interactions exist such that the criterion for species interactions is:

$$m_{1,2} < \frac{m_1 m_2}{n_d}. \tag{3.14}$$

	Total	*E.coli* (m_1) / λ_1	*P.fluorescens* (m_2) / λ_2	Co-localization M_{exp}	Prediction $\mathbb{E}(M)$	Prediction $\sigma(M)$
Number of Droplets	1489	569 / 0.48	1362 / 2.46	448	519	18

Table 3.1: Result and prediction of a co-culture of *E.coli* and *P.fluorescens* on chip.

Yet, this criterion does not integrate the standard deviation σ of the random variables M measured on chip. As the 99.73 % confidence interval for M is $[m_1 m_2 / n_d \pm 3\sigma]$, the 99.73 % confident criterion for interaction is :

$$m_{1,2} < \mathbb{E}(M) - 3\sigma = \frac{m_1 m_2}{n_d} - 3\sqrt{\frac{m_1 m_2}{n_d}\left(1 - \frac{m_1 m_2}{n_d^2}\right)}. \qquad (3.15)$$

The interesting thing about this criterion is that we do not need to know the initial number of positive droplets for each species (m_1^0 , m_2^0) to detect interactions between the two species. The end-point measurement solely indicates whether an interactions stopping one of the species growth has occurred during the experiment or not. To have more precise information to quantify an interaction, we have to follow the dynamics of each well. A dynamical measurement could also highlight other types of interactions that do not necessarily stop the bacterial growth but reduce or increase the bacteria growth dynamics. For instance, species 1 could induce a delay in the growth of species 2 or even both species could have a slower growth in the presence of each other.

Experimental Result. The digital analysis results of the experiment presented in figure 3.18 are shown in table 3.1. We see that the experimental number of co-localization is well below its expected value and verifies the interaction criterion (3.15) : $M_{exp} \sim \mathbb{E}(M) - 4\sigma < \mathbb{E}(M) - 3\sigma$. This means that there is an interaction between *E.coli* and *P.fluorescens* .

 By visual inspection of the figure 3.18a, one can see that small colonies of *P.fluorescens* are present in the droplet but they do not express fluorescence any more. This means that the interaction with *E.coli* stops either their growth or the expression of the red fluorescent protein. We have no insight about the type of interaction involved here, but for instance it has been reported that a competition exists between *P.fluorescens* and *E.coli* through the production of indole by *E.coli* . Indole is a derived product of amino acid L-tryptophan synthetised by tryptophanase (TnaA) and play a key role in the inhibition of the Quorum Sensing.[84]

3.2.4   Extension to multiple species for new *in vitro* culture conditions discovery

In previous sections, we explore the quantitative data that allow the digital approach for a single and two species. In this section, we extend the calculus derivation to any number

of species in order to find combination of species that live in symbiosis and thus identify *in vitro* culture conditions for a target species.

This work has been initiated by a collaboration between our group and the laboratory of Molecular Microbial Pathogenesis at Institut Pasteur. Sansonetti's group works with a bacteria called *Segmented Filament Bacteria* (SFB), involved in the development of mice and human immune systems. The particularity of SFB dwells in the fact that it can only be grown *in vivo* in mice guts. Working with living mice renders experiment complicated and long-standing. In 2015, they discovered a new *in vitro* culture condition for SFB but involving guts epithelial cells.[85] Yet, eukaryotic cells are very sensitive and require a long period of time to grow, which does not really simplify the SFB cultivation. The discovery of *in vitro* culture conditions involving solely prokaryotic cells is a striking challenge that would give access to a wider range of experimental investigations on bacteria strains such as SFB.
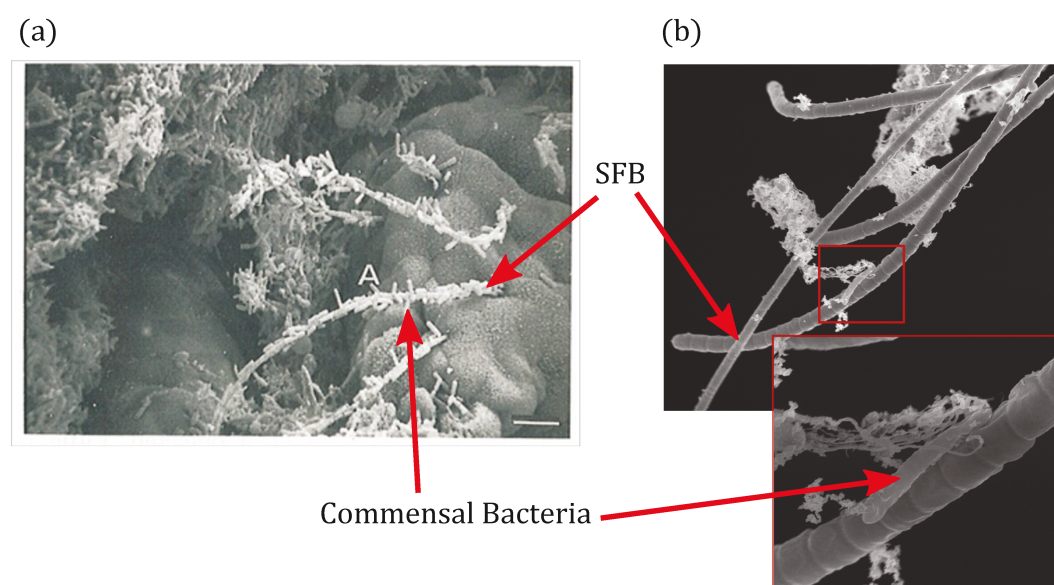
Figure 3.19: High resolution images taken with a *scanning electron microscope* (SEM). (a) Segmented Filament Bacteria (SFB) covered by commensal bacteria. (b) Zoom view of SFB with a single commensal bacteria attached to its surface. Source: Molecular Microbial Pathogenesis Lab, Pasteur's Institute.

For the last two decades, symbiotic contribution of microbiota to the key host physiological functions have been highlighted, which also suggests the existence of symbiotic interactions between microbiota species. On figure 3.19, the long and large filaments correspond to SFB cells with smaller commensal bacteria attached on its surface. It is assumed that these bacteria are feeding larger ones by providing the essential metabolite for SFB growth. Our objective is to find the minimum number of required species to grow SFB and this group

of species will be called the 'Key', such that SFB could be grown directly from the shelves. In this section we give the theoretical background showing that our generic platform can be used to determine the Key.

The general protocol envisaged for the experiment is summarized in figure 3.20. The generic platform is used to create n_d samples of the initial batch containing the commensal bacteria and SFB. After incubation, the droplets showing SFB growth are first extracted with our laser method (cf section 3.1.5) and then sequenced to determine their species composition. Bacterial species common to all the positive droplets are the best candidates to constitute the Key. This intersection of bacterial species can be either minimal if it corresponds exactly to the Key or too large if it contains species that are not essential for SFB growth.

In this problem three parameters remain unknown: the number of commensal species, the number of species contained in the Key and the cells concentration in the initial batch. Below, we evaluate the probability of finding exactly the Key after sequencing positive droplet previously extracted on a single chip. To estimate a honest value we take a very large number of commensal species and plot this probability as a function of the two remaining unknown parameters. We first estimate the probability of having at least one positive droplet on a chip. Then, we calculate the expected number of positive droplets to finally reach a simplified expression for the targeted probability. In appendix C, we provide an estimator for k based on the experimental measurements of positive droplets using moments method that is, here, equivalent to the maximum likelihood method.

Mathematical definitions To obtain an analytical expression for the probability of finding the Key, we have to convert the method scheme of the figure 3.20 into mathematical expressions. Let N be the number of commensal species and k the number of species contained in the Key K such that $\mathrm{card}(K) = k$. The initial commensal bacteria concentrations $(C_1, ..., C_N)$ are directly related to their Poisson coefficient $\lambda_j = C_j v_d$ with $v_d \sim 2$ nL, the droplet volumes. Initial SFB concentration is high enough such that it is present in every droplet and does not appear in our calculation. In each droplet $l \in [1..n_d]$ we associate a N-dimensional real valued random variable $X_l \in \{0, 1\}^N$. Its j-th component takes the value 1 if the species j is present in the droplet l, and 0 if not. Resulting from the Poisson distribution (see 3.2.2), the laws of $X_l[j]$ are given by :

$$
\begin{aligned}
\forall j \in [1..N] \quad & \mathbb{P}\{X_l[j] = 0\} & = & \quad e^{-\lambda_j}, \\
\forall j \in [1..N] \quad & \mathbb{P}\{X_l[j] = 1\} & = & \quad 1 - e^{-\lambda_j}.
\end{aligned}
\tag{3.16}
$$

We assume that the random variables $X_l[j]$ and $X_q[i]$ are independent if $i \neq j$ or $l \neq q$. Let be D_+ the index of the positive droplets. If ε_l is the set of the species labels in the
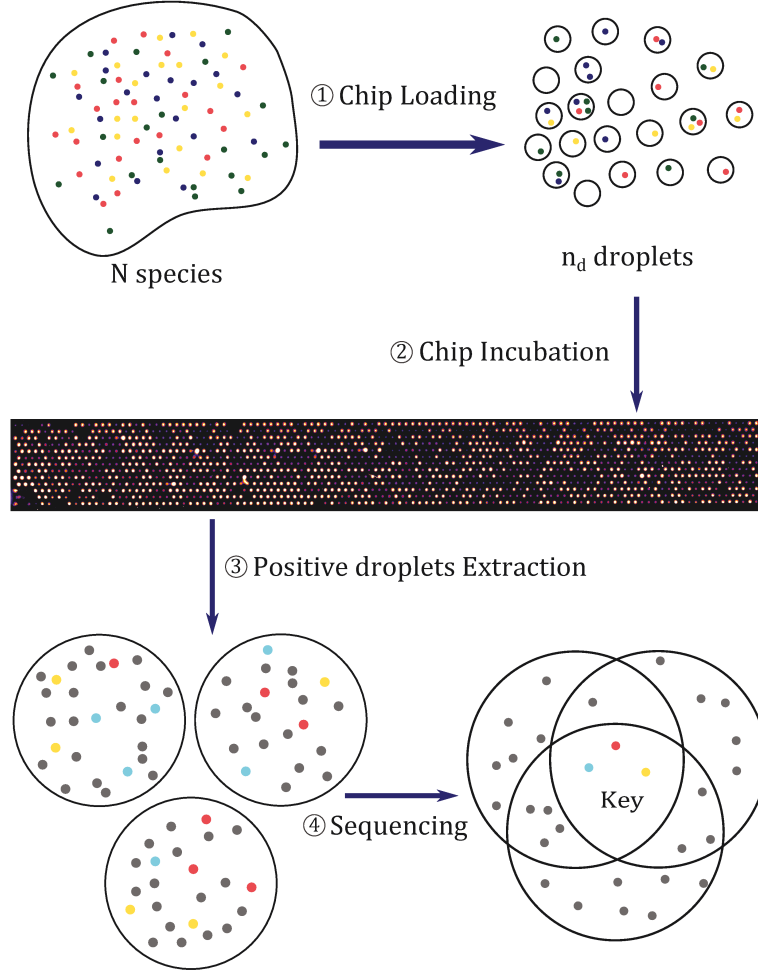
Figure 3.20: Method description to find the minimal species combination for growing SFB. 1) The initial batch containing a mix of commensal bacteria and SFB with the appropriate media is exploded in $n_d = 1,495$ droplets within the microfluidic chip. 2) The chip is incubated to allow for bacteria growth. 3) Positive droplets are extracted thanks to the laser set-up described in B.3. 4) Extracted droplets are sequenced and their content are compared to determine their common species. If this species intersection is minimal, we found the Key.

droplet content l, a droplet showing SFB growth will verify $l \in D_+$ and $K \subset \varepsilon_l$.

As we focus on the minimal combination of bacteria that gives a positive result and we want to determine the probability of the event E:

$$\textit{The intersection of the positive droplets is minimal} \Leftrightarrow \{ \bigcap_{l \in D_+} \varepsilon_l = K \}.$$

Probability of having the key K on a chip   As the distributions of all species are independent, the probability to have the key in a given droplet is :

$$\forall l \in [1..n_d]   \mathbb{P}\left(K \subset \varepsilon_l\right) = \prod_{j \in K} \left(1 - e^{-\lambda_j}\right). \tag{3.17}$$

We deduce the probability to have no positive droplet $\left(1 - \prod_{j \in K}\left(1 - e^{-\lambda_j}\right)\right)^{n_d}$ in a n_d droplets sample and immediately the probability to have at least one positive droplet:

$$\mathbb{P}\left(\{\exists l \in [1..n_d]/\ K \subset \varepsilon_l\}\right) = 1 - \left(1 - \prod_{j \in K} \left(1 - e^{-\lambda_j}\right)\right)^{n_d}. \tag{3.18}$$
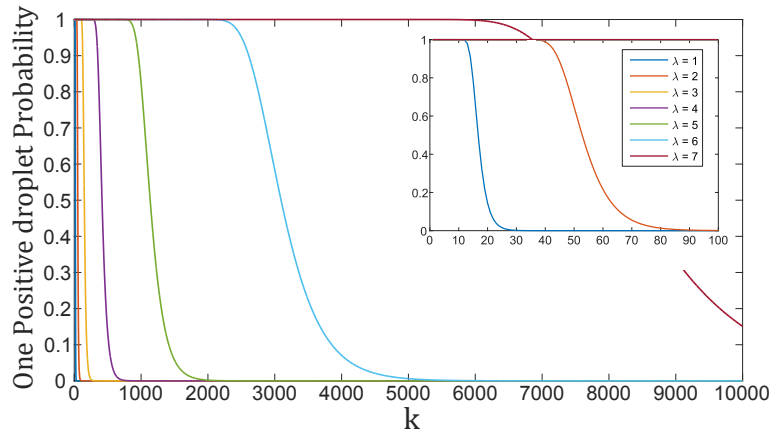
Figure 3.21: Probability to have at least one positive droplets as a function of k for different value of $1 \leq \lambda \leq 7$ and $N = 10^4$. Insert is a zoom for the k values between 0 and 100. Drawn from equation (3.18). For simplicity, the λ_j are identical and equal to λ.

Figure 3.21 is a plot of the probability to have at least one droplet positive as a function of the length of the Key K for various values of λ set by the initial concentration of each commensal species. In the diluted case ($\lambda = 1$), the presence of a positive droplet becomes very unlikely if the length of the Key is greater than 20. In the dense case ($\lambda \geq 4$), even large value of k results in at least one positive droplet. Indeed, it corresponds to the case where all the species are present in almost all droplets. This is not a satisfactory condition because the sequencing of the positive droplet will result in a too large intersection and we will not be able to determine the minimum number of species contained in K. Fortunately, microbiologists do not expect $k > 10$ which ensures the presence of at least one positive droplet. It is very important to be sure to have at least one droplet positive, such that when we perform the experiment we can prove whether SFB can grow *in vitro* or not without inferring a negative result to the possible absence of the key on chip.

Expected number of positive droplets   Let M be the random variable associated to the number of positive droplets on the chip such that $M = \text{card}(D_+)$. By definition of M we have :

$$E(M) = \sum_{m=0}^{n_d} m \, \mathbb{P}(M = m) = \sum_{m=0}^{n_d} \binom{n_d}{m} m \beta^m (1 - \beta)^{n_d - m} = n_d \beta,$$

$$\text{with} \quad \beta = \prod_{j \in K} \left(1 - e^{-\lambda_j} \right) \quad (3.19)$$

and

$$\text{Var}(M) = n_d \beta (1 - \beta). \tag{3.20}$$

One can notice that M follows a binomial distribution of parameters (n_d, β), as $n_d = 1,495$, for values of β not too low, i.e. k value not too high, the central limit theorem tells us that M can be described by a normal distribution of parameters $(n_d\beta, n_d\beta(1 - \beta))$. Therefore, according to the tables for normal distribution $m \in \left[n_d\beta \pm 3\sqrt{n_d\beta(1 - \beta)} \right]$ with a probability higher than 99.865%. Figure 3.22 draws the expected number of positive droplets as a function of k and for different values of λ. The number of positive droplets drops off quickly for low value of λ. To give an order of magnitude, the case $\lambda = 1$ is equivalent to an optical density[4] of $1/400$ for *E.Coli* and at this concentration we expect more than 150 positive droplets for $k = 10$. This is a good indication for an experimentalist when preparing the sample to test. For the experiments, several dilution will be prepared to cover a large range of λ and give us the maximum chance of finding optimal conditions. The optimal case results from a tradeoff between a sufficiently low concentration to have a good diversity of species amongst the droplets and a sufficiently high concentration to observe enough positive droplets to converge to the exact combination.

Probability of having exactly the Key   In the final step of the calculation, we want to know if we have enough positive droplets to find exactly the key. Let's be $\cap_m = \bigcap_{l \in D_+^m} \varepsilon_l$ the intersection of m positive droplets. The probability for a species i outside the Key not to be in all the m positive droplets is :

$$\forall i \in \bar{K} \quad \mathbb{P}\left(i \notin \cap_m \right) = 1 - (1 - e^{-\lambda_i})^m, \tag{3.21}$$

which enable us to calculate the probability for the intersection of all the positive droplets to be exactly the key when there are m positive droplets on the chip:

$$\mathbb{P}\left(\cap_m = K \right) = \prod_{i \in \bar{K}} \left(1 - (1 - e^{-\lambda_i})^m \right). \tag{3.22}$$

---

[4]The optical density measure the level of absorbance at 600 nm of a bacterial solution. It is used to measure bacteria cell concentration and will be further developed in chapter 5
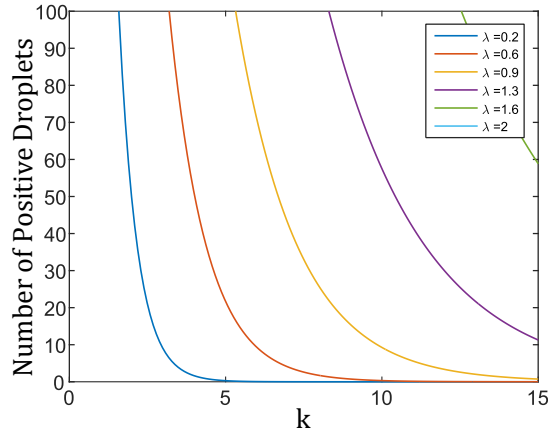
Figure 3.22: Number of positive droplets for various $1 \leq \lambda \leq 7$ and $N = 10^4$. Drawn from equation (3.19).

Therefore, the general expression of the probability to have exactly the key by looking at the intersection of all positive droplet is

$$\mathbb{P}\left(\underset{l \in D_+}{\cap} \varepsilon_l = K\right) = \sum_{1}^{n_d} \mathbb{P}(M = m)\mathbb{P}(\cap_m = K), \tag{3.23}$$

which can be written as

$$\mathbb{P}\left(\underset{l \in D_+}{\cap} \varepsilon_l = K\right) = \sum_{1}^{n_d} \binom{n_d}{m}\beta^m(1 - \beta)^{n_d - m} \prod_{i \in \bar{K}} \left(1 - (1 - e^{-\lambda_i})^m\right). \tag{3.24}$$

In the case where all the initial concentration are identical $\forall i \in [1..N] \quad \lambda_i = \lambda$, the previous expression can be written as function of λ, $\mathrm{card}(K) = k$ and n_d, the total number of droplets:

$$\mathbb{P}\left(\underset{l \in D_+}{\cap} \varepsilon_l = K\right) = \sum_{1}^{n_d} \binom{n_d}{m}p^{mk}(1 - p^k)^{n_d - m}(1 - p^m)^{N-k} \quad \text{with} \quad p = 1 - e^{-\lambda}. \tag{3.25}$$

As noticed earlier for the distribution of M, equation (3.25) can be approximated by :

$$\mathbb{P}\left(\underset{l \in D_+}{\cap} \varepsilon_l = K\right) \sim \sum_{\mu - 3\sigma}^{\mu + 3\sigma} \binom{n_d}{m}p^{mk}(1 - p^k)^{n_d - m}(1 - p^m)^{N-k},$$

$$\text{with} \quad p = 1 - e^{-\lambda}, \quad \mu = n_d p^k \quad \text{and} \quad \sigma = \sqrt{n_d p^k(1 - p^k)} \tag{3.26}$$

Figure 3.2.4 displays the result for the probability of finding exactly the key on a single chip. For $k \leq 10$, as soon as $\lambda \leq 5$, the probability to find the key on the chip is equal to 1. This means that with a single microfluidic experiment and sufficiently diluted conditions, we will be able to discover new *in vitro* culture conditions that microbiologists could not discover with their traditional techniques.
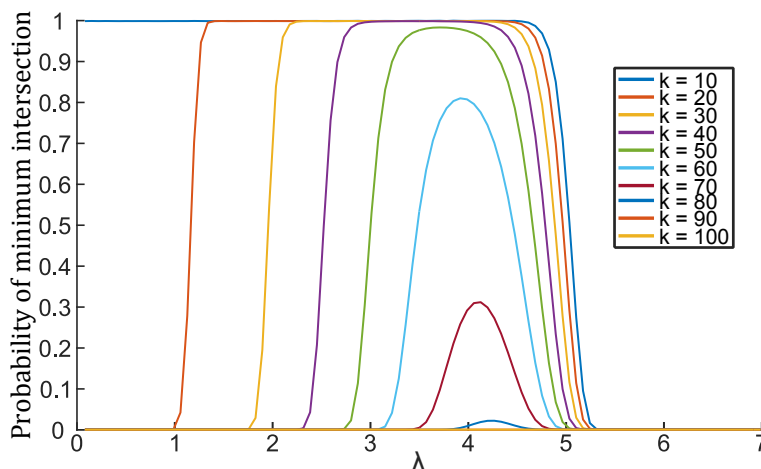
Figure 3.23: Probability to have exactly the key on a single chip with $N = 10^4$ for various value of k as a function of λ. Drawn from equation (3.26). For combination of less than 40 species we can find an initial concentration of the bacterial mix to find exactly to key by looking at the intersection of the positive droplet.

Experimental Attempt.   We performed the first experimental attempt in collaboration with the Molecular Microbial Pathogenesis lab from Institut Pasteur with the objective to observe SFB growth *in vitro*. The experimental set-up is described in figure 3.24. Bacteria cells are extracted from mice guts and diluted in appropriate medium before being loading on three different chips with three different cell concentrations. As commensal bacteria do not support oxygen, all the manipulation must be performed in anaerobic chambers, which increases the complexity of the manipulations. The particularity of SFB is that it is much bigger than the other commensal bacteria and grow in long and large filament which make it easy to distinguish on phase contrast images.

Figure 3.25 shows snapshots from our preliminary experiment. When SFB is cultivated alone on the chip, no growth is observed even after two days of incubation (Fig. 3.25a). In the case of very concentrated solution of figure 3.24c, SFB might have slightly grown but we cannot be sure as the size of the cells we found could be also found in the original batch. However, in diluted solution, large networks of SFB can be observed in several chip position (Fig. 3.24b).

The observation of figure 3.24b is very promising for several reasons. First, it proves that SFB can be grown *in vitro* with only prokaryotic cells. Second, it suggests that it exist optimal conditions for this growth in terms of initial cells densities and probably also in terms of species diversity. This preliminary experiment is very revealing for further attempts, but needs to be improved in two main aspects. The anaerobic conditions are hard to maintain during the visual inspection on motorised microscope outside the anaerobic chamber. Moreover, the experiment deals with the combination of two experimental pro-
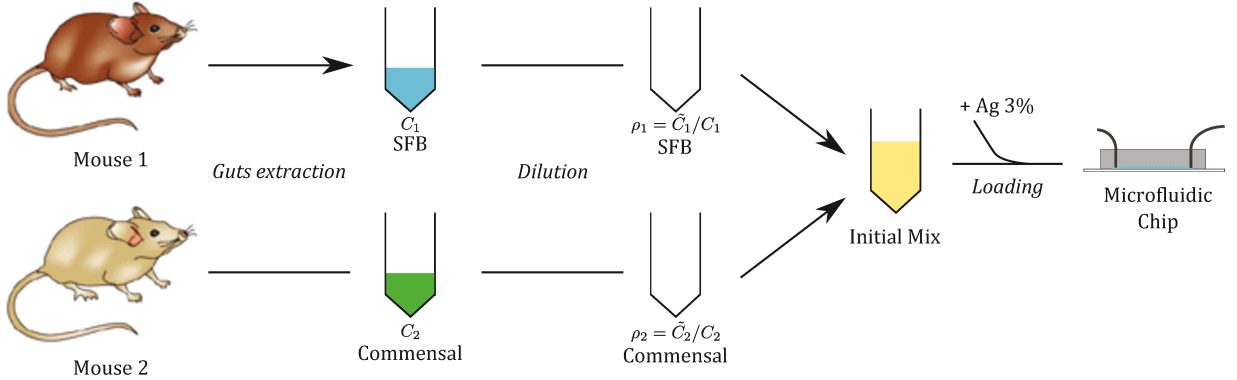
Figure 3.24: a) Schematic of the experimental method to prepare the initial mix of SFB and commensal bacteria. SFB and commensal bacteria are separately extracted from the guts of two different mice. Both guts contents are filtered and diluted in appropriate medium to form the original batches of concentration C_1 and C_2 for SFB and commensal bacteria, respectively. The original batches are diluted once again with ratios ρ_1 and ρ_2 that vary from chip to chip. The second dilution enable the creation of different initial concentration of bacteria.
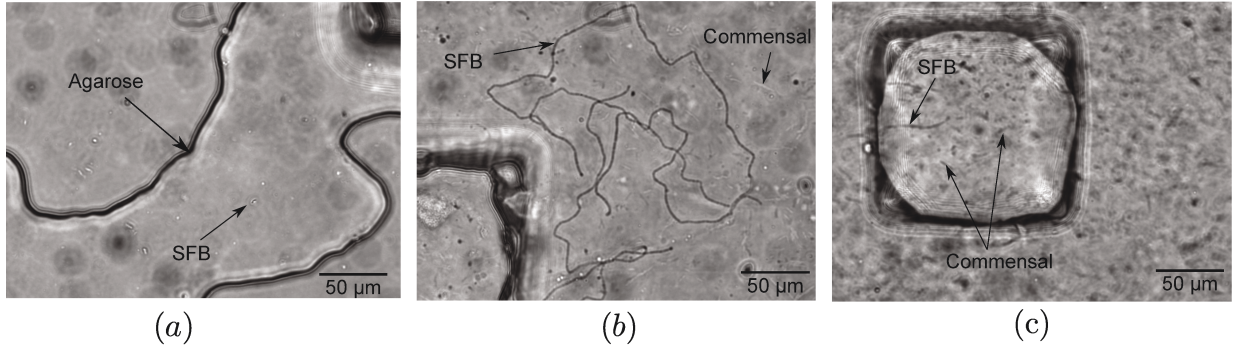
Figure 3.25: a),b),c) show snapshots of the first attempt of growing SFB in our generic platform for three different initial dilution rate ρ. The picture are taken after two days of chip incubation in anaerobic conditions at 37°C. a) Culture of SFB only with $\rho_1 = 1/100$. b) Mix of SFB and commensal bacteria (1:1 ratio) with a low initial concentration $\rho_1 = \rho_2 = 1/500$. c) Mix of SFB and commensal bacteria (ratio 1:1) with no second dilution, $\rho_1 = \rho_2 = 1$.

tocols which need to be adjusted together. Further attempts could not be performed due to PhD time constrai nts.

3.3 Summary and conclusions of chapter 3

In this chapter, a novel microfluidic platform is presented. It enables the cultivation of bacterial populations in the same way as in Petri dishes. We first demonstrate how thousands of bacterial cells can be simply encapsulated in a large droplet array. Its simplicity and robustness rely on the hard-coding of the physical mechanisms in the chip geometry. The production of $1,495$ monodisperse droplets is therefore possible without advanced instruments. This contrasts with the traditional flow-focusing method in which monodispersity depends on the precision of the flow-rate control and the quality of the surfactant.

Second, commonly studied bacteria species can be grown overnight directly on chip without requiring supplementary medium. During this time, they reach a sufficient size such that they can be observed properly as on a Petri dish. In the case of slower bacteria growth, additional medium can be brought by performing a phase change. The use of hydrogel beads, allows for the removal of the oil phase without removing the bacterial colonies. This will be detailed further in chapter 5.

Third, we take advantage of PDMS deformation and the low melting point of agarose to selectively recover any one of the droplets for further culture or analysis. This feature is particularly important for biological studies in several different respects. In biology, it is important to establish a relationship between an observed phenotype and the corresponding genotype. Therefore, the observation of a particular physiological function on chip can be directly related to a gene expression through gene sequencing. Further off chip culture is also vitally important in the case of the study of inheritance of a particular function such as the resistance to an antibiotic or the expression of a target molecule.

Fourth, quantitative measurements can be performed in the same way as on a Petri dishes by enumerating all the colonies and identifying a rare mutant with better detection limits compared to traditional microbiology techniques. The combination of the large number of droplets with the Poisson-like cell distribution enables the adaptation of a digital analysis to our device. It provides a simple and systematic method for direct measurement of the initial sample concentration, which is not ensured by classical turbidity measurement based on a calibration curve. In the case of two species, the digital approach allows for the detection of interactions between the species by the use of simple criterion.

Finally, based on the three basic features of our platform : bacterial culture, quantification and recovery, a theoretical proof of concept is developed to discover new bacterial culture conditions. The model is illustrated by the example of Segmented Filament Bacteria. Starting from the observation of symbiosis between SFB and commensal bacteria, the cell repartition according to independent Poisson distributions create multiple micro-

ecosystems on the generic chip leading to several droplets with SFB growth. The sequencing of the positive droplets containing a large amount of SFB cells would determine the essential species for growing SFB *ex vivo*.

We performed the preliminary experiment at Institut Pasteur which showed very encouraging results as we observed SFB growth on chip. Future work should first provide a clearer proof of effective SFB growth in droplets with timelapse snapshots of positive droplets. Then, successful cultures should be extracted from the chip and sequenced to determine the minimum required species and validate the theoretical predictions. On a longer term, when the culture condition will be determined, it is of particular interest to understand the type of interactions between SFB and the associated commensal bacteria. This will require testing thousands of mutants of the commensal bacteria which could be parallelized on the generic chip as well. We believe that this project is a very promising and exciting project which should be further carried out.

Although other microfluidic designs allow for the elementary operations that are enabled by our device, the ability to integrate droplet production, storage, changing the droplet contents and droplet recovery in a single device and with this level of simplicity is not possible with current techniques. Yet, these operations are critical for biology protocols and constitute the microfluidic counterparts of the functionalities fulfilled by multiwell plates. One limitation of this device is the density of droplets due to the 2D-array geometry combined with a breaking process. However, we take advantage of this geometry by developing the extraction method that hints the resolution of new biological problem that could not be solve otherwise (cf SFB). Finally, the digital approach is limited as it relies on an end-point measurement that cannot provide information on the dynamical properties of the bacterial colonies development. This will be explored in the next chapter in which another level a quantitative measurement is brought by using the static storage of droplets to follow the dynamic growth of each individual colony.

Chapter 4

Time-resolved Measurements of Bacteria Growth

There is an increasing awareness about the phenotype heterogeneity amongst bacterial populations.[42] This heterogeneity is of particular interest in the case of the study of persisters, which are bacteria cells that switch their phenotype from growing to non-growing under antibiotic pressure. They represent a small part of the bacterial population (10^{-6} to 10^{-4})[86] and can survive to antimicrobial conditions.[87] Contrary to resistant bacteria that arise from heritable mutations, the persistance results from non-heritable phenotype changes due to fluctuations in gene expression or environmental signals.[88] Persistant bacteria can switch back to growing bacteria when the antibiotic pressure is removed. This limits efficiency of lasting effect of antibiotic treatments and can yield dramatic relapse for sensitive patients. The very small appearance probability in addition to the reversibility of the phenotype switching, make the persisters a very difficult system to study such that numerous questions remain open regarding the origin and the mechanism of appearance as well as their behaviour.

Bio-reactors, which use the fermentation ability of bacteria, can also benefit from the study of specific phenotypes. The selection of cells with particularly efficient metabolisms can be relevant for instance to optimise waste treatment processes. Contrary to the case of persisters, for bio-reactors optimisation we want to target the small part of the population that presents a fast growth. For both cases, the important feature is the capacity of the cell to grow in a given condition such that quantitative information on physiological function can be obtained by measuring their proliferation.

Historical growth measurement techniques follow bacterial growth at the population level. Bacteria growth is therefore well-studied at the macroscale and quantitative measurements of the characteristic growth parameters are defined at the population level. Yet, these meth-

ods are limited in their ability to measure the heterogeneity of the population composition. For instance, how are the growth rates distributed amongst the individual population members? How does the population adapt to nutrient variation? Do all the members switch their metabolism simultaneously or gradually under selective pressure? Such problems can be solved with the advent of microfluidic techniques for bacteria growth study at the single cell level.

The direct observation of bacteria division at the single cell level displays an inherent stochasticity within a bacteria population.[44] It results that a population can be characterised by distributions of growth parameters. Each distribution corresponds to the gathering of all the individual growth parameters. Moreover, it is important to distinguish two types of stochasticity. The first type derives from the natural variability within a population, e.g. variability in their genotype. This natural variability may have an impact on the individual growth characteristics. The second source of stochasticity results from the contributions of intrinsic and extrinsic factors to the realisation of the biochemical reaction resulting in the cell division. Intrinsic factors refer to the stochasticity in the internal chemical reaction,[89] gene expression, cell aging or epigenetic regulation, whereas extrinsic factors translate the perpetual changes in the microenvironment surrounding the bacteria cell (pH, temperature, dissolved oxygen, nutrient availability). The first stochasticity is therefore inherited by the daughter cells and is called *biological variability* while the second one is experiment-dependent and is termed *stochastic variability*. This brings another level of questions. In the case of bio-reactor optimisation, is the "hit" bacteria, identified as particularly efficient, similar to other bacteria and results from the stochastic variability or does it correspond to a biological variability such that its phenotype will be transmitted to the following generation?

The discrimination of whether an observed phenotype results from stochastic processes or a biological variability can be considered through the use of growth models. The comparison of the model results with experimental measurements allows for the determination of whether the observed variability can be purely due to mathematical reasons or necessarily results from biological variability. The establishment of growth models is performed on growth curves that describe the evolution of a bacterial population in time. Historically, growth models were developed at the population level to predict the evolution of a bacterial population in a given environment especially for the risk assessment in the food industry.[90,91] These models are characterised as *deterministic* models as they rely on differential systems of equations describing the bacteria growth dynamic. More recent models have emerged from bacteria studies at the single cell level. They translate the stochasticity of the cell division process and thus rely on stochastic equations. The two classes of models are complementary and we will see that they correspond to different levels of growth observation.

This chapter is devoted to the establishment of growth curves on the generic chip. The use of an array of static droplets allows us to follow the content of each droplet and observe the proliferation of thousands bacterial colonies. We developed a Matlab-based software to extract and analyse the experimental data generated by the observation of thousands bacterial culture in parallel. The observation at the colony level enables the quantification of the variability inside a bacterial population.

The first section reviews the first analytical study of bacteria growth that has been performed by Jacques Monod[71] in the late 40's. Monod formalised the basic method of microbiology by defining growth phases in the bacterial growth curves and growth parameters that characterise each growth phase. This will be followed by the main models developed to describe each level of growth observation as well as their limitations.

The second section presents how time-resolved measurements of independent growth of microcolonies within the generic platform can be followed and how their growth curves are established. To achieve this we developed a software that automates the measurement of each individual droplet content, gathers the extracted data into growth curves and measures the growth parameters defined in the first section.

The third section exposes our experimental results and compares the on-chip growth parameters measurements to the data of existing techniques to prove that our platform can be used in the same way as classical technique to follow bacteria growth. The way we grow and observe bacteria proliferation sets particular cultivation conditions and the range of accessible information resulting in constraints for the derivation of a growth model specific to our chip.

4.1 Bacteria growth characterisation and models

4.1.1 Bacteria growth curves characterisation

The historical techniques to measure bacteria growth curves are the viable count on agar-coated Petri dishes or the turbidity in liquid batch. For both techniques, the bacteria growth is performed in liquid batch containing the cells and the growth medium. The initial time ($t = 0$) of a bacteria growth study is defined by the time at which an initial number of cells, called 'inoculum', is diluted in fresh culture medium. The viable count consists in the spreading on a Petri dish of a constant volume pipetted out of the batch culture for given time points. After an overnight incubation, it is possible to visually count the number of bacteria cells and divide the pipetted volume to obtain the cell concentration at the sampling time. The turbidity technique is a direct measurement that relies on the

batch absorbance at 600 nm. The cell concentration is linearly related to the batch turbidity for absorbance ranging from 0.01 to 0.9. High absorbance level can still be measured by diluting the pipetted sample prior the measurement. This technique requires a calibration curve to translate each absorbance measurement into cell concentration.
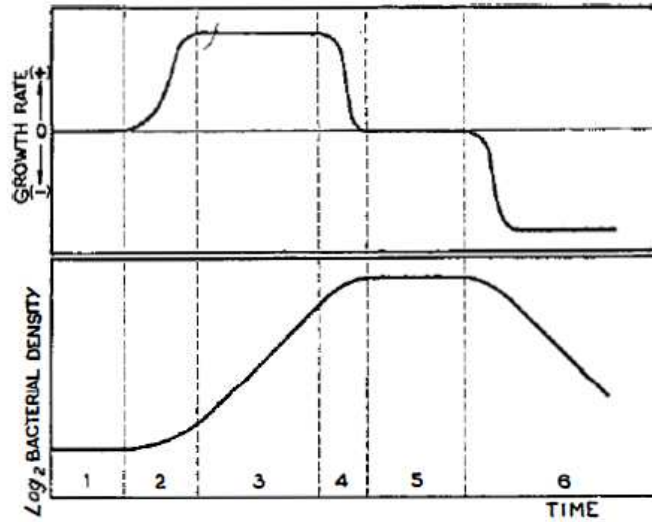
Figure 4.1: Extracted from Monod.[71] Phase of growth. Lower curve: logarithm of bacterial density. Upper curve : variation of growth rate. The dotted lines mark the limits of the growth phase define by Monod : 1. lag phase: growth rate null; 2. acceleration phase: growth rate increases; 3. exponential phase: growth rate constant; 4.retardation phase: growth rate decreases; 5. stationary phase: growth rate null; 6. phase of decline: growth rate negative. In the present work we will not study the phase 6 defined by Monod as the phase of decline.

A typical growth curve and its first derivative are shown in figure 4.1. The logarithm of the cell concentration is generally used, as the bacteria proliferate exponentially. Jacques Monod[71] formalised the characterisation of the bacteria growth by defining three main phases. All the phases are characterised by a cell density and an accompanying growth rate. The initial lag phase is characterised by no-growth or not observable growth, while the exponential phase occurs with a maximum growth rate and a strong increase of the population density. Finally, the population reaches a stationary phase where no further growth is observed.

Each phase can be characterised by its duration, cell concentration as well as the rate of cell division. Four main parameters are commonly encountered in growth models to quantify bacteria growth: (i) the inoculum size $y_0 = \log(x_0)$, with x_0 the cell density at $t = 0$; (ii) the lag time t_{lag}; (iii) the specific growth rate μ_{max} and (iv) the final colony size $y_{\mathrm{max}} = \ln(x_{\mathrm{max}})$, with x_{max} the cell density in the stationary phase. The final population size depends on the growth limitation factor which is often the nutrient quantity. The
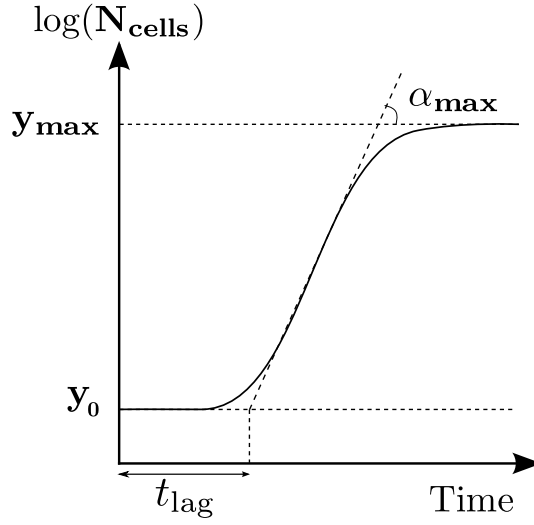
Figure 4.2: Growth parameters definition : inoculum size y_0, lag time t_{lag}, specific growth rate $\mu_{max} = \tan(\alpha_{max})$, final colony size y_{max}.

growth parameters are shown on typical growth curve in Figure 4.2. The measurement of the lag time and the specific growth rate are detailed below.

Lag Time. The lag time is the duration of the lag phase, a period during which little to no growth is observed. It results from the adaptation of the cells to a new environment or culture conditions. Thus, the length of the lag time depends on the metabolic state of the bacteria cells at the inoculation. Indeed, bacteria cells need time to increase their protein content until a threshold value before they start to divide.[92] In practice, the lag time is measured as the intersection between the tangent to the growth curve at the maximum exponential growth phase with the y_0-axis[93] as shown in figure 4.2.
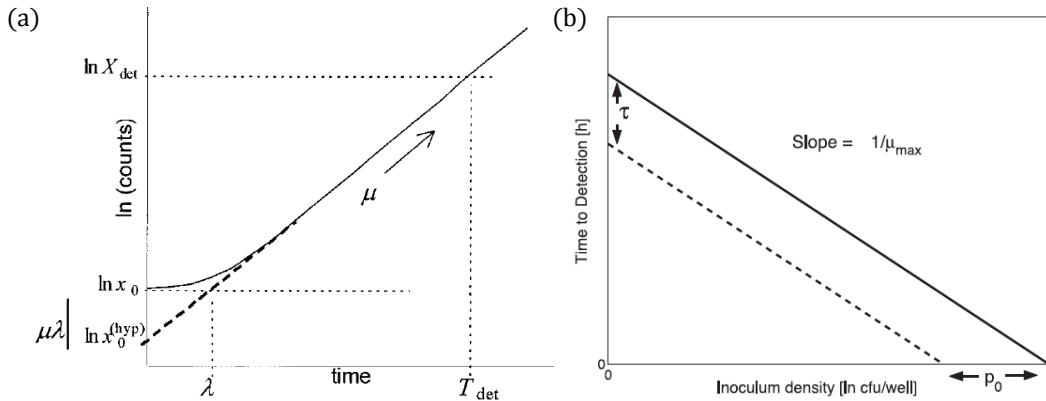
Figure 4.3: a) Impact of the detection level on the lag time measurement. (from Baranyi *et al.*[94]) b) Impact of the inoculum size on the time to detection (from Swinnen *et al.*[95]).

The measurement of the lag time must be clarified. The technique described above strongly depends on the inoculum size y_0 and the detection level of cell concentration measurement technique. Figure 4.3a displays an example of a typical case of a detection level X_{det} above the effective inoculum size x_0. Consequently, the measured lag time would correspond to a measure of the time to detection T_{det} rather than the real lag λ, time required for cells adaption to thenew environment (we keep the notation of the extracted figure). Therefore, the gap between the real and measured lag times is set by the detection limit of the technique used to follow the bacteria growth. Short lag time or lag time of highly diluted inoculum will consequently be overestimated by the time to detection rather than a real adaptation time to the new environment. The accuracy of the lag measurement will naturally be improved as the inoculum size gets closer to the detection limit as shown in figure 4.3b.

Specific Growth Rate.   The specific growth rate informs on the frequency of bacteria cell divisions. It is strongly related to the nutrient quality[92] such that a common technique to vary the bacteria growth rate is to change the culture medium composition[1]. The specific growth rate is typically defined as the maximum slope of the logarithm of the growth curve during the exponential phase:[96]

$$\mu_{max} = \max\left(\frac{d\ln x}{dt}\right) = \tan\alpha_{\max} \tag{4.1}$$

The maximum growth rate can also be defined on the linear plot of the growth curve :

$$g_{\max} = \max\left(\frac{dx}{dt}\right). \tag{4.2}$$

However, the specific growth rate is generally preferred as it is directly related to the doubling time of the population. The doubling time τ corresponds to time required to double the cell density during the exponential growth phase[96] such that:

$$\tau = \frac{\ln 2}{\mu_{max}}. \tag{4.3}$$

4.1.2   Growth Models

Now that we have seen how to describe bacteria growth and how to characterise the growth parameters, we present the underlying models developed to describe the bacteria growth

---

[1]The nutrient quality corresponds to the composition of the culure medium. A medium of good quality is rich in mineral, vitamins or lipids and contains simple carbon source that are easily processed by the bacteria cells such as glucose.

dynamics. We follow the historical path by describing first the bacteria growth model at the population level and then, the models developed for single cell analysis.

Deterministic growth models

A large amount of growth models have been developed since Monod's study and reviewed by Zwietering *et al.*[93] All those models are based on the geometry of the growth curve namely a sigmoidal shape. Baranyi *et al.*[97] generalised them by developing a family of growth fitting curves. We present here the main formalism used by Baranyi *et al.* to obtain an analytical expression of the bacteria growth curves.

1 – General Model. Let us consider bacteria cells cultivated in an environment E_1 and at $t = 0$, the cells are inoculated in an environment E_2 with a cell concentration x_0. The general mathematical formulation to model bacteria growth can be described by the first order initial value problem :

$$\dot{x} = \alpha(t)\mu(x)x \quad (0 \leq t < \infty; 0 < x)$$
$$x(0) = x_0, \tag{4.4}$$

where x is the cell concentration and $\mu(x)$ the specific growth rate. $\alpha(t)$ is called the adjustment function from E_1 to E_2 and follows the properties :

- $\alpha(t)$ depends on E_1 and E_2,
- $0 \leq \alpha(t) \leq 1$
- $\lim_{t \gg t_{lag}} \alpha(t) = 1$

Equation (4.4) is general for almost all the deterministic models and translates the exponential behaviour of the bacteria growth. Variations between the different models correspond to the exact expression of the two functions α and μ. α characterises the lag phase and increases from 0 to 1 for $0 \leq t \leq t_{lag}$. As demonstrated in Baranyi *et al.*,[97] any solution $x(t) = f(t)$ of equation (4.4) with $\alpha(t) = 1$ can be generalised with any $\alpha(t)$ through the relation :

$$x(t) = f(A(t)) \quad \text{with A(t)} = \int_0^t \alpha(s)ds \tag{4.5}$$

Therefore, it is possible to investigate first the resolution of (4.4) with $\alpha(t) = 1$ and then integrate to these solution different form for $\alpha(t)$.

2 – "Biological" μ. The function $\mu(x)$ integrates the growth limitation factors as it tends to 0 for large value of time ($t \gg t_{lag}$). It can be seen under two different perspectives.

On the one hand, the limitation can be seen as nutrients consumption by bacteria cells. Monod[71] discovered that the growth rate depends on the substrate concentration S, such that $\mu(x)$ can be defined as a function of S by the set of equations :

$$\begin{cases} \mu(x) & = \mu_{max}\frac{S}{K_S+S} \\ \frac{\mathrm{d}S}{\mathrm{d}t} & = -Y\frac{\mathrm{d}x}{\mathrm{d}t}, \end{cases} \tag{4.6}$$

where $Y > 0$ is the substrate consumption rate by bacteria cell and K_S the Michaelis-Menten constant. This expression of μ is the typical reaction rate of enzymatic reactions that underlies the substrate consumption by the bacteria. The second equation of the Monod's law (4.6) implies that the instantaneous substrate concentration in a batch culture depends linearly on the number of bacteria cells :

$$S(t) = Y(x_0 - x(t)) + S_0. \tag{4.7}$$

3 – "Geometrical" μ. Another way to define $\mu(x)$ is by choosing a function that fits the shape of the growth curve namely the logistic function:

$$\mu(x) = \mu_{max}\left(1 - \left(\frac{x}{x_{max}}\right)^m\right), \tag{4.8}$$

where m is a geometrical parameter describing the curvature of the growth curve between the exponential and the stationary phases. Baranyi *et al.*[96] derived an analytical solution for the logistic case :

$$y(t) = y_0 + \mu_{max}A(t) - \frac{1}{m}\ln\left(1 + \frac{e^{m\mu_{max}A(t)} - 1}{e^{m(y_{max}-y_0)}}\right) \tag{4.9}$$

where $y = \ln(x(t))$ and $A(t)$ is defined by (4.5). The bacteria cells concentration can be also followed by fluorescence for bacteria that constitutively express a fluorescent proteins. It is therefore useful to ask how equation (4.9) would change in such case. As the intensity produced by $x(t)$ bacteria cells is assumed to be linearly related to the emitted fluorescent intensity ($I(t) = \beta x(t)$), equation (4.9) can be expressed as a function of $I(t)$ by solely adding $\ln(\beta)$.

4 – Adjustment Function α. We now have to model the adjustment function $\alpha(t)$ to fully describe the growth function $y(t)$. Baranyi *et al.*[96] assumed that the bottle-neck in the growth process is the accumulation of a critical substance $P(t)$ in the bacteria cell following the Michaelis-Menten kinetics :

$$\alpha(t) = \frac{q(t)}{1 + q(t)} \tag{4.10}$$

where $q(t) = P(t)/K_P$ characterises the physiological state and K_P the Michaelis-Menten constant. By assuming that K_P remains constant even though E_2 is changing and that the production rate of $q(t)$ follows a first-order kinetics :

$$\frac{\mathrm{d}q}{\mathrm{d}t} = \nu q(t), \tag{4.11}$$

and an expression for $A(t)$ can be found:

$$A(t) = t + \frac{1}{\nu} \ln \left(\frac{e^{-\nu t} + q_0}{1 + q_0} \right). \tag{4.12}$$

Baranyi and Roberts[96] showed that $\nu = \mu_{max}$ and also $A(t) \sim t - t_{lag}$ when $t \gg t_{lag}$ such that :

$$t_{\mathrm{lag}} = \frac{\ln \left(1 + 1/q_0 \right)}{\mu_{max}}, \tag{4.13}$$

The dependence of t_{lag} on the initial metabolic state of a cell q_0 can be seen in this expression. The higher the initial level of the critical substance, the sooner the growth. This leads to a simpler expression for $A(t)$ function of the lag time t_{lag} and the specific growth rate μ_{max} :

$$A(t) = t + \frac{1}{\mu_{max}} \ln \left(e^{-\mu_{max} t} + e^{-\mu_{max} t_{lag}} \left(1 - e^{-\mu_{max} t} \right) \right). \tag{4.14}$$

The combination of equations (4.9) and (4.14) allow for the fitting of any growth curve with the five parameters y_0, y_{max}, t_{lag}, μ_{max} and m. y_0 and y_{max} are directly read on experimental growth curves, the fitting consists therefore in adjusting m, t_{lag} and μ_{max} for each growth curve.

Care should be taken when considering the fitting parameter μ_{max}. As observed by Perni *et al.*,[98] the parameter μ_{max} described above does not correspond to the $\max(\mu(x))$ defined in the previous section to measure the experimental specific growth rate. The μ_{max} in the Baranyi model is the experimental growth rate in the very diluted case where $x \rightarrow 0$. Here, the adjustment function α does not allow for such correspondence and thus, $\max(\mu(x)) = \max(\dot{y}(t)/\alpha(t))$.

The Baranyi's model is considered as a 'deterministic' model because it results from the resolution of the equation (4.4) that describes the general behaviour of the entire population. This model is convenient as it allows for simple fitting of the growth curves. Yet, it requires the data of the final population size y_{max} which is not possible in the case of predictive microbiology. Moreover, it provides only the behaviour of the entire population

and does not give access to the biological variability amongst the cell individualities. The deterministic models are therefore limited in the sense that they provide only global values of the population growth parameters without providing insight on the distribution of the individual parameters, which is why stochastic models have been developed.

4.1.3   Stochastic Modelling

Following bacteria growth at the single cell level has highlighted an inherent variability amongst the cells even in the same species. Let us consider a single bacteria cell in its exponential metabolic state. This bacteria cell is continuously elongating with an exponential rate depending on the quality of the nutrient until it divides into two daughter cells as shown in figure 4.4. The size at which the cell is dividing is determined by the added-size model developed by Taheri *et al.*[44] They demonstrated that the added length Δ to the newly born cell before the next division is constant and that the value of Δ depends solely on the quality of the nutrient. In this model, they also demonstrated that the stochastic variability in cell division was the result of the stochasticity of two parameters only : the elongation rate and the added-size Δ. The dispersion of the other growth parameters (generation time, division size, etc.) are mathematically correlated to the dispersion of those two parameters.[44]
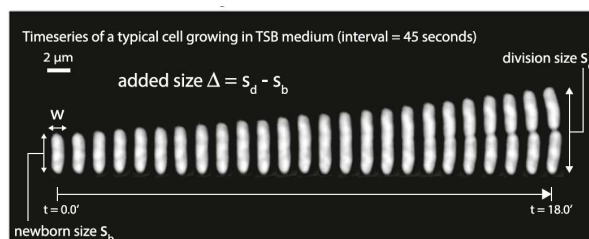
Figure 4.4: Typical timeseries of *E.coli* cell growing in rich medium, made in a mother-cell machine by Taheri *et al.*[44]

There exist two types of stochastic models. The first type considers the cell division event as a random process[99] as in Taheri *et al.*[44] The second type models the bacteria growth using the deterministic model results. The stochasticity is integrated by feeding the growth models with distribution of growth parameters. Such models aim to find correlation between the resulting population growth parameters and the individual parameters.[100,101]

Cell division as a random event

The simplest stochastic model is called the 'simple birth Poisson process' that is based on a single parameter μ such that $\mu \delta t$ is the probability for a cell to divide during an elementary time δt. μ is equivalent to the specific growth rate of the deterministic model.

It also depends on the nutrient quality surrounding the cell. The idea of the stochastic models is to estimate the probability $p_i(t)$ to have i bacteria cells at time t starting from an initial population size N at $t = 0$. Allen[99] derived the Kolmogorov differential equation for the probabilities $p_i(t)$:

$$\begin{cases} \frac{\mathrm{d}p_i(t)}{\mathrm{d}t} = \mu(i-1)p_{i-1}(t) - \mu i p_i(t), \ i \geq N, \\ \frac{\mathrm{d}p_i(t)}{\mathrm{d}t} = 0, \ i \leq N-1, \end{cases} \tag{4.15}$$

with a Dirac distribution as initial conditions $p_i(0) = \delta_{iN}$. We can see on equations system (4.15) that during δt, the probability $p_i(t)$ will increase if there is a division amongst a population of size $i - 1$ and will decrease if a division occurs amongst a population of size i. The analytical expression for $p_n(t)$ can be derived from the differential equation of the generating functions $\mathcal{P}(z,t) = \sum_{i=0}^{\infty} p_i(t) z^i$:

$$\frac{\partial \mathcal{P}(z,t)}{\partial t} = \mu z(z-1)\frac{\partial \mathcal{P}}{\partial z} \tag{4.16}$$

The analytical expression for $p_n(t)$ has been derived by Allen:[99]

$$p_n(t) = \binom{n-1}{n-N} e^{-\mu Nt}(1 - e^{-\mu t})^{n-N}, n \geq N, \tag{4.17}$$

which finally leads to the first two moments, the expected value and the standard deviation of $N(t)$:

$$m(t) = Ne^{\mu t} \quad \text{and} \quad \sigma^2(t) = Ne^{2\mu t}(1 - e^{-\mu t}). \tag{4.18}$$
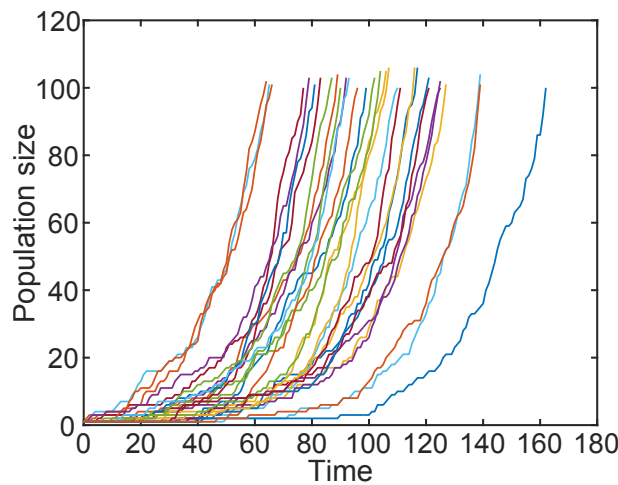
Figure 4.5: Simulation of 30 growth curves using a simple birth process with $N(t = 0) = 1$ and $\mu = 0.05$. The process is stopped when the population reaches 100 cells.

This simple birth process shows that starting with two identical cells with the same biological parameters and the same environment, we will observe variations due to the stochastic timing of the cell division. This is illustrated in figure 4.5 which displays 30 individual growth curves obtained with a simple birth algorithm. All 30 bacteria have the same characteristic parameter μ but yield different growth curves. If the number of curves is sufficiently high, the mean and variance of the number of descendants for each initial cell are described by the equations (4.18). One can also observe that the mean number of descendants corresponds to a purely exponential growth and does not integrate any lag or growth limitation factors. It translates therefore the ideal case of exponentially growing bacteria in a constant environment, i.e. constant nutrient quality and concentration. This kind of models predicts the pure stochastic variability as it does not integrate any biological variability in the parameter μ. If the moments of experimental growth curves differ from the moments expected by the stochastic model, it means that an additional variability occurs between the colonies. Therefore, such model enables to distinguish the stochastic variability from the biological variability.

Growth parameters distributions

The second approach of stochastic modelling was initiated by Baranyi[100] who obtained a relationship between the individual lag and the population lag. He started from a distribution of lag times for a given inoculum size and integrated it in a deterministic model with a constant growth rate to express the population growth parameters as a function of the individual parameters.

This work has been recently completed by Koutsoumanis *et al.*,[101] whose work cosnists of two parts. The first part is the experimental measurement of families of individual lag times τ_i and specific growth rates $\mu_{\max\ i}$ on 220 bacteria cells of *S. Typhimurium*. They fitted the obtained distributions with a log normal distribution for the lag times and a logistic distribution for the specific growth rates. This allowed them to measure the stochasticity of *S. Typhimurium* in their experimental conditions. The second part of their study relies on Monte-Carlo simulations to generate a large amount of growth curves following the same distributions of lag times and growth rates as the experimental data.

They used the following expression for N_t, the number of cells at a time t :

$$N_t = (N_0 - N_g) + \sum_{i=1}^{N_g} \begin{cases} 1, & \text{for } t \leq \tau_i \\ e^{\mu_{max}\ i(t-\tau_i)}, & \text{for } t > \tau_i, \end{cases} \tag{4.19}$$

with N_0 the inoculum size and N_g the actual number of cells that are growing – all the cells do not necessarily grow. In this equation, we can see that an exponential function is

used to model the bacteria growth as in the deterministic model with no growth for time steps below the each individual lag τ_i. Each iteration of the model generates a doublet of growth parameters $(\tau_i, \mu_{\max\ i})$ that will result in a growth curve. It is important to notice here that as the distribution of the simulated doublets $(\tau_i, \mu_{\max\ i})$ have the same profiles as the experimental data, they integrate both the biological variability and the stochastic variability. Indeed, the biological variability results from the measurement of experimental distributions on 220 naturally different bacteria.

The result of $10,000$ iterations of the Monte-Carlo simulation is shown in figure 4.6. The output of the model is a stochastic growth curve, which means that at any time point t, the number of cells is a probability distribution.
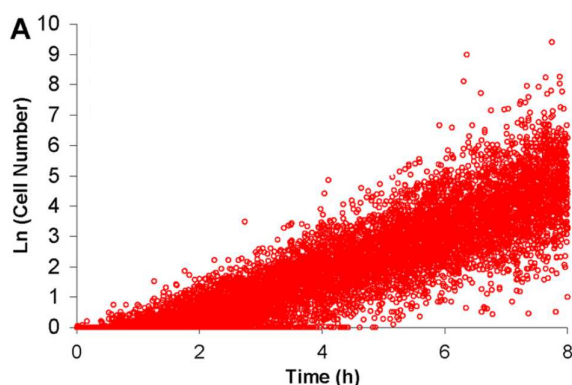
Figure 4.6: Monte Carlo simulation made by Koutsoumanis *et al.*[101] with $10,000$ iterations. The simulations are constrained by the fit of the experimental distribution observed on *S. Typhimurium*.

This type of stochastic models has a more descriptive approach than the first type. It interprets the stochasticity in terms of dispersion of the growth parameters while keeping characteristic equations as for the population level. Contrary to the first type, the biological variability cannot be distinguished from the stochastic variability. This model need to measure the growth parameters dispersions of the population members before providing stochastic growth curves whereas the first approach only required the data of a growth parameter to predict the inherent dispersion. However, Koutsoumanis' approach can determine the boundaries reachable by a population of cells. This type of models is therefore useful for food safety assessment as they can to quantify a risk of contamination in function of the inoculum size N_0.

Throughout this overview on bacteria growth modelling, we saw that the simple exponential growth of a bacterial population results from complex stochastic processes. The complexity lies in the amount of parameters that interplay in the bacteria growth as well as the lack of experimental data for each individual of a population. Therefore, it is important

to distinguish the different origin of the stochasticities through the use of models in order to identify potential biological variability. Before confronting the models derived above to our experimental data, we first present the methods used to perform time-resolved measurements on the generic chip and how quantitative data are extracted from the microscopy images for the establishment of individual growth curves.

4.2   Image Analysis Software

To follow bacteria growth in the generic chip, the static droplets storage in an array is exploited to visually control in time and to record the droplet content for multiple fluorescent channel. As bacteria cells produce fluorescent proteins, the fluorescent intensity of a given droplet is used as a proxy for the total amount of bacteria inside the droplet. A software written in Matlab is used to extract and organise the data from the raw images into individual growth curves. This tool has become essential for the members of the lab who use the same platform as the analysis of each individual well cannot be performed manually. In this section the different steps of the image analysis are detailed.

The principle of the software relies on the detection of the wells on the bright field images to create a mask for each well. The mask is used afterwards to crop each individual well at each time step and for each fluorescent channel. Finally, an algorithm is run to select the wells kept for the analysis and integrates the detected fluorescent signal to build the growth curves.

4.2.1   Initial Image Processing

Experimental set-up for timelapse experiment   Timelapse experiments are performed on an inverted microscope Nikon Eclipse Ti-U microscope, equipped with a motorized xyz stage, using the accompanying NIS software for image recording. Two types of cameras are used: the iXon Ultra 897 (EMCCD, Andor) and the ORCA-Flash 4.0 V2 (CMOS, Hamamatsu), with captor frames of 512×512 and 2048×2048 respectively. The motorisation enables large scans of the entire chip with a 10X magnification. It results that both bright field and fluorescence images (Fig. 4.7a) are taken at each xy position programmed by the NIS software. In addition, a focus surface is calculated to set the focus on droplets median plan for each position.

The software implements a large scan for each loop of the timelapse. One scan can last from 7 min for the Hamamatsu camera to 25 min for the Andor camera, which record 210 and 520 xy positions respectively to map the entire chip. Figure 4.7c shows the xy positions organisation. The number of rows and columns scanned at each loop results

from the settings of Δy and Δx. An overlay is set up to catch each well entirely. An overlay of 0% would lead to images of a large number of traps cut in half and thus a loss of information.
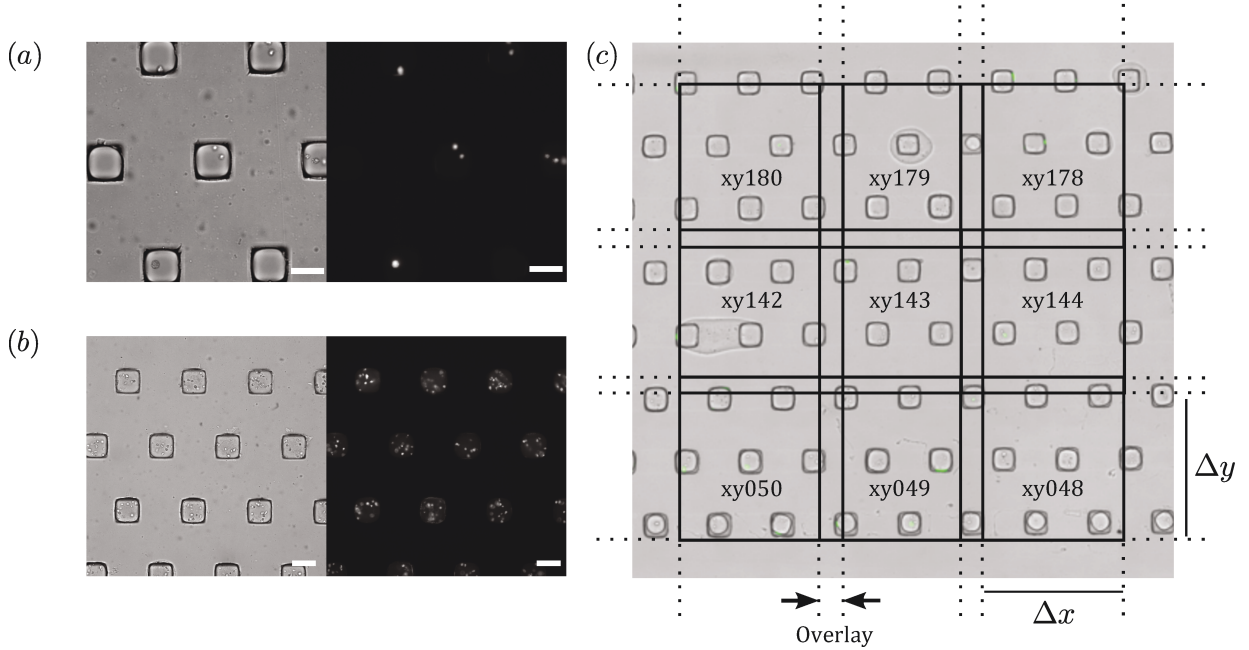
Figure 4.7: a) and b) display bright field and fluorescent images captured respectively on Andor and Hamamatsu in a single snapshot. 100 μm scale bar. c) The large scan is obtained by mapping the entire chip with programmed xy positions. Each position is referenced with three digits number starting from the bottom right of the screen and following a reverse 'Z' profile. $\Delta y = \Delta x = 0.650$ mm for the Andor and $\Delta y = \Delta x = 1$ mm for the Hamamatsu, which correspond to an overlay of 26% and 33% respectively.

Wells detection for mask The first step of our image analysis detects wells on the bright field images and creates a binary mask. The whole process is shown in figure 4.8 a,b. The binary mask is an image of the same size as the raw bright field image but with solely pixel with values '1' and '0'. The 1 pixels cover the surface occupied by the wells place and the 0 pixels the remaining surface. The binary image is generally obtained from a grey-level image by using a threshold value. All the pixels above the threshold value is set to 1 and the pixels below to 0. Binary images are particularly useful in image analysis as they allow the detection of connected pixels – namely detected objects – as well as morphological operation on these detected objects.

In practice, a Gaussian filter is applied to the raw image and the resulted blurred image is subtracted by the bright field image itself to remove any background. After this step, the

(a)

(b)
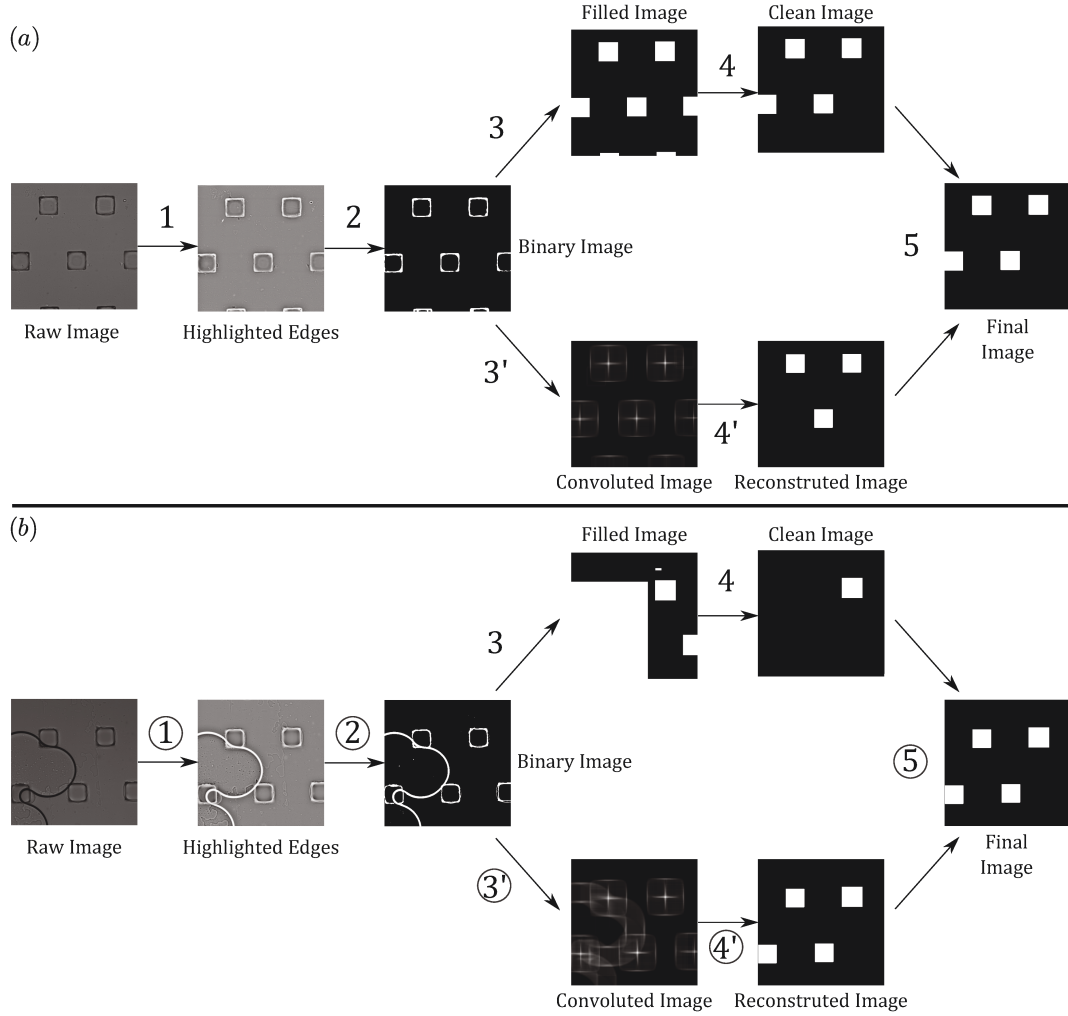
Figure 4.8: a) and b) detail the image processing to detect the wells on the bright field images. Step 1 subtracts the background with a gaussian filter and invert the image to highlight the well edges. 2 applies a threshold – found using the Otsu's algorithm – to make the post-treated image binary. From this point two analysis are performed in parallel. The first method 3 detects the connected components of the binary images, fills them and deletes in 4 the objects that are too big or too small to be a full-size well. The second method 3′ convolutes a square mask with the binary image. The square mask has the same size as the expected wells. The centres of each well can be detected using an appropriate threshold. Then, 4′ reconstructs the wells around the centres with the same mask as for the convolution. The final mask is obtained by combining the results of the two methods. While a) shows an example where the convolution method misses one trap, b) corresponds to a case where an unwanted objects is detected in the bright field image (here a bubble) which confuses the first method. Both methods are kept to cover all the situations generally encountered during our experiments.

anchors boundaries darker in the raw images are rendered brighter than the other pixels by

inverting the pixel values, see step 1 in Fig. 4.8 or Fig. 4.9. The *graythresh* function from the Matlab Image Toolbox uses the Otsu's Algorithm to find an optimum threshold that identify the bright pixels in the processed image. It allows us to produce a binary image with the anchors edges in white and the rest of the pixels in black (step 2 in 4.8).
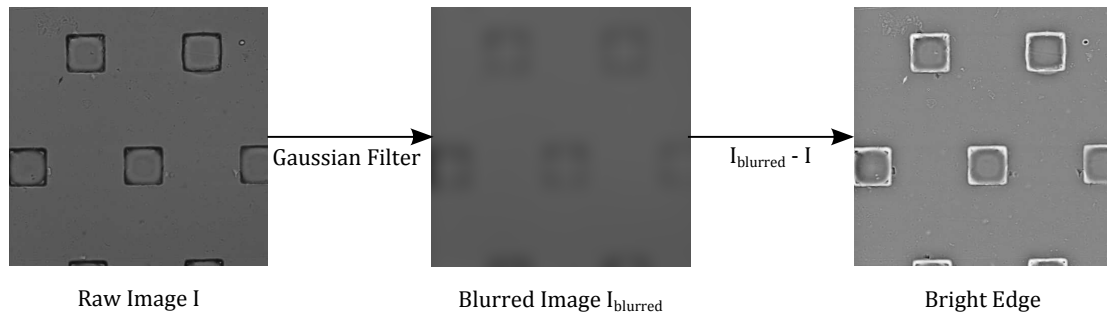
Figure 4.9: Details of the step 1 in figure 4.8. It produces an image with the brightest pixels placed on the edges of the wells.

Once the edges are detected, two methods are used. The first method (steps 3 and 4, Fig. 4.8) detects the connected components in the binary image, i.e. the well edges here, and especially what we call their bounding box. The bounding box is the smaller square that contains all the pixels of a connected pixels group. These boxes are filled with white pixels to form the mask of the detected wells (step 3 in 4.8a,b). We can see on the 'Filled Image' of figure 4.8a that some of the detected wells are partially cut. Due to our large overlay set-up, we are sure that they are fully appearing the neighbours raw images, see figure 4.7. Thus, by measuring the area of the detected wells, we can delete the wells that are too small to be entire detected in the processed image as well as objects with a long major axis that mostly correspond to unwanted dust or to the microfluidic chamber walls (step 4 in Fig. 4.8 a,b).

The second method(steps 3′ and 4′, Fig. 4.8) is used in parallel to the first one to improve the detection efficiency. A square made of the same size as the trap is convoluted to the binary image obtained by the step 2 (step 3′ in 4.8 detailed in Fig. 4.10). The convoluted image displays the center of the traps in bright pixel. By applying once again a threshold, the well centres can be therefore detected and the wells are reconstructed in step 4′ by placing the square used for the convolution at the centre positions. We obtain a set of detected wells that can vary from the one detected in the first method. This is why, the final mask (step 5 in Fig. 4.8) is built by combining the results of the two methods.

Both method are kept in parallel because it enables a more robust detection. On the one hand, if one of an anchor walls is on the edge of the camera captor, the convolution method fails to detect it properly (Fig. 4.8a). This is due to the high value of threshold set for the
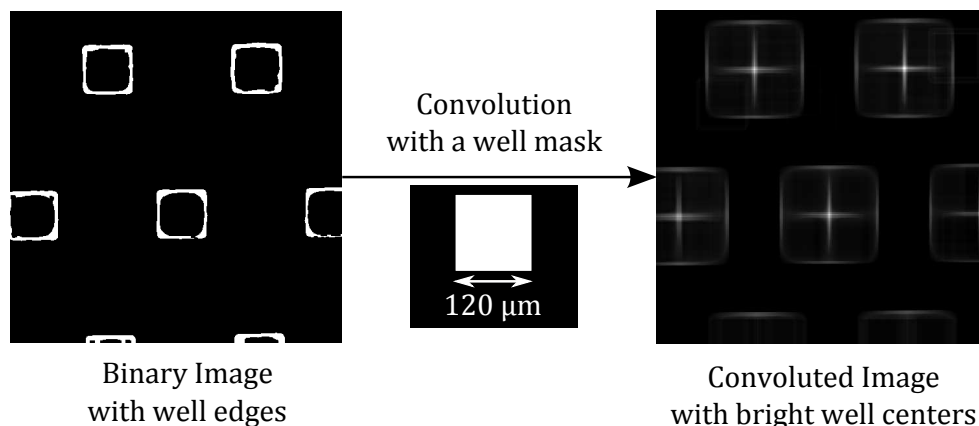
Figure 4.10: Details of the step 3′ in figure 4.8. It produces a convoluted image with the brightest pixels placed at the well centres.

centres detection in the convoluted image. The choice for the threshold is a trade off between the detection of all the centres in most of the encountered situations and the cleaning of undesired detected objects. On the other hand, during timelapse experiments which can last sometimes several days, dusts or air bubbles can unfortunately appear in the chamber. This affects the quality of the well detection as it is shown on step 3 in figure 4.8b. The boundaries of the air bubble are detected and filled by the first method which prevents the program from detecting the wells inside the bubble. However, the second method is not disturbed by the air bubble and can still detect all the square objects namely the wells. As we encountered often both situations, we decided to keep both methods, which provides satisfactory results.

Another complexity is often encountered. Although the microfluidic chip is fixed on the motorised stage, we have observed sometimes a slight movement between each timelapse resulting in a movement of the well outside the mask. To anticipate this movement, two masks made from the first and last time step images are combined to form the final mask. If the stage has moved a lot from its original position, the final mask will be large but it will follow the entire well for all the time steps.

Image Cropping.   The final mask resulting from step 5 in figure 4.8, is used to build frames for each well. All the channels from the raw images are cropped according to the frames at each time step (see Fig. 4.11). A channel can be either bright field or any fluorescence signal set for the experiment.

In addition to the easy access to individual data, this storage step also reduces drastically the memory space occupied by the raw data as it delete the useless information of the pixels outside the wells. As an example, a timelapse experiment made with the Hamamatsu cam-

era with 53 time points and 210 xy positions for the bright field and one fluorescent channel in 16−bit occupies 381 Go of memory space. After the crop processing, the same amount of data is reduced to 32 Go which also significantly increases the speed of the data processing.

Finally, the position and the mask coordinates combined with the data of Δy and Δx (cf Fig. 4.7c) enable to build the global coordinates for each well in a virtual reconstruction of the entire array that will be used to create a matrix equivalent to the array with each element of the matrix corresponding to a well, see 4.2.2.
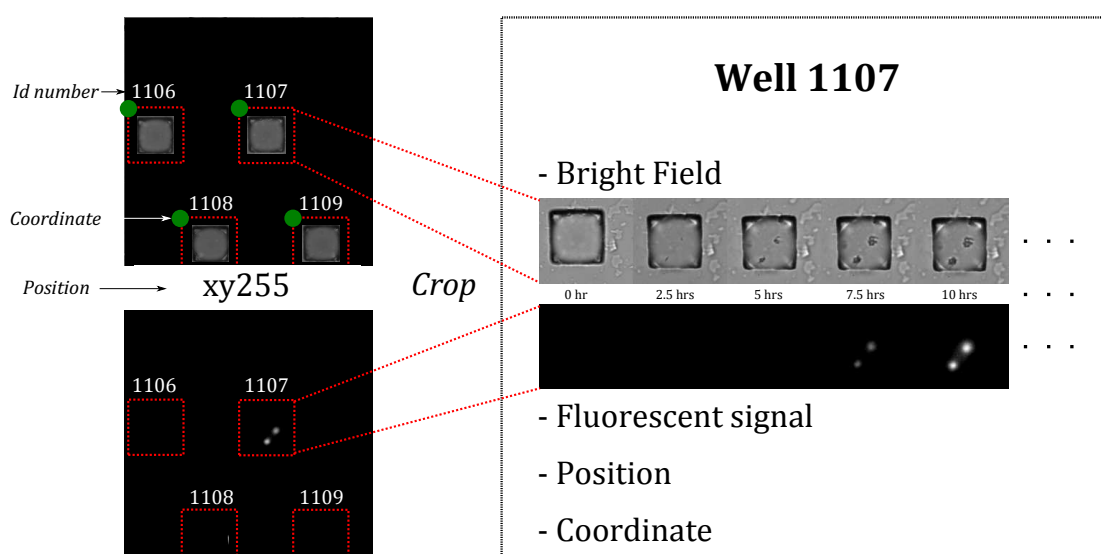
Figure 4.11: Crop and raw data organisation. The mask resulting from the wells detection is used to build a frame for each well (dotted-red). Each time lapse is cropped according to this frame and stored in individual folders. The folders are named after the identification number of the wells (here from 1106 to 1109) and contain the time lapse for the bright field and the fluorescent channel as well as the well coordinates in the raw image and the position of the raw image (here xy255).

Well selection. The global coordinates are essential for the second step of well selection. The wells present in the overlay zone (Fig. 4.7c) can be detected twice such that after the initial crop, around 2000 wells are detected instead of 1495. The selection step targets the double counted wells by analysing the global coordinate vector. First, a cluster cell is built according to the distance between all global coordinates. Data points that are closer than the minimum distance between two wells are considered as the same well and stored in the same cluster. Then, within the clusters with multiple detected wells, we select the well with a detected area closer to the expected area for a well while the other wells are removed from the analysis. The double counted wells correspond indeed to wells that are cut in half by the edge of the raw image as shown in figure 4.8a. After this selection step, the

number of wells kept for further analysis is around 1480. It is very rare to detect exactly 1495 as defaults can result from the microfabrication and irregularities in the illumination can limit the well detection efficiency.

4.2.2   Growth curves extraction

Fluorescent level integration   The pool of selected wells are analysed to obtain the growth curves. The total fluorescence intensity measured in each droplet is considered as a proxy for the total number of bacteria in the droplet. When the bacterial suspension is loaded on the chip, the position of the cells inside the droplets is not controlled. Therefore, it is very unlikely to have all the cells, and later on the colonies, in the same focus plan. The focus is initially programmed through a focus surface settings in the NIS software. The focus is set on the middle plan of the droplet at the initial time. We also observe sometimes a modification of the focus throughout the timelapses. Figure 4.12 shows the fluctuation of the integrated fluorescent signal with the focus varying from the top of the well to its bottom. We can see that the fluorescent level does not spread more than 2% from the mean level. Given this observation, a good measure of the fluorescent level is its integration on the entire well for each time step.
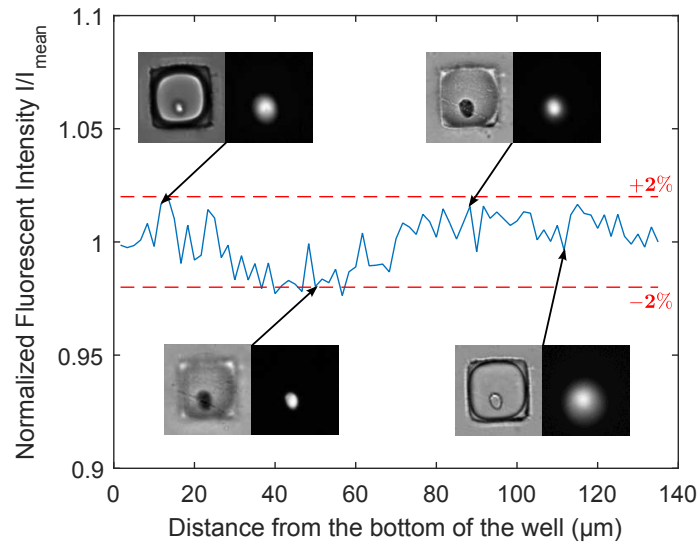
Figure 4.12: Fluorescence signal of a bacterial colony integrated on the entire trap for different z planes, from the bottom to the top of the trap.

Based on the same detection methods as described in 4.2.1, the well boundaries are detected for each time point on the bright field images containing now a single trap. This detection process allows the program to follow well boundaries even though they are moving between two time steps. Once the wells boundaries are detected, two vectors are produced. The first contains the total fluorescent signal on the entire well , and the second contains the

mean value of the 30 highest pixels and will be used for digital analysis (cf 3.2.1).

The time is then added to the fluorescent level. As the time to achieve a loop can last up to 25 min with the Andor camera, a delay is induced between the wells positioned at the beginning of the loop and the ones at the end. The delay is comparable with the doubling time of the bacterial strains used in our experiments such that it is important to adjust the time of the image capture with the well position. The stage is assumed to spend an equivalent time on each xy position, thus the time is linearly correlated to the well position. The time is finally concatenated with the fluorescent profile and stored in each individual well folder.

Data gathering. The main challenge when dealing with large amount of data is to find a good way of accessing them and presenting them. As our microfluidic chip consists of an array of droplets, we found that gathering the data in a matrix of size 13×115 was relevant. Each well can be referenced by a row and a column of a matrix. A third dimension is added to the associated matrix for the time.

An example of the global position reconstruction for one chip is presented on figure 4.13 (left). The positions are not perfectly horizontal for two reasons. First, the plasma sealing of the PDMS channel on the glass slide is performed manually. Second, even though the glass slide is adjusted on the motorised stage to be horizontal and compensate the error made during microfabrication, it always remains a small angle. The global positions are thus numerically modified to render all the well rows horizontal using a basic rotation matrix. The angle θ is determined using the ratio of $\vec{u} \times \vec{v}$ with $\vec{u} . \vec{v}$, which corresponds to the tangent of θ. The sign of the angle is set by the sign of the determinant of $(\vec{u}, \vec{v}, \vec{z})$. Thus, the angle θ is calculated after the equation :

$$\theta = \frac{\det(\vec{u}, \vec{v}, \vec{z})}{|\det(\vec{u}, \vec{v}, \vec{z})|} \arctan\left(\frac{\vec{u} \times \vec{v}}{\vec{u} . \vec{v}}\right). \tag{4.20}$$

When the global positions are horizontal (see Fig. 4.13 (right)), wells with similar Y-coordinate are gathered in the same row. Once the rows are determined, the X-coordinate is used to address a column to each well. By comparing the distance between two consecutive wells in the same row, we are also able to detect whether a well is missing or not. In the end, we obtain one (row,column) coordinate for each selected well associated to its identification number.

Finally, the integrated fluorescent signal is stored in a single matrix structure of size 13×115 with the well identification number as well as the well global position. Using the value of
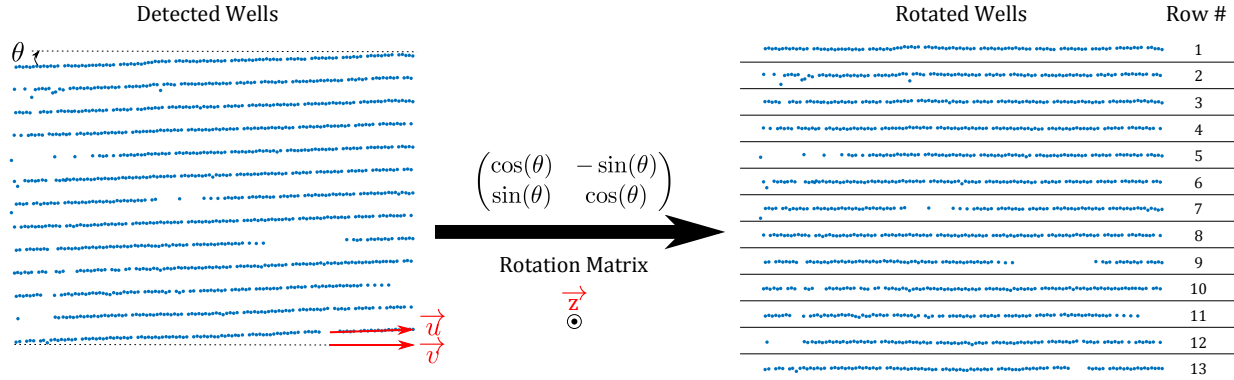
Figure 4.13: Details of the method used to organise the data in a matrix. The detected wells are never perfectly horizontal which renders complicated the process of addressing the row for each well. The vectors u and v are used to determine the angle θ that form the chip with a horizontal line (see equation (4.20)). By applying rotation matrix of an angle θ we obtain nice and horizontal droplets array. The rows are thereafter easily addressed to each well.

the highest pixel of each selected well, a threshold is set to determine positive droplets from empty ones in a 'binary' matrix as for the digital analysis 3.2.1.

4.3   Time-resolved Measurements

In this section, we measure two sets of thousand growth curves on two strains : *E.coli* pGlo and *B.subtilis* . The quantitative analysis is performed by measuring the growth parameters described in section 4.1 on the *B.subtilis* strain.

4.3.1   Growth Curves presentation

Figure 4.14 shows around $1,000$ fluorescent monoclonal colonies of two bacterial strains. They are monitored over time by scanning the entire chip every 30 minutes on a motorized microscope. An example of timelapse snapshots of bacterial culture in both liquid and agarose droplets is presented in the figure 3.6 of the chapter 3. The total fluorescence intensity is measured in each droplet as a proxy for the total number of bacteria in the drop, leading to the individual growth curves. Each green curve in figure 4.14 represents the evolution of the total fluorescence intensity of a single droplet, the thick blue curve shows the average behaviour at each time step taken as the mean fluorescent intensity over all the positive droplets, and black curves highlight randomly chosen example curves. Droplets where no fluorescence is detected are not shown in the figure.

(a) *E.Coli* HB101 - K12 - pGlo

(b) *Bacillus Subtilis* GM2919
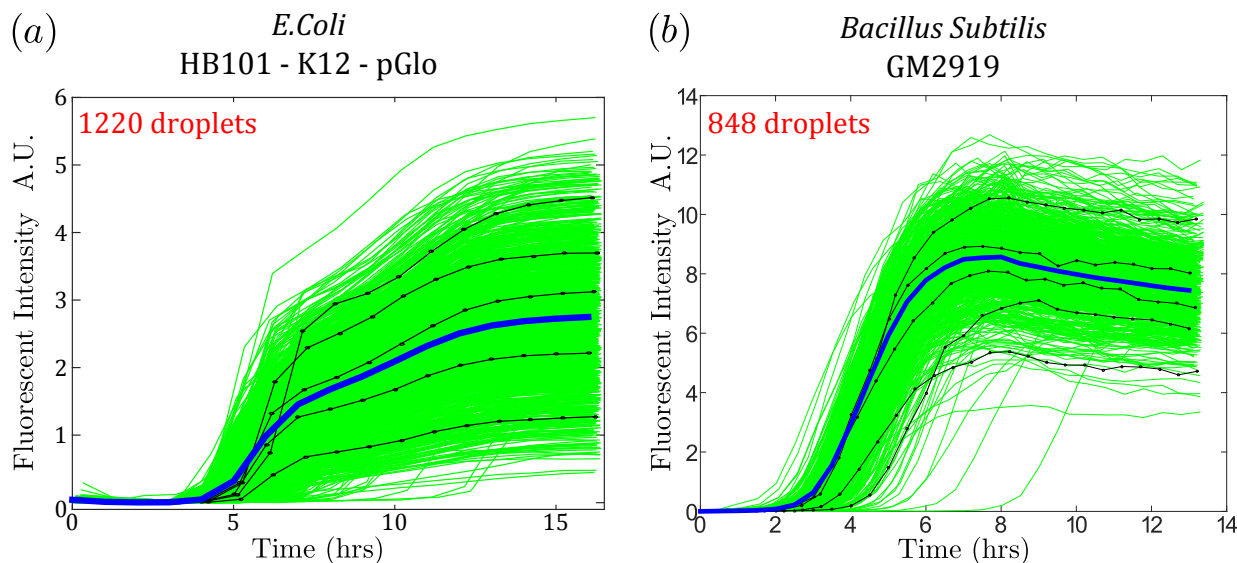
Figure 4.14: Growth curve superposition for two different strains. Points are taken every 30 min. Five random black curves are highlighted for better reading for each strain. a) 1220 growth curves of *E.Coli* pGlo modified with a commercial plasmid expressing GFP when it is replicated. b) 848 growth curves of *B. subtilis* with a constitutive expression of RFP.

Several observations on these growth curves can be made prior to any quantitative analysis. First, we observe the different growth phases described by Monod[71] namely the lag phase, the exponential growth phase and the stationary phase. The duration and the intensity of each phase display a variability amongst the individual growth curves. This means that even in identical growth conditions bacteria cells of a same strain display different physiological responses. This variability is especially important in the case of *E.coli* which displays final colony intensities ranging from 1 to 5 (arbitrary units).

By looking at the shape of the growth curves of *E.Coli* pGlo (Fig. 4.14a), two exponential phases can be observed with two different growth rates. This phenomenon may translate a diauxic effect defined by Monod.[71] This effect results from the adaptation of bacteria cells to different carbon sources. Baev *et al.* showed in a series of three papers[102–104] that LB contains indeed a large variety of carbon sources which can be used by *E.coli* . To switch between carbon sources bacteria cells adapt their physiological state which often results in the reduction of their growth rate. We can also notice that no change in the growth rates is observed for *B.subtilis* (Fig. 4.14b).

An initial decrease of the fluorescence level can occur for *E.coli* (Fig. 4.14a). This results from the use of the green fluorescent protein (GFP) to identify the bacteria growth in agarose droplets. Indeed, agarose gel beads also emit a fluorescent signal under UV excitation at the same wave length as GFP. The observed decrease corresponds to the bleaching

Data Set	State	t_{lag} (hrs)	τ (min)	μ_{max} (hrs^{-1})
Device	Liquid	3.37 $\pm$ 0.68	21 $\pm$ 2	2.01 $\pm$ 0.18
Batch	Liquid	$\sim$ 2	30	1.38

Table 4.1: Comparison between the measurements of lag times (t_{lag}), doubling times (τ) and specific growth rates (μ_{max}) for *B.Subtilis* culture on device and batch culture. For on chip culture, the mean values of each parameter are given with an error corresponding to the standard deviation of the data set (Fig. 4.14b).

of the agarose gel until it is overpassed by the fluorescent signal of the bacteria cell. This is not observed in liquid droplet or in strain using the Red Fluorescent Protein (RFP) such as *B.subtilis* , which has a different excitation spectrum. By pre-exposing the agarose under UV-light, the initial fluorescence level of the agarose is reduced but we cannot erase it completely. This constitutes a limitation of our measurements as it increases the level of detection and thus, lowers the accuracy on the lag time measurement. Future design of new bacteria strains must take this effect into account and favours the expression of other fluorescent proteins such as RFP and YFP (Yellow).

Growth Parameters Measurements

Even though growth conditions are identical in every droplet, a variability is observed for each strain in terms of final colony size, growth rate and lag time. As shown on figure 4.15, the values of each parameter are distributed around a well-defined peak. Moreover, all distributions are unimodal and no sub-populations can be detected, implying that neither the initial number of bacterial cells per droplet – ranging from 1 to 7 cells/droplet – nor the droplet position on chip have significant impact on the measured growth parameters. Reversely, the well position and its initial number of cells per droplet cannot be measured through the growth parameters. In parallel, we perform a batch culture using the same strain and same culture medium. Parameter values measured both in our device and on the batch colony are gathered in table 4.1. The same order of magnitude between the growth parameters measured on chip and in batch indicates that the device does not induce any major changes in the growth behaviour of the bacterial culture (see table 4.1).

The spreading in each distribution highlights the inherent stochasticity in bacterial growth. The device thus allows to observe the dispersion of growth behaviours and in particular to detect events falling in the tails of the distribution. For instance, in identical growth conditions, *B.subtilis* colonies can display doubling times ranging from 15 to over 25 min in the same chip. The platform is therefore able to identify specific phenotype, e.g. with particularly high growth rates.
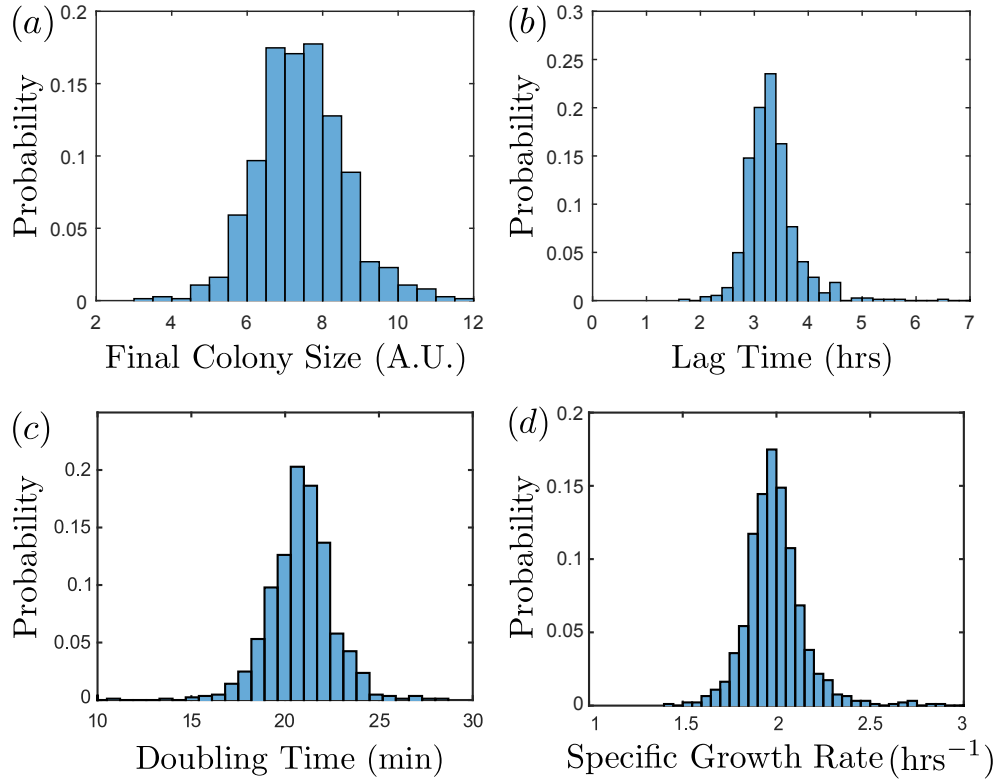
Figure 4.15: Histograms of four parameters characterising *B.Subtilis* growth : a) final colony size, b) lag time, c) doubling time and d) specific growth rate.

However, similarly to the measurements of Koutsoumanis *et al.*, the measured distributions integrate both stochastic and biological variabilities. We need to derive a stochastic model mimicking the growth conditions inside the droplet to predict the spreading expected by a pure stochastic model such as the simple birth model. Therefore, we could identify whether the dispersions observed on the chip are likely to come from a biological variability or not. Strategies to build such model will be investigated in the last section of this chapter.

Comparison between individual growth parameters and population growth parameters

The experimental observation of individual growth parameters would not be observable in classical batch measurements. It provides a completely different range of information as it informs on the mean value as well as the standard deviation of the growth parameters. In addition, it allows for the comparison of growth parameters of the mean on-chip population level (blue curve in Fig. 4.14)with the mean value of the individual growth parameters. We compare the lag time and the specific growth rate measured on the mean growth profile to the lag time and specific growth rates distributions in figure 4.16. Both parameters measured on the mean curve (red dotted line) underestimates the mean of the growth pa-

rameters.
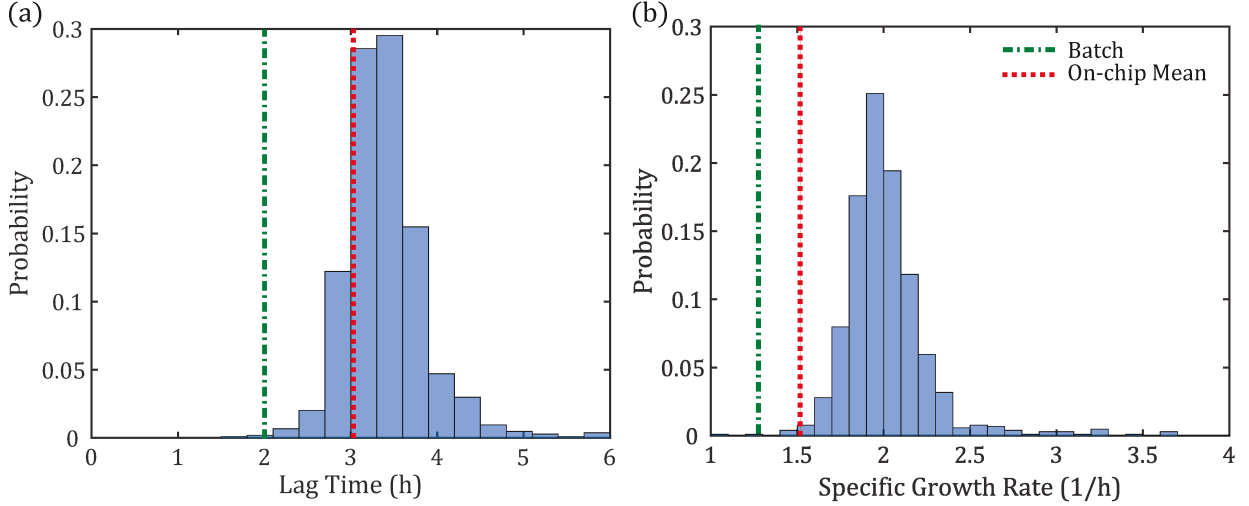
Figure 4.16: Growth parameters of *B.subtilis* from figure 4.14b. Distributions of the lag times (a) and the specific growth rates (b) with the value of the same parameters measured either on the mean population growth curve (red dotted line) or on batch measurement growth curve (green dash-dotted line).

First, the lag time is underestimated because the colonies with a short lag times are defining the lag of the mean growth curve. When colonies with long lag times start to grow, the total amount of bacterial cells has already passed over the detection limit and initiated the population exponential phase. This was analytically predicted by Barany[100] in the specific case where the initial cell population displays identical growth rates μ but identically distributed independent random lag times τ_i. He demonstrated that in this case the population lag τ^{pop} and the mean lag $\tau^{\mathrm{mean}} = \mathbb{E}(\tau_i)$ converge to the relation :

$$\tau^{\mathrm{pop}} = \frac{\ln\left(1 + \mu\tau^{\mathrm{mean}}\right)}{\mu}. \tag{4.21}$$

And for $x > 0$, $\ln(x+1) < x$, therefore, the population lag will always be smaller than the mean of the lag times :

$$\tau^{\mathrm{pop}} < \tau^{\mathrm{mean}}. \tag{4.22}$$

Second, the underestimation of the specific growth rate is also purely due to the mathematical definition of the specific growth rate. Briefly, if each individual growth curve is defined by a function $x_i(t)$, the mean growth curve is defined by $X(t) = 1/N \sum_{i=1}^{N} x_i(t)$ and thus :

$$\mu_{max}^{pop} = \max\frac{\mathrm{d}\ln X}{\mathrm{d}t} = \max\frac{\sum_{i=1}^{N} \dot{x}_i(t)}{\sum_{i=1}^{N} x_i(t)}. \tag{4.23}$$

During the exponential phase, $x_i(t) > 0$ and $\dot{x}_i > 0$ such that $\sum_{i=1}^{N} \dot{x}_i(t)/\sum_{i=1}^{N} x_i(t) \leq \sum_{i=1}^{N} \dot{x}_i(t)/x_i(t)$ and the operators '$\sum$' and 'max' are invertible, therefore we will always have :

$$\mu_{max}^{\text{pop}} \leq \mu_{max}^{\text{mean}}. \tag{4.24}$$

Therefore, the measurement of growth parameters on the mean growth curve does not correspond to the mean value of the individual parameters. In addition to the mean population growth parameters, we also indicate the growth parameters values on figure 4.16. One can see that the batch measurements underestimate not only the mean individual parameters but also the mean population parameters. This means that the mean growth curve cannot be assimilated to the batch growth curve which is due to the dissimilarities between on-chip and batch culture conditions.

4.3.2   Comparison between generic chip and batch cultures

We identified two main dissimilarities between batch and on-chip cultures: the access to the nutrient and the level of observation. In order to simplify the discussion, we place ourselves in the case where on-chip droplets contain a single cell. Let us consider a population of cells from a single strain, e.g. *E.coli* . The stochastic and biological variabilities induce different physiological parameters within the population. For instance, the population can contain rapid and slow growers, soon and late growers, etc. Through the two axis of access to nutrient and level of observation, we highlight how this variability of phenotypes induce differences between on-chip and batch cultures.

Access to nutrient.

In the case of batch culture, the cells are grown all together such that they have access to the same nutrient reservoir. It ensues a competition between slow and fast growers (*capitalistic mode*). Fast growers consume nutrient more rapidly such that they can consume nutrient that slow growers do not have time to process. They can therefore replicate more than what they would have in the case of equivalent culture medium volumes distribution to each cell of the inoculum.

In the case of the generic chip, the droplets monodispersity gives each cell access to the same amount of nutrient (*communist mode*). Thus, there is no competition in the access of the nutrient and the observed growth renders exactly the ability of each individual cell to convert a fixed quantity of nutrient into cell mass. Therefore, the blue curve on figure 4.14 is not equivalent to the growth curve obtained in a batch culture but to the mean profile of a bacteria population with each cell grown in identical conditions.

However, a similarity exists between growth culture in the generic chip and in batch which is the confinement. In both cases, bacteria cells are confined in a fixed volume of culture medium which is consumed until the end of the growth. This contrast with the mother cell machine[43] in which the culture medium is continuously renewed. As the specific growth rate strongly depends on the culture medium concentration,[71] a constant specific growth rate is maintained in the mother cell machine while individual growth rate in the generic chip are progressively decreasing as described by the logistic behaviour of the bacteria growth rate as described in the deterministic model.

Level of observation.

In addition to the access to nutrient, the level of observation also impacts the nature of the information measured on chip compared to batch culture and induce dissimilarities between the measured growth parameters.

In the case of batch culture, the measurement of the global cell concentration lacks of insights on the composition of the population. In other words, at a given time t, we do not know whether the majority of the cells are issued from a small amount of cells or there is an equipartition of the descendants from all the initial cells.

On the generic chip, all the growth curves are established individually for each cell, which results in the observation of all the existing phenotypes amongst the population whether fast or slow growers. Therefore, the growth curves obtained on the generic chip are not equivalent to the repetition of $1,000$ batch cultures but give access to the individual phenotype variability inside a bacterial population of thousand cells grown in identical culture conditions. Therefore, the culture on chip repeats the experiment of following the growth of a single cell placed in a given amount of medium.

Moreover, the confinement of droplet format allows for the isolation of all the descendants of a single cell. This contrasts with the mother machine method that can solely follow a single descendant lineage.[43] The generic chip measurements gives therefore access to the total number of descendants which can be useful to confront experimental result with stochastic models as described in the first section.

The comparison between the different techniques used for the study of bacteria growth highlights the importance of understanding the culture conditions as well as the way data are measured. This understanding is very important to correctly define a model that suits the cultivation method and will be used to propose a design of growth model in the very last section.

4.3.3 Correlations between growth parameters

The measurements of the growth parameters can be used to identify potential correlations. Figure 4.17a displays the cross-plots between the maximum growth rate g_{max} and the final colony size x_{max} calculated on the timelapse of *B.Subtilis* (Fig. 4.14b). A strong correlation is observed between the final colony size and the maximum growth rate with a correlation factor of 0.71 and a linear fit is obtained by using the least squares method. No strong correlations are observed for the other parameters with correlation factors below 0.21, see figure 4.17b and appendix D for the other growth parameters correlations.
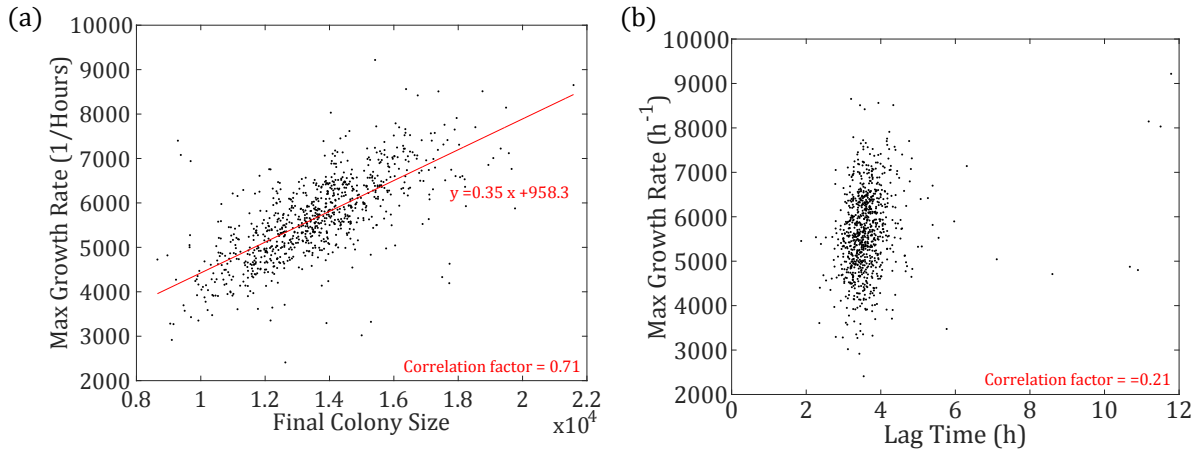
Figure 4.17: a) Cross-plot between the maximum growth rate g_{max} and the final colony size y_{max} which displays the strongest correlation factor of 0.71. The linear fit is obtained by the least squares method. b) Cross-plot between $g_{max} = \max(\dot{x})$ and the lag time. No correlation is observed as for the other growth parameters cross-plots, see appendix **??**. Both plot are for the strain *B.Subtilis*.

We identify two potential applications in the investigation of correlations between the growth parameters: the validation or invalidation of growth models consistency or the determination of sub-populations within all the observed droplets. We present solely the first application here, while the second one is presented in appendix D.

The linear correlation found between the maximum growth rate and the final size in figure 4.17 is characteristic of an exponential growth. The value of the fitted linear coefficient is consistent with the Baranyi's model that approaches the growth limitation with a logistic function, see 4.1.2. By taking the logistic form for the specific growth rate μ (cf Eq. (4.8)) with $m = 1$ and for time points t above the lag time, the bacteria growth is driven by the differential equation :

$$\dot{x}(t) = \mu_{max}\left(1 - \frac{x(t)}{x_{max}}\right)x(t). \tag{4.25}$$

At the time t_{max} where $\dot{x}(t)$ is maximum, $\frac{d\ln(\dot{x}(t))}{dt} = 0$ such that an expression of g_{max} can be derived as a function of x_{max} and μ_{max} :

$$g_{max} = \frac{\mu_{max}}{4} x_{max}. \tag{4.26}$$

This equation means that in the logistic case a linear relationship is expected between the maximum growth rate and the final cell density with the linear coefficient $\mu_{max}/4$. By taking a constant value for the specific growth rate namely the mean value of the specific growth rate distribution of figure 4.15d, $\mu_{max} = 2.02$, equation (4.26) remains for the standard deviations of both g_{max} and x_{max} :

$$\sigma_{g_{max}} = \frac{\mu_{max}}{4} \sigma_{x_{max}}. \tag{4.27}$$

The coefficient $a = 0.35$ found in figure 4.17a depends linearly on the correlation factor between g_{max} and x_{max} as well as their standard deviations such that :

$$a = \text{Corr}(g_{max}, x_{max}) \frac{\sigma_{g_{max}}}{\sigma_{x_{max}}}. \tag{4.28}$$

We can deduce the that $\frac{\sigma_{g_{max}}}{\sigma_{x_{max}}} = 0.49$ which is very close to the value $\frac{\mu_{max}}{4} = 0.50$ expected by Baranyi's model. As the Baranyi's model seems to be consistent with our experimental data, we will now fit our experimental growth curves with a deterministic model.

4.3.4   Fitting with Baranyi's deterministic model

We fit our experimental growth curves with the deterministic model of Baranyi *et al.*[96] described in section 4.1. Equations (4.9) and (4.14) are used to fit each individual growth curve of *B.subtilis* (Fig. 4.14b) using the lag time t_{lag} and the specific growth rate μ_{max} as the two fitting parameters. The parameters y_0 and y_{max} are set by the experimental data and m is taken equal to 1. The fit is performed only during the growth, which is between t_{lag} and the beginning of the stationary phase. It allows to avoid the noise in the fluorescent signal often observed during the lag and stationary phases.

Figure 4.18a shows an example of one growth curve with its fitted curves. The curvature of the transition from the lag to the exponential phase is slightly different between the experimental and fitted curve. A decrease of the experimental fluorescent signal is observed for the stationary phase on figure 4.18a. This is due to the bleaching of the GFP remaining in the bacteria cell and not to cell death, because if the chip is not exposed to UV, the colonies can be observed even after few days.
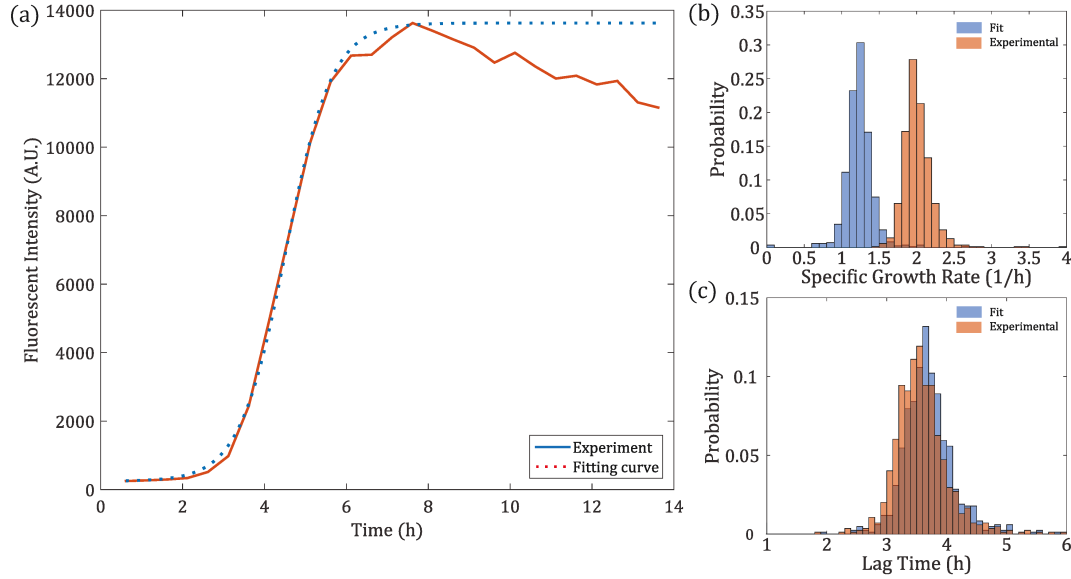
Figure 4.18: a) Example of one growth curve from figure 4.14b with its fitting curve using equations (4.9) and (4.14). b,c) Fitting parameters distribution for the experimental and fitted curves for the specific growth rate and the lag time respectively.

The curve fitting results also in two families of growth parameters namely the lag times and the specific growth rates. The corresponding distributions are compared to the experimental ones in figure 4.18b,c. We find a good agreement between the fits and the experimental data for the lag times, but the specific growth rates are underestimated. The underestimation may come from the time resolution. As we measure the fluorescent intensity every 30 min, which is the typical doubling time, the experimental derivatives lack of precision. For instance, if the time derivatives are calculated using the upwind scheme or the central difference, we observe a shift of the specific growth rate distribution.

This represents a limit to our current way of observing the bacteria growth. The precision could be increased by reducing the time between two measurements which cannot be done with the camera Andor used for this experiment. Indeed, the time to scan the entire chip is around 25 min, which impose the 30 min gap between two measurement times. The larger scale of the Hamamatsu camera allows for better resolution time (down to 10 min), but at the cost of a poorer sensitivity which increases the detection level and thus, the precision on the lag time.

The deterministic models are interesting as they enable the prediction of the end of the growth curves when the lag times and specific growth rates distributions are known. Yet, these models cannot predict the spreading of these distributions which limits the amount of biological information.

4.3.5   Towards a stochastic model for on-chip growth curves.

The stochastic model presented in section 4.1 cannot be confronted to our experimental results as it describes the case of a constant environment for all the descendants of the inoculum which is not reproduced in our experiment. A corresponding experimental set-up would isolate each new born cell in continuously renewed culture medium and would allow for the observation of all the descendants to build the growth curve. To our knowledge, such system does not exist.

However, the droplet format allows for the confinement and the observation of all the descendant in the same droplet. This results in the depletion of the nutrient as well as the emergence of social interactions with the increase of the number of cells. Two strategies can be considered to integrate to the nutrient depletion and the social interaction.

The first one is the establishment of a fully stochastic model. As for the deterministic model that integrates the confinement by modelling the increase of the population with a modification of the growth parameter μ, the logistic function could be used in the simple birth model for a nonhomogeneous birth process with a non-constant parameters $\mu(t)$ such that the generating function of the number of cells per droplets becomes[99] :

$$\mathcal{P}(z,t) = \left[1 + \frac{1}{\frac{e^{-\mu(t)}}{z-1} - \int_0^t \mu(\tau) e^{-\mu(\tau)} \mathrm{d}\tau} \right]^N, \tag{4.29}$$

with N the inoculum size. From this, one could deduce the distribution of the growth parameters and compare them to what it is found on chip.

The second approach is to consider that at the beginning of the bacteria growth inside the droplet, the number of cells is sufficiently low not to change significantly the amount of nutrient as well as to be seen by the neighbour cells. The 'ideal' conditions required by the simple birth model are assumed valid during the first cell divisions. When the number of cells reaches a certain level where the ideal conditions are not observed, we can use a deterministic model that integrates the nutrient depletion and the social interactions. The initial conditions for the deterministic model would be the last point evaluated by the simple birth model. Similarly to the first approach, growth parameters can be calculated afterwards on the resulting growth curves.

For both approaches, the lag time cannot be modelled such that the comparison between the model and the experimental data would occur for the specific growth rate and the final colony size. The lag time induces solely a delay in the start of the growth curve such that it can be easily removed from the experimental data. Another possibility to avoid the

problem of the lag phase is to synchronise the bacteria cell in the same metabolic state such that they will start to grow at the same time.

A last component has to be integrated to suggested models which is the cell distribution within the generic chip after its loading. As we saw in chapter 3, the distribution of the cells within the droplets follows a Poisson distribution. This induces a inhomogeneity in the initial conditions between all the droplets. Therefore, the probability distribution function derived from the stochastic birth models must integrate the probability of having N bacteria inside a droplet at $t = 0$. For instance the mean number of cells found by Allen[99] for the simple birth model would become :

$$m_\lambda = \lambda e^{\mu t}, \tag{4.30}$$

with λ a Poisson coefficient.

A confrontation between the time-resolved measurement and the different models suggested above would provide an explanation on which component contributes the most to the variability observed on chip.

4.4   Summary and conclusions of chapter 4

In this chapter, another block was added to the microfluidic platform by exploring its ability to follow bacteria growth through time-resolved measurements. We have exploited the static storage of the droplets to observe in parallel the independent growth of a thousand bacterial colonies.

On the technological point of view, nothing has been changed in the chip design nor in its manipulation. The ability of dynamical measurements is brought by the use of a motorised microscope as well as the development of a Matlab program. The software extracts and analyses the large amount of data produced by the experimental images. Even though the extraction of data was partitioned as much as possible, the time required for analysing the images becomes large as the resolution of the camera and the number of timelapses increase. The translation of the Matlab code into C-code would bring better computational performances for more rapid results. Moreover, the analysed images are produced by the commercial software NIS provided by Nikon. This software allows the access to the image solely at the end of the timelapses. An improved protocol would record the images through a MicroManager macro and perform the data analysis right after each snapshot. Empty droplets could be avoided and the space occupied by the experimental data on disk could be reduced.

The bacterial proliferation was measured by fluorescence. The constant emission of fluorescent signal by the bacteria cells strongly depends on the way fluorescent proteins are produced during the cell division cycle. For instance, GFP is produced in *E.coli* pGlo by an additional plasmid. The control of this plasmid replication is supposed to be correlated to *E.coli* cell division cycle. Moreover, the GFP in *E.coli* pGlo is induced by a carbon source called 'arabinose' which is the less preferred sugar processed by *E.coli* .[102–104] This means that the protein composition of the bacteria cell may not be adapted to arabinose at the very beginning of the colony growth. This could induce a delay in the production of GFP and results in a shift of the measured lag time.

In the case of *B.subtilis* , RFP is constitutively produced. This means that the gene coding for the RFP is integrated to the chromosome of the bacteria cell. Therefore, it is supposed to be expressed at each cell cycle. Yet, it has been recently shown by Manina *et al*[105] that the fluorescent protein expression varies during the cell division cycle. A variation in the level of the protein expression can be therefore expected depending on the metabolic state of the colony. For reliable quantitative measurements using fluorescence, we suggest to verify that the impact of the fluctuations in the fluorescent proteins expression is not significant enough to alter the proliferation measurements.

Once the growth curves were established, the growth parameters were measured and used to quantitatively characterise the growth of each individual colony. The measurements displayed a distribution for each growth parameter which translates the stochastic and

biological variabilities of the bacteria growth. However, we could not distinguish whether the observed variability was due to a pure stochastic effect or if the difference between the each colony phenotype result partially from an effective biological diversity. Therefore, we define guidelines to build a stochastic model of the bacteria growth within the generic chip. The model based on a single specific growth rate parameter would predict a set of growth curves on which the growth parameters distributions could be measured. A comparison between the resulting growth parameters dispersions and the on-chip measurements could help to distinguish the stochasticity from the biological variability. It is known that there exist a variability within the genotype of a same species but it is not clear that this variability results in significant variation in the phenotypes, as phenotypic characteristics are generally maintained within a bacterial species.[44]

In the opposite case of actual biological variability, we could imagine to combine the dynamical measurements with the laser-based extraction technique to select for instance only the fast growers. The recovered bacteria cells could be further cultured to prove the inheritance of their phenotype to the following generation. This protocol could be used to perform directed evolution and enrich a population with solely efficient bacteria.

Finally, this ability to perform quantitative measurements on bacteria growth dynamics can be of deep interest when the colonies are under selective pressure. Indeed, the exposition of bacteria cells to antibiotic stresses can induce mutation or phenotypic switches.[106] The method as well as the technological features developed in this chapter can be used to quantify the effect of such selective pressure on the bacteria growth. This will be presented in the next chapter.

Chapter 5

Effect of time-dependent antibiotic stress on bacteria growth

Bacteria cells are constantly confronted to various chemicals that either promote or limit their growth, termed probiotics and antibiotics, respectively. The study of antibiotics is a major public health challenge as over 300 millions deaths are expected for the next 35 years due to the emergence of resistance to antibiotics with a mortality rate of 10 millions per year by 2050.[107,108] Therefore, new methods and tools are needed to understand the bacterial response to an antimicrobial stress. The most common way to study antibiotic effects on bacteria in the clinical world is the antibiogram, which measures *minimal inhibitory concentration* (MIC). It corresponds to antibiotic concentration required to kill all the bacteria in infected patients.

The classical methods for performing antibiograms observe the bacterial response to a range of antibiotic concentrations and determine the concentration above which no growth is observed. With these methods, the antibiotic concentration is fixed during the batch preparation. Thus, it is neither possible to vary the concentration in time nor to observe the evolution of the population composition in response to variation of the antibiotic stress. However, in their natural environment bacteria cells are exposed to constantly varying antibiotic concentrations.[109] For instance, after a drug intake, the antibiotic diffuses inside the patient body and is eventually progressively eliminated.

A dynamical monitoring of the antibiotic concentration and exposure duration would replicate more accurately the natural environment of bacteria cells. This would answer multiple questions to optimise treatment pathways. How long should the antibiotic concentration be maintained to kill all the bacteria? Does an antibiotics stress have a lasting effect on the bacteria growth once it is removed? How does the intake frequency of an antibiotic stress affect the drug efficiency? These questions are correlated to the problems encountered in

pharmacokinetics which investigates how the human body is responding to eliminate drug molecules depending on the dose or frequency of intake.

In this chapter, we adapt the generic chip in order to quantify the antibiotic impact on bacteria growth with a dynamical monitoring of the drug stresses. The objective is to demonstrate the abilities of the platform to run combinations of experiments relevant for drug susceptibility testing. The study is also based on the analysis tools developed in the previous chapters which can provide quantitative information. As we perform a proof of concept, the study is restricted to the model strain *E.coli* MG1655 p8356[110] and to two similar aminoglycoside antibiotics namely gentamycin and tobramycin.

After presenting the mode of action of aminoglycosides on bacteria growth, previous works on drug susceptibility testing are reviewed, which yields the definition of characteristic parameters essential to investigate the impact of antibiotics on bacteria growth. The second section is dedicated to the microfluidic chip modification that combines the generic platform of chapter 3 with the continuous gradient producer studied in the chapter 2. The specific use of gelified droplets allows us to replace the surrounding oil phase with an aqueous phase without removing the droplets from the array and perfuse the antibiotic concentration gradient. This chip modification enables a dynamical control of antibiotic stresses on the bacterial colonies and therefore the monitoring of the characteristic parameters defined in the first section.

The third section explores the impact of the characteristic parameters on the drug susceptibility of the model strain *E.coli* . This section exploits the digital analysis by performing solely end-point measurements whereas the last section investigates the dynamical response for fixed characteristic parameters.

5.1   Impacts of cell growth rate, antibiotic exposure time and concentration on bacteria growth

5.1.1   Ribosome-targeting antibiotics mode of action on protein synthesis

Antibiotics are natural molecules released in the environment by microbial species to limit the growth of competitors. Tobramycin and gentamycin are aminoglycoside antibiotics that are ribosome-targeting antibiotics. As all the chemical reactions in living cells are catalysed and initiated by proteins, the division of bacteria cells depends on the proteins

synthesis. To link the aminoglycosides mode of action on bacteria growth, one must understand the principle of protein synthesis described in figure 5.1a. Proteins are assembled in ribosomes which translate mRNA into polypeptidic chains. The mRNA results from the DNA transcription and is constituted of a codons chain. Each codon encodes a specific amino-acid that is assembled to the growing polypeptidic chain in the ribosome. A ribosome is a complex made of a small and a large sub-units, 30S and 50S respectively, both containing rRNA and proteins. Amino-acids are brought to the mRNA-ribosome complex through a tRNA-EF-GTP complex in the 30S sub-unit by pairing the anti-codon with the current codon of mRNA in the site A. Finally, the 50s sub-unit ensures the growth of the polypeptide chain by adding the amino-acid specific to tRNA anti-codon using the energy brought by GTP.
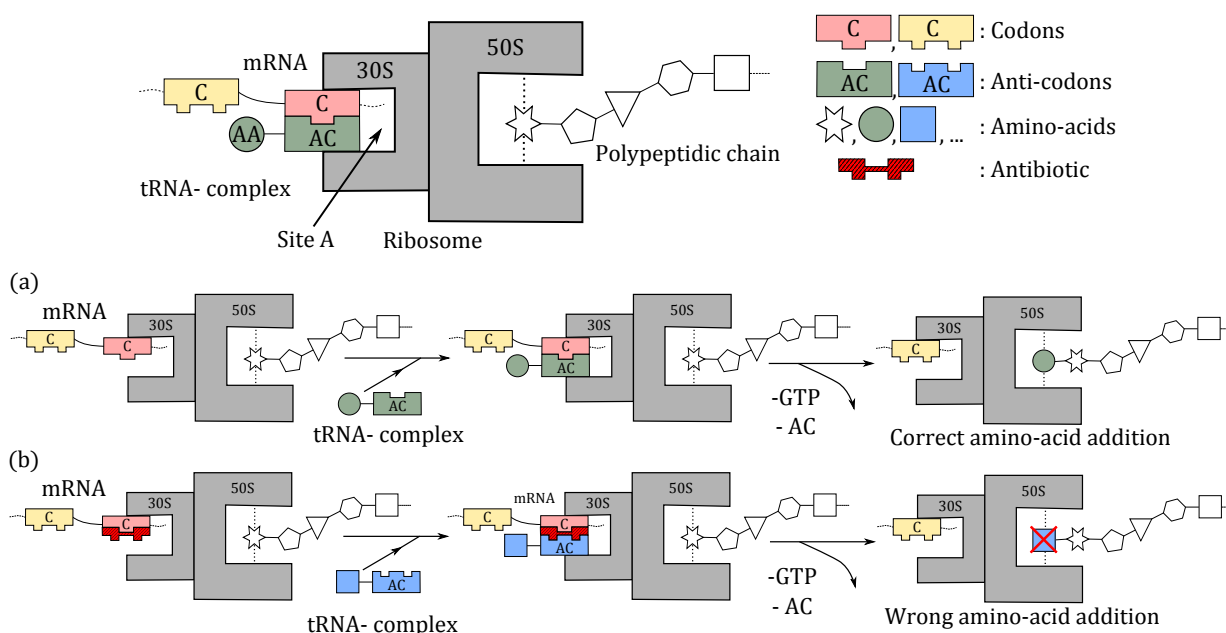
Figure 5.1: Scheme of a ribosomal complex synthesizing a protein. a) Regular case without antibiotic leading to the correct amino-acid addition. b) Case with an antibiotic, the wrong amino-acid is added.

Antibiotics can operate at different levels of the protein synthesis by either targeting the replication, the transcription or the translation. In this PhD, we mainly focus on ribosome-targeting antibiotics : gentamycin and tobramycin. They both belong to the aminoglycosides family. The aminoglycosides bind irreversibly to the site *A* of the 30S sub-unit[111] and favour pairing errors between the codon and anti-codon as shown in figure 5.1b. This results in the production of truncated proteins or wrong amino-acids sequences which are not functional. The accumulation of wrong proteins leads to the death of the bacteria cells. These antibiotics have been chosen as they display concentration-dependent bactericidal activity against gram-negative bacteria such as *E.Coli*.

5.1.2 Classical methods to test antibiotic susceptibility

The most common way to study the effect of antibiotics on bacterial strains in the clinical world is to perform an antibiogram. The antibiogram provides two types of results: the list of known antibiotics to which the patient sample is sensitive and the corresponding *minimal inhibitory concentration* (MIC). The first result indicates the antibiotic effective against the infection and the second one the amount of antibiotic needed to treat the infection. In this chapter we focus solely on the MIC determination.
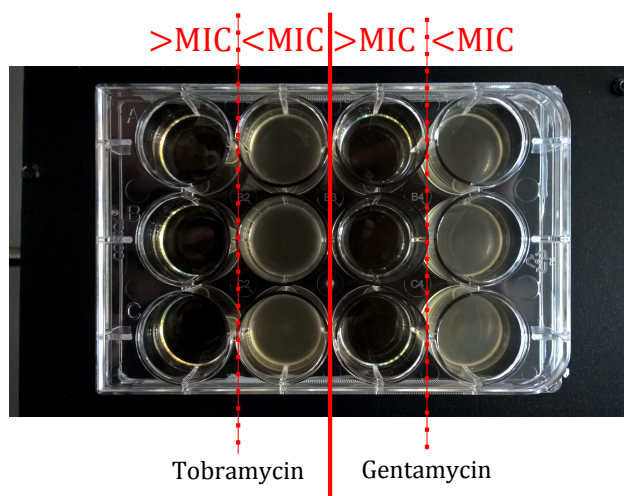
Figure 5.2: Pictures of classical methods used for MIC determination : Batch culture method using antibiotic dilution in multi-wells plate for two antibiotics.

Most of the methods commonly encountered in microbiology labs to determine the MIC measurements have been reviewed by Reller *et al.*,[112] we focus here on solely the batch cultures. The batch culture technique consists in a series of 6 or more dilutions in a multi-wells plate for each tested antibiotics, see figure 5.2. A pre-culture in the exponential phase (OD > 0.4)[1] or stationary phase (OD > 1.5) is inseminated in the tubes with an initial OD of 1/200 and incubated under agitation at 37 °C. After 16 hrs of incubation, the MIC is determined by identifying the well where no growth is observed with the lower concentration (OD < 0.01).

The MIC we measured for bacteria in both stationary and exponential phases are gathered in table 5.1 as well as the range of concentration measured by Stock *et al.* for a large scope of *E.coli* strains. A lower MIC is measured for bacteria in exponential phase compared to cells in stationary phase, but they remain in the same order of magnitude as the MIC found in the literature.

---

[1] OD : Optical Density, this corresponds to the measurement of the bacterial solution turbidity. These values are used to estimate the bacteria cell concentration.

Antibiotics	Stationary Batch MIC (μg/mL)	Exponential Batch MIC (μg/mL)	Range of MIC found in[113] (μg/mL)
Gentamycin	10	6	$0.5 - 4$
Tobramycin	9	5	$0.5 - 8$

Table 5.1: Measurements of minimal inhibitory concentration with various techniques and conditions for MG1655. Column 2 and 3 are batch measurement for cells in the stationary and exponential phase respectively.

With the classical methods,[112] a binary result is obtained as for each antibiotic concentration a growth or no growth is claimed. For antibiotic concentrations just below the MIC for which cells are growing, the composition of the sample is not known in term of percentage of survivors. Have all cells divided or just a fraction of them? Are the non-growing cells dormant cells that can grow again if the antibiotic stress is withdrawn or not? To answer those questions, microbiologists have developed further quantitative measurement methods called susceptibility tests that measures the bacteria response under or after an antimicrobial stress. We review below some studies on this subject.

5.1.3 Post Antibiotic Effect

The impact of the exposure duration on bacteria growth was first reported by Bigger *et al.* in 1944.[114] This is of particular interest for infection treatment regimens, during which antibiotics intakes may vary. The quantification of the post-treatment lasting effect can improve the therapeutic pathways, e.g. it enables the comparison of one daily dose with multiple dose regimens to reduce the treatment toxicity while keeping its efficiency.

Eagle *et al.*[115] initiated the investigations on the so-called *post-antibiotic effect* (PAE), which characterises the suppression of bacterial growth after a short exposition (1 to 2 hrs) to several times the minimal inhibitory concentration (MIC). It is measured as the time necessary for a batch culture to restart its growth. Bundtzen *et al.* provided a large amount of data on the impact of antibiotic concentration and exposure duration on the PAE for various antibiotics.[116] They observed an increase of the PAE with the drug concentration (Fig. 5.3a) and with the exposure duration (Fig. 5.3b). The same behaviours have been reported by Isaksson *et al.* for *E.Coli* exposed to aminoglycosides.[117] The origin of the PAE is not well understood, it can correspond to the time required for bacteria to synthesise necessary ribosome to restart the growth.

More recent studies also explore the post-antibiotic effect. Kwan *et al.*[118] explored the impact of the environment in the appearance of antibiotic persistence. They pre-exposed *E.Coli* to a large range of antibiotics for a short period of time (30 min) involved either in transcription, translation or ATP synthesis inhibition. Then, they exposed the survivors to $10\times$ MIC of ampicillin or ciprofloxacin for 3 hrs. All three pre-treatments yield increased
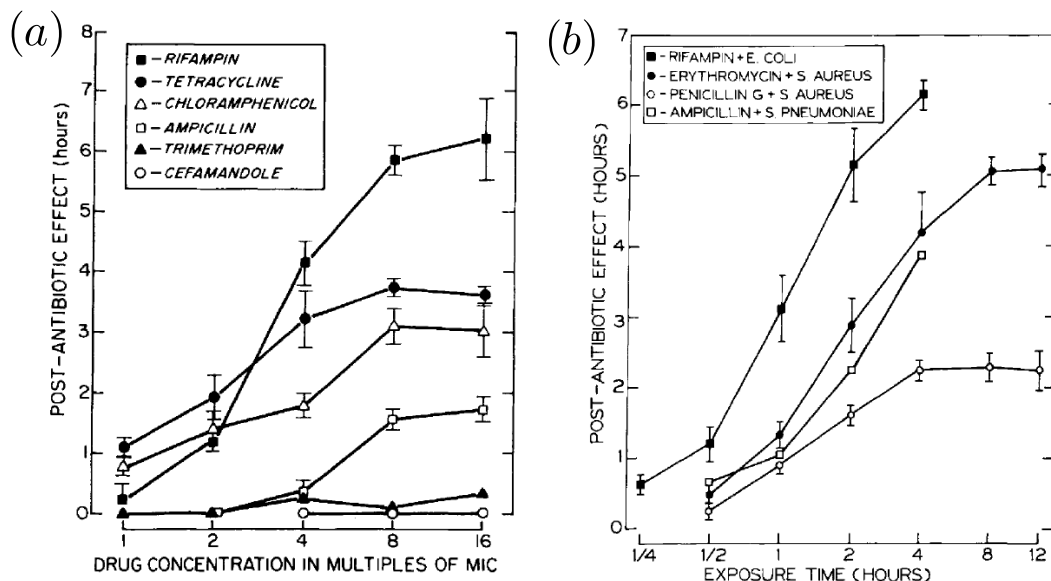
Figure 5.3: Effect of antibiotic concentration (a) and exposure duration (b) on the PAE of *E.Coli* for various antibiotics. Both graphs are extracted from Bundtzen *et al.*[116]

persistent rate (10 to 100 fold). It is one of the early studies on the emergence of persistence not as a stochastic effect but as environmental chemical stress. This is particularly interesting because they observed a longer lag time for persister and they assume that the reduced protein synthesis due to the pre-treatment increases the lag time.

Rather than investigating antibiotic resistance, which is the capacity to grow under a constant antibiotic pressure, Fridman *et al.*[119] studied the tolerance[2] evolution of *E.Coli* to ampicillin. They repeated 15 cycles of *E.Coli* treatment with $10 \times$ MIC of ampicillin for 3, 5 and 8 hrs followed by an overnight growth in fresh LB. They found that under antibiotic stress, bacteria cells seem to adapt their division cycle time inducing a modification of their lag times such that after a few generations the population lag times correspond to the drug exposure duration : 3.4, 5.31 and 10 hrs, in opposition to 1 h lag without pretreatment.

The presented studies give a brief state of the art of the possible impacts of antimicrobial treatment on future growth. The alteration of protein synthesis impacts the lag time and the tolerance to other antibiotics with or without genotypic changes, which seem to be nonetheless inherited by the daughter cells. Note also that all these studies used the lag time as a quantitative parameter, none of them report any measurement on the growth rates.

---

[2]Bacteria cells are tolerant to an antibiotic when they resist to its antimicrobial effect by modifying their metabolism. They differ from resistant bacteria cells which result from gene mutations. The tolerance is therefore not transmitted to the following generations.

5.1.4   Growth-rate dependent Antibiotic Effect

The role of the bacteria growth rate in the antimicrobial susceptibility has been initially studied to understand the development of persister in biofilm commonly encountered in the hospital. This kind of investigation is particularly complex as it involves many parameters such as drug structure, strains, nature of the nutrients and metabolic state of the bacteria cells. It has been reported that slow growers of *E.coli* display lower susceptibility to antibiotics than fast grower[120, 121] and that bacteria in stationary phase show a recalcitrance to antibiotics as the nutrient shortage results in deep changes in the cell membrane structure and growth rate.[122] Yet, a clear connection between the antibiotic mode of action and the bacteria physiological functions was exposed only recently by Greulich *et al.* in the case of exponentially growing *E.coli* exposed to ribosome-targeting antibiotics.

Greulich *et al.* observed different trends in growth inhibition curves for bactericidal and bacteriostatic[3] antibiotics as shown on figure 5.4. Bactericidal antibiotics used here are aminoglycosides which induce translational errors while the bacteriostatic antibiotics stop the protein synthesis by inhibiting tRNA binding on the ribosome or by preventing peptide bond formation. The two classes of antibiotics differ not only by their mode of action, but also in the type of interaction with the ribosomes. The bactericides irreversibly bind to ribosomes whereas bactoristatic bonds are reversible. On the one hand, *E.coli* shows an increasing susceptibility with the drug free growth rate in the case of irreversible antibiotics (Fig. 5.4b). The decrease can be defined as a 'threshold-like' decrease because the relative growth rate drops off above a treshold concentration (Fig. 5.4a). On the other hand, for reversible binding antibiotics, *E.coli* susceptibility decreases as the nutrient quality is increased (Fig. 5.4d) with a progressive decrease of its growth inhibition curves (Fig. 5.4c).

This example is important as it reports that the growth-dependent impact of antibiotic treatment does not follow a unique trend and strongly depends on the type ribosome-antibiotic interaction.

5.1.5   Surviving rate for sub-MIC stress

The study of sub-MIC regimes pictures the composition of a bacterial population and its eventual evolution such as the enrichment of resistant cells[109] under low antibiotic concentration stress. Deris *et al.*[124] investigated the composition of a bacterial population under antibiotic pressure for a *E.coli* wild-type and its resistant mutant to chloramphenicol (Cm).

---

[3]Bacteriostatic antiobitics inhibit the bacteria growth without killing them whereas bactericidal antibiotics kill the bacteria cells.
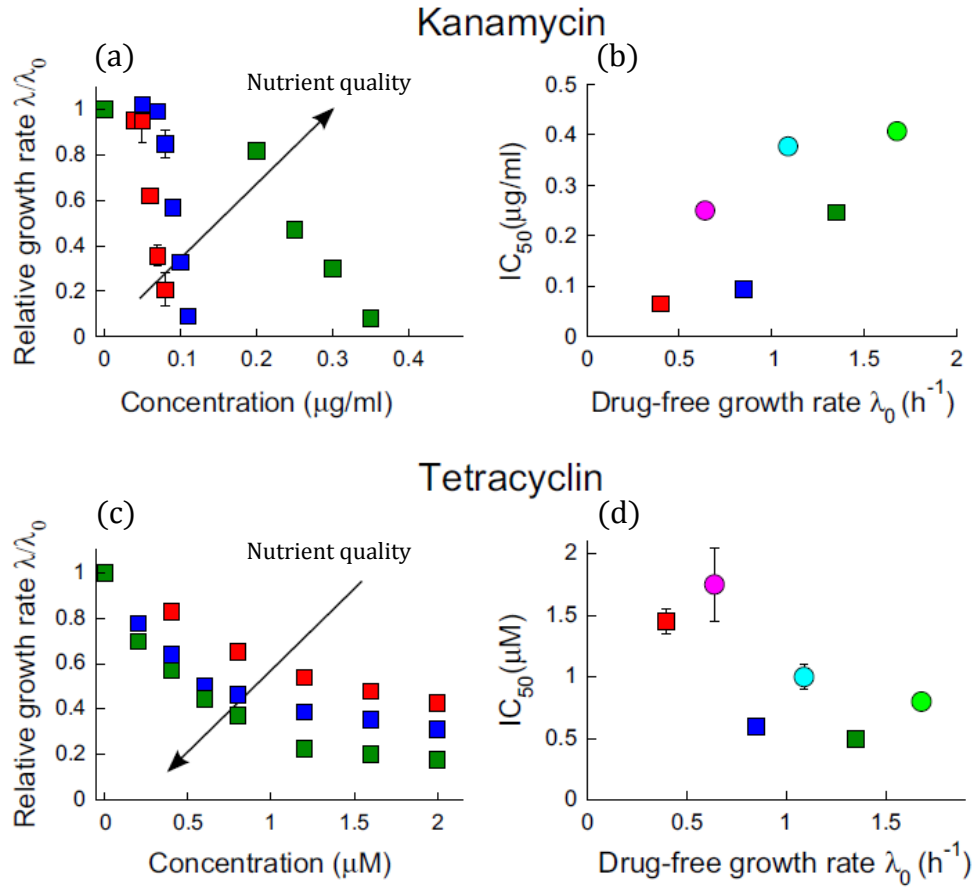
Figure 5.4: Extracted from Greulich *et al.*[123] Growth inhibition curves for Kanamycin and Tetracyclin for various nutrient quality (a,c) with their corresponding susceptibility curves (b,d). The susceptibility is measured as the antibiotics concentration to halve the drug-free growth-rate in exponential phase (λ_0) and noted IC_{50}.

In their study, they exposed the bacteria in their exponential phase to 5 antibiotic concentrations ($OD = 0.7$). They inspected the surviving rate (Fig. 5.5a) and the growth rate (Fig. 5.5b) evolutions as a function of Cm concentration.

They found that the wild-type and the mutant strain display different susceptibility curves (Fig. 5.5a). The wild type has a fairly constant surviving rate and drops off at the MIC, while the mutant surviving rate decreases slowly until 0 % at the MIC. They demonstrated that the slow decrease was due to the increase of non-growing bacteria rate with the antibiotic concentration. The Cm-resistance mechanism is based on the *E.coli* efflux pump which stop the bacteria growth. It results that under sub-MIC stress, two sub-population coexist, one growing (non-zero growth rate in Fig. 5.5b) and one non-growing populations (zero growth rate in Fig. 5.5b).
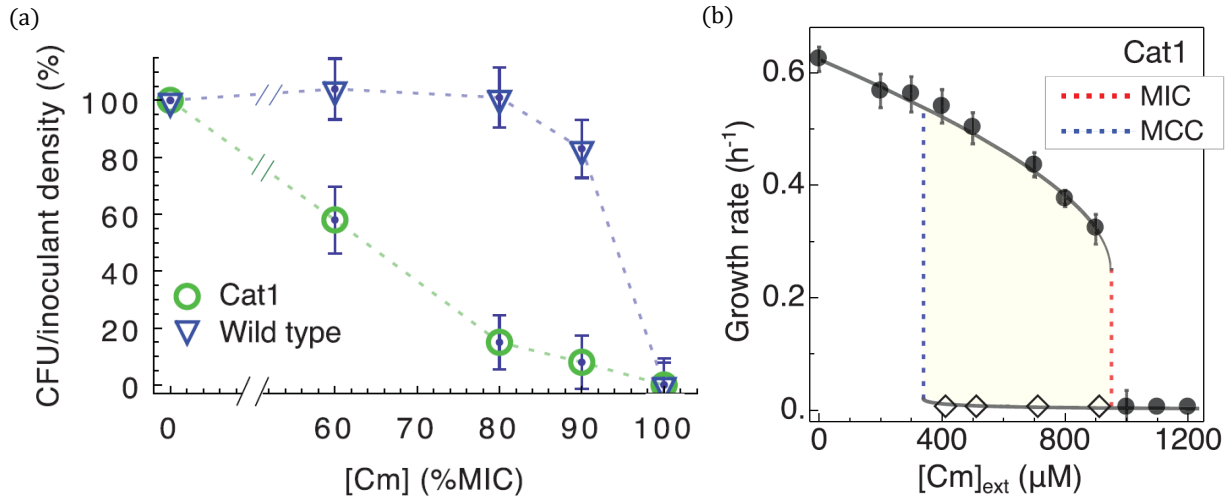
Figure 5.5: a) Susceptibility curves for sub-MIC concentration for wild-type and Cm-resistant strain CAT1. b) Impact of the antibiotic stress on the growth rate of the resistant strain. Graph extracted from Deris *et al.*[124]

This is an example of susceptibility testing to investigate and predict population behaviour under sub-MIC stress. They performed their quantitative measurements with classical methods (agar plate and batch) which limits their number of repetitions and the number of conditions (only 5 concentrations tested).

5.1.6 Variables for antibiotic susceptibility testing

After reviewing the works presented above, we identified the key variables to investigate in order to improve the susceptibility testing. The binary results of the classical methods are not sufficient enough to understand the emergence of new antibiotic resistance as it involves numerous dynamical and quantitative parameters. The chosen variables are listed in table 5.2. For a given strain, it has been shown that the culture medium as well as the antibiotics family have an impact on dynamical response of *E.coli* to drug stress,[123] but we fixed in this chapter the culture medium and the antibiotics to LB and aminoglycosides as we aim to prove that our platform can be used for susceptibility testing. The remaining parameters, defined as *control parameters*, are the antibiotic concentration C, the exposure duration τ and the exposition time t_0.

Figure 5.6a defines the control parameters with regards to the typical bacteria growth profile. The *exposition time* t_0 indicates the moment at which the drug stress starts. When no antibiotic is applied, a bacteria cell will proliferate into a colony that will follow the typical growth profile (Fig. 5.6b). Different values of t_0 will therefore result in different colony sizes. The *exposure duration* τ corresponds to the time during which the antibiotic

Strain	Medium	Antibiotics	Control Parameters
E.coli MG1655	LB	Gentamycin Tobramycin	C
			t_0
			τ

Table 5.2: Variables involved for drug susceptibility testing. In our study, the strain, medium and antibiotics are fixed.

stress is applied. At the end of the drug stress, the antibiotic is replaced by pure culture medium such that surviving bacteria cells resume their growth. The technical challenge about varying τ relies on the possibility of removing completely the antibiotic from the culture batch. Fridman *et al*[119] use washing method, but this method does not ensure the entire antibiotic removal. It is generally assumed that a small fraction remains in the batch.
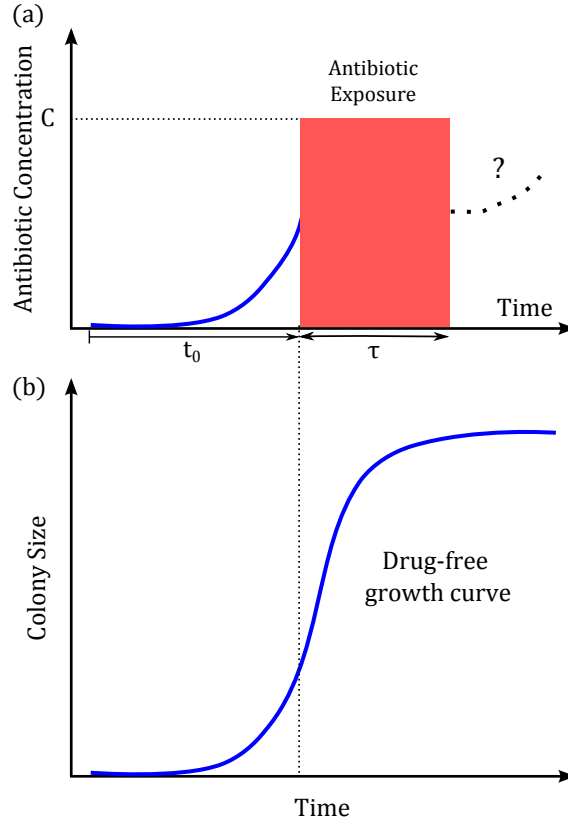
Figure 5.6: Definition of the control parameters to test drug susceptibility.

In addition to the variables controlled for the susceptibility testing, we referenced three different types of results which seem to be correlated to the drug susceptibility and derive from two types of measurements (Table 5.3). In Deris *et al.*,[124] the susceptibility is measured at the final time as the percentage of surviving cells, which required a single point measurement after colony growth. The second type of measurement is when the growth

Measurements Type	Output Data
End-Point	% Survivors
Time-lapse	Lag time
	Growth Rate

Table 5.3: Output data function of the measurements type.

Reference	Variables				Results type		
	Medium	Concentration C	τ	t_0	% Survivors	Lag Time	Growth Rate
Bundtzen *et al.*[116]		$1 - 16 \times$ MIC	~ 2 h			✓	
		$\sim 4 \times$ MIC	$0.25 - 12$ h			✓	
Fridman *et al.*[119]		$10 \times$ MIC	$3 - 8$ h			✓	
Greulich *et al.*[123]	✓	6 Concentrations $<$ MIC	∞				✓
Deris *et al.*[124]		5 Concentrations $<$ MIC	∞		✓		✓

Table 5.4: Summary of previous work on the antibiotic susceptibility with variables used and the type of measurements they provided. ∞ means that the antibiotics were not removed from the bacterial culture.

dynamic is followed such that we can have access to the lag time (PAE[116]) and growth rate (growth-dependent studies[123]) for each conditions.

We summarize the studies we reviewed above in table 5.4 indicating the control parameters they used. Although none of them investigates the impact of t_0, we integrate this parameter in our study because it has been shown that the ribosomal composition of the bacterial cells varies with their metabolic state[125–127] and the metabolic state is changing throughout the colony growth. We will show in this chapter that it has effectively an impact on the drug susceptibility.

The microfluidic platform developed in chapters 3 and 4 can be used to monitor dynamically the control parameters (C, τ, t_0) while providing end-point and dynamical measurements in order to answer the current challenges drug susceptibility testing. The generic platform requires however few adaptations and changes that are presented in the next section.

5.2 Microfluidic Chip Adaptation and Optimisation for Drug Susceptibility testing

5.2.1 Chip modification for gradient production and protocol

Concentration gradient production. Implementing the concentration gradient requires minor chip modifications. The outlet part is replaced by a distribution channel perpendicular to the main chamber, see Fig. 5.7a. To ensure the production of a concentration gradient the height of the distribution channel is kept much larger than the height of the main chamber (see 2.4). Figure 5.7b shows a concentration gradient of fluorescein (A) in pure water (B) with an inlet flow rate of 2×3 μL/min in a 15 μm chamber. The concentration gradient is established perpendicular to the flow such that each row of the array is exposed to a single concentration.
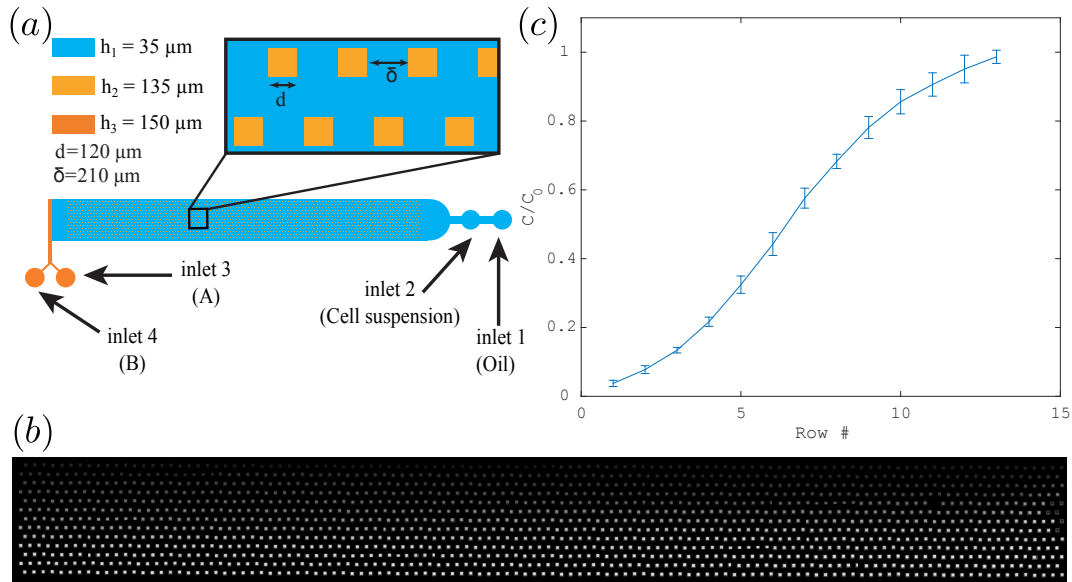
Figure 5.7: a) General chip geometry for the production of a continuous concentration gradient within the chip. Inlets 1 and 2 are used for breaking the droplets on the anchors. The modification relies on the addition of inlets 3 and 4, which are used to produce the antibiotic concentration gradient.[53] We used different heights for the main chamber : both 35 μm or 15 μm height can be used for the chamber. b) Large scan of a concentration gradient produced on chip with pure water and a solution of fluorescein. The fluorescein concentration increases gradually from top to bottom rows of the array. c) Calibration curve for the 15 μm chamber chip presented in b) with an inlet flow rate of 3 μL/min. The error bars are calculated from the standard deviation of each concentration along each row.

Figure 5.8a displays the concentration gradient profiles of a 15 μm and 35 μm gradient chips obtained with a 1 μL/min for all chip entrances. The 35 μm chamber leads system-

atically to a saturation towards high concentration (rows $11, 12, 13$, Fig. 5.8a) whereas the $15\ \mu m$ chamber yields a nicer contrast. As we aim to test as many different concentrations as possible, $15\ \mu m$ chambers will be preferred as well as inlet flow rates of $3\ \mu L/min$. The corresponding calibration curve is shown in figure 5.7c with concentration ranging from 3.7% to 98.7% of the initial solute concentration C_0. This curve is valid only for solutes that have similar molecular size to fluorescein such that their diffusion coefficient can be assumed identical [4].
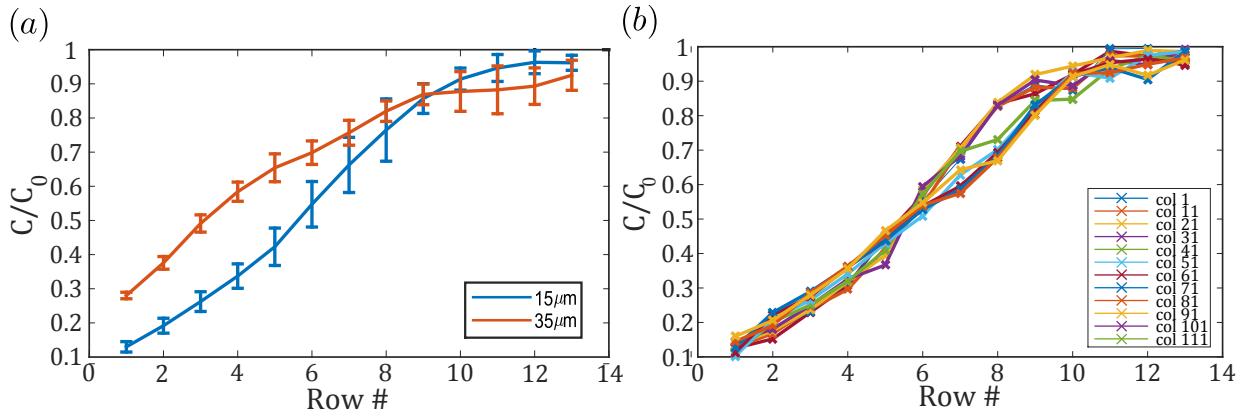

Figure 5.8: a) Comparison between calibration curves of a $35\ \mu m$ chip with a $15\ \mu m$ for inlet 3 and inlet 4 flow rates of $1\ \mu L/min$. b) Comparison of the concentration gradient profile for different column along the droplet array for a $15\ \mu m$ chip with $1\ \mu L/min$ flow rates.

The use of a very thin chamber results in high fluid velocities inside the chip (~ 0.1 mm/s) which ensures the gradient stability along the rows. For inlet flow rates of $3\ \mu L/min$, the Péclet number is over 400 such that the solute does not transversally diffuse more than 27% of the distance between 2 anchors during its flow through the entire chamber. We compare on figure 5.8b the concentration profiles measured along the chamber cross-section for different column positions. The curves superposition demonstrates the gradient stability.

Protocol. The exposure of bacteria cells to a solute concentration gradient begins with the standard protocol of section 3.1.1 and proceeds to the cell suspension encapsulation in gelified droplets. Then, a concentration gradient can be applied at any time of the bacteria growth for any period of time by performing a phase change. The phase change consists in four steps. First, the surrounding oil is cleaned with pure FC40 to remove the

---

[4]We should warn the reader that in some of the experiments in this section $35\ \mu m$ chambers are used because at the beginning of the experimental work we wanted to keep the same device as for chapter 3 until we realise of that breaking the droplet with a $15\ \mu m$ worked perfectly fine and yields better concentration gradient profiles. The calibration curve is adapted function of the height of the used chamber

surfactant used for droplets breaking. Then, a co-flow of two solution A and B is flowed at 2×3 μL/min through inlets 3 and 4, which slowly replaces the oil phase by a continuous concentration gradient orthogonally to the flow direction. When the desired exposure time is reached, the device is washed with pure LB to allow further growth. Finally, the aqueous phase is replaced by a new oil phase, thereby re-encapsulating the hydrogel droplets and preventing communication between them and then the device is placed in the incubator at 37 °C.
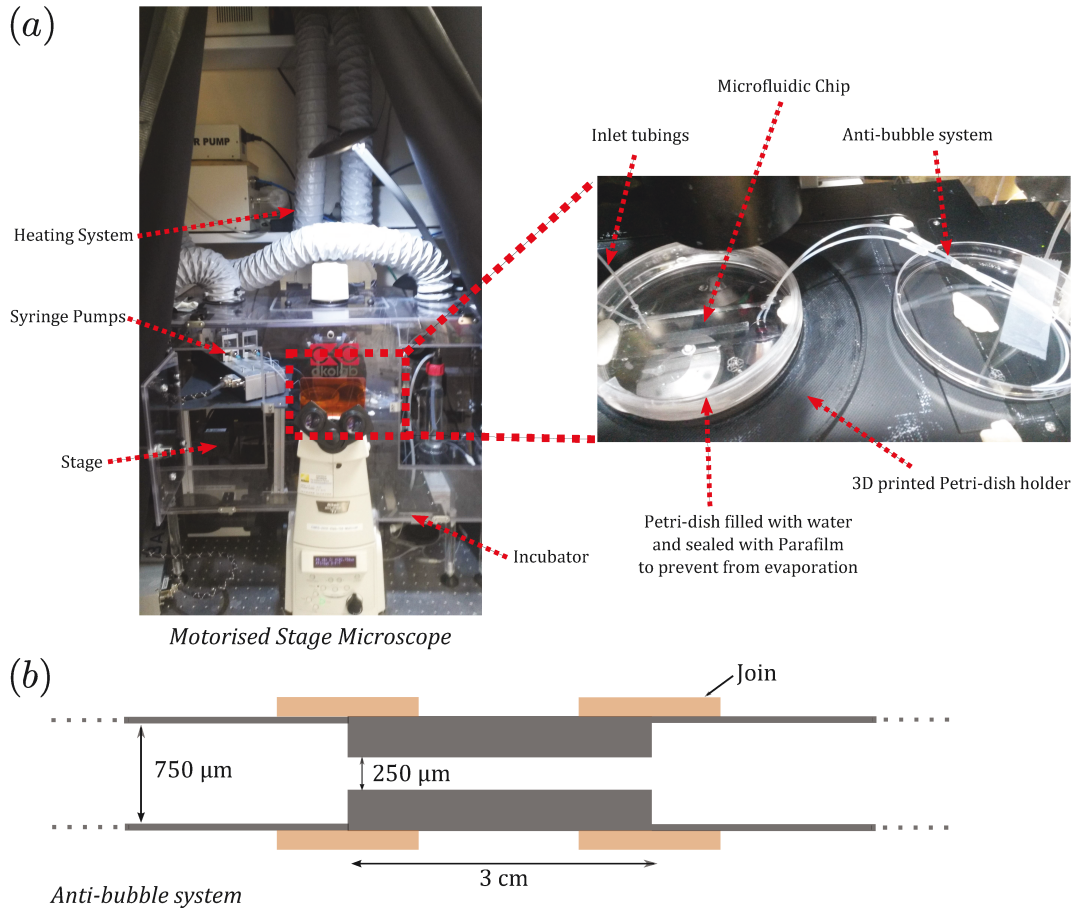
Figure 5.9: a) Experimental set-up for time lapse experiment with a continuous gradient. b) Anti-bubble system branched to the outlet tubes. It prevents from bubble nucleation inside the main chamber. 3 cm of 250 μm inner diameter tubes are inserted to the 750 μm tubes normally used. Tubes are connected thanks to larger tubes, *join* on the scheme.

Figure 5.9a shows the experimental set-up for timelapse experiment with a continuous gradient application. As PDMS presents a high permeability to water, all the droplets dry out after few hours in the incubator, as described in chapter 4. The microfluidic chip is therefore placed in a Petri-dish filled with PBS and sealed with Parafilm to prevent evaporation. The Petri-dish is maintained on the motorised stage through a 3D-printed holder.

Small holes are drilled into the Petri-dish ceiling to allow for the tubing connection to the chip. The inlets are connected to syringe pumps whereas the outlets are connected to an anti-bubble system to prevent air bubbles from nucleating in the microfluidic chamber, which would disturb the gradient profile.

The principle of the anti-bubble system relies on increasing the pressure inside the chamber while maintaining the same flow rate. The overpressure is induced by increasing the hydrodynamic resistance of the outlet tubing by branching 3 cm of 250 μm diameter tubing to the regular 750 μm diameter tubing (Fig. 5.9b). The entire system is surrounded by a incubation box connected to an heating system that maintain the environmental temperature at 37 °C.

The phase change described earlier can be performed in both platforms : the generic platform and its concentration gradient producer adaptation. In the case of the generic platform, a phase change is generally used to bring or remove a given solute such as growth medium or antibiotic.

5.2.2 Experimental Settings for Phase Change

Time for phase change. To estimate the required time to infuse a new solute concentration all over the chip, we fill a 35 μm chip with fluorescein and measure the fluorescent level of the furthest wells from the inlet in two spots (wells 1 and 2 on Fig. 5.10a). For both flow rates, 5 μL/min and 20 μL/min, well 2 requires more time to reach its steady state concentration. As the PDMS chamber bends under the flow pressure, the height of the chamber is larger in its centre compared to the side parts which results in higher flow rates in the centre and therefore, a swifter diffusion inside the gelified beads. The minimum time required for a phase change is thereby defined by the time for well 2 to reach its desired concentration. For 20 μL/min, after 1.5 min we can consider that all the wells have reached the final concentration, while for 5 μL/min, 2 min are required. The time to fill up the microfluidic chips with a new solute is therefore fast compared to the typical time scale of the biological systems (> 10 min).

Contamination during the phase change. In chapter 3, we proved that our experimental process does not imply external contamination as no growth is observed if a chip is loaded solely with culture medium and without bacteria. However, during experiments involving phase change, a cross contamination between the wells is observed. During a phase change, culture medium is flown through the chip which sometimes tears bacteria cells out of their droplet. Extracted bacteria can fix to other droplet such that negative droplets are likely to become positive after the phase change. As an example, we load a generic chip
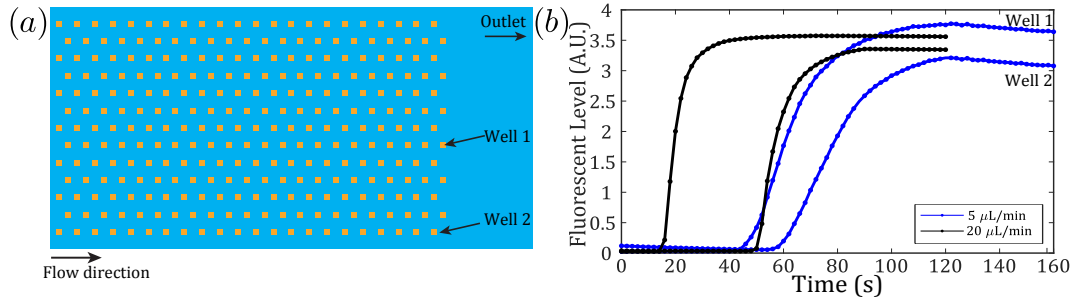
Figure 5.10: a) Both well 1 and well 2 concentrations are observed to determine the time necessary to diffuse a new solute in every droplet. b) Fluorescent signal profile of the observed wells for inlet flow rates of 5 μL/min and 20 μL/min with time lapse images taken every 2 s.

with *E.coli* cell suspension in LB medium and agarose, and incubate it overnight. The result of the scan is shown on figure 5.11a where 206 wells are counted positive using the digital approach described in section 3.2.1. Then, we perform a phase change to bring new medium to the gelified droplet and incubate overnight the chip a second time. The second scan reveals 567 positive droplets on the fluorescent image (Fig. 5.11b), which means that 361 have been contaminated during the phase change. Moreover, we can see that the newly positive droplets are downward in the flow direction which supports the fact that the cross-contamination is induced by the flow of the phase change.
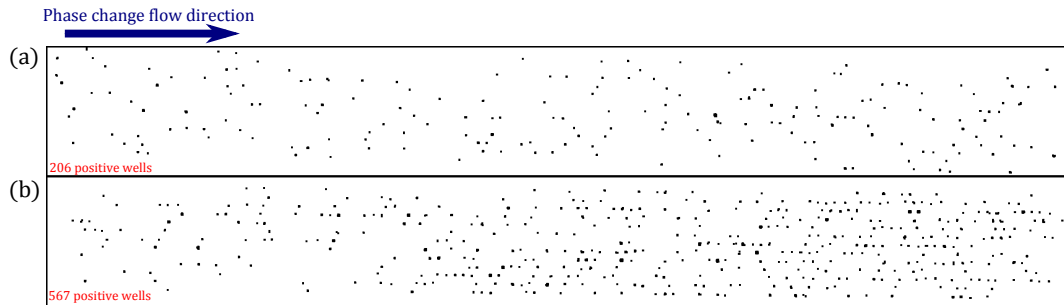
Figure 5.11: Positive wells detected before (a) and after (b) a phase change. The flow direction is from left to right to perform the 5 min phase change under 20 μL/min flow rate.

Post-treatment limiting quantification errors with cross-contamination   No particular technological solution is found to avoid cross-contamination, but it is possible to overcome this during the post-treatment analysis. Figure 5.12 displays an example of a positive and contaminated droplets. We can see in figure 5.12a that a positive droplet is characterised by a round shaped colony that results in a well defined peaked fluorescent signal, here with a maximum intensity of $I_{max} = 43,787$ (16bit). In the contaminated case (Fig. 5.12b), the cells colonise the droplet surface and produce a more diluted fluorescent

signal with no distinguishable peak and a maximum intensity $I_{max} = 7126$ (16bit). For the empty droplets, we measure an average intensity around 250. Therefore, we have an order of magnitude between each of the three droplet sub-populations : empty, contaminated and positive droplets, which allows for the discrimination of each group. Contrary to the digital analysis, where solely two sub-populations were sought, we use here a camera with a higher sensitivity and resolution (1.6 μm /px for Andor Camera) than the scanner used in section 3.2.1.
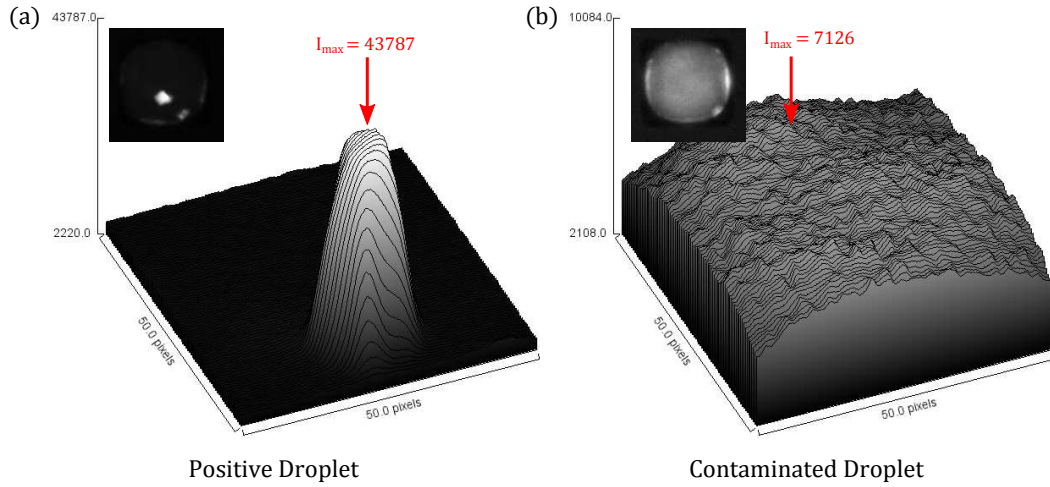
Figure 5.12: Example of a positive (a) and contaminated(b) droplet with their intensity surface plot.

In practice, the distribution profiles of the average intensity on the 50 brightest pixels are plotted in linear and logarithm scale (Fig. 5.13). Both graphs are used to set the two thresholds that separate the three sub-populations. The first and highest peak with its low mean intensity corresponds to the empty droplets and is easily identified on figure 5.13a. On the same graph, we can identify a global minimum that corresponds to the second threshold, but due to the large spreading of the measured intensities the minimum is not always giving satisfactory results. In this case, we resort to the logarithm scale plot (Fig. 5.13b) to evaluate a more accurate threshold.

5.3 End-point measurements after time-dependent antibiotic stress

In this section, we demonstrate the abilities of the platform to explore the three control parameters space (C, τ, t_0) for antibiotic susceptibility testing using only the end-point measurement type (cf table 5.3). As we aim to prove the technological features of the

Figure 5.13: Histograms profile of the maximum intensity pixels integrated for each well in linear (a) and logarithm (b) scale.

platform, the space (C, τ, t_0) is first reduced to the plan (C, t_0) by determining the optimal exposure duration to observe the full antibiotic effect. Then, we present how MIC can be directly measured on chip at a fixed t_0. Finally, a complete drug susceptibility screening is performed by varying both parameters C and t_0.
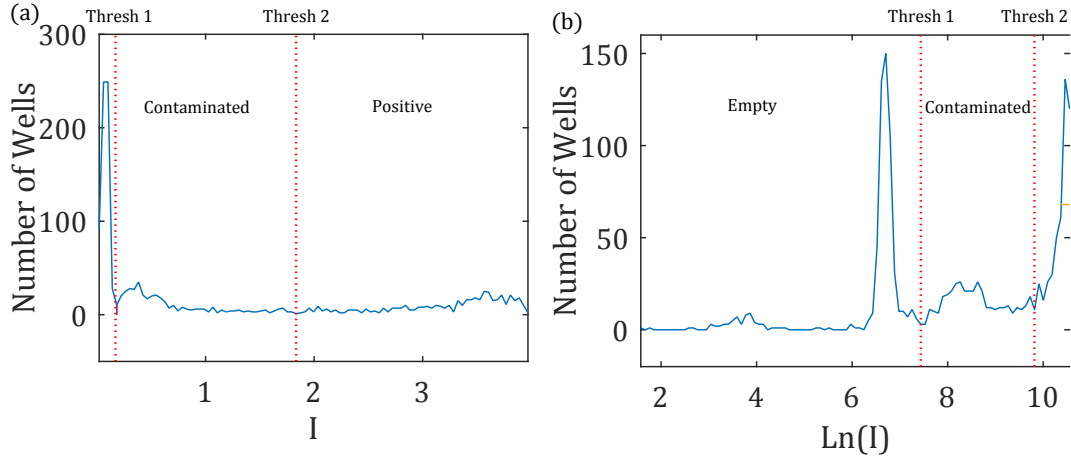
5.3.1 Exposure time optimisation for drug susceptibility testing.

To reduce the control parameters space (C, τ, t_0) to the plan (C, t_0), we investigate the impact of the exposure time τ on the susceptibility of *E.coli* MG1655 to tobramycin using the generic chip. The antibiotic concentration is fixed to the MIC value found in batch culture (C = 9 μg/mL) and the metabolic state t_0 is set to 0. To test six exposition durations $\tau = [0, 1, 2, 3, 4, 5]$, six generic chips [5] are loaded with an overnight batch culture diluted in fresh medium at the initial OD of 1/200. Five of them are loaded with the antibiotic tobramycin and the remaining chip without tobramycin ($\tau = 0$ hr). Figure 5.14a summarises the experiment. The red zone length corresponds to the antibiotic exposure duration, while green zones stand for the chip incubation with pure LB medium. The switch from red to green zones is performed by a phase change, during which a chip is rinsed with pure LB and incubated to allow for the growth of the surviving cells. All 6 chips are scanned the day after for digital analysis and the number of positive droplets is determined and plotted on figure 5.14b.

We observe that the number of survivors decreases rapidly with the exposure time. For

---

[5]NB: the generic chip is used here and not the gradient chip because we performed these experiments before deciding to stick with the gradient chip for the rest of our work.
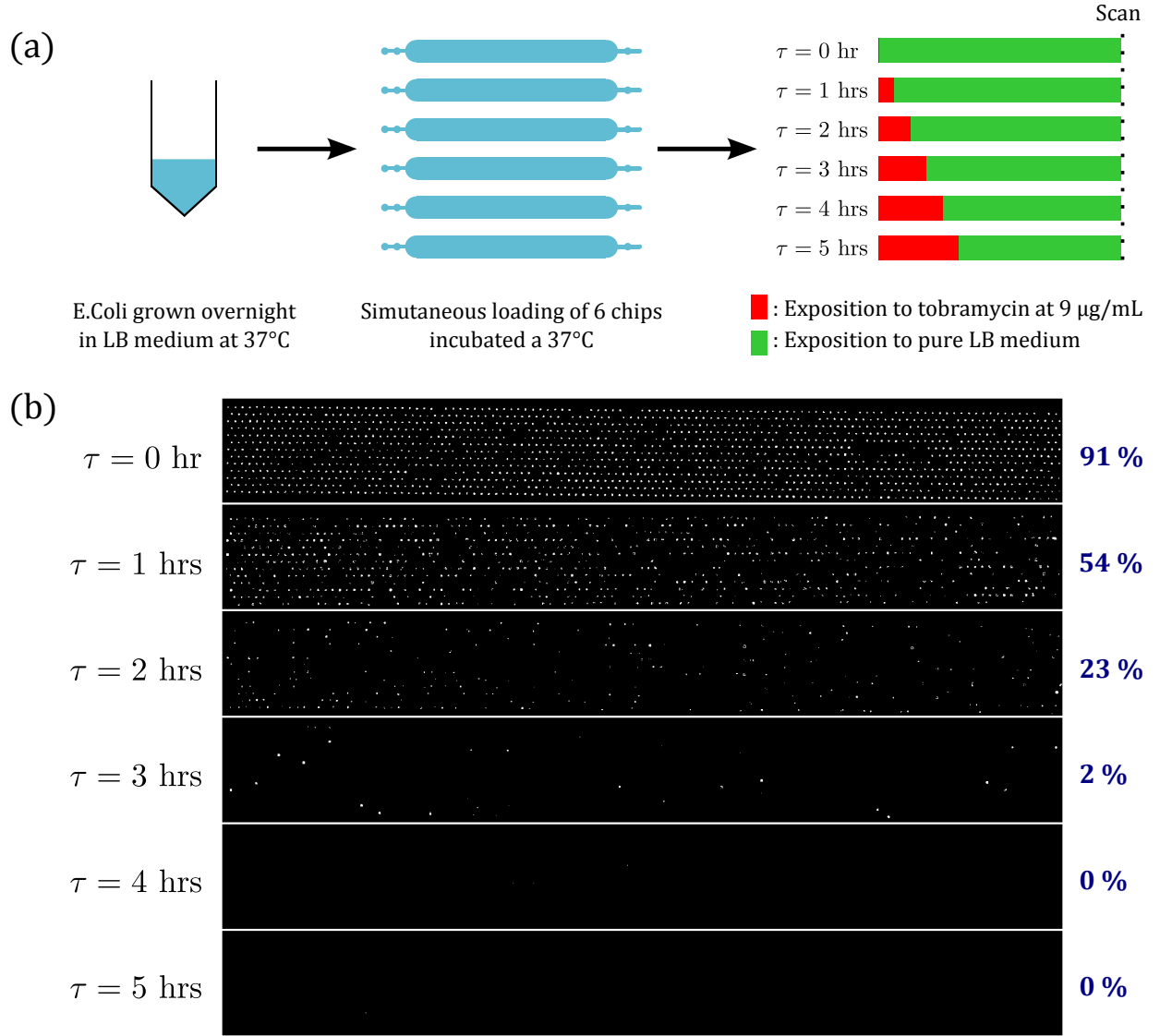
Figure 5.14: a) Scheme of the experiment exposing MG1665 strain to tobramycin at 9 $\mu g/mL$ for different durations $\tau = [0, 1, 2, 3, 4, 5]$ hrs. b) The six chips are scanned the day after to reveal the amount of surviving wells.

antibiotic exposure above 3 hrs, less than 2 % of the droplets remain positive. Therefore, at the MIC, an exposure of 3 hrs is enough to completely observe the antibiotic effect and eradicate all the bacteria cells. In the following sections, we will set τ between 3 and 4 hrs to reduce the number of variables and demonstrate the platform ability to explore the impact of the parameters (C, t_0) on the drug susceptibility.

This result proves that the antibiotic effect is time dependent, such that a value of MIC should be given as a function of τ. Here, the value of MIC is taken as the MIC measured

in batch in which the antibiotic is not removed. Therefore, we measured the time required to kill all the bacteria cell for this particular concentration. This time is very likely to decrease with antibiotic concentrations above the MIC.

5.3.2   On-chip antibiogram

In this section, we perform on-chip antibiograms by measuring MICs at fixed $t_0 = 0$ and $\tau = 4$ h. For the proof of concept, a gradient microfluidic device is loaded with an *E.coli* suspension and droplets are gelified within the anchors. Afterwards, a co-flow of LB culture medium and of LB with the drug gentamycin (c = 25 μg/mL) is imposed, replacing the oil phase. A gradient of gentamycin establishes across the width of the microfluidic chamber, with drug concentrations ranging between zero and 21 μg/mL for the 35 μm chip. The gradient is applied here at room temperature, before any growth can occur such that $t_0 = 0$. After $\tau = 4$ hours of gradient exposition, the chamber is washed with pure LB culture medium. The device is incubated at 37 °C for one day, after which it is imaged on a slide scanner, see Fig. 5.15a.

The concentration profile of gentamycin is plotted in figure 5.15b as a function of the well position in the chamber. The lower part of the chip corresponds to the high antibiotic concentration region while the upper part is the low concentration region. Cells on a given row on the chip are exposed to the same drug concentration. Our two-dimensional array of anchors consists of 13 rows and 115 columns, so that 13 different drug conditions can be probed on the chip, and each condition is repeated 115 times. The percentage of surviving cells, determined by fluorescence digital analysis, is shown in the same graph for each drug concentration. The number of survivors starts to decrease for concentration greater than 9 μg/mL, and no cells survive for concentrations larger than 17 μg/mL, which defines the MIC for this particular *E.coli* strain (pGlo) and control parameters ($t_0 = 0$ and $\tau = 4$ hrs).

The on-chip measurements method can be used routinely with other bacterial strain and other antibiotics. We test another *E.coli* strain (MG1655) and two antibiotics gentamycin and tobramycin as for the bacth measurements, see section 5.1.2. Figure 5.16 display the susceptibility curves for both antibiotics at fixed t_0 and τ. We find an identical MIC value of 7.9 μg/mL for both gentamycin and tobramycin. They are similar to the values we obtained earlier in batch culture, see table 5.1.

Contrary to the batch measurement that provides a binary result : growth or no growth, the use of our platform gives larger range of information as we obtain the percentage of surviving colonies as a function of the drug concentration. It allows us to identify different patterns of susceptibility function of the antibiotic used. On figure 5.16, we can see that
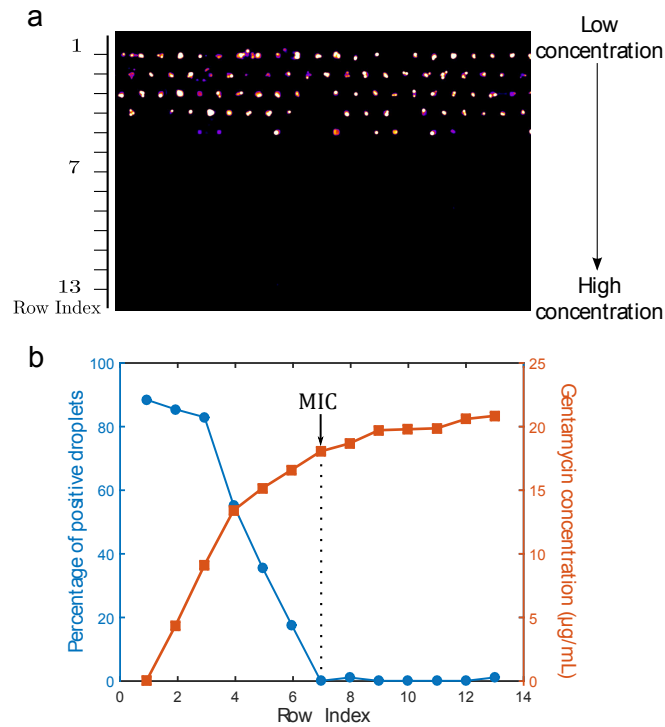
Figure 5.15: On-chip antibiogram method: (a) Zoom on the microfluidic chip. Fluorescence signal after 4 hrs exposure of an *E.coli* pGlo culture to a concentration gradient of gentamycin at 3 μL/min, and one day of culture in LB medium without antibiotic at 37 °C. (b) Gentamycin concentration (orange squares, right y-axis), and percentage of droplets where *E. coli* grow (blue circles, left y-axis), as a function of the row number.
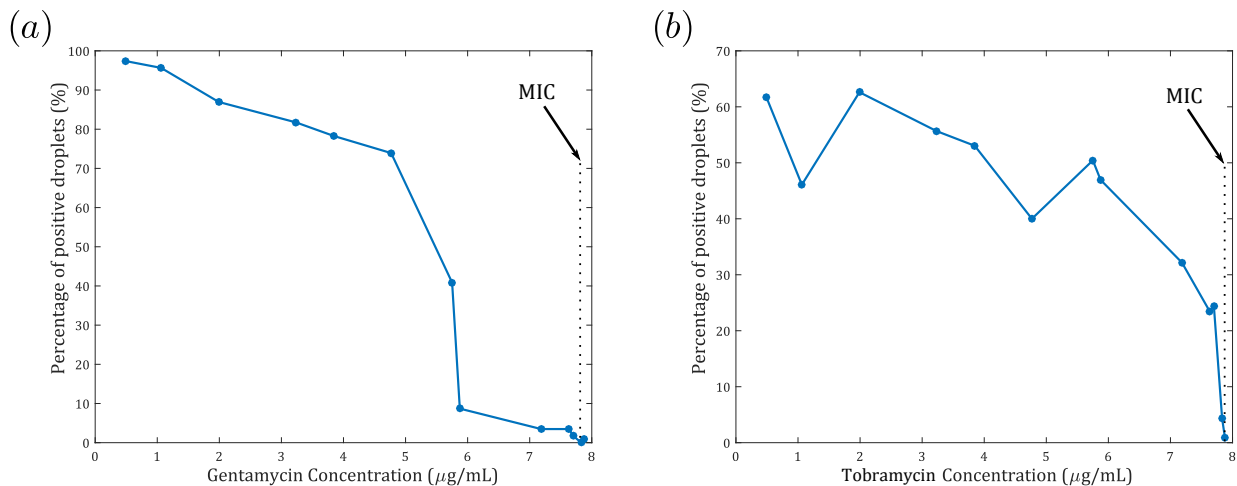
Figure 5.16: On-chip antibiograms for MG1655 strain with two antibiotics: (a) Gentamycin, $t_0 = 0$, $\tau = 4$ hrs. MIC = 5.9 μg/mL. (b) (a) Tobramycin, $t_0 = 0$, $\tau = 3.5$ hrs. MIC = 7.9 μg/mL.

the response of the *E.coli* strain MG1655 to gentamycin is different from its response to tobramycin. For gentamycin, the amount of survivors drops to 10 % at a concentration of 5.9 μg/mL and observes a slow decrease towards the MIC, while for tobramycin the drop-off occurs at the MIC.

5.3.3   Impact of Colony Growth Phase on Drug Susceptibility

In this last end-point measurements section, both parameters C and t_0 are monitored with a fixed $\tau = 3.5$ hrs and the susceptibility curves with tobramycin are sought for different colony growth states t_0.

As shown in figure 5.17a, four 35 μm gradient chips are loaded with an overnight batch culture of *E.coli* MG1655. The antibiotic gradient with concentration ranging from 0.4 to 7 μg/mL, is applied at various instants $t_0 = [0, 2, 4, 6]$ which correspond to different points of the mean growth profile (red strips on figure 5.17b). Each instant is assumed to correspond, on average, to a different colony growth state : stationary state ($t_0 = 0$ hr), beginning of the exponential phase ($t_0 = 2$ hrs), middle of the exponential phase ($t_0 = 4$ hrs) and end of the exponential phase ($t_0 = 6$ hrs). Before and after the gradient exposure at room temperature, the chips are incubated with pure LB medium at 37 °C.

After an overnight incubation, the four chips are scanned as shown in figure 5.18. The lower part of each chip corresponds to the low concentration while the top part to the high concentration. As expected, in both cases $t_0 = 0$ h and $t_0 = 2$ h, positive droplets are found for low concentrations, and above a threshold concentration no more growth is observed.

For the cases $t_0 = 4$ h and $t_0 = 6$ h, the distinction between the positive and negative droplet is more complex as we also observe remaining colonies in droplets from the high concentration region ($C > 5$ μg/mL). For better visualisation, two examples of each chip are shown in figure 5.19. Colonies exposed to high antibiotic concentration (Fig. 5.19a,b,e,f) are much smaller than the ones from the low antibiotic concentration (Fig. 5.19a,b,e,f). Moreover, at the same high concentration stress, the colonies of the case $t_0 = 4$ h are smaller than the colonies of the case $t_0 = 6$ h.

The presence of these unexpected colonies in high concentrations region are due to the design of the experiment. Before the antibiotic exposure, bacteria cells are allowed to grow in the gelified droplets. At 4 h and 6 h, they have already formed round shaped colonies contrary to the cases $t_0 = [0, 2]$ where only a few cells are present in the droplets at the

(a)

E.Coli grown overnight in LB medium at 37°C

Simutaneous loading of 4 gradient incubated at 37°C

$t_0 = 0$ hr

$t_0 = 2$ hrs

$t_0 = 4$ hrs

$t_0 = 6$ hrs

Scan

■ : Exposition to tobramycin gradient
■ : Exposition to pure LB medium

(b)

Starts of tobramycin gradient exposition
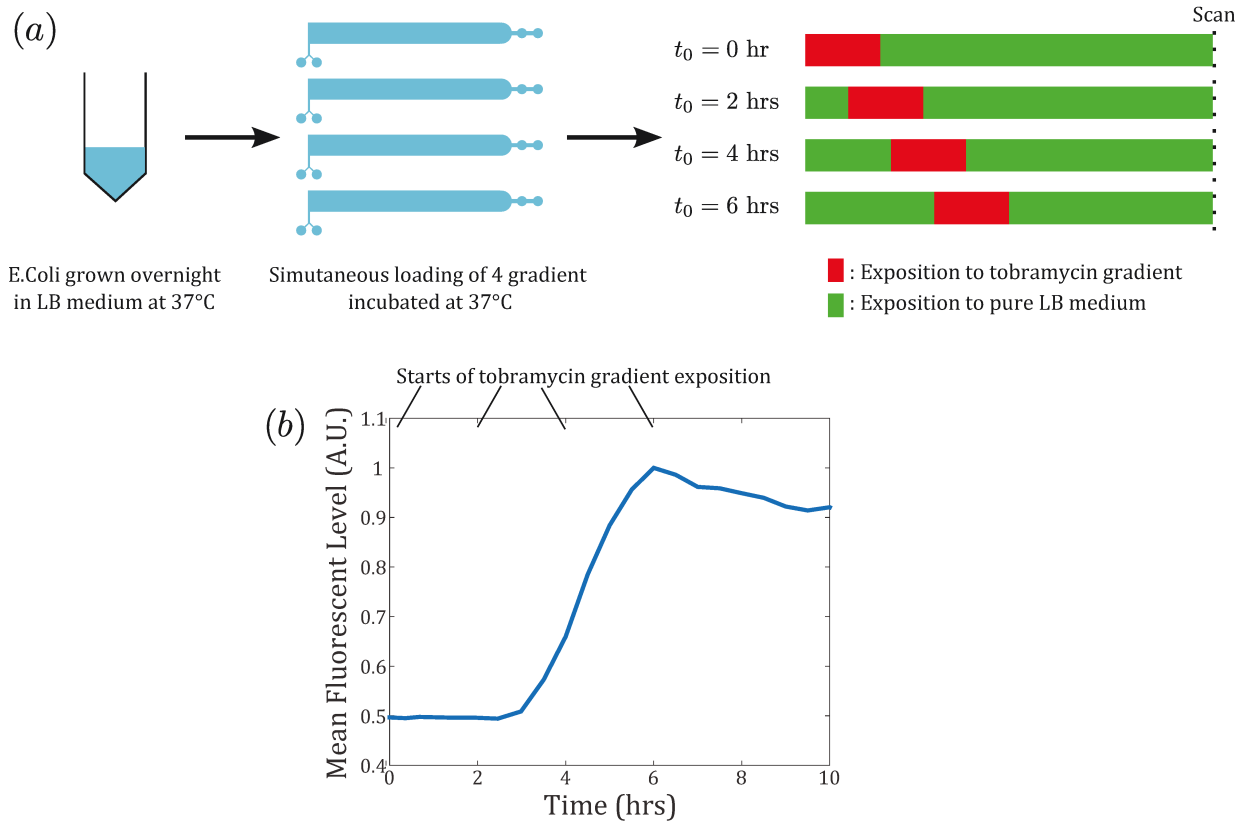
Figure 5.17: a) Scheme of the experiment exposing *E.coli* MG1655 to a tobramycin gradient at different colony growth state $t_0 = [0, 2, 4, 6]$. Antibiotic concentrations are ranging from 0.4 to 7 μg/mL. b) Mean growth profile of MG1655 strain in pure LB medium. A vertical red strip indicates the instant when the gradient is applied for the four chips.

$t_0 = 0$ hr

$t_0 = 2$ hrs

$t_0 = 4$ hrs

$t_0 = 6$ hrs
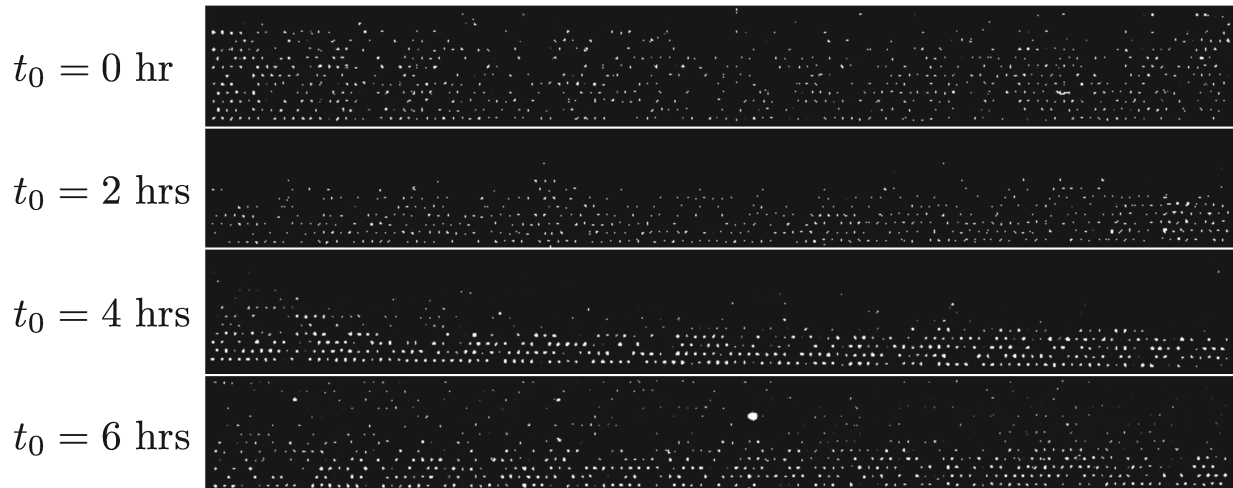
Figure 5.18: Scan results of the experiment shown in figure 5.17.

moment of the antibiotic exposure. The initial inoculum size is therefore larger in chip 3/4 than in the chip 1/2. For large inoculum size, the exposure time set in section 5.3.1 could be too short to kill all the bacteria present in the droplet at the drug exposition and therefore some of them would remain in the high concentration region droplets.

Moreover, it has been shown that the inoculum size also affects the tolerance of *E.coli* to antibiotic. Bacteria cells have indeed a form of social behaviour through chemical communication called Quorum Sensing (QS) that allows for the production of bio-surfactant at their surface which limits the penetration of antibiotic in their cytoplasm and thus alters the antibiotic efficiency.[128] This could be coupled with the structure of the round shaped colonies. We do not know exactly their structure but it is likely that they have a biofilm structure. A biofilm results from the production by the bacteria cells of an extra-cellular matrix made of polysaccharides. This matrix changes the diffusion of nutrient and oxygen inside the colony which can reduce the metabolic activity of the lower bacterial layer and induce the emergence of supplementary persistance.[129,130] In such case, the remaining bacteria would be the persisters.

However, after the antimicrobial stress, the chips are rinsed with pure LB medium and incubated, which allow for the growth of the surviving bacteria in a new colony. Thus, a regular surviving bacteria cell would divide into a regular colony size. The typical growth of a regular colony – without antibiotics – is also shown on figure 5.19i,j,k,l for the instants corresponding to the start of the antibiotic stress (4 and 6 h) as well as the final colonies size. We can see that surviving colonies in the high concentration region (Fig. 5.19a,b,e,f) display a smaller size than the size of a regular colony even after the regrowth. This indicates that exposition to high concentration modifies the cell efficiency to grow in given culture conditions and that the antibiotic have a lasting effect on the following generations. Finally, these colonies do not correspond to non-growing bacteria cells because tobramycin induces the lysis (explosion) of the cells which dilutes their content in the environment such that dead cells cannot be observed.

To explore this observation at the chip level, we measure the mean fluorescent intensity for each row of the droplets array against the antibiotic concentration on figure 5.20. We observe effectively a decrease of the fluorescent signal globally (red curve). This decrease could be due to the increase of the negative droplet in the calculation of the mean intensity values, but even for solely positive droplets (dark curve), the decrease is observed. This means that the higher the antibiotic concentration during the stress, the less intensity is produced during the re-growth. In chapter 4, we saw that the final fluorescent intensity of the bacterial colony was strongly correlated to its growth rate. This suggests that there are concentration dependent effects of the antibiotic stress on dynamical parameters, which will be further studied in the next section (5.4). The intensities of the surviving colonies in high concentrations region are therefore comparable with the background intensity measured in the empty droplets. Therefore, the digital analysis for the chips 3 and 4 measure
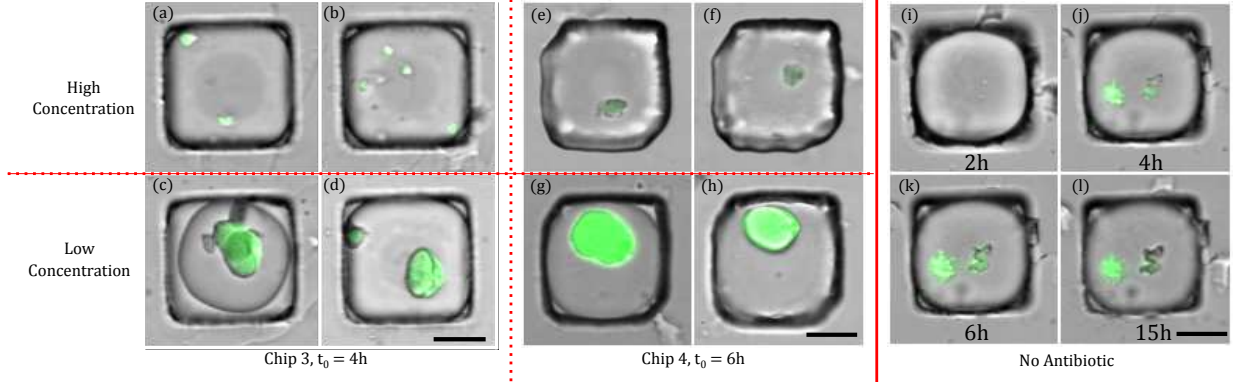
Figure 5.19: End-point snapshots of chip 3 and 4 (($\tau = 3.5$ h,$t_0 = 4$ h) and ($\tau = 3.5$ h,$t_0 = 6$ h) respectively). In each case, two colonies from the high concentration of antibiotic region and two others from the low concentration of antibiotic region. a) C = 7.04 μg/mL; b) C = 6.93 μg/mL; c) C = 0.95 μg/mL; d) C = 0.44 μg/mL; e) C = 7.04 μg/mL; f)C = 6.93 μg/mL; g) C = 0.95 μg/mL; h) C = 0.44 μg/mL. i,j,k,l : regular timelapse snapshots, which shows the typical colony size at $2, 4, 6, 15$ h, with areas of Scale bars : $50 \ \mu m$.

the amount of droplets in which the colony level has reached a sufficiently large size determined by the threshold.
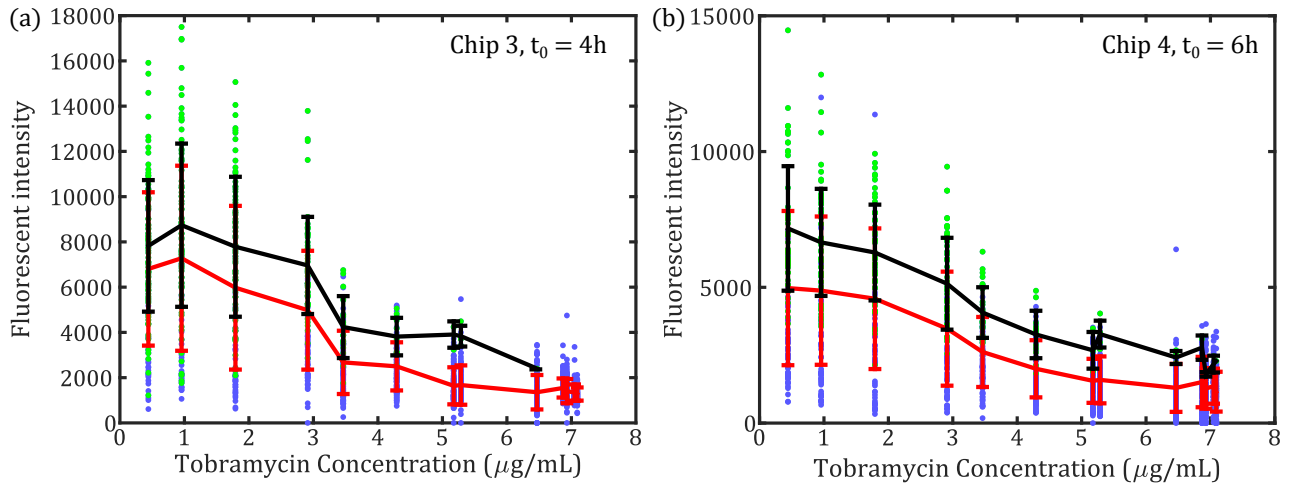
Figure 5.20: Mean fluorescent intensity along each row of the droplet array as a function of the tobramycin concentration. The red curve corresponds to the mean intensity over all the well contained in a row while the black curve is the mean fluorescent intensity of solely the positive droplets. The error bars correspond to the standard deviations.

The number of positive droplets for each row of each chip is finally drawn on figure 5.21a. The susceptibility curves display as expected, a decrease as a function of the antibiotic concentration and the curve $t_0 = 0$ h is consistent with our previous result of a MIC

around 7 μg/mL. We can also observe the difference of response for each chip to the same antibiotic gradient. Even though, chips corresponding to $t_0 = 2$, 4 and 6 hrs have an identical MIC of 6.5 μg/mL, they display different susceptibility profiles. The tobramycin concentration above which the number of survivors starts to decrease and the intensity of the decrease (curve slope) differ from a chip to another.

To evaluate the susceptibility of MG1655 to tobramycin, we define the tenth-inhibition concentration IC_{10}. This is the tobramycin concentration for which 10 % of the droplets are positives. The measured IC_{10} values are plotted against the colony growth state t_0 on figure 5.21b. The susceptibility decreases as we move from the stationary state to the exponential phase (t_0 from 0 to 4 h) and increases as we reach the end of the exponential phase with a lower level than stationary and beginning of exponential phases.
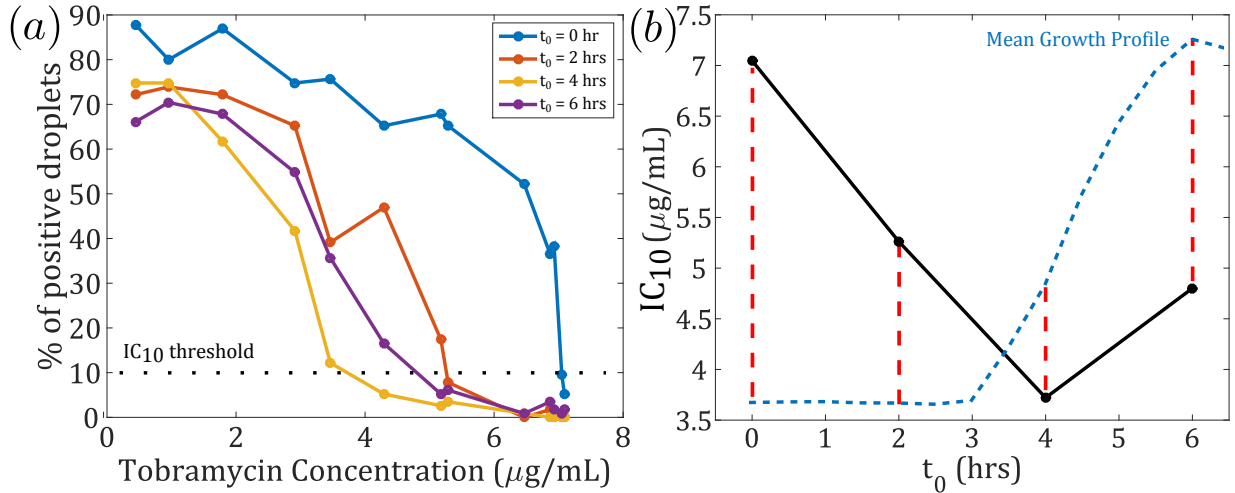
Figure 5.21: a) Positive droplets as a function of the tobramycin concentration for each chip. b) Measured IC_{10} for each colony growth state. The dashed curve is the instantaneous growth rate.

The physiological changes can be characterised by the instantaneous growth rate which increases from the lag phase to the exponential phase where it reaches its maximum and then decreases until the stationary phase. We could be tempted to compare our results to the results presented by Greulich *et al.*[123] who investigated the correlation between the growth rate and the ribosome-targeting antibiotic susceptibility. Yet, the two experiments differ in many points. First, they modulate the colony growth rate with nutrient quality while here the growth rate varies with the metabolic state of the bacteria cells. Second, Greulich *et al.* measure the susceptibility by comparing growth rates under antibiotic stress and the drug-free growth rate for exponential growing bacteria cells, while here we measure the percentage of survivors. Both measurements cannot be compared. Finally, in their case the antibiotic is maintained during the whole experiment while in our case we expose the

bacteria only temporary.

In this section, we have provided an example of mapping for the plan (C, t_0) for $\tau = 3.5$ h. We have also highlighted that the digital analysis does not render all the information accessible by a finer analysis of the fluorescent intensity level which suggested a concentration-dependent effect of the antibiotics on the bacteria growth dynamic. Although the digital analysis is very practical as it allows for a rapid measurement, it can be completed with a dynamical measurements of the bacteria response to the antibiotic stress.

5.4 Dynamical Bacteria Response to Antibiotic Stresses

In this section we combine all the features developed throughout this PhD : the bacteria cell culture platform, the concentration gradient generator and the dynamical measurement. The quantification of the dynamical response of *E.coli* MG1655 after its exposition to gentamycin enables us to explore another type of results for susceptibility testing : the measurements of the lag time and the colony growth rate after antibiotic exposure (cf table 5.3). In this section $t_0 = 0$ h and $\tau = 3$ h.

As a proof of concept, the initial batch culture is encapsulated in agarose beads on a gradient chip. Right after the gelification, droplets are exposed to a gentamycin concentration with on-chip concentrations ranging from 0.5 to 7.9 μg/mL, see figure 5.22a. The chip is rinsed afterwards with pure LB medium and incubated on the motorised stage microscope (Fig. 5.9). Growth is followed by timelapse scans as described in section 4.2 in order to measure the growth curve for each positive wells.

As observed in the previous section, the number of positive droplets goes below 10 % for concentrations above 5.9 μg/mL such that no sufficient number of growth curve can be measured for the high concentrations. Where colony growth curves are measured, the growth parameters defined in chapter 4 can be calculated and plotted as a function of the applied gentamycin concentration.

Figures 5.22b,c show the variation of the mean lag time and specific growth rate as a function of the antibiotic concentration. For concentrations below 3.2 μg/mL, no particular trend is observed for both parameters whereas expositions to concentrations above 3.2 μg/mL result in increasing lag and decreasing specific growth rate. The observed time to restart bacterial growth ranges from direct growth for low concentration to 4 hrs for the slower droplet in high concentration regions. The slope of the specific growth rate decrease is -0.16 hrs^{-1} per μg/mL, which corresponds to an increase of the doubling time of 7 min per μg/mL. The errors are important on this experiment. This needs to be repeated to
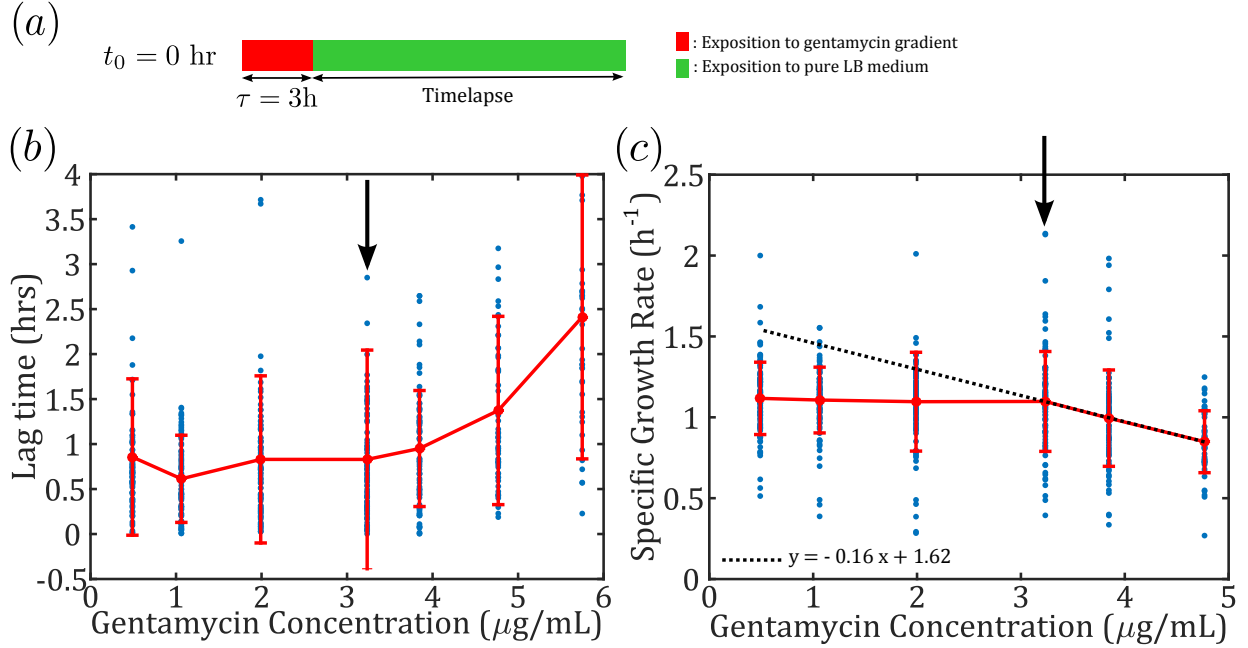
Figure 5.22: a) Scheme of the experiment exposing MG1665 strain to gentamycin gradient in a 35 μm chamber with LB medium and 10 $\mu g/mL$ solutions at 2×3 μL/min for $\tau = 3$ hrs. b) and c) show respectively the mean lag time and mean specific growth rate as a function of the gentamycin concentration. The error bars are the standard deviation along each row of the array. The arrows indicate the gentamycin concentration of 3.2 μg/mL above which the lag time increases and the specific growth rate decreases.

validate the biological consistency of these results.

As for the growth curve in section 4.3, a cross-plot can be plotted for any combination of growth parameters. Figure 5.23a is an example of the biggest correlation found earlier between the maximum growth rate and the final fluorescent intensity of each well. A linear fitting for each concentration has been performed and no particular variation is observed for the slope of the linear fitting. Yet, the coefficient of variation for both the final colony size and the maximum growth rate increases with the gentamycin concentration. Figure 5.23b shows the different coefficient of variations ($\text{CV}_X = \sigma_X / \mathbb{E}_X$) for the lag time, the final colony size and the maximum growth rate. A slight decrease of 20 % is observed for the lag time between the low and high concentration whereas the remaining parameters increase their CV of more than 50 %. This means that the variability inside a population is likely to be increased after an exposition to antibiotics.

These observations bring two relevant information. First, the antibiotic stress has an impact not only on the percentage of survivors but also on their dynamical growth properties. Second, the antimicrobial exposure at room temperature has a lasting effect on the daugh-
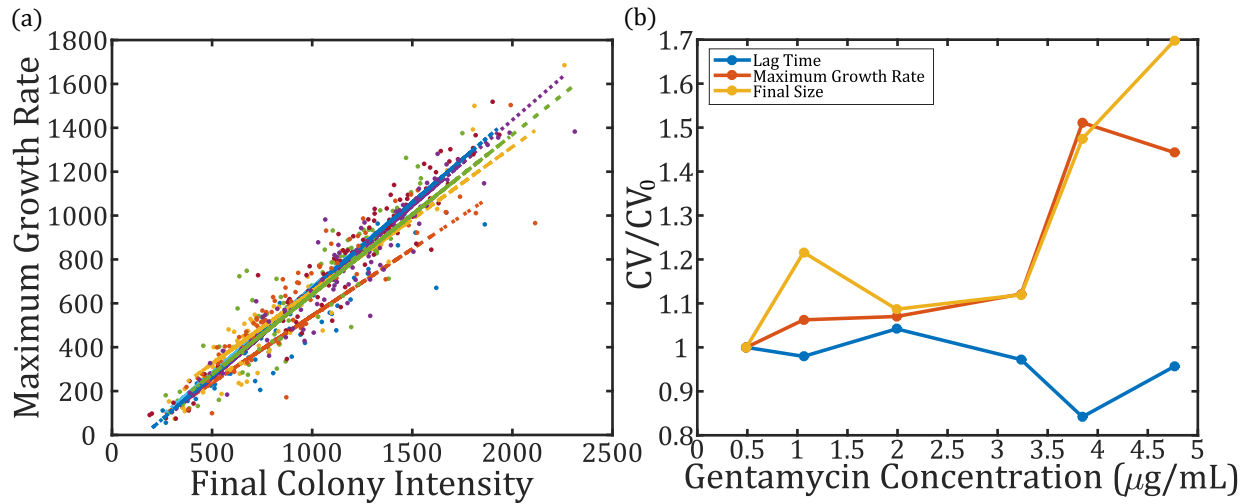
Figure 5.23: (a) Cross-plot of the maximum growth rate and the final fluorescent intensity of each well with their linear fit for each concentration. The insert displays the coefficient of the linear fits as a function of the gentamycin concentration. (b) Reduced coefficient of variation for the lag time, the maximum growth rate and the final colony size.

ter cells born after the drug exposure, because the impact on the growth parameters is measured on the descendants of the exposed cells.

These results are amongst the first quantitative reports of the sub-lethal exposure effect on the dynamical growth parameters at the colony level. Moreover, our platform provides a double information on the growth parameters : the mean population value as in[49, 123] and also the dispersion of the population around its mean value.

5.5   Summary and discussion of chapter 5

In this last chapter, the culture platform developed in chapter 3 is combined with the gradient producer studied in chapter 2 to grow on a single chip bacteria cells under 13 different concentrations. This allows us to enrich the platform with the feature of testing bacteria susceptibility to antibiotics. Our platform is capable of rapidly switching from a concentration gradient of antibiotics to pure culture medium at any time and for any duration. This makes it very versatile and convenient to monitor dynamically antimicrobial stresses in term of instant of application, level of concentration and exposure duration.

Coupled with the digital analysis we showed that the technology can explore the space of the control variables (C, τ, t_0) . Using an end-point measurement we first optimise the time required for tobramycin to eradicate all the bacteria cells at its batch MIC. The use of the gradient chip instead of the generic chip for this experiment can perform the exploration of the (C, τ) plan at fixed t_0 on a single chip. After fixing the value of τ, we presented how the MIC can be determined on chip as well as the exploration of the (C, t_0) plan. We found that the drug susceptibility depends on t_0 which displays its maximum during the exponential growth phase. Yet, this result is obtained after one experiment and for a single value of τ. To enhance the biological consistency of such results, this experiment must be repeated at least three times – as it is commonly performed in biology – and various values of τ should be also tested. The number of experiments left to perform the entire study can be estimated.

For now, only two variables of the (C, τ, t_0) space are explored with experiments using 9 chips which led to the test 9 pairs (τ, t_0) for a given strain and a given antibiotic. A measurement of the surviving rates for the entire space constituted of 13 concentrations, 6 values of τ and 4 values of t_0, i.e. 312 surviving rates, would solely require the loading of 15 supplementary chips for a total of 24 chips (6×4 as the number of (τ, t_0) doublets). With the current state of technological development and number of syringe pumps to control the gradient, experiment involving 6 chips can be performed in one day. This means that in 4 days we can provide 312 surviving rates. With an automated loading system integrating the phase changes and gradient exposure, the time could be reduced to one day and thus three days in total with the two repetitions. The same amount of data using classical techniques as in Deris *et al.*[124] would require a very long and tedious man work to inseminate close to a thousand Petri Dishes (3×312).

During the end-point measurements, a large range of colony sizes is observed which depends on the antibiotic concentration. This suggests that for the same amount of nutrient, surviving bacteria grow in different manners depending on their previous antibiotic stress. In such cases, the digital analysis is limited as it provides only the binary result of growth or no growth and lacks of informing on how the colonies proliferate. Therefore, the end-point measurements was completed with the study of the dynamical response of *E.coli* to gentamycin. The impact of an antibiotic stress on the lag time and growth rate was quan-

tified. The array format of the microfluidic platform allows for the repetition of growth in identical concentrations such that the variability of the response was measured. Even 3 h of antibiotic exposure at sub-inhibitory concentration leads to an increase in the lag time and doubling time as well as their variability.

A very last observation on the particularity of our experiments is the possibility of applying and removing the antibiotics dynamically. This contrasts with other droplet-based microfluidic technique or Petri dishes. For instance, in the case of the MDA technology[46] presented in the introduction of the manuscript, the antibiotic is encapsulated directly in the droplets which defines the total amount of antibiotic molecules exposed to the bacteria cells. This amount – and consequently the concentration – is likely to vary as the bacteria population grows. In our case, the antibiotic concentration is maintained by the continuous flow which renews indefinitely the antibiotic surrounding the bacteria cells. As the concentration and the time of administration characterises the antibiotic treatment, this difference can have an impact on the results obtained in our experiments and drug susceptibility testing made on others droplet-based technologies.[46,131]

Chapter 6

Conclusion

The purpose of this PhD project was the parallelization and the assembly of microfluidic tools previously developed in the lab to explore potential applications in microbiology. In my opinion, this work led to four main achievements in fluid dynamics, study of bacteria growth, antibiotics studies and microfluidic technology.

From the fluid dynamics point of view, we demonstrated that the parallelization of microchannels yields non-trivial flow rates distribution within microfluidic ladder networks. Beyond the resolution of advection-diffusion within the same network, this study can be used for microfluidic process optimisation. For instance, when the droplet production through step emulsification is parallelized as shown in figure 6.1, the injectors placed on the side produce not only droplets first, but also at a larger rate which can impede the homogeneous filling of a $2D$ chamber with a droplet emulsion. At a larger scale, we can imagine the use of such resistance network to optimise oil extraction in porous media or even predict public road traffic.
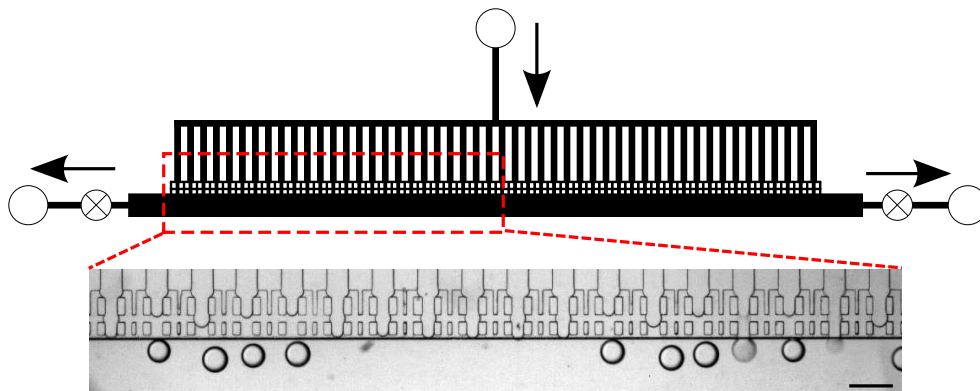

Figure 6.1: Parallelisation of droplet production through step emulsification. Scale bar : 200 μm .

From the bacteria growth point of view, a state of the art on the current opinion on the bacteria growth mechanism was performed. We made a summary of the main challenge of modelling bacteria growth and how a stochastic model could be used to investigate biological variability within a bacterial population. This summary have required to position the growth culture conditions on the chip compared to existing techniques. This could form the foundation for further theoretical developments.

From the antibiotics studies point of view, we identified the main challenges and characteristic parameters for the study of antibiotics on the developed microfluidic chip. We also demonstrated that the ability of our microfluidic platform to dynamically monitor the antibiotic exposure combined with the possibility of describing the composition of a bacterial population need a new definition of the MIC as a function of the characteristic parameters.

From the microfluidic technology point of view, we set up the experimental framework for the parallel culture and observation of bacterial systems in an array of nanoliter droplets. The main technological characteristics of the developed platform are the easy handling for droplets production, the ability of extracting droplets and finally the possibility of applying a concentration gradient with a minimal design and microfabrication footprint. The automation of the experimental data analysis and the simple handling were very important for the chip adoption by other operators. Indeed, this framework will be the starting point for other PhD projects that will address more fundamental biological questions. For instance, the platform is now used in the lab to quantify the efficiency of DNA-transfection in eukaryotic cells using liposomes.

A technological transfer of the platform outside microfluidics labs would require the integration of the entire experimental protocol and the results reading in a single instrument, using the microfluidic chips as disposable cartridges. This would allow to address fundamental problems or to perform routine experiments. Fundamental research in microbiology could benefit from this platform in many areas using one or several of the developed features. For example, we could consider its use for the discovery of new *in vitro* culture conditions, the study of the emergence of antibiotic resistance, pharmacokinetic studies in order to establish more efficient treatment pathways or any other investigations requiring the measurements of an heterogeneous response to an external stress within a population.

Finally, a broader range of applications can be considered for the developed technology. With the advent of genome sequencing, the presence of microbial communities has been highlighted in tremendous amount of environments such as ocean,[132] soil rizosphere[133] or even human body.[134] In all these areas, bacteria species are organised in complex ecosystems which often play key role functions for their host or environment. Yet, a huge lack of information remains on the physiological characteristics of these communities especially for their development and stability[135–137] as well as their interaction with the

environment. This underscores the increased need for such technologies dedicated to the investigations of complex microbial ecosystems. The implication of bacteria cells in the development and the response of our immune system,[138–140] skin[141] and mental health,[142] and even ageing[143,144] promise for such technologies important societal and commercial benefits.

Appendix A

Numerical resolution of advection-diffusion model

Here we give the details of the numerical calculation we perform to solve the advection-diffusion equation described in section 2.3 along the inlet channel and between the nodes. Between node i and $i+1$ we have the equation :

$$\mathrm{Pe}\,\tilde{Q}_i\frac{\partial \tilde{C}}{\partial \tilde{x}} = \frac{\partial^2 \tilde{C}}{\partial \tilde{y}^2},\tag{A.1}$$

with $\tilde{x} = x/L$ and $\tilde{y} = y/w$, the non-dimensional coordinates, and the Péclet number,

$$\mathrm{Pe} = \frac{Q_1 w}{DLh}.\tag{A.2}$$

We divide the $x-y$ plane in a grid of $N_x \times N_y$ pixels of a size of $\delta x \times \delta y$. By indexing the y-coordinate by j and the x-coordinate by n, the concentration of a grid point is referred by c_j^n. We used a *Crank-Nicolson* scheme to discretize the equation (A.1), in particular the x-derivative is estimated on the points $(c_{j-1}^n, c_j^n, c_{j+1}^n)$ with the weights $(1/12, 5/6, 1/12)$:

$$\left(\frac{\mathrm{d}c}{\mathrm{d}x}\right)_j^n = \frac{c_{j-1}^{n+1} - c_{j-1}^n}{12\delta x} + 5\frac{c_j^{n+1} - c_j^n}{6\delta x} + \frac{c_{j+1}^{n+1} - c_{j+1}^n}{12\delta x}\tag{A.3}$$

and thus,

$$\forall j \in [\![2; N_y - 1]\!] \ \forall n \in [\![1; N_x - 1]\!]$$
$$(1-k)c_{j+1}^{n+1} + (10+2k)c_j^{n+1} + (1-k)c_{j-1}^{n+1} = (1+k)c_{j+1}^n + (10-2k)c_j^n + (1+k)c_{j-1}^n\tag{A.4}$$

with $k = \frac{6\delta x}{\mathrm{Pe}\tilde{Q}_i\delta y^2}$.

The boundary condition of no-flux at the walls imposes to create two virtual points on the

y-grid $\forall n \in [\![1; N_x]\!]$ $c_0^n = c_1^n$ and $c_{N_y+1}^n = c_{N_y}^n$. By applying those two points in (A.4), it leads to two additional equations :

$$\forall n \in [\![1; N_y - 1]\!] \begin{cases} 2(1-k)c_2^{n+1} + (10+2k)c_1^{n+1} &= 2(1+k)c_2^n + (10-2k)c_1^n \\ (10+2k)c_{N_x}^{n+1} + 2(1-k)c_{N_x-1}^{n+1} &= (10-2k)c_{N_x}^n + 2(1+k)c_{N_x-1}^n \end{cases}$$
$$(A.5)$$

Therefore, the discretized system leads to a linear relationship between two consecutive steps on the x axis:

$$A_1 C^{n+1} = A_2 C^n \tag{A.6}$$

where $C^n = \left(c_j^n\right)_{j \in [\![1;N_x]\!]}$ and A_1 and A_2 two square matrix:

$$A_1 = \begin{pmatrix} (10+2k) & 2\,(1-k) & & & & \\ (1-k) & \ddots & (1-k) & & & \\ & \ddots & \ddots & \ddots & & \\ & & (1-k) & \ddots & (1-k) & \\ & & & 2\,(1-k) & (10+2k) \end{pmatrix}_{N_x \times N_x}$$

$$A_2 = \begin{pmatrix} (10-2k) & 2\,(1+k) & & & & \\ (1+k) & \ddots & (1+k) & & & \\ & \ddots & \ddots & \ddots & & \\ & & (1+k) & \ddots & (1+k) & \\ & & & 2\,(1+k) & (10-2k) \end{pmatrix}_{N_x \times N_x}$$

Given the initial concentration profile at the entrance of an inter-nodes channel C^1, we can deduce the concentration profile along the entire channel seciton by solving (A.6) step by step:

$$\forall n \in [\![1; N_y]\!] \ C^n = \left(A_1^{-1} A_2\right)^{n-1} C^1 \tag{A.7}$$

Appendix B

Experimental Details of Generic Platform

Here, we provide further data on the experimental setting for the droplet formation in the generic chip, the biological strains, the culture medium, the PCR and the laser set-up. Further data on the droplet sizes distribution to support the consistency of the results shown in section 3.1.

B.1   Droplet formation

For droplet formation, a first syringe (SGE–R Analytical Technologies, 1 mL) containing fluorinated oil (FC − 40, 3M Fluoroinert) with 0.5% (w/w) pegylated surfactant (008–FluoroSurfactant, RAN Biotechnologies) was connected to inlet 1 of the microfluidic device. A second syringe (SGE–R Analytical Technologies, 100 μL) containing the cell suspension in 1.5% (w/w) low-gelling agarose (Agarose Type IX, Sigma-Aldrich) was connected to inlet 2, see Fig. 3.2a. The process of droplet formation comprises 3 steps: (i) the chamber is first entirely filled with oil; (ii) the oil flow is stopped and the cell sample is flown in at a flow rate of 10 μL/min, eventually filling the microfluidic chamber entirely; and (iii) the cell sample flow is stopped and a flow of oil pushes the cell sample towards the exit at a flow rate that increases between 10 and 50 μL/min, creating droplets of the cell sample immobilised on each trap, see Fig. 3.2b.

The microfluidic chip was then immersed into a water bath to prevent evaporation (cf 3.1.2), and incubated at 37 °C for the duration of the experiment. In the case of agarose droplets, an additional step was required prior to incubation: the chip was placed at 4 °C during 30 minutes to ensure agarose gelification. After 16 hours at 37 °C, a very conservative estimate of the droplet average volume change shows a 12% decrease in volume, with more than 80% of droplets showing less than a 4% decrease in volume.
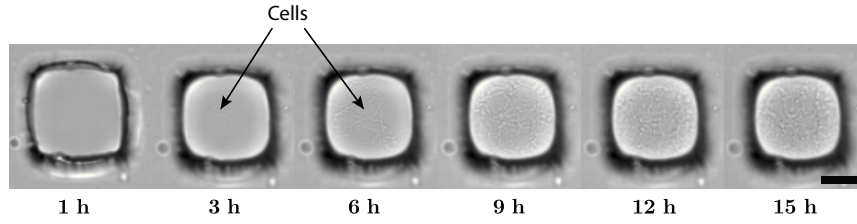
Figure B.1: Bacterial growth in a liquid droplet. Scale bar: 50 μm.

B.2 Bacterial strains, growth and PCR conditions

Four bacterial strains were grown in our device : *Bacillus subtilis* GM2919,[145] *Escherichia coli* HB101 K-12 (pGLO™Bacterial Transformation Kit, Biorad), MG1655 K-12 8372[110] (a kind gift from Zeynep Baharoglu and Didier Mazel, UMR3525, Institut Pasteur, Plasticité du Génome Bactérien, Paris, France) and *Pseudomonas fluorescens* F113 (a kind gift of Claire Prigent-Combaret and Sebastien Renoud, UMR 5557, Ecologie Microbienne Lyon). Cells were grown overnight (180 r.p.m.) in an incubator set at 28°C for *P. fluorescens* and at 37°C for *E. coli* and *B. subtilis*. Luria-Bertani (LB) medium was supplemented with arabinose 0.2% for *E. coli* and the relevant antibiotic as follows: gentamycin 25 μg/mL (*P. fluorescens*), spectinomycin 100 μg/mL (*B. subtilis*), ampicillin 100 μg/mL (*E. coli*). Cell cultures were harvested in late exponential phase and resuspended to a concentration of $1.0 \cdot 10^6$ cells/mL or $1.0 \cdot 10^7$ cells/mL, depending on the number of cells expected per droplets. 15 μL of the cell suspension were mixed with 15 μL of sterile water for liquid droplets, or with 15 μL of a 3% (w/w) low-melting agarose solution for gel droplets.

PCR amplifications of 16S rRNA genes of E. coli strain were done according to the Taq polymerase manufacturer (New England Biolabs, Ipswich, MA) in 25 μL using the 1492r (5'-TACCTTGTTACGACTT) and the 27f (5'-AGAGTTTGATCCTGGCTCAG) primers. The amplification cycle consisted in initial step of 5 min at 98°C; 35 cycles of 10s at 98°C, 15s at 55°Cand 1 min at 72°C; followed by a final elongation step of 2 min at 72°C. Extracted droplets were resuspended in 10 μL of sterile water and 5 μL of the suspension were used as PCR sample.

B.3 Laser Setup

To liquefy the agarose droplets of interest, a continuous infrared laser at $\lambda = 1480$ nm (Fitel Furukawa FOL1424) was mounted on a Nikon TE2000 microscope, such that the laser beam passes through the microscope's objective, as described in Cordero *et al.*[146] The laser position on the microfluidic chip was adjusted in real-time using 2 galvanometric mirrors (Cambridge Technologies 6210H), controlled by a custom-made LabView program.

Appendix C

Estimator for the length of the Key

Here we present a method to estimate the length of the Key, k. We use here the method of moment which is equivalent in this case to the maximum likelihood estimation. Let's take a moment of order 1 to estimate k from the data of m, the number of positive droplets. Let be X_i the random variable that evaluate the presence of K in the droplet i. As in section 3.2, it is defined by the probability law :

$$
\begin{array}{rcl}
\mathbb{P}(X_i = 1) & = & \prod_{j \in K}(1 - e^{-\lambda_j}) \\
\mathbb{P}(X_i = 0) & = & 1 - \prod_{j \in K}(1 - e^{-\lambda_j})
\end{array}
\tag{C.1}
$$

Let's define the function $f : \mathbb{R} \to \mathbb{R}$ such that

$$
k \to f(k) = \mathbb{E}_k[X] = \prod_{j \in K}(1 - e^{-\lambda_j}) = (1 - e^{-\lambda})^k \quad \text{with} \quad \forall j \; \lambda_j = \lambda
\tag{C.2}
$$

Thus, we have $k = f^{-1}\left(\mathbb{E}_k[X]\right)$ and we can define an estimator for k :

$$
\hat{k}_{n_d} = f^{-1}\left(\frac{1}{n_d}\sum_{i=1}^{n_d} X_i\right) = \frac{\ln\left(\frac{m}{n_d}\right)}{\ln\left(1 - e^{-\lambda}\right)}
\tag{C.3}
$$

The property 4.1 demonstrated by Marc Hoffman in *Introduction aux méthodes statistique, Promo 2014 p.81* gives :

$$
\sqrt{n_d}\left(\hat{k}_{n_d} - k\right) \xrightarrow{d} \mathcal{N}\left(0, \frac{1}{f'(k)^2}Var_k(X_1)\right) = \mathcal{N}\left(0, \frac{1}{(\ln(1 - e^{-\lambda}))^2}\left(\frac{1}{(1 - e^{-\lambda})^k} - 1\right)\right)
\tag{C.4}
$$

We can therefore, plot the standard deviation for $\hat{k}_{n_d} - k$ as a function of λ for various concentration and compare it to 1 in order to know the error on k made by the data of
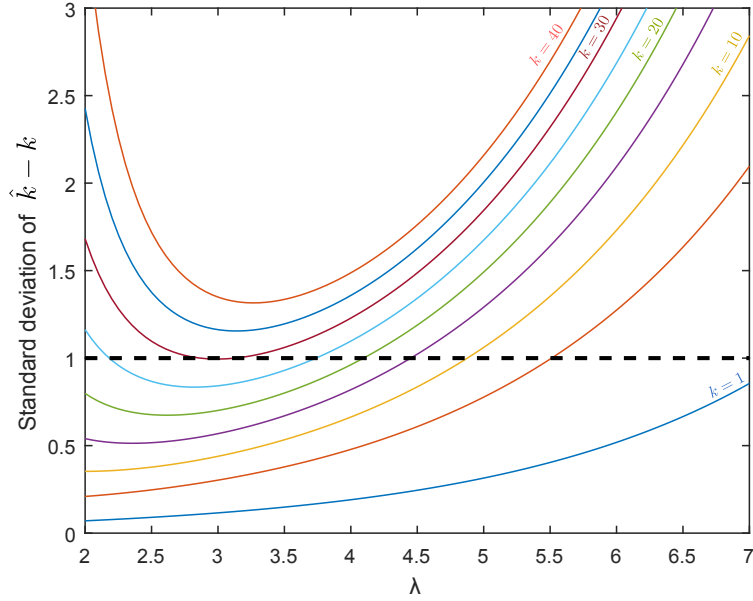
Figure C.1: Error made on k by taking the value of $\hat{k}_{n_d}$.

$\hat{k}_{n_d}$. Figure C.1 shows the error made on k by taking the value of $\hat{k}_{n_d}$. The optimum case correspond to $3\sigma(\hat{k}_{n_d} - k) < 1$, such that we are sure to have the exact number for k.

As the λ_i are unknown, we can assume that they are close enough to have $\mathbb{P}(X = 1) \sim (1 - e^{-\lambda})^k$. By loading two chips with two different optical densities OD_1 and OD_2, we will have m_1 and m_2 the number of positively droplets for chip 1 and 2 respectively. As the combination is naturally fixed to a single value, we should have $\hat{k}_{1n_d} \sim \hat{k}_{2n_d}$. By using the ratio $q = \frac{OD_2}{OD_1}$, we can deduce λ with

$$\frac{\ln\left(\frac{m_1}{n_d}\right)}{\ln\left(1 - e^{-\lambda}\right)} = \frac{\ln\left(\frac{m_2}{n_d}\right)}{\ln\left(1 - e^{-q\lambda}\right)} \tag{C.5}$$

Appendix D

Growth Parameters Correlations

D.1 Cross-plots of growth parameters

Here we present the cross-plots between the main growth parameters where no particular correlations are found.

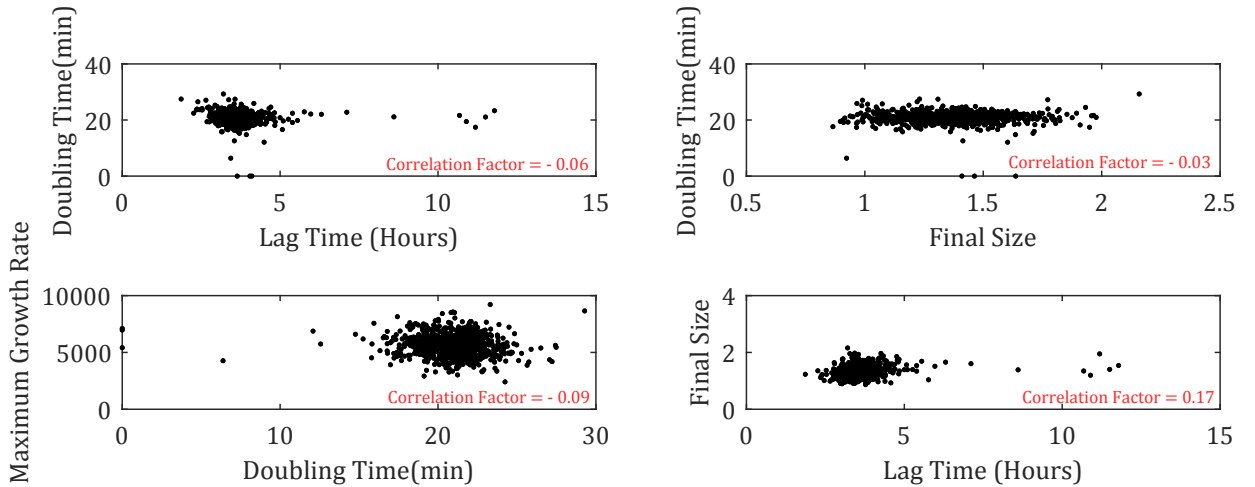Figure D.1: Cross-plots of the growth parameters for *B.Subtilis*. No correlation are found between the presented growth parameters with most of the correlation factors are around 0.

D.2 Sub-population identification

The growth parameters enable not only a mapping of the population members physiological characteristics but also the discrimination of several sub-populations in the case of bacterial

interaction or environments leading to growth heterogeneity. Similarly to our study on bacteria interaction through the digital analysis (cf section 3.2.3), we loaded *P.fluorescens* cells with *E.coli* pGlo in a generic chip with culture medium. These strain have been chosen as they are known to have competitive interactions (cf section 3.2.3) that will result in their growth modification. The objective is to use the dynamical growth parameters of *P.fluorescens* to identify droplets where there is a co-localisation with *E.coli*. Both strains can synthesise fluorescent proteins (RFP for *P.fluorescens* and GFP for *E.coli*) such that each strain growth curves are followed independently and we can confirm our results. *P.fluorescens* has been loaded with an initial concentration 4 times higher than *E.coli* concentration such that *P.fluorescens* are present in 1459 and *E.coli* in 366 droplets with 340 droplets containing both strains.
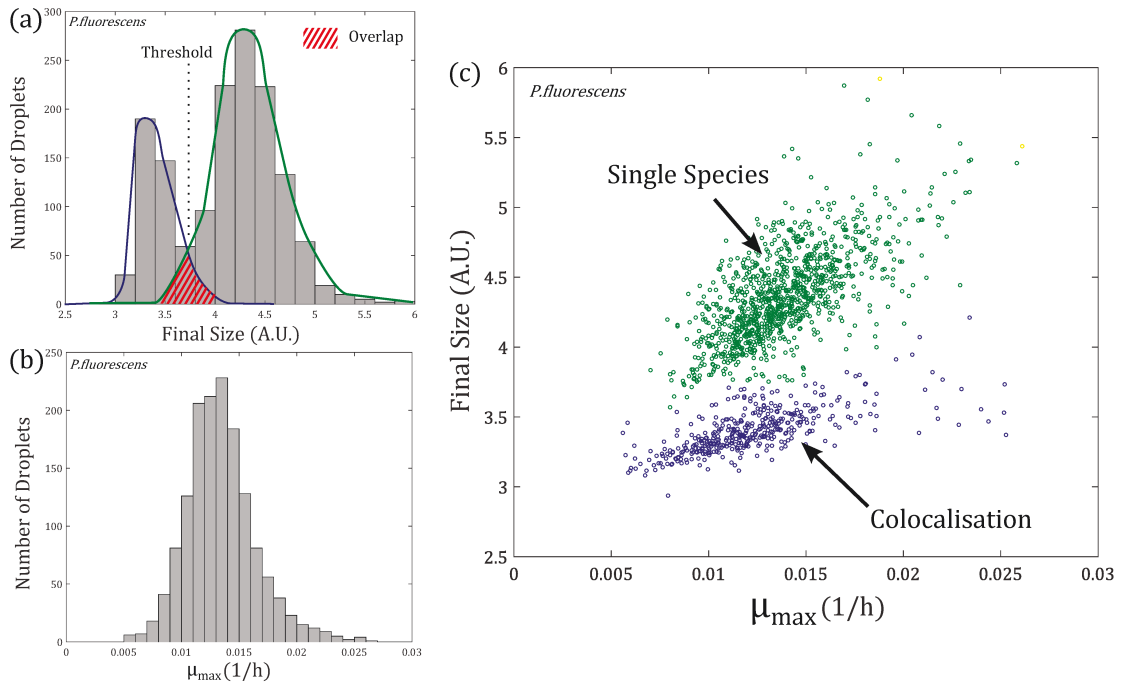
Figure D.2: *P.fluorescens* co-cultivated with *E.coli* pGlo. a) Histogram of the final colony size with the overlapping zone of the two sub-population distributions for *P.fluorescens*. b) Histogram of the specific growth rate for *P.fluorescens*. c) Cross-plot between the specific growth rate and the final colony size for *P.fluorescens* with the clustering result using a hierarchical clustering method with an euclidean distance. The green circles corresponds to droplets containing solely *P.fluorescens*, while the blue circles result from co-localisation of both *P.fluorescens* and *E.coli* in the same droplet.

An end-point measurement gives access to solely the distribution of the final size as shown in figure D.2a. Two peaks are identifiable and indicate the presence of two sub-populations. The simple method to discriminate the two sub-populations is the use of threshold value setting the delimitation between co-localisation and single species droplets. Yet, the two sub-population distributions overlap, which means that an amount of colonies with similar

final sizes can be either in co-localisation or alone in their droplet, see red stripes zone in figure D.2a. Although the presence of two sub-populations cannot be similarly observed on the specific growth rates distribution as shown in figure D.2b, the cross-plot of the final colony sizes with the specific growth rates exhibits two distinguishable groups of points (Fig. D.2c) corresponding to the two sub-populations. Using a hierarchical clustering algorithm with an euclidean distance, the two sub-populations are separated such that we obtain the indexes of wells contained in each sub-population group. Using the two fluorescent signals, we verified afterwards that the blue circles correspond to co-localisation droplets while the green circles belongs to single species droplets.

We estimate the error made with the threshold technique compared to the clustering of the growth parameters technique. It results that, for this particular example, 43 droplets were wrongly addressed by the threshold technique. This means that the threshold technique is rather accurate. The clustering technique developed above can nevertheless be useful in more complex or tricky situations, e.g. if the two peaks observed in the final size distribution are closer, the overlapping region would be larger which yields an increase of the error made with the threshold technique.

Finally, we used here two-dimensional cross-plot because it was sufficient to separate the population but any number of growth parameters could have been used and more clusters could have been sought in more complex environment.

Bibliography

[1] UNGER M.A., CHOU H.P., THORSEN T., SCHERER A., & QUAKE S.R. Monolithic microfabricated valves and pumps by multilayer soft lithography. *Science*, **288**(5463):113, 2000

[2] DERTINGER S.K., CHIU D.T., JEON N.L., & WHITESIDES G.M. Generation of gradients having complex shapes using microfluidic networks. *Analytical Chemistry*, **73**(6):1240, 2001

[3] HOLDEN M.A., KUMAR S., CASTELLANA E.T., BESKOK A., & CREMER P.S. Generating fixed concentration arrays in a microfluidic device. *Sensors and Actuators B: Chemical*, **92**(1):199, 2003

[4] SAADI W., RHEE S.W., LIN F., VAHIDI B., CHUNG B.G., & JEON N.L. Generation of stable concentration gradients in 2d and 3d environments using a microfluidic ladder chamber. *Biomedical microdevices*, **9**(5):627, 2007

[5] MILLER O.J., EL HARRAK A., MANGEAT T., BARET J.C., FRENZ L., EL DEBS B., MAYOT E., SAMUELS M.L., ROONEY E.K., DIEU P. *et al.* High-resolution dose–response screening using droplet-based microfluidics. *Proceedings of the National Academy of Sciences*, **109**(2):378, 2012

[6] HUFT J., HAYNES C.A., & HANSEN C.L. Microfluidic integration of parallel solid-phase liquid chromatography. *Analytical chemistry*, **85**(5):2999, 2013

[7] THORSEN T., ROBERTS R.W., ARNOLD F.H., & QUAKE S.R. Dynamic Pattern Formation in a Vesicle-Generating Microfluidic Device. *Physical Review Letters*, **86**(18):4163, 2001

[8] GAÑÁN-CALVO A.M. & GORDILLO J.M. Perfectly Monodisperse Microbubbling by Capillary Flow Focusing. *Physical Review Letters*, **87**(27):274501, 2001

[9] ANNA S.L., BONTOUX N., & STONE H.A. Formation of dispersions using "flow focusing" in microchannels. *Applied Physics Letters*, **82**(3):364, 2003

[10] AHN K., KERBAGE C., HYNT T., WESTERVELT R., LINK D., & WEITZ D. Dielectrophoretic manipulation of drops for high-speed microfluidic sorting devices. *Applied Physics Letters*, **88**:024104, 2006

[11] CORDERO M.L., BURNHAM D.R., BAROUD C.N., & MCGLOIN D. Thermocapillary manipulation of droplets using holographic beam shaping: Microfluidic pin ball. *Applied Physics Letters*, **93**(3):034107, 2008

[12] FRANKE T., ABATE A.R., WEITZ D.A., & WIXFORTH A. Surface acoustic wave (SAW) directed droplet flow in microfluidics for PDMS devices. *Lab on a Chip*, **9**(18):2625, 2009

[13] BAROUD C., GALLAIRE F., & DANGLA R. Dynamics of microfluidic droplets. *Lab on a Chip*, **10**(16):2032, 2010

[14] SEEMANN R., BRINKMANN M., PFOHL T., & HERMINGHAUS S. Droplet based microfluidics. *Reports on Progress in Physics*, **75**(1):016601, 2012

[15] AGRESTI J.J., ANTIPOV E., ABATE A.R., AHN K., ROWAT A.C., BARET J.C., MARQUEZ M., KLIBANOV A.M., GRIFFITHS A.D., & WEITZ D.A. Ultrahigh-throughput screening in drop-based microfluidics for directed evolution. *Proceedings of the National Academy of Sciences of the United States of America*, **107**(9):4004, 2010

[16] BECKER H. Hype, hope and hubris: the quest for the killer application in microfluidics. *Lab on a Chip*, **9**(15):2119, 2009

[17] THORSEN T., MAERKL S.J., & QUAKE S.R. Microfluidic large-scale integration. *Science (New York, N.Y.)*, **298**(5593):580, 2002

[18] POLLACK M.G., FAIR R.B., & SHENDEROV A.D. Electrowetting-based actuation of liquid droplets for microfluidic applications. *Applied Physics Letters*, **77**(11):1725, 2000

[19] CHO S.K., MOON H., & KIM C.J. Creating, transporting, cutting, and merging liquid droplets by electrowetting-based actuation for digital microfluidic circuits. *Journal of microelectromechanical systems*, **12**(1):70, 2003

[20] ABDELGAWAD M., FREIRE S.L., YANG H., & WHEELER A.R. All-terrain droplet actuation. *Lab on a Chip*, **8**(5):672, 2008

[21] SACKMANN E.K., FULTON A.L., & BEEBE D.J. The present and future role of microfluidics in biomedical research. *Nature*, **507**(7491):181, 2014

[22] KAMINSKI T.S., SCHELER O., & GARSTECKI P. Droplet microfluidics for microbiology: techniques, applications and challenges. *Lab on a Chip*, **16**(12):2168, 2016

[23] KORCZYK P.M., DERZSI L., JAKIEŁA S., & GARSTECKI P. Microfluidic traps for hard-wired operations on droplets. *Lab on a Chip*, **13**(20):4096, 2013

[24] KREUTZ J.E., MUNSON T., HUYNH T., SHEN F., DU W., & ISMAGILOV R.F. Theoretical design and analysis of multivolume digital assays with wide dynamic

range validated experimentally with microfluidic digital pcr. *Analytical chemistry*, **83**(21):8158, 2011

[25] SCHNEIDER T., YEN G.S., THOMPSON A.M., BURNHAM D.R., & CHIU D.T. Self-Digitization of Samples into a High-Density Microfluidic Bottom-Well Array. *Analytical Chemistry*, **85**(21):10417, 2013

[26] CASAVANT B.P., BERTHIER E., THEBERGE A.B., BERTHIER J., MONTANEZ-SAURI S.I., BISCHEL L.L., BRAKKE K., HEDMAN C.J., BUSHMAN W., KELLER N.P., & BEEBE D.J. Suspended microfluidics. *Proceedings of the National Academy of Sciences*, **110**(25):10111, 2013

[27] DANGLA R., KAYI S.C., & BAROUD C.N. Droplet microfluidics driven by gradients of confinement. *Proceedings of the National Academy of Sciences of the United States of America*, **110**(3):853, 2013

[28] AMSELEM G., BRUN P., GALLAIRE F., & BAROUD C.N. Breaking anchored droplets in a microfluidic hele-shaw cell. *Physical Review Applied*, **3**(5):054006, 2015

[29] DU Y., SHIM J., VIDULA M., HANCOCK M.J., LO E., CHUNG B.G., BORENSTEIN J.T., KHABIRY M., CROPEK D.M., & KHADEMHOSSEINI A. Rapid generation of spatially and temporally controllable long-range concentration gradients in a microfluidic device. *Lab on a Chip*, **9**(6):761, 2009

[30] COHEN D.E., SCHNEIDER T., WANG M., & CHIU D.T. Self-digitization of sample volumes. *Analytical chemistry*, **82**(13):5707, 2010

[31] CHOI C.H., JUNG J.H., RHEE Y.W., KIM D.P., SHIM S.E., & LEE C.S. Generation of monodisperse alginate microbeads and in situ encapsulation of cell in microfluidic device. *Biomedical microdevices*, **9**(6):855, 2007

[32] SHIM J.U., OLGUIN L.F., WHYTE G., SCOTT D., BABTIE A., ABELL C., HUCK W.T., & HOLLFELDER F. Simultaneous determination of gene expression and enzymatic activity in individual bacterial cells in microdroplet compartments. *Journal of the American Chemical Society*, **131**(42):15251, 2009

[33] SCHMITZ C.H., ROWAT A.C., KÖSTER S., & WEITZ D.A. Dropspots: a picoliter array in a microfluidic device. *Lab on a Chip*, **9**(1):44, 2009

[34] COHEN D.E., SCHNEIDER T., WANG M., & CHIU D.T. Self-digitization of sample volumes. *Analytical chemistry*, **82**(13):5707, 2010

[35] SUN M., BITHI S.S., & VANAPALLI S.A. Microfluidic static droplet arrays with tuneable gradients in material composition. *Lab on a Chip*, **11**(23):3949, 2011

[36] DERZSI L., KAMINSKI T.S., & GARSTECKI P. Antibiograms in five pipetting steps: precise dilution assays in sub-microliter volumes with a conventional pipette. *Lab on a Chip*, **16**(5):893, 2016

[37] Huebner A., Bratton D., Whyte G., Yang M., deMello A., Abell C., & Hollfelder F. Static microdroplet arrays: a microfluidic device for droplet trapping, incubation and release for enzymatic and cell-based assays. *Lab on a Chip*, **9**(5):692, 2009

[38] Abbyad P., Dangla R., Alexandrou A., & Baroud C.N. Rails and anchors: guiding and trapping droplet microreactors in two dimensions. *Lab on a Chip*, **11**(5):813, 2011

[39] Pan J., Stephenson A.L., Kazamia E., Huck W.T., Dennis J.S., Smith A.G., & Abell C. Quantitative tracking of the growth of individual algal cells in microdroplet compartments. *Integrative Biology*, **3**(10):1043, 2011

[40] Joensson H.N. & Andersson Svahn H. Droplet microfluidics–a tool for single-cell analysis. *Angewandte Chemie (International ed. in English)*, **51**(49):12176, 2012

[41] Boitard L., Cottinet D., Kleinschmitt C., Bremond N., Baudry J., Yvert G., & Bibette J. Monitoring single-cell bioenergetics via the coarsening of emulsion droplets. *Proceedings of the National Academy of Sciences*, **109**(19):7181, 2012

[42] Dusny C. & Schmid A. Microfluidic single-cell analysis links boundary environments and individual microbial phenotypes. *Environmental microbiology*, **17**(6):1839, 2015

[43] Wang P., Robert L., Pelletier J., Dang W.L., Taddei F., Wright A., & Jun S. Robust growth of escherichia coli. *Current biology*, **20**(12):1099, 2010

[44] Taheri-Araghi S., Bradde S., Sauls J.T., Hill N.S., Levin P.A., Paulsson J., Vergassola M., & Jun S. Cell-size control and homeostasis in bacteria. *Current Biology*, **25**(3):385, 2015

[45] Churski K., Kaminski T.S., Jakiela S., Kamysz W., Baranska-Rybak W., Weibel D.B., & Garstecki P. Rapid screening of antibiotic toxicity in an automated microdroplet system. *Lab on a Chip*, **12**(9):1629, 2012

[46] Baraban L., Bertholle F., Salverda M.L., Bremond N., Panizza P., Baudry J., de Visser J.A.G., & Bibette J. Millifluidic droplet analyser for microbiology. *Lab on a Chip*, **11**(23):4057, 2011

[47] Jeong H.H., Jin S.H., Lee B.J., Kim T., & Lee C.S. Microfluidic static droplet array for analyzing microbial communication on a population gradient. *Lab on a Chip*, **15**(3):889, 2015

[48] Boedicker J.Q., Vincent M.E., & Ismagilov R.F. Microfluidic Confinement of Single Cells of Bacteria in Small Volumes Initiates High-Density Behavior of Quorum Sensing and Growth and Reveals Its Variability. *Angewandte Chemie International Edition*, **48**(32):5908, 2009

[49] Jiang L., Boitard L., Broyer P., Chareire A.C., Bourne-Branchu P., Mahé P., Tournoud M., Franceschi C., Zambardi G., Baudry J. *et al.* Digital antimicrobial susceptibility testing using the millidrop technology. *European Journal of Clinical Microbiology & Infectious Diseases*, **35**(3):415, 2016

[50] Leung K., Zahn H., Leaver T., Konwar K.M., Hanson N.W., Pagé A.P., Lo C.C., Chain P.S., Hallam S.J., & Hansen C.L. A programmable droplet-based microfluidic device applied to multiparameter analysis of single microbes and microbial communities. *Proceedings of the National Academy of Sciences*, **109**(20):7665, 2012

[51] Cottinet D., Condamine F., Bremond N., Griffiths A.D., Rainey P.B., de Visser J.A.G., Baudry J., & Bibette J. Lineage tracking for probing heritable phenotypes at single-cell resolution. *PloS one*, **11**(4):e0152395, 2016

[52] Dangla R., Lee S., & Baroud C.N. Trapping microfluidic drops in wells of surface energy. *Physical review letters*, **107**(12):124501, 2011

[53] Guermonprez C., Michelin S., & Baroud C.N. Flow distribution in parallel microfluidic networks and its effect on concentration gradient. *Biomicrofluidics*, **9**(5):054119, 2015

[54] Amselem G., Guermonprez C., Drogue B., Michelin S., & Baroud C.N. Universal microfluidic platform for bioassays in anchored droplets. *Lab on a Chip*, 2016

[55] Sip C.G., Bhattacharjee N., & Folch A. A modular cell culture device for generating arrays of gradients using stacked microfluidic flows. *Biomicrofluidics*, **5**:022210, 2011

[56] Laval P., Lisai N., Salmon J., & Joanicot M. A microfluidic device based on droplet storage for screening solubility diagrams. *Lab Chip*, **7**(7):829, 2007

[57] Cai L.F., Zhu Y., Du G.S., & Fang Q. Droplet-based microfluidic flow injection system with large-scale concentration gradient by a single nanoliter-scale injection for enzyme inhibition assay. *Analytical Chemistry*, **84**(1):446, 2011

[58] Fradet E., Abbyad P., Vos M.H., & Baroud C.N. Parallel measurements of reaction kinetics using ultralow-volumes. *Lab on a Chip*, **13**(22):4326, 2013

[59] Niu X., Gielen F., Edel J.B. *et al.* A microdroplet dilutor for high-throughput screening. *Nature chemistry*, **3**(6):437, 2011

[60] Sun M. & Vanapalli S.A. Generation of chemical concentration gradients in mobile droplet arrays via fragmentation of long immiscible diluting plugs. *Analytical chemistry*, **85**(4):2044, 2013

[61] MILLER O.J., HARRAK A.E., MANGEAT T., BARET J.C., FRENZ L., DEBS B.E., MAYOT E., SAMUELS M.L., ROONEY E.K., DIEU P., GALVAN M., LINK D.R., & GRIFFITHS A.D. High-resolution dose-response screening using droplet-based microfluidics. *Proceedings of the National Academy of Sciences*, **109**(2):378, 2012

[62] JEON N.L., DERTINGER S.K., CHIU D.T., CHOI I.S., STROOCK A.D., & WHITE-SIDES G.M. Generation of solution and surface gradients using microfluidic systems. *Langmuir*, **16**(22):8311, 2000

[63] IRIMIA D., LIU S.Y., THARP W.G., SAMADANI A., TONER M., & POZNAN-SKY M.C. Microfluidic system for measuring neutrophil migratory responses to fast switches of chemical gradients. *Lab on a Chip*, **6**(2):191, 2006

[64] HU Y., ZHANG X., & WANG W. Simulation of the generation of solution gradients in microfluidic systems using the lattice boltzmann method. *Industrial & Engineering Chemistry Research*, **50**(24):13932, 2011

[65] SELIMOVIĆ S., SIM W.Y., KIM S.B., JANG Y.H., LEE W.G., KHABIRY M., BAE H., JAMBOVANE S., HONG J.W., & KHADEMHOSSEINI A. Generating nonlinear concentration gradients in microfluidic devices for cell studies. *Analytical Chemistry*, **83**(6):2020, 2011

[66] FRADET E., MCDOUGALL C., ABBYAD P., DANGLA R., MCGLOIN D., & BAROUD C.N. Combining rails and anchors with laser forcing for selective manipulation within 2d droplet arrays. *Lab on a Chip*, **11**(24):4228, 2011

[67] MORTENSEN N.A., OKKELS F., & BRUUS H. Reexamination of hagen-poiseuille flow: Shape dependence of the hydraulic resistance in microchannels. *Physicak Review E*, **71**(5):057301, 2005

[68] CORDERO M.L., VERNEUIL E., GALLAIRE F., & BAROUD C.N. Time-resolved temperature rise in a thin liquid film due to laser absorption. *Physical Review E*, **79**(1):011201, 2009

[69] DANGLA R., KAYI S., & BAROUD C. Droplet microfluidics driven by gradients of confinement. *Proceedings of the National Acadademy of Sciences of the United States of America*, **110**(3):853, 2013

[70] FUJIKAWA H. & MATSUSHITA M. Fractal growth of bacillus subtilis on agar plates. *Journal of the physical society of japan*, **58**(11):3875, 1989

[71] MONOD J. The growth of bacterial cultures. *Annual Reviews in Microbiology*, **3**(1):371, 1949

[72] BRENNAN M.D., REXIUS-HALL M.L., ELGASS L.J., & EDDINGTON D.T. Oxygen control with microfluidics. *Lab on a Chip*, **14**(22):4305, 2014

[73] Zimmermann H.F., Anderlei T., Büchs J., & Binder M. Oxygen limitation is a pitfall during screening for industrial strains. *Applied microbiology and biotechnology*, **72**(6):1157, 2006

[74] Mahler L., Tovar M., Weber T., Brandes S., Rudolph M.M., Ehgartner J., Mayr T., Figge M.T., Roth M., & Zang E. Enhanced and homogeneous oxygen availability during incubation of microfluidic droplets. *RSC Advances*, **5**(123):101871, 2015

[75] Abbyad P., Tharaux P.L., Martin J.L., Baroud C.N., & Alexandrou A. Sickling of red blood cells through rapid oxygen exchange in microfluidic drops. *Lab on a Chip*, **10**(19):2505, 2010

[76] Li L., Xiao Z., Tan S., Pu L., & Zhang Z. Composite pdms membrane with high flux for the separation of organics from water by pervaporation. *Journal of Membrane Science*, **243**(1):177, 2004

[77] Merlin A., Salmon J.B., & Leng J. Microfluidic-assisted growth of colloidal crystals. *Soft Matter*, **8**(13):3526, 2012

[78] Breed R.S. & Dotterrer W.D. The Number of Colonies Allowable on Satisfactory Agar Plates. *Journal of bacteriology*, **1**(3):321, 1916

[79] Najah M., Griffiths A.D., & Ryckelynck M. Teaching single-cell digital analysis using droplet-based microfluidics. *Analytical chemistry*, **84**(3):1202, 2012

[80] Vogelstein B. & Kinzler K. Digital pcr. *Proc. Nat. Acad. Sci., USA*, **96**(16):9236, 1999

[81] Fradet E., McDougall C., Abbyad P., Dangla R., McGloin D., & Baroud C.N. Combining rails and anchors with laser forcing for selective manipulation within 2D droplet arrays. *Lab on a Chip*, **11**(24):4228, 2011

[82] Dube S., Qin J., & Ramakrishnan R. Mathematical analysis of copy number variation in a DNA sample using digital PCR on a nanofluidic device. *PLoS ONE*, **3**(8):1, 2008

[83] Le Cam L. *et al.* An approximation theorem for the poisson binomial distribution. *Pacific J. Math*, **10**(4):1181, 1960

[84] Lee J.H., Wood T.K., & Lee J. Roles of indole as an interspecies and interkingdom signaling molecule. *Trends in microbiology*, **23**(11):707, 2015

[85] Schnupf P., Gaboriau-Routhiau V., Gros M., Friedman R., Moya-Nilges M., Nigro G., Cerf-Bensussan N., & Sansonetti P.J. Growth and host interaction of mouse segmented filamentous bacteria in vitro. *Nature*, **520**(7545):99, 2015

[86] Dhar N. & McKinney J.D. Microbial phenotypic heterogeneity and antibiotic tolerance. *Current opinion in microbiology*, **10**(1):30, 2007

[87] Balaban N.Q., Merrin J., Chait R., Kowalik L., & Leibler S. Bacterial persistence as a phenotypic switch. *Science*, **305**(5690):1622, 2004

[88] Helaine S. & Kugelberg E. Bacterial persisters: formation, eradication, and experimental systems. *Trends in microbiology*, **22**(7):417, 2014

[89] Delbrück M. Statistical fluctuations in autocatalytic reactions. *The Journal of Chemical Physics*, **8**(1):120, 1940

[90] Cassin M.H., Lammerding A.M., Todd E.C., Ross W., & McColl R.S. Quantitative risk assessment for escherichia coli o157: H7 in ground beef hamburgers. *International journal of food microbiology*, **41**(1):21, 1998

[91] Nauta M.J. Modelling bacterial growth in quantitative microbiological risk assessment: is it possible? *International Journal of Food Microbiology*, **73**(2):297, 2002

[92] Scott M., Gunderson C.W., Mateescu E.M., Zhang Z., & Hwa T. Interdependence of cell growth and gene expression: origins and consequences. *Science*, **330**(6007):1099, 2010

[93] Zwietering M., Jongenburger I., Rombouts F., & Van't Riet K. Modeling of the bacterial growth curve. *Applied and environmental microbiology*, **56**(6):1875, 1990

[94] Baranyi J. & Pin C. Estimating bacterial growth parameters by means of detection times. *Applied and Environmental Microbiology*, **65**(2):732, 1999

[95] Swinnen I., Bernaerts K., Dens E.J., Geeraerd A.H., & Van Impe J. Predictive modelling of the microbial lag phase: a review. *International journal of food microbiology*, **94**(2):137, 2004

[96] Baranyi J. & Roberts T.A. A dynamic approach to predicting bacterial growth in food. *International Journal of Food Microbiology*, **23**(3-4):277, 1994

[97] Baranyi J., Roberts T., & McClure P. A non-autonomous differential equation to modelbacterial growth. *Food Microbiology*, **10**(1):43, 1993

[98] Perni S., Andrew P.W., & Shama G. Estimating the maximum growth rate from microbial growth curves: definition is everything. *Food microbiology*, **22**(6):491, 2005

[99] Allen L.J. *An introduction to stochastic processes with applications to biology.* CRC Press, 2010

[100] Comparison of stochastic and deterministic concepts of bacterial lag. *Journal of Theoretical Biology*, **192**(3):403, 1998

[101] KOUTSOUMANIS K.P. & LIANOU A. Stochasticity in colonial growth dynamics of individual bacterial cells. *Applied and environmental microbiology*, **79**(7):2294, 2013

[102] BAEV M.V., BAEV D., RADEK A.J., & CAMPBELL J.W. Growth of escherichia coli mg1655 on lb medium: monitoring utilization of sugars, alcohols, and organic acids with transcriptional microarrays. *Applied microbiology and biotechnology*, **71**(3):310, 2006

[103] BAEV M.V., BAEV D., RADEK A.J., & CAMPBELL J.W. Growth of escherichia coli mg1655 on lb medium: monitoring utilization of amino acids, peptides, and nucleotides with transcriptional microarrays. *Applied microbiology and biotechnology*, **71**(3):317, 2006

[104] BAEV M.V., BAEV D., RADEK A.J., & CAMPBELL J.W. Growth of escherichia coli mg1655 on lb medium: determining metabolic strategy with transcriptional microarrays. *Applied microbiology and biotechnology*, **71**(3):323, 2006

[105] MANINA G., DHAR N., & MCKINNEY J.D. Stress and host immunity amplify mycobacterium tuberculosis phenotypic heterogeneity and induce nongrowing metabolically active forms. *Cell host & microbe*, **17**(1):32, 2015

[106] BOITARD L., COTTINET D., BREMOND N., BAUDRY J., & BIBETTE J. Growing microbes in millifluidic droplets. *Engineering in Life Sciences*, **15**(3):318, 2015

[107] FUKUDA K. Antimicrobila resistance : Global report surveillance, who, 2014. Online; accessed 29 January 2014

[108] O'NEILL J. Antimicrobial resistance: Tackling a crisis for the health and wealth of nations. the review on antimicrobial resistance. 2014 dec

[109] ANDERSSON D.I. & HUGHES D. Microbiological effects of sublethal levels of antibiotics. *Nature Reviews Microbiology*, **12**(7):465, 2014

[110] BAHAROGLU Z., KRIN E., & MAZEL D. Connecting environment and genome plasticity in the characterization of transformation-induced sos regulation and carbon catabolite control of the vibrio cholerae integron integrase. *Journal of bacteriology*, **194**(7):1659, 2012

[111] DAVIS B.D. Mechanism of bactericidal action of aminoglycosides. *Microbiological reviews*, **51**(3):341, 1987

[112] RELLER L.B., WEINSTEIN M., JORGENSEN J.H., & FERRARO M.J. Antimicrobial susceptibility testing: a review of general principles and contemporary practices. *Clinical infectious diseases*, **49**(11):1749, 2009

[113] STOCK I. & WIEDEMANN B. Natural antibiotic susceptibility of escherichia coli, shigella, e. vulneris, and e. hermannii strains. *Diagnostic microbiology and infectious disease*, **33**(3):187, 1999

[114] BIGGER J.W. The bactericidal action of penicillin on staphylococcus pyogenes. *Irish Journal of Medical Science (1926-1967)*, **19**(11):553, 1944

[115] EAGLE H., FLEISCHMAN R., & LEVY M. Continuous vs. discontinuous therapy with penicillin: the effect of the interval between injections on therapeutic efficacy. *New England journal of medicine*, **248**(12):481, 1953

[116] BUNDTZEN R.W., GERBER A.U., COHN D.L., & CRAIG W.A. Postantibiotic suppression of bacterial growth. *Review of Infectious Diseases*, **3**(1):28, 1981

[117] ISAKSSON B., NILSSON L., MALLER R., SÖR L. *et al.* Postantibiotic effect of aminoglycosides on gram-negative bacteria evaluated by a new method. *Journal of Antimicrobial Chemotherapy*, **22**(1):23, 1988

[118] KWAN B.W., VALENTA J.A., BENEDIK M.J., & WOOD T.K. Arrested protein synthesis increases persister-like cell formation. *Antimicrobial agents and chemotherapy*, **57**(3):1468, 2013

[119] FRIDMAN O., GOLDBERG A., RONIN I., SHORESH N., & BALABAN N.Q. Optimization of lag time underlies antibiotic tolerance in evolved bacterial populations. *Nature*, **513**(7518):418, 2014

[120] TUOMANEN E., COZENS R., TOSCH W., ZAK O., & TOMASZ A. The rate of killing of escherichia coli by β-lactam antibiotics is strictly proportional to the rate of bacterial growth. *Microbiology*, **132**(5):1297, 1986

[121] COZENS R., TUOMANEN E., TOSCH W., ZAK O., SUTER J., & TOMASZ A. Evaluation of the bactericidal activity of beta-lactam antibiotics on slowly growing bacteria cultured in the chemostat. *Antimicrobial Agents and Chemotherapy*, **29**(5):797, 1986

[122] BROWN M., COLLIER P.J., & GILBERT P. Influence of growth rate on susceptibility to antimicrobial agents: modification of the cell envelope and batch and continuous culture studies. *Antimicrobial agents and chemotherapy*, **34**(9):1623, 1990

[123] GREULICH P., SCOTT M., EVANS M.R., & ALLEN R.J. Growth-dependent bacterial susceptibility to ribosome-targeting antibiotics. *Molecular systems biology*, **11**(3):796, 2015

[124] DERIS J.B., KIM M., ZHANG Z., OKANO H., HERMSEN R., GROISMAN A., & HWA T. The innate growth bistability and fitness landscapes of antibiotic-resistant bacteria. *Science*, **342**(6162):1237435, 2013

[125] AZAM T.A., IWATA A., NISHIMURA A., UEDA S., & ISHIHAMA A. Growth phase-dependent variation in protein composition of the escherichia coli nucleoid. *Journal of bacteriology*, **181**(20):6361, 1999

[126] WADA A., MIKKOLA R., KURLAND C.G., & ISHIHAMA A. Growth phase-coupled changes of the ribosome profile in natural isolates and laboratory strains of escherichia coli. *Journal of bacteriology*, **182**(10):2893, 2000

[127] Maki Y., Yoshida H., & Wada A. Two proteins, yfia and yhbh, associated with resting ribosomes in stationary phase escherichia coli. *Genes to cells*, **5**(12):965, 2000

[128] Meredith H.R., Srimani J.K., Lee A.J., Lopatkin A.J., & You L. Collective antibiotic tolerance: mechanisms, dynamics and intervention. *Nature chemical biology*, **11**(3):182, 2015

[129] Lebeaux D., Ghigo J.M., & Beloin C. Biofilm-related infections: bridging the gap between clinical management and fundamental aspects of recalcitrance toward antibiotics. *Microbiology and Molecular Biology Reviews*, **78**(3):510, 2014

[130] Lewis K. Multidrug tolerance of biofilms and persister cells. In *Bacterial Biofilms*, pp. 107–131. Springer, 2008

[131] Boedicker J.Q., Li L., Kline T.R., & Ismagilov R.F. Detecting bacteria and determining their susceptibility to antibiotics by stochastic confinement in nanoliter droplets using plug-based microfluidics. *Lab on a Chip*, **8**(8):1265, 2008

[132] DeLong E.F. Microbial community genomics in the ocean. *Nature Reviews Microbiology*, **3**(6):459, 2005

[133] Daniel R. The metagenomics of soil. *Nature Reviews Microbiology*, **3**(6):470, 2005

[134] Preidis G.A. & Versalovic J. Targeting the human microbiome with antibiotics, probiotics, and prebiotics: gastroenterology enters the metagenomics era. *Gastroenterology*, **136**(6):2015, 2009

[135] Allesina S. & Tang S. Stability criteria for complex ecosystems. *Nature*, **483**(7388):205, 2012

[136] Coyte K.Z., Schluter J., & Foster K.R. The ecology of the microbiome: Networks, competition, and stability. *Science*, **350**(6261):663, 2015

[137] Korkut A., Wang W., Demir E., Aksoy B.A., Jing X., Molinelli E.J., Babur Ö., Bemis D.L., Sumer S.O., Solit D.B. *et al.* Perturbation biology nominates upstream–downstream drug combinations in raf inhibitor resistant melanoma cells. *eLife*, **4**:e04640, 2015

[138] Hooper L.V., Littman D.R., & Macpherson A.J. Interactions between the microbiota and the immune system. *Science*, **336**(6086):1268, 2012

[139] Cebra J.J. Influences of microbiota on intestinal immune system development. *The American journal of clinical nutrition*, **69**(5):1046s, 1999

[140] Round J.L. & Mazmanian S.K. The gut microbiota shapes intestinal immune responses during health and disease. *Nature Reviews Immunology*, **9**(5):313, 2009

[141] Grice E.A., Kong H.H., Conlan S., Deming C.B., Davis J., Young A.C., Bouffard G.G., Blakesley R.W., Murray P.R., Green E.D. *et al.*

Topographical and temporal diversity of the human skin microbiome. *science*, **324**(5931):1190, 2009

[142] Cryan J.F. & Dinan T.G. Mind-altering microorganisms: the impact of the gut microbiota on brain and behaviour. *Nature reviews neuroscience*, **13**(10):701, 2012

[143] Dominguez-Bello M.G., Blaser M.J., Ley R.E., & Knight R. Development of the human gastrointestinal microbiota and insights from high-throughput sequencing. *Gastroenterology*, **140**(6):1713, 2011

[144] Claesson M.J., Jeffery I.B., Conde S., Power S.E., O'Connor E.M., Cusack S., Harris H.M., Coakley M., Lakshminarayanan B., O'Sullivan O. *et al.* Gut microbiota composition correlates with diet and health in the elderly. *Nature*, **488**(7410):178, 2012

[145] Ferguson M.L., Le Coq D., Jules M., Aymerich S., Declerck N., & Royer C.A. Absolute quantification of gene expression in individual bacterial cells using two-photon fluctuation microscopy. *Analytical Biochemistry*, **419**(2):250, 2011

[146] Cordero M.L., Rolfsnes H.O., Burnham D.R., Campbell P.A., McGloin D., & Baroud C.N. Mixing via thermocapillary generation of flow patterns inside a microfluidic drop. *New Journal of Physics*, **11**(7):075033, 2009